

# Capacitive-Gap MEMS Resonator-Based Oscillator Systems for Low-Power Signal Processing

*Thura Lin Naing*



Electrical Engineering and Computer Sciences  
University of California at Berkeley

Technical Report No. UCB/EECS-2017-14

<http://www2.eecs.berkeley.edu/Pubs/TechRpts/2017/EECS-2017-14.html>

May 1, 2017

Copyright © 2017, by the author(s).  
All rights reserved.

Permission to make digital or hard copies of all or part of this work for personal or classroom use is granted without fee provided that copies are not made or distributed for profit or commercial advantage and that copies bear this notice and the full citation on the first page. To copy otherwise, to republish, to post on servers or to redistribute to lists, requires prior specific permission.

**Capacitive-Gap MEMS Resonator-Based Oscillator Systems for Low-Power  
Signal Processing**

by

Thura Lin Naing

A dissertation submitted in partial satisfaction of the

requirements for the degree of

Doctor of Philosophy

in

Engineering – Electrical Engineering and Computer Sciences

in the

Graduate Division

of the

University of California, Berkeley

Committee in charge:

Professor Clark T.-C. Nguyen, Chair

Professor Elad Alon, Co-chair

Professor Ali Javey

Professor Liwei Lin

Summer 2015

**Capacitive-Gap MEMS Resonator-Based Oscillator Systems for Low-Power  
Signal Processing**

Copyright 2015  
by  
Thura Lin Naing

## Abstract

Capacitive-Gap MEMS Resonator-Based Oscillator Systems for Low-Power Signal Processing

by

Thura Lin Naing

Doctor of Philosophy in Engineering – Electrical Engineering and Computer Sciences

University of California, Berkeley

Professor Clark T.-C. Nguyen, Chair

Professor Elad Alon, Co-chair

Wireless technology, which already plays a major part in our daily lives, is expected to further expand to networks of billions of autonomous sensors in coming years: the so-called Internet of Things. In one vision, sensors employing low-cost, low-power wireless motes collect and transmit data through a mesh network while operating only on scavenged or battery power. RF MEMS provides one approach to the stringent power and performance required by sensor networks.

This dissertation presents improvement to these MEMS technologies and introduces new approaches for wireless communication in low power wireless networks. First, this work presents oscillators based on the capacitive-gap transduced MEMS resonator. As wireless radio needs at least one such oscillator, the space and power savings offered by these MEMS oscillators make them compelling alternatives over bulky quartz-based devices. The high quality factors ( $Q$ )  $> 100,000$  possible in these on-chip resonators allow for phase noise performance of the oscillator exceeding even the challenging GSM specifications using less than  $100 \mu\text{W}$  of power consumption. Despite their small size and tiny capacitive gaps, MEMS-based oscillators are found to be insensitive to vibration and achieve only a few ppm shift in frequency over 10 months of measurement: the performance shown is on par or better than the off-the-shelf crystal oscillators. Interestingly, exploiting nonlinearities in the MEMS resonators also allows multiple simultaneous oscillation frequencies using one amplifier. Combined with electrical stiffness-based frequency tuning, this enables Frequency-Shift Keyed modulation of the output waveform, offering a space and power-efficient multichannel transmitter, as desired for mobile applications requiring long battery life.

Intrinsically, oscillator systems involve positive feedback loops, which regeneratively amplify signals in the loop. Taking advantage of this property, MEMS oscillator systems may be used for other wireless signal processing applications. This dissertation explores such systems applied to: 1) a narrow channel-select filter with low insertion loss unachievable using passive resonators only and 2) a super-regenerative amplification-based channel-selecting

radio transceiver. Finally, this dissertation presents two capacitive-gap transduced micromechanical resonator designs which can achieve the high  $Q$  at GHz frequencies needed for many wireless communication standards. The methods and solutions provided here pave a path towards realization of future low-power wireless technologies.

Dedicated to my parents, Myint Naing and Khin Shwe.

# Contents

<b>Contents</b>	<b>ii</b>
<b>List of Figures</b>	<b>v</b>
<b>List of Tables</b>	<b>xv</b>
<b>1 Introduction</b>	<b>1</b>
1.1 Challenges Associated with Achieving Low-power Reference Oscillators . . . .	2
1.1.1 Frequency Instability due to Vibration and Long-term Drift . . . . .	4
1.2 Oscillator-Based Low-Power Signal Processors . . . . .	6
1.3 Organization of Dissertation . . . . .	7
<b>2 Capacitive-Gap Disk Device Design</b>	<b>8</b>
2.1 Device Structure and Operation . . . . .	8
2.1.1 Excitation and Detection . . . . .	8
2.2 Resonator Frequency Design . . . . .	10
2.3 Lumped Parameter Equivalent Circuits . . . . .	11
2.3.1 Lumped Parameter Mechanical Equivalent Circuit . . . . .	12
2.3.2 Lumped Parameter Electrical Equivalent Circuit . . . . .	14
2.3.3 Electrical Stiffness . . . . .	15
2.3.4 Reduced 2-Port Model . . . . .	16
<b>3 Oscillator Design</b>	<b>20</b>
3.1 Basic Oscillator Concepts . . . . .	20
3.2 Pierce Amplifier Design . . . . .	21
3.2.1 Lossless Analysis . . . . .	24
3.2.2 Lossy Analysis . . . . .	27
3.2.3 Minimizing Power Consumption . . . . .	27
3.3 TransImpedance Amplifier Design . . . . .	28
3.4 Pierce vs. Transimpedance Amplifier Oscillators . . . . .	33
3.5 Amplifier-Derived Frequency-Pulling . . . . .	35
3.6 Oscillation Start-up . . . . .	35

<b>4</b>	<b>Device Fabrication and Measurement Methods</b>	<b>37</b>
4.1	Self-Aligned Stem Process . . . . .	37
4.2	Planarized Process . . . . .	39
4.3	Measurement Methods . . . . .	41
4.3.1	Resonator Measurement Methods . . . . .	41
4.3.2	Oscillator Measurement Methods . . . . .	43
<b>5</b>	<b>61-MHz Low-Power Pierce Oscillator</b>	<b>47</b>
5.1	Phase Noise . . . . .	47
5.2	Experimental Verification . . . . .	53
<b>6</b>	<b>Oscillator Frequency Stability</b>	<b>59</b>
6.1	Acceleration Sensitivity . . . . .	59
6.1.1	Acceleration-Induced Oscillator Frequency Instability . . . . .	60
6.1.2	Resonator Acceleration Sensitivity . . . . .	61
	Mechanical Stress-Induced Frequency Instability . . . . .	61
	Electrical Stiffness-Induced Frequency Instability . . . . .	62
6.1.3	Measurement Setup . . . . .	64
	Parasitic Acceleration Sensitivity . . . . .	65
6.1.4	Measurement Results . . . . .	67
6.2	Long-Term Stability . . . . .	71
6.2.1	Stable Measurement Environment . . . . .	71
	Packaging . . . . .	71
	Temperature Control . . . . .	73
	Frequency Measurement . . . . .	74
6.2.2	Measurement Results . . . . .	75
<b>7</b>	<b>Oscillator Systems for Signal Processing</b>	<b>78</b>
7.1	Simultaneous Multi-Frequency Switchable Oscillator and FSK Modulator . . . . .	78
7.1.1	Device Design and Operation . . . . .	79
7.1.2	Oscillator Design and Limiting . . . . .	81
	Amplifier Limiting . . . . .	82
	Resonator Limiting . . . . .	82
7.1.3	Experimental Results . . . . .	83
7.2	Active $Q$ -Control for Improved Insertion Loss Micromechanical Filters . . . . .	88
7.2.1	$Q$ and Insertion Loss Adjustable Resonator . . . . .	88
	Resonator-Amplifier Electrical Model . . . . .	90
	Amplifier-Derived Frequency-Pulling . . . . .	92
7.2.2	Active $Q$ -Boosted Filter Implementation . . . . .	93
	Adjustable Dynamic Range . . . . .	94
	Power Consumption Considerations . . . . .	95
7.2.3	Experimental Results . . . . .	95

<b>8 Super-Regenerative Transceiver</b>	<b>99</b>
8.1 Background	99
8.2 The Regenerative Transceiver	100
8.3 Experimental Realization	103
8.3.1 Measurements	104
<b>9 Avenues Towards Higher Frequency Operation</b>	<b>107</b>
9.1 Whispering-Gallery Mode Disk Resonators	107
9.2 Spoke-Supported Ring Resonators	111
9.3 Measurement Results	114
9.3.1 Whispering-Gallery Mode Disk Resonator Results	114
9.3.2 Spoke-Supported Ring Resonator Results	116
9.4 Device Design Insights	121
<b>10 Conclusions</b>	<b>123</b>
<b>Bibliography</b>	<b>126</b>
<b>A Spoke-Supported Ring Resonator Design Details</b>	<b>134</b>
A.1 Device Structure and Operation	134
A.2 Resonator Frequency Design	136
A.3 Support Design	139
A.3.1 Maximizing Resonator $Q$	140
A.3.2 Realizing Exact Quarter-Wavelength Dimensions	141
A.3.3 Quarter-Wavelength Spoke Support Design	141
A.3.4 The Center Anchor Advantage	144
A.3.5 Practical Spoke-Supported Ring Design	146
A.4 Lumped Parameter Equivalent Circuits	147
A.4.1 Lumped Parameter Mechanical Equivalent Circuit	147
A.4.2 Lumped Parameter Electrical Equivalent Circuit	149
A.4.3 Reduced Model	152
<b>B Planarized Process Traveler</b>	<b>154</b>

# List of Figures

1.1	Motivation: Internet of Things . . . . .	1
1.2	A simplified schematic of a typical receiver showing the desired signal masked by the in-band interference which is modulated with the noisy local oscillator (LO) signal. . . . .	3
1.3	Block diagram of a local oscillator using a Phase-Locked Loop (PLL). . . . .	3
1.4	(a) $g$ -force number in environment. (b) Conceptual drawing of an oscillator output power spectrum: the blue line represents the spectrum without acceleration while the red curve illustrates a broad spectrum of increased phase noise under random vibration. . . . .	4
2.1	(a) Perspective view of a Wine-Glass mode disk resonator in typical two-port bias schemes, (b) resonator mode shape, and (c) top-view schematic diagram of the MEMS resonator. Note: electrodes with the same color are electrically connected together. . . . .	9
2.2	(a) Complete equivalent circuit model for a Wine-Glass disk resonator. (b) The load circuit model of a single electrode for the disk resonator. (c) Physically consistent model using actual values of damping, stiffness and mass for elements in a two-port configuration when all input electrodes and output electrodes are connected as shown in Fig. 2.1. . . . .	13
2.3	(a) Resonator small-signal equivalent circuit with the core tank circuit of the resonator shown in red. Parasitic capacitance and resistance elements are shown in black. (b) Rearrangement of components of (a) in a more intuitive configuration. . . . .	17
2.4	Calculated (a) frequency shift, (b) motional resistance, (c) $(C_x/C_o)$ , (d) $C_x$ , (e) static overlap capacitance $(C_o)$ , and $(C_x/C_o^2)$ as a function of the electrode subtended angle $(\Delta\theta)$ for a compound (2,1) mode polysilicon disk resonator with $32\ \mu\text{m}$ radius and $80\ \text{nm}$ capacitive gaps designed for a 61-MHz frequency of operation ( <i>cf.</i> Fig. 2.1(b)). . . . .	18
3.1	Perspective-view schematic of the capacitive-gap micromechanical disk resonator combined with a sustaining transconductance amplifier. . . . .	21

3.2	(a) Small-signal equivalent circuit of the complete Pierce oscillator using lumped impedances $Z_1$ , $Z_2$ , and $Z_3$ , which model all capacitance and resistance components of the transistors $M_1$ (except its transconductance $g_{m1}$ ), $M_2$ , and $M_3$ . (b) Small-signal equivalent circuit of the complete TIA-based oscillator. . . . .	22
3.3	Schematic of the CMOS amplifier used in the Pierce oscillator, including bias network and parasitic capacitance at input and output nodes. . . . .	23
3.4	Complete small-signal oscillator circuit model indicating the division between amplifier and resonator used for impedance modeling. Here, $C_{1,r}$ , $C_{2,r}$ , and $C_{3,r}$ in Fig. 2.3 are combined with $C_1$ , $C_2$ , and $C_3$ in $Z_1$ , $Z_2$ , and $Z_3$ . . . . .	24
3.5	(a) Theoretical plots of amplifier gain, $-R_{amp}$ , vs. transconductance, $g_{m1}$ , of the $M_1$ transistor, together with the required power consumption to achieve this $g_{m1}$ , and (b) corresponding plots of amplifier reactance, $X_{amp}$ . The black dashed lines correspond to calculated motional resistances of the resonator for different $V_P$ 's. The green line represents a lossless oscillator with typical values for $C_{1-3}$ that easily generates sufficient gain for oscillation, while the black curve illustrates the detriment of increasing $C_3$ by two times, resulting in no oscillation for $V_P$ of 6.6 V. Increasing $C_1$ and $C_2$ by three times allows the oscillation for $V_P = 6.6$ V case at the cost of burning significantly larger power as shown by the blue curve. The red curve includes typical parasitic loss/resistance of the amplifier and resonator. $V_{DD} = 2$ V and $V^* = 0.16$ V are used. Here, $V^* = 2I_{D1}/g_{m1}$ where $I_{D1}$ is the drain current of $M_1$ . . . . .	26
3.6	(a) Theoretical predictions of $g_{m1,crit}$ and power consumption requirements to achieve oscillation vs. resonator capacitive-gap spacing. The green curve assumes the lossless case of Eqn. (3.9), where power consumption decreases without limit as gap is shrunk. The blue curve includes amplifier loss/resistance while the red curves also include additional resonator parasitic resistance, showing a minimum power plateau regardless of decreased gap spacing. Here, $V_{DD} = 2$ V, $V^* = 0.16$ V, and $V_P = 8.7$ V with the same capacitor values as in Fig. 3.5. . . . .	29
3.7	Schematic of the CMOS amplifier used in the TIA-based oscillator. . . . .	30
3.8	Complete small-signal oscillator circuit model indicating the division between amplifier and resonator used for impedance modeling. Here, $C_{1,r}$ and $C_{2,r}$ , and $C_{3,r}$ in Fig. 2.3 are combined with $C_1$ and $C_2$ . . . . .	31
3.9	(a) Theoretical prediction of resistance (black) and reactance (dotted blue) parts of the impedance, $Z_{amp}$ , looking into the TIA amplifier as the feedback resistor, $R_F$ , increases. Here, resistance and capacitance values used are given in Fig. 3.10. (b) Theoretical prediction of magnitude (black) and phase (dotted blue) of $Z_{amp}$ . Note: the operating frequency simulated here is 61 MHz. . . . .	32

3.10	Theoretical plots of amplifier gain, $-R_{amp}$ , vs. $g_{m1}$ of the $M_1$ transistor, together with the required power consumption to achieve this $g_{m1}$ . Here, $V_{DD}=2$ V and $V^* = 0.16$ V are used to calculate power numbers. The black dashed lines corresponds to calculated motional resistances of the resonator for different $V_P$ 's. The red line represents an oscillator with typical values of $C_1$ and $C_2$ that easily generates sufficient gain for oscillation for $V_P$ of both 6.6 V and 8.7 V. The dotted blue line is generated using Eqn. (3.22) and illustrates that the approximation of ( $A_v \gg 1$ ) gives similar values for $-R_{amp}$ . . . . .	33
3.11	Theoretical plots of amplifier gain, $-R_{amp}$ , vs. the required power consumption. The black dashed lines correspond to calculated motional resistances of the resonator for different $V_P$ 's. The red line and the blue line represents the TIA-based oscillator and the Pierce oscillator with typical values for parasitic capacitance and resistance given in Fig. 3.5 and Fig. 3.9. $V_{DD}=2$ V is used. . . . .	34
4.1	Fabrication process flow for polysilicon and microcrystalline diamond disk resonators. (a)-(d) illustrate the resonator construction through repeated LPCVD film depositions, lithography, and plasma etches, followed by a 49% HF wet etch process to remove the sacrificial oxide to yield the final released structure of (e). Note: the Wine-Glass disk resonator normally does not have a center stem. Here, a center stem such as used for a contour-mode disk resonator is included in the process flow to illustrate the self-align feature of this process. . . . .	38
4.2	Fabrication process flow for polysilicon and microcrystalline diamond disk resonators. (a)-(c) illustrate the resonator construction through repeated LPCVD film depositions, lithography, chemical-mechanical polishing, and plasma etches, followed by a 49% HF wet etch process to remove the sacrificial oxide to yield the final released structure of (d). Note: the process cross sections presented here are for thick polysilicon interconnects. . . . .	40
4.3	Schematics comparing (a) a typical two-port measurement scheme and (b) the mixing measurement scheme used here to bypass the parasitic feedthrough path for the fabricated devices. In both cases, measurements employ a network analyzer with $R_S = R_L = 50\Omega$ . . . . .	41
4.4	SEMs of a fabricated Wine-Glass disk resonator (a) using the self-aligned stem process described in Section 4.1 and (b) using the planarized process described in Section 4.2. . . . .	44
4.5	The measured frequency response of a typical Wine-Glass disk resonator. . . . .	44
4.6	(a) IC die photo of the Pierce oscillator. (b) IC die photo of the TIA oscillator. . . . .	45
4.7	(a) Photo of the packaged oscillator in a custom-designed vacuum box. (b) Photo of the wire-bond oscillator on a Printed Circuit Board (PCB) in a bell-jar vacuum environment. . . . .	46

5.1	(a) impulse sensitivity function $\Gamma_{OUT}$ (red) for current noise injected at node $v_{OUT}$ , with oscillator output waveform for reference (black) and, (b) $\Gamma_{RES}$ (red) for voltage noise injected in series with the resonator, together with resonator current, $i_x$ (black) as a function of oscillation phase. Here, simulations assume operating conditions of the 43 $\mu$ W bias in Table 5.1. . . . .	50
5.2	(a) Phase-dependent shaping functions, $\alpha$ , and (b) effective $\Gamma(\theta)$ functions of transistor $M_1$ (red) and $M_2$ (blue) operating at the 43 $\mu$ W bias condition in Table 5.1. Here, the corresponding rms and $c_0$ values are found: $\Gamma_{rms,M1} = 2.13 \times 10^{-5}$ , $\Gamma_{rms,M2} = 2.58 \times 10^{-5}$ , $c_{0,M1} = 8.46 \times 10^{-7}$ , and $c_{0,M2} = -9.25 \times 10^{-7}$ . . . . .	51
5.3	The predicted phase noise plot (solid black) generated using Eqn. (5.6) and the simulated functions of Fig. 5.1 and Fig. 5.2 overlaid on top of the measured phase noise (red). The dashed black line predicts phase noise performance when resonator $Q$ is reduced to 800 while maintaining constant motional resistance. Here, the flicker noise corner frequencies of $M_1$ and $M_2$ are found in simulation to be 16.6 MHz and 1.6 MHz, respectively, while the flicker noise corner frequency of $v_{n,B}^2$ is 648 kHz with noise floor of $1.29 \times 10^{-15}$ V <sup>2</sup> /Hz. . . . .	53
5.4	(a) Pierce oscillator output waveform measured on an oscilloscope and (b) output spectrum as measured on a spectrum analyzer. . . . .	54
5.5	Measured start-up time response of the oscillator when $V_P$ of the resonator is turned on at $t=0$ . An increased resonator bias voltage increases total loop gain, and hence speeds start-up time of the blue curve compared to the red as expected from Eqn. (3.31). . . . .	54
5.6	Measured phase noise of 61-MHz oscillators comparing the new Pierce topology and an TIA topology similar to [13], as well as the Pierce oscillator phase noise divided down to 13 MHz for comparison to the GSM spec. . . . .	55
5.7	Measured phase noise of the oscillator operating on varying supply voltages. A reduction in $V_{DD}$ and $I_{BIAS}$ can be seen to decrease power consumption by 61% with only a modest decrease in phase noise performance. . . . .	55
5.8	Measured phase noise of oscillators using two resonators with two different gaps. A reduction in gaps from 80 nm to 40 nm can be seen to decrease power consumption by 4.9 $\times$ . Note: the phase noise plots are divided down to 13 MHz oscillation frequency. . . . .	57
6.1	A typical oscillator output power spectrum in the presence of vibration with frequency $f_v$ . The ratio between the sidebands and output characterizes the acceleration sensitivity of the oscillator. The red curve illustrates a broad spectrum of increased phase noise under random vibration. . . . .	60
6.2	Finite Element Simulation (FEM) of the resonator subjected to (a) lateral acceleration and (b) vertical acceleration, showing stress concentrations in the structure. . . . .	61
6.3	(a) Schematic of the resonator along with the electrical stiffness formula. (b) Overlapping area and (c) gap spacing change when the resonator experiences vertical and lateral acceleration, respectively. . . . .	62

6.4	The measured output power spectrum of the Wine-Glass disk oscillator. Inset: its measured output waveform. . . . .	64
6.5	(a) Schematics of measurement setups used to measure the voltage noise induced by various electronic components under acceleration. The table summarizes the measured <i>rms</i> voltage noise caused by various electronic components under a sinusoidal acceleration with 5.66 <i>g</i> amplitude. (b) Theoretical prediction of the required sinusoidal noise voltage amplitude to be applied on the $V_P$ line to produce the same equivalent $\Gamma$ -factor for the 61-MHz Wine-Glass disk resonator under 5.66 <i>g</i> amplitude of sinusoidal acceleration. Here, the resonator's thickness is 3 $\mu\text{m}$ , its gap is 80 nm, and its $Q$ is 100k. The frequency pull-in due to amplifier is assumed to be zero. . . . .	65
6.6	Acceleration sensitivity measurement setup. . . . .	66
6.7	Plot of measured $\Gamma$ components versus vibration frequency. . . . .	68
6.8	Plot of measured $\Gamma$ vector sum versus vibration frequency for the 61-MHz micromechanical disk oscillator alongside similar plots for previous work using a similar resonator device and a measured 66.67-MHz off-the-shelf crystal oscillator. . . . .	68
6.9	Plot of $\Gamma$ vector sum versus vibration frequency for the 61-MHz micromechanical disk oscillator alongside lines indicating the performance of oscillators in the literature and that of the theoretical expectation. . . . .	69
6.10	Plot of measured $\Gamma$ components versus vibration frequency. . . . .	70
6.11	Measured Wine-Glass disk MEMS resonator $Q$ as a function of ambient air pressure. . . . .	72
6.12	Hemmermetic vacuum packaging tool with zoom-in (inset) on a DIP package sealed via the tool. . . . .	73
6.13	Experimental measurement setup showing the oscillator mounted in the first temperature controlled oven (inset) and placed in a second environmental chamber oven for further temperature stability. The oscillator frequency is measured via a zero dead-time counter referenced to an atomic clock. . . . .	74
6.14	Typical oscillator stability over 24 hours with a 1 s averaging time. . . . .	75
6.15	Measured frequency drift and temperature stability of the MEMS oscillator. Frequency measurements were made using an Agilent 53230A frequency counter and shown here with a 100s measurement time. . . . .	76
6.16	Amplitude of oscillation during a long-term measurement. . . . .	76
6.17	Allan deviation as calculated from stability data with differing averaging times. Data with averaging time below 400 s was calculated from shorter data sets taken at 0.01 s sample time, while longer averaging time data was calculated from the full long-term stability data. . . . .	77
7.1	Schematic of the Pierce topology multi-oscillator circuit used in this work. Independent tuning voltages and input bit streams are applied to Res. 1 and Res. 2. In each array-composite resonator, electrodes with the same color are electrically connected together. Inset shows FEM mode shape simulation of the two-disk array. . . . .	79

7.2	Perspective view of a single MEMS two-disk array-composite comprising two suspended, mechanically-coupled disk resonators (orange) anchored at their 4 nodal points. Tuning electrodes (green) on one disk allow for electronic frequency control while input (blue) and output electrodes (purple) on the second one connect to bus bars to provide a multi-port multi-resonator device. . . . .	80
7.3	(a) Oscillation frequency tuning vs. applied voltage across the capacitance gap of the tuning resonator. (b) Frequency response as measured by an Agilent E5071C network analyzer for a two-disk array-composite with both resonators turned ‘on’ via applied bias voltage. . . . .	81
7.4	SEMs of the fabricated MEMS circuit and die photo of the custom-made CMOS amplifier IC. Wirebond connections shown in orange. . . . .	83
7.5	(a) Measured (solid lines) and theoretical (dashed lines) spring softening and damping nonlinear response as a function of increasing drive voltage. (b) The phase response for a modeled resonator at the same frequency and drive levels as the experimental data. . . . .	84
7.6	Pierce oscillator output spectra measured on an Agilent N9030A spectrum analyzer. (a) shows oscillator output with resonator 1 turned on via an applied bias of 9.35 V, (b) with 11.6 V applied to resonator 2, and (c) simultaneous oscillation with bias voltages applied to both. . . . .	85
7.7	Measured oscillator output waveform of the Pierce-based circuit with two resonators active. . . . .	86
7.8	TIA-based oscillator output spectra with (a) one resonator turned on and (b) both resonators on and loop gain increased by $\sim 30\%$ in an attempt to produce simultaneous oscillation. Oscillation at one frequency desensitizes the TIA, suppressing output at the other. . . . .	86
7.9	Applying the 40 kbps modulation bit stream of (a) to the tuning electrodes on one disk array-composite generates the measured FSK modulated waveform of (b), shown mixed down to $\sim 20$ kHz to facilitate visualization. . . . .	87
7.10	$Q$ -boosted parallel filter comprised of two independent Wine-Glass disk resonator and amplifier circuits, all in a typical measurement circuit. Here, the filter input is driven differentially while output currents are combined to generate the response of Fig. 7.14. . . . .	89
7.11	Circuit schematic of an active $Q$ -controlled resonator. A transimpedance amplifier provides closed-loop feedback using two electrodes of a Wine-Glass resonator, while the remaining two electrodes serve as input/output. . . . .	89
7.12	Equivalent small signal circuit model for the $Q$ and insertion loss adjustable resonator of Fig. 7.11, with electrodes 1-2 used for input and output and electrodes 3-4 embedded in a feedback loop with the amplifier to enable control of $Q$ . . . . .	90
7.13	Theoretical prediction of resistance (dotted blue) and reactance (black) parts of the impedance, $Z_{amp}$ , looking into the TIA amplifier as the feedback resistor, $R_F$ , increases. Here, approximate resistance and capacitance values for the amplifier in this work are used for simulation. . . . .	91

7.14	Description of parallel filter operation, where two differentially driven bandpass biquad responses add to form a flat passband (between the peaks) and subtract in the stopband (outside the peaks) to provide greater stopband rejection. . . . .	93
7.15	Simulated parallel filter responses for a narrow 0.002% bandwidth filter with low $Q$ (intrinsic device's $Q$ equivalent to $1.36 \times BW_{fil}$ (blue), $Q$ -boosted by two times (black), and $Q$ -boosted by 22 times (red). (a) shows responses for constant $R_Q$ (its value is the needed $R_Q$ for highest $Q$ case) and $IL$ improvement of 12 dB. (b) illustrates that the filter can be terminated properly by adjusting the bias voltage across input and output gaps while $R_Q$ is kept constant. Boosting $Q$ by 22 times improves $IL$ by 23 dB. Note that the $Q$ equivalent to $1.36 \times BW_{fil}$ (blue case) is too small for the filter to be terminated properly. . . . .	94
7.16	Single resonator $Q$ -boosting as a function of amplifier gain with constant $V_P = 8.5$ V. As $V_{GAIN}$ is decreased amplifier gain increases, boosting effective resonator $Q$ (blue curves) from an initial intrinsic $Q=57,000$ to a maximum boosted $Q$ of 2.3 million (red). On the other hand, decreasing $V_{GAIN}$ further allows control of amplifier phase shift, leading to negative feedback and allowing controlled loading of $Q$ (green curves). The inset demonstrates independent tuning of frequency and insertion loss via control of the voltage across input-output electrode-disk gap, all while holding $Q$ constant by holding $V_{GAIN}$ constant. . . . .	96
7.17	Measured effective quality factor (red) and insertion loss (blue) of the resonator with constant $V_P = 8.5$ V as $V_{GAIN}$ of the amplifier changes. . . . .	97
7.18	Measured transmission for a two-resonator filter hooked up as in Fig. 7.10 and terminated by the designed (i.e., required) value of 1.7 k $\Omega$ at both input and output for the cases with (red) and without (blue) $Q$ -boosting TIA's. . . . .	97
8.1	Perspective-view schematic (a) of the micromechanical disk resonator circuit used in this work. (b) presents the high $Q \sim 100,000$ resonator frequency response, which may be tuned as in (c) via negative electrical stiffness with applied voltage to select one of several communication channels as illustrated in (d). . . . .	100
8.2	Schematic of the regenerative MEMS radio transceiver configured in receive-mode. Here, the MEMS resonator applies the needed channel-selecting filter to RF signals picked up by the antenna. The ASIC amplifier regeneratively amplifies this weak received in-band signal to produce a growing oscillation output, periodically quenched via $V_{CON}$ . An envelope detector, comparator and flop-flop latch recovers the original transmitted digital data. . . . .	101
8.3	Conceptual operation of the regenerative receiver. The BFSK modulated and transmitted waveform of (a) gives rise to the periodically restarted oscillation of (b), where the on-resonance signal generates faster oscillation growth. Here, amplifier output drops to zero when $V_{con}$ is raised, though resonator motion decays with a time constant based on resonator $Q$ . Finally, envelope amplitudes which exceed $V_{th}$ in (c) allow discrimination of 0s and 1s, recovering the original data in (d). . . . .	101

8.4	Schematic of the MEMS radio transceiver configured in transmit-mode where demodulating circuitry is switched out for an FSK modulating input to the capacitive-gap disk. With TIA gain no longer quenched, a continuous RF carrier is generated. . . . .	102
8.5	Measurement setup consisting of the regenerative transceiver dies mounted on a Printed Circuit Board (PCB) and measured in a bell-jar vacuum environment. The inset displays the MEMS and ASIC dies, both fabricated with many devices on a single die, one each of which is bondwired to the PCB. . . . .	103
8.6	Measured receiver operation for a 1 kbps bit-stream transmitted across a distance of 4 m as in Fig. 8.2 using a Binary-FSK modulated transmitter with 1kHz shift and output power of -17 dBm (20 $\mu$ W). The transmitted data-stream (a) is BFSK encoded and transmitted on a 60.6 MHz RF carrier (b) using a bench-top signal generator (shown mixed down to 2 kHz). Regenerative detection yields (c) amplitude following envelope detection; (d) shows resultant signal following comparator; and (e) presents the final recovered data-stream clocked by the output flip-flop. Here, the MEMS resonator is biased with 10.3 V, and the ASIC is operated on a 2.1 V supply drawing $\sim$ 233 $\mu$ A. . . . .	105
8.7	Measured regenerative receiver signal when transmitter is shifted by 4 kHz to a near-by channel and increased 30dB in power. . . . .	106
8.8	Measured FSK modulation at a 1kHz mark-space frequency separation generated using the transmit-mode configuration of Fig. 8.4. With the applied modulation signal (a), a continuous-phase output modulation is produced (b), shown here mixed down to $\sim$ 2 kHz for presentation. . . . .	106
9.1	Perspective views of disk resonators in typical two-port bias schemes for 3 <sup>rd</sup> Whispering-Gallery Mode. Note: electrodes with the same color are electrically connected together. . . . .	108
9.2	Finite element simulated modes for the 2 <sup>nd</sup> , 4 <sup>th</sup> , 6 <sup>th</sup> , and 10 <sup>th</sup> Whispering-Gallery Modes. It shows that the movement of the disk moves to the edge as the mode number increases. . . . .	108
9.3	Plots of (a) the resonance frequency and (b) the motional resistance, $R_x$ , of the disk with $R = 20 \mu\text{m}$ versus the mode number. Plots of (c) the disk radius and (b) the motional resistance, $R_x$ , of the disk for the 1 GHz resonance frequency design versus the mode number. . . . .	109
9.4	Perspective views of ring resonators in typical two-port bias schemes for (a) electrode configuration A; and (b) electrode configuration B. . . . .	111
9.5	Finite element simulated modes for the spoke-supported ring resonator and longitudinal supporting beam of Fig. 9.4(a). (a) 1 <sup>st</sup> contour mode (symmetric). (b) 2 <sup>nd</sup> contour mode (anti-symmetric). . . . .	112
9.6	FEM simulations comparing modal displacements when the supports are (a) quarter-wavelength and (b) non-quarter-wavelength. . . . .	113

9.7	SEM showing the fabricated disk device. The micromechanical resonator consists of a 17 $\mu\text{m}$ -radius, 2 $\mu\text{m}$ -thick micro-crystalline HF CVD diamond disk. The inset zooms in on the tiny 100 nm capacitive gap between disk . . . . .	114
9.8	Measured responses for diamond disk resonators operating (a) in the radial contour mode with $Q=17.3\text{k}$ at 309 MHz; and (b) in the 4 <sup>th</sup> Whispering-Gallery mode for the same device with $Q = 47.9\text{k}$ at 510 MHz, which constitutes a 4.6 $\times$ improvement in $f \cdot Q$ product. . . . .	115
9.9	Measured frequency characteristic for a second diamond disk device with a remarkable $Q = 109.2\text{k}$ at 515 MHz. While of the same diamond resonator design, this device did not have fully notched electrodes, so had significantly less coupling.	115
9.10	SEM's of fabricated ring resonators: (a) a 900-MHz diamond ring with polysilicon stem using electrode configuration B; and (b) a 3-GHz diamond ring with polysilicon using electrode configuration A . . . . .	116
9.11	Mixing-measured frequency response of a 2 <sup>nd</sup> mode 900-MHz diamond spoke-supported ring with polysilicon stem. . . . .	118
9.12	Mixing-measured frequency response of the 2 <sup>nd</sup> mode 2.97-GHz ring demonstrating the highest to-date $f \cdot Q$ product of $1.27 \times 10^{14}$ . . . . .	119
9.13	Measured frequency response (black dots) of the two strongest modes of several 900 MHz ring resonators as their support beam lengths change. The data matches well the FEM-simulated blue and red curves. . . . .	120
9.14	Measured difference in resonator insertion loss (blue dots) of the two strongly coupled modes shown in Fig. 9.13 as support beam length changes. When the beam length approaches $\lambda/4$ , the ring is virtually "levitated", so behaves as if it had no supports. This enhances its motional amplitude and lowers its insertion loss, all while suppressing the 2 <sup>nd</sup> hybrid mode. . . . .	120
9.15	The $f \cdot Q$ products of previously published high $f \cdot Q$ acoustic resonators along with the ring resonators presented here. . . . .	121
A.1	Plot of the resonance frequency of a spoke-supported ring with $r_o=20 \mu\text{m}$ and variable $r_i$ in its 1 <sup>st</sup> , 2 <sup>nd</sup> , 3 <sup>rd</sup> , and 4 <sup>th</sup> modes. The dotted lines show the behavior using Eqn. (A.16). $f_d$ is the fundamental resonance frequency of a solid disk with radius $r_o$ . . . . .	138
A.2	The first, second, third, and fourth mode shapes for spoke-supported rings with $r_i/r_o=0.2$ , $r_i/r_o=0.5$ , and $r_i/r_o=0.8$ , all with $r_o=20 \mu\text{m}$ . . . . .	139
A.3	Perspective-views of (a) a radial ring resonator in [79] and (b) an extensional Wine-Glass mode ring resonator of [80]. . . . .	140
A.4	Equivalent lumped mechanical model for a micromechanical spoke-supported ring resonator (a) using the mobility analogy, in which nodes represent velocities; and (b) using the impedance analogy, in which nodes represent forces. . . . .	142
A.5	Equivalent circuits for supporting beams. The beam (a) is modeled as a general transmission-line to give the effective $T$ -network models (b). (c) shows the ideal $T$ -network model when exact quarter wavelength design is used. . . . .	143

A.6	Effective mechanical impedance, $(Z_a + Z_c)/j$ , seen by a 433 MHz ring resonator for a 1 $\mu$ m-wide, 2 $\mu$ m-thick diamond support beam. . . . .	145
A.7	(a) Complete equivalent circuit model for a spoke-supported ring resonator with four inner (electrode 1-4) and two outer (electrode 5-6) electrodes. (b) Physically consistent model using actual values of damping, stiffness and mass for elements in a two-port configuration when all input electrodes and output electrodes are connected respectively as shown in Fig. 9.4(a) and (b). . . . .	150

# List of Tables

2.1	Materials' properties [37], [38] and their corresponding constants in Eqn. (2.9) . . . . .	12
3.1	The 61MHz compound (2,1) mode disk resonator's parameters for different $V_P$ 's . . . . .	22
5.1	Resonator and amplifier design summary. . . . .	49
5.2	Oscillator performance comparison . . . . .	57
7.1	Design and extracted parameters of the fabricated MEMS array-composite. . . . .	84
9.1	Spoke-supported ring resonator design and performance summary. . . . .	117

## Acknowledgments

My seven years of doctoral research life has been quite a journey. I've lost count of the number of memorial moments during the last seven years as well as the number of nights I spent in Cory Hall and the Berkeley Nanolab. I would not have possibly passed through this journey without help and support from many wonderful people. I would like to take this opportunity to express my gratitude to each and every one of them.

First I would like to thank my research advisor Prof. Clark T.-C. Nguyen. Coming from an integrated circuit background, I learned much of my RF MEMS and fabrication knowledge from him. During the first two years, his mandatory weekly meetings made me transform from a mediocre beginning graduate student to a capable researcher. I am very grateful that he gave me the freedom and support to explore ideas that interested me in the last three years. Perhaps the most important skill I learned from him might be attention to detail. His attention to detail taught me how to deconstruct my research problems into the most fundamental pieces. His understanding and support helped me achieve many of the results presented in this dissertation.

I would also like to show my gratitude to my co-advisor Prof. Elad Alon. I learned much of communication IC design from him, either during his lectures or from the discussions with him. During our weekly meeting, I was always amazed by his ability to effortlessly see through my research problems. His constructive questions which followed always pointed me to a direction for me to investigate.

I thank Prof. Ali Javey and Prof. Liwei Lin for being a part my qualification exam and dissertation committee and providing valuable feedback.

It was truly my pleasure to work and share experience with past and current Nguyen group members. I wish to thank Zeying Ren for fabricating MEMS devices used in some of the results in this work, Dr. Mehmet Akgul for sharing his fabrication experience, Turker Beyazoglu; Ruonan Liu; and Jalal Naghsh Nilchi for helping me with measurements, and Bobby Schneider and Henry Barrow for giving me a chance to work with them in their projects. I would like to acknowledge useful discussion with Divya Kashyap, Dr. Bongsang Kim, Wei-Chang Li, Dr. Yang Lin, Alper Ozgurluk, Dr. Tommi Riekkinen, Lingqi Wu, and Victor Yen.

I am blessed to have a chance to work with Berkeley Nanolab staffs and members for up-keeping the lab and sharing useful process information. Particularly, I thank Dr. Bill Flounders, Rich Hemphill, Joe Donnelly, Ryan Rivers, Jay Morford, David Lo, Eric Chu, and Jason Chukes for their efforts on maintaining various tools needed for my fabrication.

Being a BSAC member gives one many opportunities for networking with industry members and opens technical discussion with other researchers. For this, I would like to thank the BSAC co-directors, and particularly John Huggins, for their efforts in making the center one of the best MEMS research centers. Richard Lossing and Kim Ly deserves my appreciation for making IAB meetings run perfectly and for their efforts to make the center a better place for all the researchers.

Without the financial support from DARPA S&T program, DARPA CSSA program, and BSAC industry fundings, most of the results presented in this dissertation would not be possible. It was my pleasure for having a chance to interact with John Parsey from ON Semiconductor and Jon Kindred from Starkey.

I would like to express my appreciation to Shirley Salanio for patiently explaining to me and making sure I have all the confusing paperwork done properly, Lars Rohrbach for his help and saving my day from problems associated with the complicated EECS computer administration, and Ferenc Kovac for willing to go an extra mile for helping me to get some of the equipments I needed.

I am also thankful to Prof. Robert Brodersen and Prof. Seth Sanders for advising me and giving me a chance to perform research during my undergraduate senior year. Helping Dr. Jing Yang with her ADC chip gave me a chance to design a real CMOS circuit and helped me prepare for my graduate study.

I cherish many friends for bringing laughter and memories in the last seven years.

Here, I would like to take a moment to express my gratitude and appreciation to Dr. Tristan O. Rocheleau who has been my mentor, my colleague, and my good friend. Many of the results presented in this dissertation were collaborative efforts with him. Working with him on numerous projects was quite a ride for me. From him, I learned how to design custom measurement setups which included working with machine shops and putting all custom parts together. Through out my doctoral life, I have spent many hours in Berkeley Nanolab and Cory measurement labs working with him: it was not only a rewarded experience but also a very good learning experience. I am blessed to have him as a friend who is always willing to go many extra miles in helping me.

I am indebted and grateful to my family for their selfless support, love, and help. I would like to express my gratitude to my big sister, Zin Min Thein, for all the sacrifice she made for her siblings; my big brother, Aung Aung Naing, for being my best buddy and helping me with my life; and my little brother, Kyaw Myo Naing, for cheering and encouraging me. I cannot imagine how my life would have been in the last seven years without my life partner, Tran B. Ta. I am blessed and grateful for her unconditional support and encouragement. Last but not least, I would like to give my deepest gratitude to my parents, Myint Naing and Khin Shwe, for their love, support, belief in me, and encouragement. Without them, I would not have made it this far.

# Chapter 1

## Introduction

The increasing role of wireless technology in our daily lives is accompanied by a need for reduced radio power consumption. This will be especially important as wireless devices become ubiquitous, going beyond the smartphones of today to perhaps networks of more than a trillion autonomous sensors of tomorrow: the so-called Internet of Things (IoT) [1]. In one vision (*cf.* Fig. 1.1), sensors employing tiny, low-cost wireless motes collect and transmit data through a mesh network while operating only on scavenged or battery power. Here, small form-factor, spectrum efficient, and low-power wireless communication links are essential to realize a true “set-and-forget” autonomous sensor network. To this end, vibrating RF MEMS technology, with already available products ranging from compact low-phase-noise MEMS-based reference oscillators [2], to band-selecting RF front-end duplexers [3], offers a compelling potential route towards such a vision.

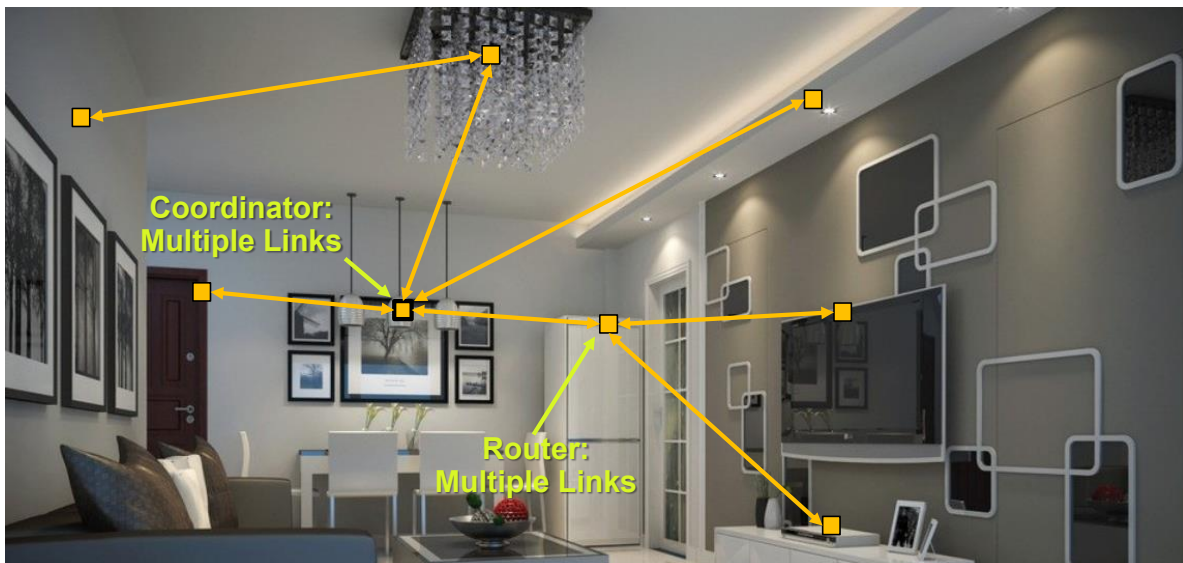


Figure 1.1: Motivation: Internet of Things

Recently, conventional wireless products from companies such as Dust Networks or ZigBee have been developed for IoT applications. These provide versatile low-power radios using time-synchronized communications to allow their relatively high-power conventional radios to be kept in shut-down mode most of the time, allowing battery life measured in months. While sufficient for many applications, this conventional technology is unable to operate for long periods of on-time on battery power alone, such as desired for a coordinator or router Fig. 1.1.

The performance of electronic circuits and systems used in wireless communications depends strongly on the accuracy and stability of timing and frequency reference oscillators. One of the challenges in achieving low-power sensor radios is having a low-power reference oscillator while maintaining good frequency stability. Traditional quartz-based oscillators have incredible frequency stability performance, but their large form-factors and power consumption ( $> 1$  mW) make them uncompetitive for wireless sensor applications. In the last decade, MEMS-based reference oscillators [4], [5] have emerged as low cost, on-chip alternatives, but their power consumption were still in 10's of mW range. More recently, SiTime introduced ultra small  $\mu$ Power oscillators, SiT8021 [6], for IoT applications. While their small form factor is quite impressive, their power consumption is still more than 100  $\mu$ W and their frequency stability performance is 2-3 order of magnitude worse than their siblings, SiT8208 [5].

Improving upon this to achieve oscillators operating on less than 100  $\mu$ W while maintaining low phase noise performance, this dissertation introduces the oscillator referencing to a capacitive-gap MEMS disk resonator. Furthermore, this work presents new methods of using these stable oscillators as signal processors for low-power wireless communications. Before jumping into the technical details, it is always beneficial to have a broad overview of the work.

## 1.1 Challenges Associated with Achieving Low-power Reference Oscillators

To illustrate the challenges associated with designing reference oscillators, Figure 1.2 shows a simplified schematic of a typical receiver. Here, a band-select RF front-end filter follows the antenna and feeds all the in-band interference to the succeeding circuits. A strong near-by in-band interference modulated with the local oscillator's noise (or frequency instability) masks the desired signal as shown in Fig. 1.2. Often, this local oscillator is generated by an on-chip  $LC$  voltage controlled oscillator (VCO) which is then locked to a low frequency reference oscillator using a Phase-Locked Loop as shown in Fig. 1.3. With the frequency stability of the radio locked to the reference oscillator, it is this reference that ultimately limits the performance of the wireless communication.

From a practical standpoint, there are three main ways to improve the short-term frequency stability of a reference oscillator [7]: 1) increase its loop signal power; 2) increase

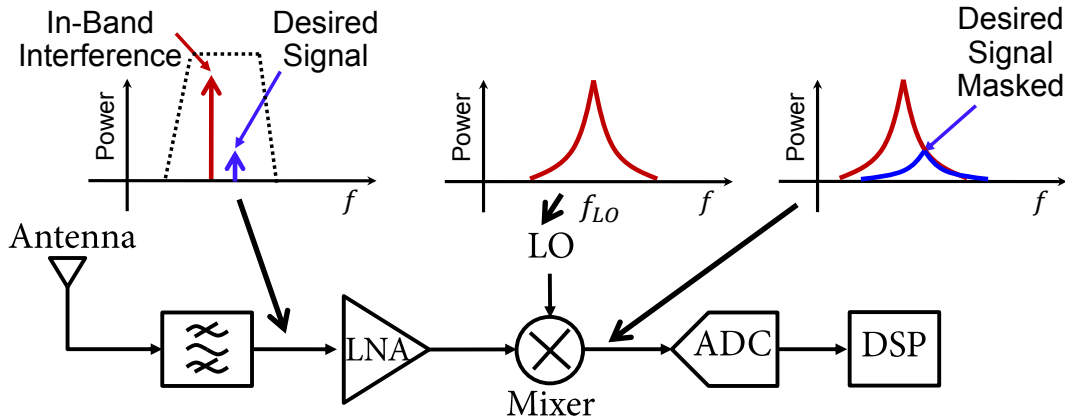


Figure 1.2: A simplified schematic of a typical receiver showing the desired signal masked by the in-band interference which is modulated with the noisy local oscillator (LO) signal.

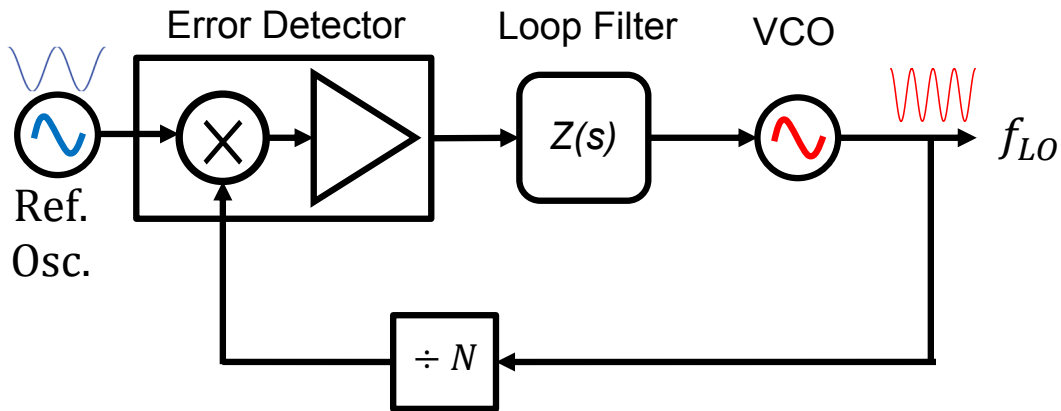


Figure 1.3: Block diagram of a local oscillator using a Phase-Locked Loop (PLL).

the quality factor ( $Q$ ) of its resonator; and 3) suppress its noise. Traditional quartz-based reference oscillators have incredible frequency stability performance due to their high  $Q$  and large power handling capability, but their large form factors and parasitic capacitance (hence, large power consumption  $>1$  mW [8]) make them unattractive for low-power sensor networks. Reference oscillators based on high- $Q$  MEMS resonators have emerged as low cost, on-chip alternatives to traditional quartz frequency references for use in timing applications [9]. Exploiting the exceptional  $Q$ -factors of above 100,000 made possible in these on-chip resonators, such oscillators offer the potential for low phase noise in compact packages. Indeed, oscillators using such resonators are already available commercially [5], [10] for timing applications.

Use of mechanically-coupled resonator array-composites post further performance increases, achieving marks that meet even the challenging Global System for Mobile Communications (GSM) specification while consuming only  $350$   $\mu$ W of power [11]. While such

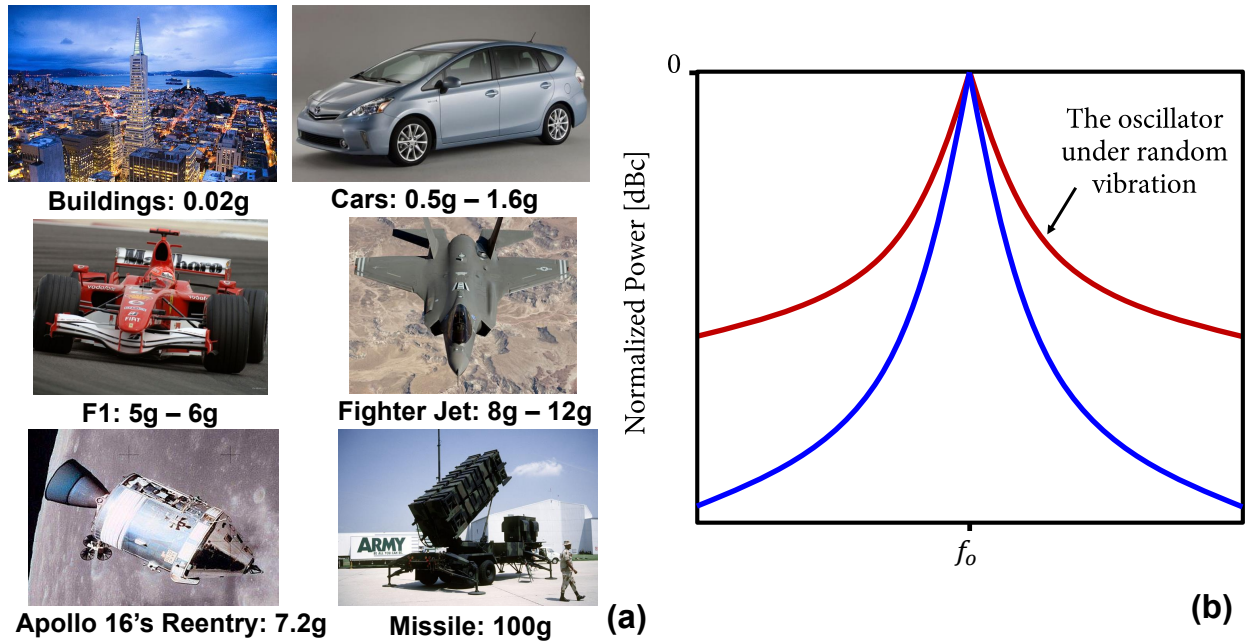


Figure 1.4: (a)  $g$ -force number in environment. (b) Conceptual drawing of an oscillator output power spectrum: the blue line represents the spectrum without acceleration while the red curve illustrates a broad spectrum of increased phase noise under random vibration.

devices offer compelling savings in power and space compared to quartz for mobile applications, further reductions in power are still desired for future autonomous wireless sensor networks [12], where nodes would be expected to operate for long periods using exclusively on-board battery or scavenged power.

Such devices offer not only valuable space savings in ever-shrinking consumer devices, such as cellular handsets, but also offer paths towards meeting the ultra-low-power requirements demanded by future wireless sensor networks [12]. Pursuant to further reducing power and area consumption while retaining the high performance of previous such efforts [11], [13], this dissertation explores lower power and improved performance MEMS oscillators. In particular, a Pierce-topology [14] oscillator referenced to a single polysilicon Wine-Glass disk resonator is designed and tested. Measurements attained phase noise performance marks of -119 dBc/Hz at a 1-kHz offset and -139 dBc/Hz at far-from-carrier offsets, satisfying even challenging GSM specifications [13] while consuming only 78  $\mu$ W power.

### 1.1.1 Frequency Instability due to Vibration and Long-term Drift

Unfortunately, for many applications (such as IoT) simply lowering electrical phase noise is only half the battle. Other effects, such as acceleration-induced frequency shift, may also degrade phase noise. Vibration, of course, is everywhere, from buildings with typical

accelerations of  $0.02g$ , to aeronautic environments with accelerations up to  $100g$  (*cf.* Fig. 1.4(a)). Normally, vibration occurs randomly at all frequencies up to a few kHz, resulting in a broad spectrum of increased phase noise, as illustrated by the red curve in Fig. 1.4(b). In traditional quartz-based oscillators, the primary cause of this acceleration sensitivity is often changes in stress at the mounting points of the crystal. Unlike quartz, the MEMS resonators used in this work do not suffer significantly from stress-induced frequency shifts, but are instead limited more by an electrical stiffness effect. This dissertation will study the acceleration sensitivity of a low phase noise oscillator referenced to a 61-MHz vibrating Wine-Glass disk resonator.

While short-term stability of MEMS-based oscillators has proven to be quite good, meeting even the challenging GSM phase noise specifications [13], the long-term reliability and stability of such resonators have been largely unstudied. Long-term frequency stability of reference oscillators is essential to maintain reliable radio communication without signals drifting into nearby bands. Typical frequency stability requirements are application-dependent and can range from tens of ppm per year to less than one ppm [15]. Cell phone requirements, for instance, remain one of the most challenging, with GSM requiring  $\pm 0.1$  ppm reference oscillator stability [16]. Requirements for local-area wireless standards are much more lenient, however, with typical stability requirements of  $\pm 40$  ppm [17]. Although the small size of MEMS resonators make them an exciting alternative to traditional quartz, at the same time they raise concerns of increased aging effects due to mass loading, package leaks, or stress fatiguing [18].

Some of the first published investigations on wafer-scale encapsulated resonators [19] indicated good stability, but measurements were of resonators only, not full oscillators, and were limited by experimental setup fluctuations to an accuracy of only  $\pm 3.1$  ppm. Some more recent efforts have shown limited stability data of oscillators. One study [20] used an Aluminum-Nitride bulk acoustic wave resonator reference over 50 days of measurement. Here too, measurement setup fluctuations and lack of vacuum packaging, a necessary component for achieving the high  $Q$  of MEMS resonators, limited measurements to shorter time-scales and frequency fluctuations of  $\pm 1.2$  ppm. Another study on a commercial device fabricated by SiTime [2] demonstrated exceptional short-term frequency stability of  $\pm 3$  ppb, but only made measurements over periods of up to 15 minutes. Yet another study [21] demonstrated very close differential frequency tracking of two resonators over periods up to 30 days, but again intrinsic frequency stability was limited by measurement setup fluctuations.

To remedy this, this work studies a first measurement of the MEMS oscillator, comprised of a Wine-Glass disk resonator bond-wired to an ASIC transimpedance amplifier and hermetically packaged in a custom-built vacuum-packaging system capable of maintaining torr pressures. A double-oven system maintains a constant oscillator temperature at  $34^\circ\text{C}$  with less than  $0.001^\circ\text{C}$  deviation, a key improvement over previous studies.

## 1.2 Oscillator-Based Low-Power Signal Processors

Applications of low-power high-stability oscillators based on capacitive-gap MEMS resonators are not limited to just reference oscillators. Their inherent regenerative amplification, electrical stiffness frequency tuning, and high quality factor makes them interesting candidates as low-power signal processors for wireless communication. To motivate these systems, wireless communication in IoT application needs to consume less than 100  $\mu\text{W}$  [22] and utilize spectrum efficiently. From this perspective, the high- $Q$  SAW and FBAR vibrating mechanical devices that make up today's RF bandpass filters are already responsible for significant power savings in wireless handsets. Indeed, their  $Q$ 's in the low thousands make possible 3% bandwidth filters that reject potentially large out-of-band interferers immediately after the antenna, allowing for significant LNA and mixer dynamic-range reductions. MEMS-based radios [23] offer even more interesting possibilities. While impressive, these previous MEMS circuits lack the ability to simultaneously communicate on separate channels, have limited frequency tuning capability, and could not reject the interference from the adjacent channels. To elaborate the last point, although good enough to select a frequency band of many channels, the  $Q$ 's attainable by commercial resonator technology are not sufficient to realize filters with bandwidths small enough to select single channels. Unfortunately, the resonator  $Q$  required for such a channel-selecting filter is quite daunting. For example, a 400-kHz bandwidth filter designed to select a single 200-kHz wide GSM-850 channel (and reject all others) would need constituent resonators with  $Q$ 's greater than 15,000 to maintain less than 2 dB of insertion loss (I.L) [24]. If possible, this would then provide further reduction in power consumption [25].

Pursuant to solving these deficiencies, this work presents an oscillator system that combines a single amplifier with a plurality of MEMS resonators capable of not only outputting multiple independent frequencies in the vicinity of 61 MHz; but also, by exercising voltage-controlled electrical stiffness tuning [26] of individual resonator array-composites, Frequency Shift Key (FSK) modulating each frequency to generate waveforms suitable for simultaneous wireless transmission in multiple channels. To achieve  $Q$ 's required for narrow bandwidth filters, this work explores the use of active positive feedback to boost the  $Q$ 's of the constituent passive resonators in a parallel-class filter and thereby make possible sub-0.01% bandwidth and its associated radio power savings for sensor network nodes. Specifically, the use of active feedback in closed-loop with two electrodes of a four-electrode capacitive-gap transduced Wine-Glass disk resonator has enabled boosting of the effective resonator  $Q$  and independent control of insertion loss across the two other electrodes. Unlike past efforts [27], [28] operating at kHz-frequencies, the split electrode design used here removes the amplifier feedback loop from the signal path allowing independent control of input-output coupling,  $Q$ , and frequency.

Furthermore, this work presents a FSK super-regenerative transceiver by quenching the capacitive-gap MEMS oscillator demonstrating a fully-functional tunable RF channel-selecting radio transceiver. Unlike previous super-regenerative receivers [23], [29], this rendition harnesses the high  $Q$  filtering and voltage-controlled frequency tuning of its capacitive-

gap transduced disk resonator to enable selection of 1-kHz-wide RF channels across a 80-kHz range. Furthermore, the split electrode resonator design made possible here isolates the loop amplifier from the antenna, greatly relaxing circuit linearity requirements and eliminating the need for an isolation amplifier, thus saving considerable power. The chosen 61-MHz frequency is ideal for long-range unlicensed operation in the 52-74 MHz band white-space [30] and ISM bands at 27.12 MHz and 40.68 MHz [31]. The demonstrated signal processor at VHF frequency is already useful, but as many wireless communication standards operate at GHz frequencies similar MEMS systems for these frequency are also desired. In order to achieve high- $Q$  resonator at GHz frequencies, this dissertation finally presents improvements to resonator design which offer similar  $Q$ -performance at GHz frequencies and above.

### 1.3 Organization of Dissertation

This dissertation focuses on low-power oscillators and oscillator systems based on capacitive-gap MEMS resonators. It begins in Chapter 2 detailing the complete design and modeling of the capacitive-gap disk resonators used. Chapter 3 follows with a discussion of oscillator design based on the Pierce and TransImpedance (TIA) topologies used in this work, emphasizing the design methodology needed to achieve low-power oscillators. Next, in Chapter 4, the fabrication process required to make the MEMS devices is discussed along with measurement methods for the released MEMS resonators and oscillators. Chapter 5 further models the Phase Noise of 61-MHz MEMS Pierce oscillators using Hajimiri's theory [32] and presents the experimental results of the oscillators. Chapter 6 then studies additional frequency stability challenges in the 61-MHz Wine-Glass disk oscillators: short-term acceleration-induced frequency shift and long-term frequency drift. After a thorough study of these oscillators, Chapter 7 and Chapter 8 apply oscillator concepts to uses in low-power signal processing. By exploiting nonlinearities and electrical stiffness in the MEMS resonator, the first part of Chapter 7 introduces multiple simultaneous frequencies Frequency-Shift Keyed modulator. The rest of Chapter 7 shows a method to implement very narrow bandwidth filters using active  $Q$ -boosted resonators. Combining the regenerative amplification effect in an oscillator loop and the electrical stiffness tuning effect in the multi-electrode high- $Q$  resonator, Chapter 8 introduces the first working super-regenerative channel-selecting radio transceiver. Finally, Chapter 9 presents two capacitive-gap transduced micromechanical resonator designs which can achieve the high  $Q$  at GHz frequencies needed for many wireless communication standards. Finally, Chapter 10 summarizes the work in this dissertation and provides some thoughts to the future.

## Chapter 2

# Capacitive-Gap Disk Device Design

Capacitive-gap resonators offer an on-chip resonator with high  $Q$  and CAD-definable frequency. In these resonators, electrical to mechanical coupling is provided by tiny capacitive gaps to which a DC bias voltage is applied, producing mechanical-to-electrical transduction of ac signals at the resonance frequency. With this coupling mechanism, various surface micro-machined materials—diamond and polysilicon in the work here—may be used to construct high  $Q$  resonators. To better understand the design and operation of these resonators, this Chapter reviews a full analysis of operation of the MEMS device used here. Though most of the analyses presented here are already in the literature [33]–[35], it is beneficial to review them before jumping into the full oscillator design in the following chapter.

### 2.1 Device Structure and Operation

Figure 2.1(a) presents the perspective-view schematic of a Wine-Glass mode disk resonator under a two-port bias, excitation, and measurement scheme, identifying key features to be used later for analysis. As shown, this device consists of a disk structure constructed in doped polysilicon or diamond, with thickness  $h$  and radius  $R$ , supported by beams at the quasi nodal points for the Wine-Glass disk resonator.

#### 2.1.1 Excitation and Detection

The disk is surrounded by doped polysilicon capacitive transducer electrodes spaced less than 100 nm from its outer edge. To excite the device of Fig. 2.1(a) in its two-port configuration, a dc-bias voltage  $V_P$  is applied to the conductive disk and an ac signal  $v_{in}$  to its drive or input electrodes. Note that the application of the dc-bias  $V_P$  serves only to charge the electrode-to-resonator capacitance. No dc current flows, so no dc power is consumed. Together, these voltages applied across the small capacitive gaps generate a electrostatic input force  $F_{in}$  at the frequency of  $v_{in}$  given by

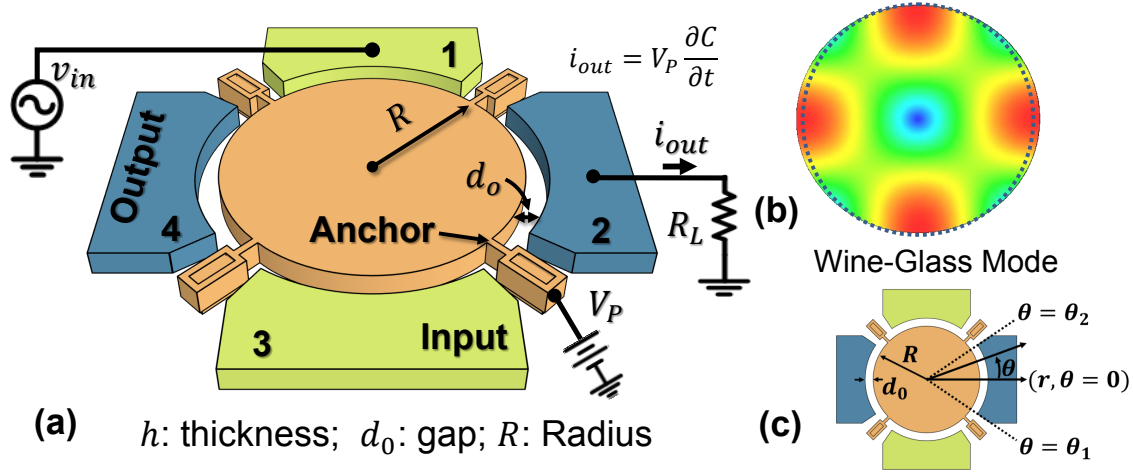


Figure 2.1: (a) Perspective view of a Wine-Glass mode disk resonator in typical two-port bias schemes, (b) resonator mode shape, and (c) top-view schematic diagram of the MEMS resonator. Note: electrodes with the same color are electrically connected together.

$$F_{in} = \frac{1}{2} \left( \frac{\partial C_{o,in}}{\partial r} \right) (V_{PG} - v_{in})^2 \cong -V_{PG} \left( \frac{\partial C_{o,in}}{\partial r} \right) v_{in} \quad (2.1)$$

where the rightmost form retains only the ac term at the frequency of  $v_{in}$ .  $V_{PG}$  is the voltage across the resonator-to-electrode gap, which is  $V_P - V_{CM}$  in Fig. 2.1:  $V_{CM}$  is the dc voltage on the electrodes ( $V_{CM}$  is normally the common-mode bias voltage at the input and output of the amplifier).  $\partial C_{o,in}/\partial r$  is the change in electrode-to-resonator overlap capacitance per unit radial displacement at the input port, given under a small-signal parallel-plate approximation as

$$\frac{\partial C_{o,in}}{\partial r} = \frac{\epsilon_0 A_{in}}{d_o^2} \quad (2.2)$$

where  $A_{in}$  is the combined static electrode-to-resonator overlap area of all input ports in the hookup of Fig. 2.1(a), and  $d_o$  is the electrode-to-resonator gap spacing. When the frequency of  $v_{in}$  matches that of one of the resonance modes, the resulting force applied to the disk drives it into the vibration shape of that mode. Figure 2.1(a) presents the Wine-Glass mode. As shown, one of the locations where the maximum displacement occurs is  $(R, 0)$ , which is taken as a reference point. The corresponding resonance displacement amplitude at the reference is given by

$$\Re_{re} = \frac{Q F_{in}}{k_{mre}} = \frac{Q}{k_{mre}} V_{PG} \frac{\partial C_{o,in}}{\partial r} V_{in} \quad (2.3)$$

where  $k_{mre}$  is the equivalent dynamic stiffness at the reference location that includes both mechanical and electrical [26] components.  $V_{in}$  is the voltage amplitude of the input signal. If

the reference location at the output electrodes is at the maximum displacement locations, the displacement amplitude in Eqn. (2.3) equates to the output amplitude. The driven resonant motion in turn modulates the output electrode-resonator gap size and hence gap capacitance, which, with a constant electrode-gap voltage, produces an output current amplitude at resonance:

$$\begin{aligned} I_{out} &= V_P \frac{\partial C_{o,out}}{\partial r} \frac{\partial \Re(r_o)}{\partial t} \\ &= \frac{Q\omega_o}{k_{mre}} \frac{\partial C_{o,in}}{\partial r} \frac{\partial C_{o,out}}{\partial r} V_{PG}^2 V_{in} = \frac{Q\omega_o}{k_{mre}} \eta_{e,in} \eta_{e,out} V_{in} \end{aligned} \quad (2.4)$$

where  $\partial C_{o,out}/\partial r$  is the change in electrode-to-resonator overlap capacitance per unit radial displacement at the output port. The output current is proportional to the change in electrode-to-resonator overlap capacitance per unit radial displacement at both the input and output ports, and inversely proportional to the equivalent dynamic stiffness.

As derived, Eqn. (2.4) corresponds to the case where the input force is applied at precisely the resonance frequency of the disk. This can be further simplified through the introduction of the equivalent series motional resistance of the device,  $R_x$ , given by

$$R_x = \frac{V_{in}}{I_{out}} = \frac{k_{mre}}{Q\omega_o \eta_{e,in} \eta_{e,out} V_{PG}^2} \quad (2.5)$$

With this substitution and incorporating the standard Lorentzian frequency response of any resonator, the overall transfer function from input voltage to output current becomes

$$\frac{i_{out}}{v_{in}} = \frac{1}{R_x} \frac{(\omega_o/Q) s}{s^2 + (\omega_o/Q) s + \omega_o^2} \quad (2.6)$$

Recognizing Eqn. (2.6) as the transfer function for a classic bandpass biquad, the electrical response of the micromechanical resonator in the hook-up of Fig. 2.1(a) equates to that of a single  $LCR$  electrical circuit. In short, via action of the disk resonator, the electrical input signal  $v_{in}$  is converted to a mechanical signal at the input port, filtered (with high  $Q$ ) in the mechanical domain, then re-converted to an electrical signal at the output port, ready for further processing by subsequent stages.

As with other capacitively transduced resonators, note that output current ensues only if the dc-bias voltage  $V_{PG}$  is non-zero. If the dc-bias voltage between the output electrode and the disk is zero, then no current flows, and the device is effectively “off.” Thus,  $V_{PG}$  provides an on/off “self-switching” for this device that removes the need for external switches in multi-band RF front-end architectures [36].

## 2.2 Resonator Frequency Design

Having described the qualitative operational aspects of the disk, analytical formulations governing the precise frequency design of this device are now in order. Pursuant to maintain-

ing a practical formulation, this analysis assumes that the disk thickness is thin compared to its lateral dimensions ( $h \ll R$ )—a very reasonable assumption for the surface-micromachined devices of this work, where thicknesses on the order of 2 or 3  $\mu\text{m}$  are indeed small compared to lateral dimensions of tens of microns. The analysis further assumes that the top and bottom faces of the disk are free of intrinsic stress; and since the structure is thin and forces are applied in only the lateral directions, the vertical stress components also vanish throughout its bulk.

With these assumptions, the frequency of the resonance is determined by the transcendental equation [33]:

$$\left[ \Psi_{mn} \left( \frac{\zeta}{\xi} \right) - mn - q \right] \cdot [\Psi_{mn}(\zeta) - mn - q] = (mn \cdot q - mn)^2 \quad (2.7)$$

where

$$\begin{aligned} \Psi_{mn}(x) &= \frac{x J_{mn-1}(x)}{J_{mn}(x)}, & \zeta &= 2\pi f_{nom} R \sqrt{\frac{\rho(2+2\sigma)}{E}} \\ \xi &= \sqrt{\frac{2}{1-\sigma}}, & q &= \frac{\zeta^2}{2mn^2 - 2} \end{aligned} \quad (2.8)$$

and where  $J_n(x)$  is Bessel function of first kind of order  $n$ ,  $f_{nom}$  is the resonance frequency,  $R$  is the disk radius,  $mn$  is the mode number, and  $E$ ,  $\sigma$ , and  $\rho$  are the Young's modulus, Poisson ratio, and density of the structural material, respectively. Table 2.1 summarizes the material constant for polysilicon and diamond. The Wine-Glass mode corresponds to  $(mn, m) = (2, 1)$ , denoting the first solution of Eqn. (2.7) for  $mn = 2$ .

After solving Eqn. (2.7) to obtain frequency parameter  $\zeta$ , the mechanical resonance frequency of the disk structure,  $f_{nom}$ , readily follows via

$$f_{nom} = \frac{\omega_{nom}}{2\pi} = \frac{\zeta}{2\pi R} \sqrt{\frac{E}{\rho(2+2\sigma)}} = \frac{K_{WG}}{R} \sqrt{\frac{E}{\rho(2+2\sigma)}} \quad (2.9)$$

where  $\omega_{nom}$  is the radian nominal mechanical resonance frequency and  $K_{WG} = \zeta/2\pi$ . For the given material,  $K_{WG}$  is a constant and its values are given in Table 2.1.

## 2.3 Lumped Parameter Equivalent Circuits

Given that the disk resonator will be used with CMOS circuits, where the device will populate some form of mechanical circuit [39], [40] that in turn must interface with transistor circuits [41], an electrical equivalent model for the device is paramount. Such a model is best derived by first specifying a lumped mechanical equivalent circuit for the disk, then using this to formulate an electrical circuit suitable for simulation using SPICE [42] or other circuit simulators.

Table 2.1: Materials' properties [37], [38] and their corresponding constants in Eqn. (2.9)

	Polysilicon	Microcrystalline Diamond	Unit
Density, $\rho$	2300	3500	kg/m <sup>3</sup>
Young's modulus, $E$	150	1198	GPa
Poisson ratio, $\sigma$	0.226	0.07	-
Acoustic velocity of an extensional wave, $\sqrt{E/\rho}$	8076	18501	m/s
$(E \cdot \rho)$ product	$3.45 \times 10^{14}$	$4.193 \times 10^{15}$	Pa·kg/m <sup>3</sup>
$K_{WG}$	0.373	0.3723	-

### 2.3.1 Lumped Parameter Mechanical Equivalent Circuit

Since this lumped circuit attempts to model a device that is actually distributed in nature, the elements of the circuit are location dependent, which means there is a unique equivalent circuit for every specific location on the disk. Regardless of location, the element values will depend fundamentally on the peak total kinetic energy in the vibrating disk, which can be determined for the disk operating in a Wine-Glass mode by integrating the kinetic energies of all infinitesimal mass elements  $dm$  making up the disk to yield

$$KE_{tot} = \frac{1}{2} \int_0^{2\pi} \int_0^R dm \times [v(r, \theta)]^2 \quad (2.10)$$

where  $v(r, \theta)$  is the radial velocity magnitude at location  $(r, \theta)$  given by

$$v(r, \theta) = \omega \Re(r, \theta) \quad (2.11)$$

Here,  $\omega$  is the frequency of motion in radians, and the infinitesimal mass element takes the form  $dm = \rho \times h \times r d\theta \times dr$ .  $\Re(r, \theta)$  describes the radial mode shape at the location  $(r, \theta)$  and takes on the form [33]:

$$\Re(r, \theta) = \left[ \frac{\partial}{\partial r} J_{mn} \left( \frac{\zeta}{\xi R} r \right) + mn \frac{B}{A} \frac{1}{r} J_{mn} \left( \frac{\zeta}{R} r \right) \right] \cos(mn \cdot \theta) \quad (2.12)$$

where  $B/A$  is the ratio of the coefficients of the rotation and the areal dilatation in displacements of the compound mode and is defined as:

$$\frac{B}{A} = \frac{2 \Psi_{mn} \left( \frac{\zeta}{\xi} \right) + \zeta^2 - 2 mn \cdot (mn + 1)}{2 mn \cdot [\Psi_{mn}(\zeta) - (mn + 1)]} \quad (2.13)$$

The equivalent mass at position  $(r, \theta)$  is defined as peak kinetic energy divided by one-half the square of the velocity at that location [34] and yields

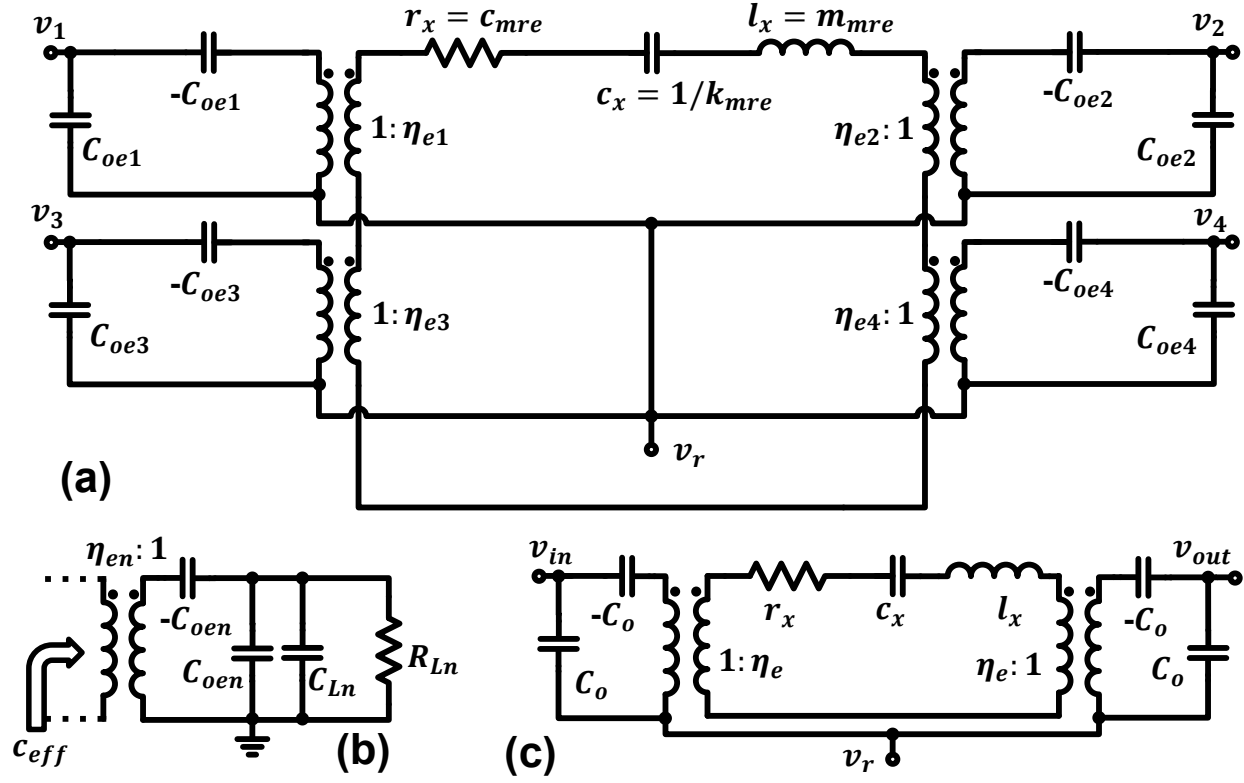


Figure 2.2: (a) Complete equivalent circuit model for a Wine-Glass disk resonator. (b) The load circuit model of a single electrode for the disk resonator. (c) Physically consistent model using actual values of damping, stiffness and mass for elements in a two-port configuration when all input electrodes and output electrodes are connected as shown in Fig. 2.1.

$$m_{mr}(r, \theta) = \frac{KE_{tot}}{0.5 [\nu(r, \theta)]^2} = \frac{\rho h \int_0^{2\pi} \int_0^R r' [\Re(r', \theta')]^2 dr' d\theta'}{[\Re(r, \theta)]^2} \quad (2.14)$$

The equivalent stiffness at a location  $(r, \theta)$  is simply the multiplication of the equivalent mass at the location and the square of the resonance frequency. For  $(r, \theta)$  location, it takes form as:

$$k_{mr}(r, \theta) = \omega_{nom}^2 m_{mr}(r, \theta) \quad (2.15)$$

To specify an equivalent circuit like that of Fig. 2.2(a), a reference point must be chosen that determines the values of the core mass-spring-damper circuit. The convention is typically to choose the highest velocity (or largest displacement) point on the resonator, which is the location  $(R, 0)$ . This means the core equivalent mass and stiffness for the disk merely takes on the value of Eqns. (2.14) and (2.15), or

$$m_{mre} = m_{mr}(R, 0) \quad \text{and} \quad k_{mre} = k_{mr}(R, 0) \quad (2.16)$$

Expressions for the equivalent damping then readily follow from

$$c_{mre} = \frac{\omega_{nom} m_{mre}}{Q} = \frac{k_{mre}}{\omega_{nom} Q} = \frac{\sqrt{k_{mre} m_{mre}}}{Q} \quad (2.17)$$

### 2.3.2 Lumped Parameter Electrical Equivalent Circuit

Having determined the lumped parameter mechanical equivalent circuit for the disk, an electrical equivalent circuit can now be generated to model the action of applied electrical signals that drive the disk into resonance and to predict the magnitudes and phases of the ensuing output currents. To be amenable to circuit simulation via well-established software, like SPICE, this circuit should utilize only electrical elements. Pursuant to this, dualities between the roles of mass, stiffness, and damping, and inductance, capacitance, and resistance, in the respective differential equations governing mechanical and electrical dynamics allow one to equate the different quantities as follows [39]:

$$l_x = m_{mre}; \quad c_x = 1/k_{mre}; \quad r_x = c_{mre} \quad (2.18)$$

where mass, stiffness, and damping values corresponding to the maximum displacement locations are chosen by convention.

As an illustration, there are four electrodes surrounding the disk of Fig. 2.1(a), and thus four distinct ports through which to access the device, each of which can be used as an input, an output, or for something else, e.g., electrical stiffness-based frequency pulling. A complete model should include the electrical stiffness contributions from each port and be general enough to be independent of whether a port is used for input or output. Figure 2.2 presents a lumped parameter electrical equivalent circuit that satisfies all of the above criteria for the disk devices such as in Fig. 2.1. Here, both the electrical-to-mechanical transformations occurring at the electrode-to-resonator capacitive gaps are all modeled by transformers that specify the particular transformations via their turn ratios. It is important to note that, for a Wine-Glass mode disk device with electrodes configured as in Fig. 2.1, the electrodes adjacent to each other should not be connected together since this will canceled out the current: i.e., electrode 1 and 2 in Figures 2.1 and 2.2 should not be used for a single electrical signal.

The turns ratio  $\eta_{en}$  models the electromechanical conversion at the  $n$ th port. Specifically, the voltage-to-force and/or velocity-to-current transfer function with respect to the reference location (at  $r = R$  and  $\theta = 0$  in the inset of Fig. 2.1).

$$\eta_{en} = V_{PGn} \frac{\partial C_{oen}}{\partial r} = V_{PGn} \frac{C_{oen}}{d_o \Delta\theta} \int_{\theta_1}^{\theta_2} \frac{\Re(R, \theta')}{\Re(R, 0)} d\theta', \quad \text{and} \quad C_{oen} = \frac{\varepsilon_0 R h \Delta\theta}{d_o} \quad (2.19)$$

where  $h$  is the disk thickness,  $C_{oen}$  and  $V_{PGn}$  are the overlap capacitance, and dc voltage, respectively, across the  $n^{\text{th}}$  electrode-to-resonator gap, and  $\Delta\theta = \theta_2 - \theta_1$  is the subtended

angle of the  $n$ th electrode. Note that this coupling factor depends only on the electrode-to-resonator overlap geometry, the dielectric constant of the capacitor, and the voltage applied across it—just as it should.

Finally, static capacitors  $C_{oen}$  model the physical electrode-to-resonator overlap capacitance at each port  $n$ . Note how the bottom terminals of these capacitors all go to a terminal that represents the physical conductive disk structure. In the normal case where the resonant structure is connected to the dc-bias voltage  $V_P$  (*cf.* Fig. 2.1), this terminal in the small-signal equivalent circuit should go to ground. Sometimes, however, an ac signal is applied to the structure terminal to effect mixing for certain applications [43], in which case the terminal in the small-signal circuit should receive the ac source. In either case, one must be careful to include any series resistance present between the disk edge overlapping the electrode and the ultimate point where the dc-bias or ac voltage is applied, as this resistance can heavily influence the performance of devices when used in oscillators. Section 2.3.4 will give more information about the parasitic resistance of the device.

### 2.3.3 Electrical Stiffness

During operation, the gap spacing between resonator and electrode changes, which in turn generates a changing electric field, and hence varying electrostatic force in the gap. In a small-signal model, this force is in phase and proportional to disk edge displacement, and thus meets the definition of stiffness. Popularly termed electrical stiffness, this “softens” the equivalent stiffness of the resonator resulting a negative shift in the resonance frequency [26]. Though often modeled with a simple voltage-dependent change in motional capacitance,  $c_x$ , Fig. 2.2(a) instead models electrical stiffness via “negative” capacitors in series with each of the electrodes that more clearly elucidate the mechanisms behind external load-dependent frequency shifts [35]. For example, when loaded by a complex impedance modeled by  $C_{Ln}$  and  $R_{Ln}$  in Fig. 2.2(b), the resultant electrical stiffness generated from each individual electrode-to-resonator gap takes the form

$$k_{en} = -\frac{1}{c_{eff}} = \eta_{en}^2 \left[ \frac{1}{C_{oen}} - \frac{\omega^2 R_{Ln}^2 (C_{oen} + C_{Ln})}{1 + \omega^2 R_{Ln}^2 (C_{oen} + C_{Ln})^2} \right] \quad (2.20)$$

where  $c_{eff}$  is the effective capacitance seen by the resonator as shown in Fig. 2.2(b). The electrical stiffness components then perturb the total equivalent stiffness of the resonator to

$$k_{re} = k_{mre} - \sum_n k_{en} \quad (2.21)$$

which in turn yields for resonance frequency

$$f_o = \frac{\omega_o}{2\pi} = f_{nom} \sqrt{\left[ 1 - \sum_n \frac{k_{en}}{k_{mr}(r_{en}, 0)} \right]} \quad (2.22)$$

where electrical stiffness clearly reduces the resonance frequency from its nominal purely mechanical value. When the device is used in an oscillator, the loading condition is not as simple as in Fig. 2.2(b) and, therefore, the resultant electrical stiffness in Eqn. (2.20) will be different. Section 3.5 will discuss this in further detail. Nevertheless, evaluating Eqn. (2.20) with  $\omega \approx \omega_{nom}$  (valid when mechanical stiffness is much larger than all the electrical stiffnesses combined, as is typically the case here), the maximum electrical stiffness occurs when  $R_{Ln} = 0$  (effectively shorting the electrode to ground) in which case  $k_{en}$  becomes

$$k_{en,max} = \frac{\eta_{en}^2}{C_{oen}} = \frac{\varepsilon_0 R h}{d_o^3 \Delta \theta} V_{PGn}^2 \left[ \int_{\theta_1}^{\theta_2} \frac{\Re(R, \theta')}{\Re(R, 0)} d\theta' \right]^2 \quad (2.23)$$

recovering the well-known electrical stiffness equation given in [26], valid for cases where the voltage across the electrode-to-resonator gap is kept constant.

If instead of a zero- $\Omega$  load,  $C_{oen} \gg C_{Ln}$  and  $R_{Ln} \rightarrow \infty$ , the electrical stiffness in Eqn. (2.20) approaches zero. In this loading condition, total charge (rather than voltage) remains constant across the electrode-to-resonator gap, resulting in a position-independent electrical field, and thus an absence of electrical stiffness.

### 2.3.4 Reduced 2-Port Model

The circuit of Fig. 2.2(a) provides a very general model for the device of Fig. 2.1, where the ports can be assigned to different purposes at will. In practice specification of port purpose greatly simplifies the equivalent circuit, as shown in Fig. 2.2(c), which presents the equivalent circuit in Fig. 2.2(a) corresponding to the disk wired as in Fig. 2.1(a) and (b). Here, the disk in Fig. 2.1(a) and (b) uses all the odd numbered electrodes as the input and all the even numbered electrodes as the output. The constituent electrodes for each input and output can be combined into one equivalent input electrode and one output electrode. Since all the electrodes have the same overlapping area with the disk structure and both input and output have the same number of electrode, the electromechanical coupling factors modified as

$$\begin{aligned} \eta_{e,in} &= \eta_{e1} + \eta_{e3} = 2 \cdot \eta_{en}; & \eta_{e,out} &= \eta_{e2} + \eta_{e4} = 2 \cdot \eta_{en} \\ \eta_e &= \eta_{e,in} = \eta_{e,out} = 2 \cdot \eta_{en} \end{aligned} \quad (2.24)$$

where  $\eta_{e1}$  to  $\eta_{e4}$  and  $\eta_{en}$  are defined in Eqn. (2.19). Similarly, the equivalent input and output electrode-to-resonator overlap capacitances becomes

$$\begin{aligned} C_{o,in} &= C_{oe1} + C_{oe3} = 2 \cdot C_{oen}; & C_{o,out} &= C_{oe2} + C_{oe4} = 2 \cdot C_{oen} \\ C_o &= C_{o,in} = C_{o,out} = 2 \cdot C_{oen} \end{aligned} \quad (2.25)$$

where  $C_{oe1}$  to  $C_{oe4}$  and  $C_{oen}$  are defined in Eqn. (2.19). Using equations (2.24) and (2.25), Fig. 2.2(a) can be simplified into Fig. 2.2(c). So far, the discussion has focused on the core resonator. Unfortunately, the real device has parasitic resistance and capacitance. To include these, Figure 2.3 presents a complete small-signal equivalent circuit model of the mechanical

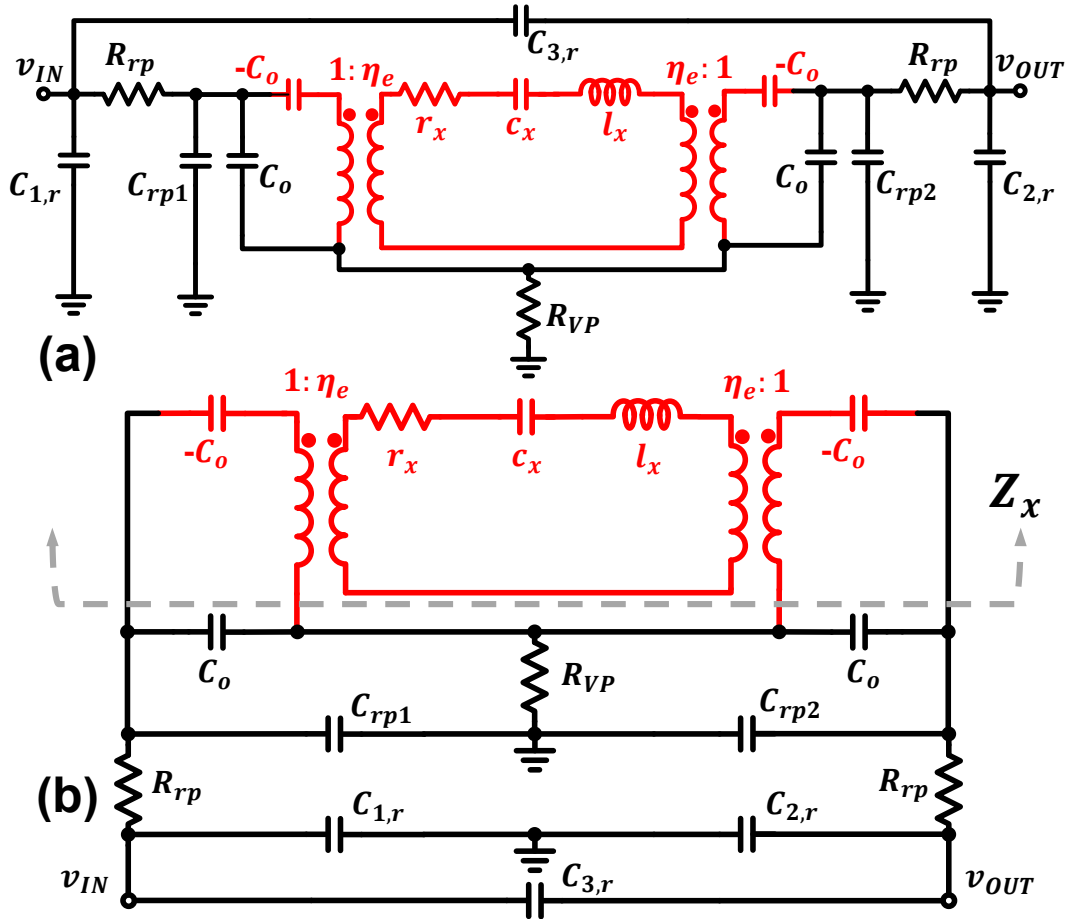


Figure 2.3: (a) Resonator small-signal equivalent circuit with the core tank circuit of the resonator shown in red. Parasitic capacitance and resistance elements are shown in black. (b) Rearrangement of components of (a) in a more intuitive configuration.

resonator. This circuit has two portions: 1) the core tank circuit in red, including series  $rlc$  elements and transformers with negative capacitors modeling the capacitive-gap transducers and, 2) parasitic elements drawn in black. The additional portions of the Fig. 2.3 modeled in black represent the unavoidable trace resistances,  $R_{rp}$  and  $R_{VP}$ , parasitic capacitance at the input and output electrodes of the resonator,  $C_{rp1}$  and  $C_{rp2}$ , capacitance at the input and output bondpads,  $C_{1,r}$  and  $C_{2,r}$ , and feedthrough capacitance of the device,  $C_{3,r}$ . These parasitic components both contribute to the oscillator operation as well as set limits to performance as detailed in Chapter 3.

Focusing on the tank circuit shown in red in Fig. 2.3, the core red circuits can be further simplified to a series  $rlc$  circuit without need for coupling transformers in order to facilitate oscillator analysis. These equivalent  $rlc$  elements can be found:

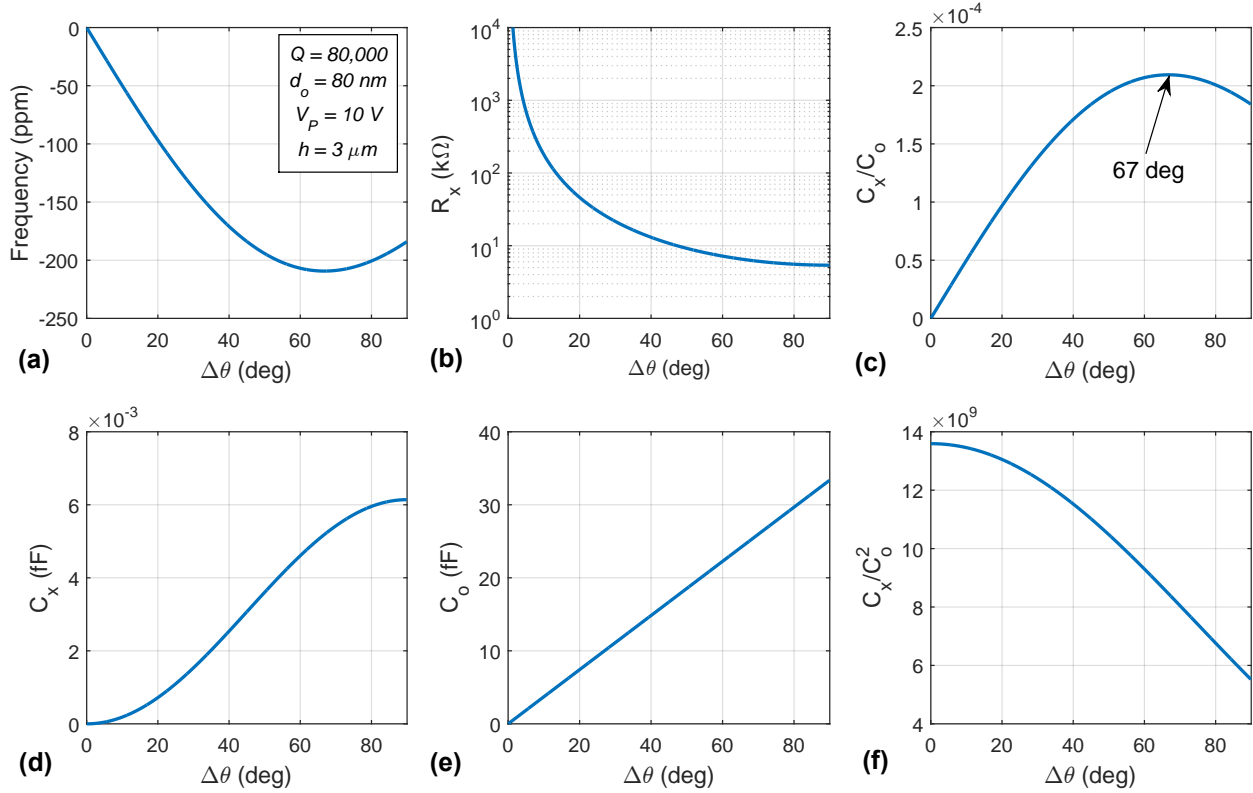


Figure 2.4: Calculated (a) frequency shift, (b) motional resistance, (c)  $(C_x/C_o)$ , (d)  $C_x$ , (e) static overlap capacitance ( $C_o$ ), and  $(C_x/C_o^2)$  as a function of the electrode subtended angle ( $\Delta\theta$ ) for a compound (2,1) mode polysilicon disk resonator with 32  $\mu\text{m}$  radius and 80 nm capacitive gaps designed for a 61-MHz frequency of operation (*cf.* Fig. 2.1(b)).

$$L_x = \frac{m_{mre}}{\eta_e^2}; \quad C_x = \frac{\eta_e^2}{k_{mre}}; \quad R_x = \frac{c_{mre}}{\eta_e^2} \rightarrow R_x \propto \frac{c_{mre} d_o^4}{V_{PG}^2} \quad (2.26)$$

The impedance seen looking into the mechanical resonator (illustrated in red in Fig. 2.3) may then be expressed simply as:

$$Z_x = R_x + j \left( \omega L_x - \frac{1}{\omega C'_x} \right) \quad (2.27)$$

Here,  $R_x$ , known as the resonator motional resistance, sets the resistance that the amplifier must overcome to permit oscillation. It is important to note that the resonator tank circuit is fundamentally a three terminal device. Therefore, the simplification in Equations (2.26) and (2.27) is only valid when the input and output of the resonator are identical (meaning both input and output transformers have the same turn ratio). This electrical stiffness effect may be modeled using negative  $C_o$  terms in series with  $C_x$  [35], giving resultant total effective ( $C'_x$ ) capacitance of the tank:

$$C'_x = \frac{-C_x C_o}{(2C_x - C_o)} \quad (2.28)$$

The resultant resonance frequency can readily found as:

$$\omega_{oe} = \sqrt{\frac{1}{L_x C'_x}} = \omega_{nom} \sqrt{1 - \frac{2C_x}{C_o}} = \omega_{nom} \sqrt{1 - \frac{k_e}{k_{mre}}} \quad (2.29)$$

Using Eqn. (2.26), the expression for the electromechanical coupling factor ( $C_x/C_o$ ), which effectively equals the popular  $k_{eff}^2$  at low values, take the form:

$$(C_x/C_o) \approx \frac{\varepsilon_o V_{PG}^2}{d_o^3 \Delta\theta} \cdot \frac{\sqrt{2+2\sigma}}{2\pi^2 f_{nom} \Lambda \zeta \sqrt{E \cdot \rho}} \left[ \int_{\theta_1}^{\theta_2} \frac{\Re(R, \theta')}{\Re(R, 0)} d\theta' \right]^2 \quad (2.30)$$

where  $\Lambda$  relates the static mass of the disk to its dynamic mass and depends on the mode shape function (2.12). From Eqn. (2.30), ( $C_x/C_o$ ) depends most heavily on bias voltage,  $V_{PG}$ , and electrode-resonator gap,  $d_o$ , where the latter shows a strong third power dependence. Equation (2.29) suggests that a large ( $C_x/C_o$ ) will give a large frequency tuning through the electrical stiffness effect: a large tuning is desirable for many applications as explained in later chapters. From Eqn. (2.30), it is not immediately apparent how the electrode subtended angle ( $\Delta\theta$ ) effects ( $C_x/C_o$ ). Figure 2.4 plots various resonator design parameters as the function of  $\Delta\theta$  for a compound (2,1) mode polysilicon disk resonator with 32  $\mu\text{m}$  radius and 80 nm capacitive gaps designed for a 61 MHz frequency of operation. The maximum ( $C_x/C_o$ ) (or the maximum frequency tuning) occurs when  $\Delta\theta = 67^\circ$ .

Often times, the MEMS community uses ( $C_x/C_o$ ) to compare different resonators' performance. ( $C_x/C_o$ ) is a useful parameter for filter applications, particularly wideband filter applications, but does not inform performance in oscillator applications. For oscillators, ( $C_x/C_o^2$ ) is a better metric for reasons that will be explained upon in Section 3.2.3.

# Chapter 3

## Oscillator Design

Creating an oscillator requires two primary components: first, a frequency selecting element—here provided by the MEMS resonators of the previous chapter—and, second, a source of gain used to start and sustain oscillation. Implementing low-power and compact oscillators using MEMS technology motivates the use of co-chip amplifiers to provide gain, achieved here by designing custom CMOS circuits. This chapter introduces the design and implementation of Pierce and TransImpedance Amplifier (TIA) circuits, the two electronic amplifier topologies used in this work.

### 3.1 Basic Oscillator Concepts

For an electronic oscillation to occur, two conditions must hold: 1) the total closed-loop phase shift must be zero; and 2) the loop gain must be larger than unity. During oscillation start-up, oscillation amplitude is small—initially constituted of only thermal noise—and the whole circuit stays linear. Therefore, the oscillator can be modeled using small signal equivalent circuits. Figure 3.2 shows the small signal equivalent circuits for two types of oscillators studied in this dissertation: 1) Pierce oscillator [14] and 2) TransImpedance Amplifier (TIA) based oscillator [13]. The details of the small signal circuits will be covered in the Sections 3.2 and 3.3. Focusing first on the basic oscillator concepts, the best way to understand these oscillators is using the impedance approach presented in [44]. In this approach the critical condition for oscillation occurs when [44]:

$$Z_{res} + Z'_{amp} = 0 \quad (3.1)$$

where  $Z_{res}$  and  $Z'_{amp}$  are the impedance looking the resonator and amplifier, respectively, as shown in Fig. 3.2. This condition can be further split into real and imaginary components:

$$-\operatorname{Re} [Z'_{amp}] = \operatorname{Re} [Z_{res}]; \quad -\operatorname{Im} [Z'_{amp}] = \operatorname{Im} [Z_{res}] \quad (3.2)$$

Here, the real component requires that the effective resistance looking into the amplifier be negative (gain) to compensate the positive resistance (loss) of the resonator; while the imag-

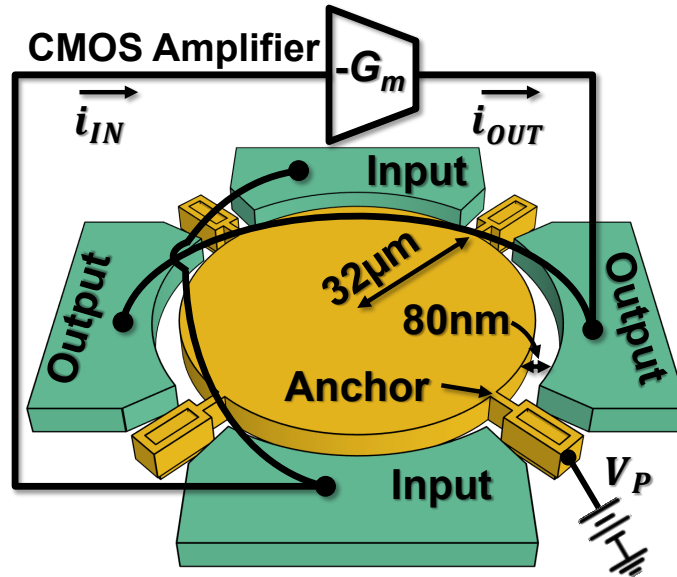


Figure 3.1: Perspective-view schematic of the capacitive-gap micromechanical disk resonator combined with a sustaining transconductance amplifier.

inary component sets the phase shift at oscillation. This simple impedance-based approach provides a versatile framework in the following sections for the design and analysis of the topologies used here.

An oscillator used in this dissertation combines a two-port frequency selective MEMS resonator wired in closed-loop feedback with an amplifier as shown in Fig. 3.1. The MEMS resonator, as shown in Fig. 3.1, used in most of the dissertation is a compound (2,1) mode polysilicon disk resonator with  $32\mu\text{m}$  radius and  $80\text{nm}$  capacitive gaps designed for a 61 MHz frequency of operation. Table 3.1 presents the design parameters of the resonator generated using equations in Chapter 2.

## 3.2 Pierce Amplifier Design

The Pierce topology [14] has long been a standard circuit for traditional crystal oscillators due to its low complexity and high performance. More recently, use of this topology in piezoelectric resonator oscillators have demonstrated the capability to achieve low power operation in an on-chip MEMS system [45]–[47].

Until now, however, the Pierce topology has not been investigated for use in capacitive-gap MEMS disk resonators, where the high  $Q$ -factors possible would be expected to yield improved phase noise marks without requiring power-hungry amplifiers. Indeed, the low noise figure of this simple amplifier design used here may yield an oscillator with no degradation in phase noise performance even while total power consumption is drastically reduced compared to work using trans-impedance amplifier topologies [11], [13].

Table 3.1: The 61MHz compound (2,1) mode disk resonator's parameters for different  $V_P$ 's

Parameter	$V_P$			Unit
	6.6 V	7.45 V	8.7 V	
Structure Material	Polysilicon			-
Radius, $R$	32			$\mu\text{m}$
Thickness, $h$	3.0			$\mu\text{m}$
Electrode overlapping angle, $\Delta\theta$	67			deg
Electrode-to-resonator gap, $d_0$	80			nm
Resonator mass, $m_{mre}$	$8.06 \times 10^{-12}$			kg
Resonator stiffness, $k_{mre}$	$1.15 \times 10^6$			N/m
Damping factor, $c_{mre}$	$3.8 \times 10^{-8}$			kg/s
Quality factor in vacuum, $Q$	80,000			-
Series Resistance, $R_x$	18.2	13.8	9.8	k $\Omega$
Inductance, $L_x$	3.85	2.93	2.08	H
Capacitance, $C_x$	1.82	2.39	3.37	aF
Electromech. coupling, $\eta_e$	$1.45 \times 10^{-6}$	$1.66 \times 10^{-6}$	$1.97 \times 10^{-6}$	C/m
DC-biased voltage across the gap, $V_{PG}$	5.913	6.778	8.046	V
Parasitic Trace Resistance, $R_{VP}$ & $R_{rp}$	~1.5			k $\Omega$
Static Overlap Capacitance, $C_o$	24.8			fF

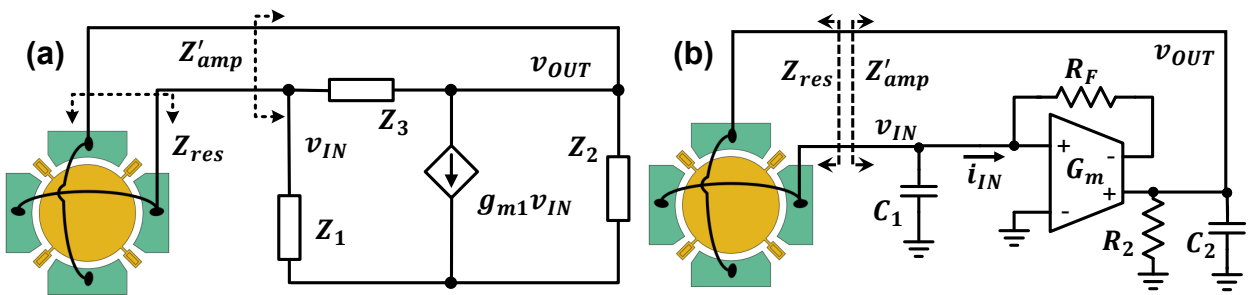


Figure 3.2: (a) Small-signal equivalent circuit of the complete Pierce oscillator using lumped impedances  $Z_1$ ,  $Z_2$ , and  $Z_3$ , which model all capacitance and resistance components of the transistors  $M_1$  (except its transconductance  $g_{m1}$ ),  $M_2$ , and  $M_3$ . (b) Small-signal equivalent circuit of the complete TIA-based oscillator.

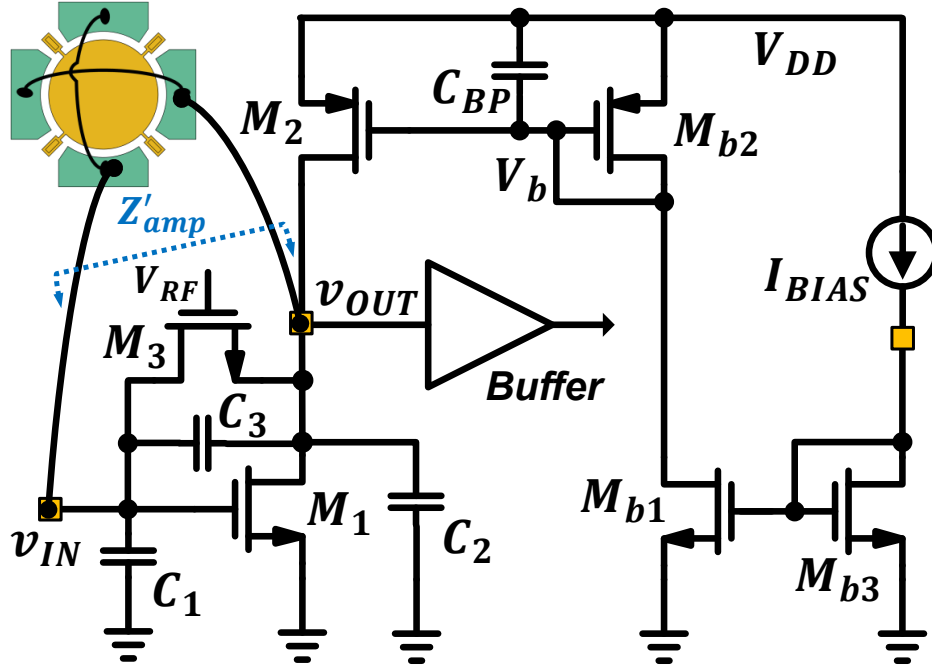


Figure 3.3: Schematic of the CMOS amplifier used in the Pierce oscillator, including bias network and parasitic capacitance at input and output nodes.

The Pierce oscillator topology here combines a two-port frequency-selective MEMS resonator wired in closed-loop feedback with a single transconducting gain device. Figure 3.3 presents the CMOS circuit, where MOS transistor  $M_1$  acts as the gain element and  $M_2$  serves as a load transistor, while  $M_3$  provides feedback to properly dc-bias  $M_1$ . Here, transistor  $M_1$  introduces  $180^\circ$  of phase shift between the input and output voltages. At resonance, the phase shift across the Wine-Glass mode disk resonator is  $0^\circ$ , so an additional  $180^\circ$  is needed to satisfy oscillation criterion. To supply this, the resonator must operate in the inductive region, i.e., with frequency slightly above that of the series resonance, and resonate with  $C_1$ ,  $C_2$ , and  $C_3$ , which comprise the total parasitic capacitance from the resonator, the amplifier, and surrounding structures (e.g., bond pads) at the input and output nodes. The impedance looking into the gate and drain of  $M_1$  can then be modeled using the small signal equivalent circuits of Fig. 3.2(a). Here, impedances  $Z_1$ ,  $Z_2$ , and  $Z_3$  include the resistive and reactive components of devices  $M_1$  (excluding its transconductance  $g_{m1}$  which is separated out for further analysis),  $M_2$  and  $M_3$ .

To describe oscillator operation first requires a small-signal analysis of the complete amplifier-resonator system. Continuing to follow the impedance-based approach, the amplifier topology of Fig. 3.3 with equivalent small-signal model of Fig. 3.2(a), produces an impedance looking into the amplifier of

$$Z'_{amp} = \frac{Z_1 Z_3 + Z_2 Z_3 + Z_1 Z_2 Z_3 g_{m1}}{Z_1 + Z_2 + Z_3 + Z_1 Z_2 g_{m1}} \quad (3.3)$$

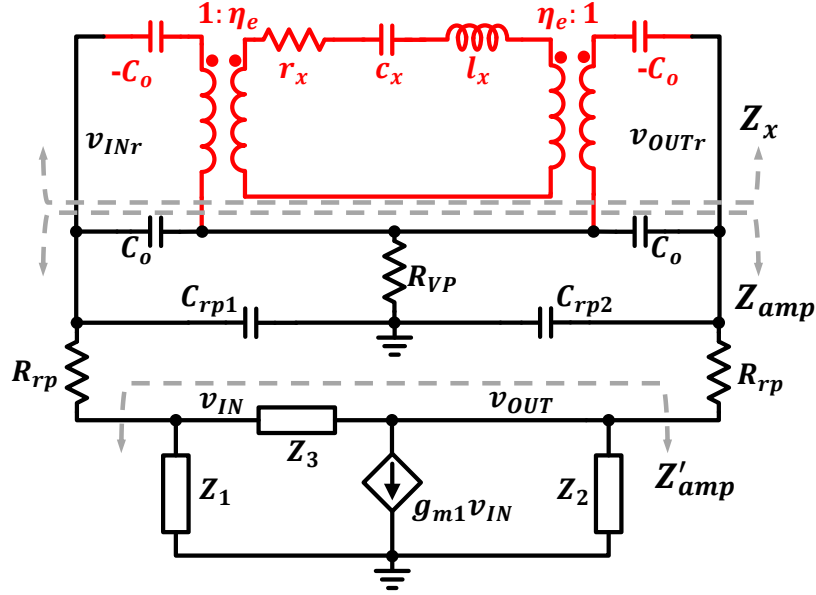


Figure 3.4: Complete small-signal oscillator circuit model indicating the division between amplifier and resonator used for impedance modeling. Here,  $C_{1,r}$ ,  $C_{2,r}$ , and  $C_{3,r}$  in Fig. 2.3 are combined with  $C_1$ ,  $C_2$ , and  $C_3$  in  $Z_1$ ,  $Z_2$ , and  $Z_3$ .

Further combining the complete small-signal model for the resonator (*cf.* Fig. 2.3) with this amplifier model (*cf.* Fig. 3.2) gives the resultant complete model of the oscillator shown in Fig. 3.4. Here, the additional resonator parasitics  $C_{1,r}$ ,  $C_{2,r}$ , and  $C_{3,r}$  are included in  $C_1$ ,  $C_2$ , and  $C_3$ . Analyzing the impedance  $Z_{amp}$  seen by the resonator tank, which includes the impedances of the amplifier circuit and all parasitic elements, provides the requirements for oscillation from Eqns. (3.1), (3.2):

$$-R_{amp} = \text{Re}[Z_x] = R_x; \quad -X_{amp} = \text{Im}[Z_x] = \omega L_x - \frac{1}{\omega C'_x} \quad (3.4)$$

### 3.2.1 Lossless Analysis

For the simplest lossless case, all resistance elements except the resonator's motional resistance,  $R_x$ , are assumed to be zero; i.e. trace resistance is zero ( $R_{rp} = 0$  and  $R_{VP} = 0$ ) and the losses in the amplifier are small (implying the real parts of  $Z_1 - Z_3$  are large). Combining capacitors,  $C_{rp1}$ ,  $C_{rp2}$ , and  $C_o$  from the resonator into  $C_1$ ,  $C_2$ , and  $C_3$ , the real and imaginary components of  $Z_{amp}$  can be found:

$$R_{amp} = -\frac{g_{m1}C_1C_2}{(g_{m1}C_3)^2 + \omega^2(C_1C_2 + C_1C_3 + C_2C_3)^2} \quad (3.5)$$

$$X_{amp} = -\frac{g_{m1}^2 C_3 + \omega^2 (C_1 + C_2) (C_1 C_2 + C_1 C_3 + C_2 C_3)}{\omega [(g_{m1} C_3)^2 + \omega^2 (C_1 C_2 + C_1 C_3 + C_2 C_3)^2]} \quad (3.6)$$

For oscillation to start,  $-R_{amp}$  must be larger than the motional resistance  $R_x$ . However,  $C_1$ ,  $C_2$ , and  $C_3$  constrain the achievable  $-R_{amp}$  to a maximum value. The green curve in Fig. 3.5(a) illustrates this effect by plotting  $-R_{amp}$  versus  $g_{m1}$  for typical device values, together with typical resonator  $R_x$  values for two different bias voltages,  $V_P$ . The green curve in Fig. 3.5(b) similarly shows the theoretical plot of  $X_{amp}$ . In Fig. 3.5 (a) and (b), the values of  $C_1$ ,  $C_2$ , and  $C_3$  are kept constant: in general, they are not constant. Particularly, the parasitic capacitances of transistors change with their  $g_m$ . Nevertheless, for the small  $g_{m1}$ ,  $C_1$ ,  $C_2$ , and  $C_3$  are dominated by other parasitics. Therefore, conclusions drawn in this section are valid for low-power oscillator designs. Refocusing on  $-R_{amp}$ , the maximum value of  $-R_{amp}$  occurs when:

$$g_{m1,max} = \omega_{oe} \left( C_1 + C_2 + \frac{C_1 C_2}{C_3} \right) \quad (3.7)$$

with resultant  $|R_{amp}|_{max}$ :

$$|R_{amp}|_{max} = \frac{1}{2C_3\omega_{oe} \left( 1 + \frac{C_1+C_2}{C_1 C_2} C_3 \right)} \quad (3.8)$$

For a given  $R_x$ , achieving the lowest possible power operation necessitates operating at the lowest possible  $g_{m1}$ . This minimum, or critical,  $g_{m1}$  can be found:

$$g_{m1,crit} = \frac{C_1 C_2}{2C_3^2 R_x} \left[ 1 - \sqrt{1 - \frac{R_x^2}{|R_{amp}|_{max}^2}} \right] \quad (3.9)$$

If  $(g_{m1} C_3)^2 \ll \omega^2 (C_1 C_2 + C_1 C_3 + C_2 C_3)^2$ , as is the case for the low-power single-chip oscillators studied here, then Eqn. (3.9) can be further simplified, leading to an approximate solution:

$$g_{m1,crit} = C_1 C_2 \omega_{oe}^2 \left( 1 + \frac{C_1 + C_2}{C_1 C_2} C_3 \right)^2 R_x \quad (3.10)$$

As power consumption is proportional to  $g_{m1}$ , Eqn. (3.10) suggests that low power operation necessitates minimizing  $C_1$ ,  $C_2$ , and  $C_3$ . From Eqn. (3.8), there are two ways to increase  $|R_{amp}|_{max}$ : 1) raise the values of  $C_1$  and  $C_2$  at the cost of burning more power; and 2) reduce the input-to-output feedthrough capacitance  $C_3$ . The first of two has a limitation since the maximum possible gain irrespective of power budget is set at a ceiling of  $1/(2C_3\omega_{oe})$ . To illustrate the effect of the capacitances on  $-R_{amp}$  better, the black curve in Fig. 3.5(a) shows reduced  $-R_{amp}$  when  $C_3$  is increased from that of the green curve. In this case,  $|R_{amp}|_{max}$  becomes less than the motional resistance corresponding to  $V_P$  of 6.6 V, and,

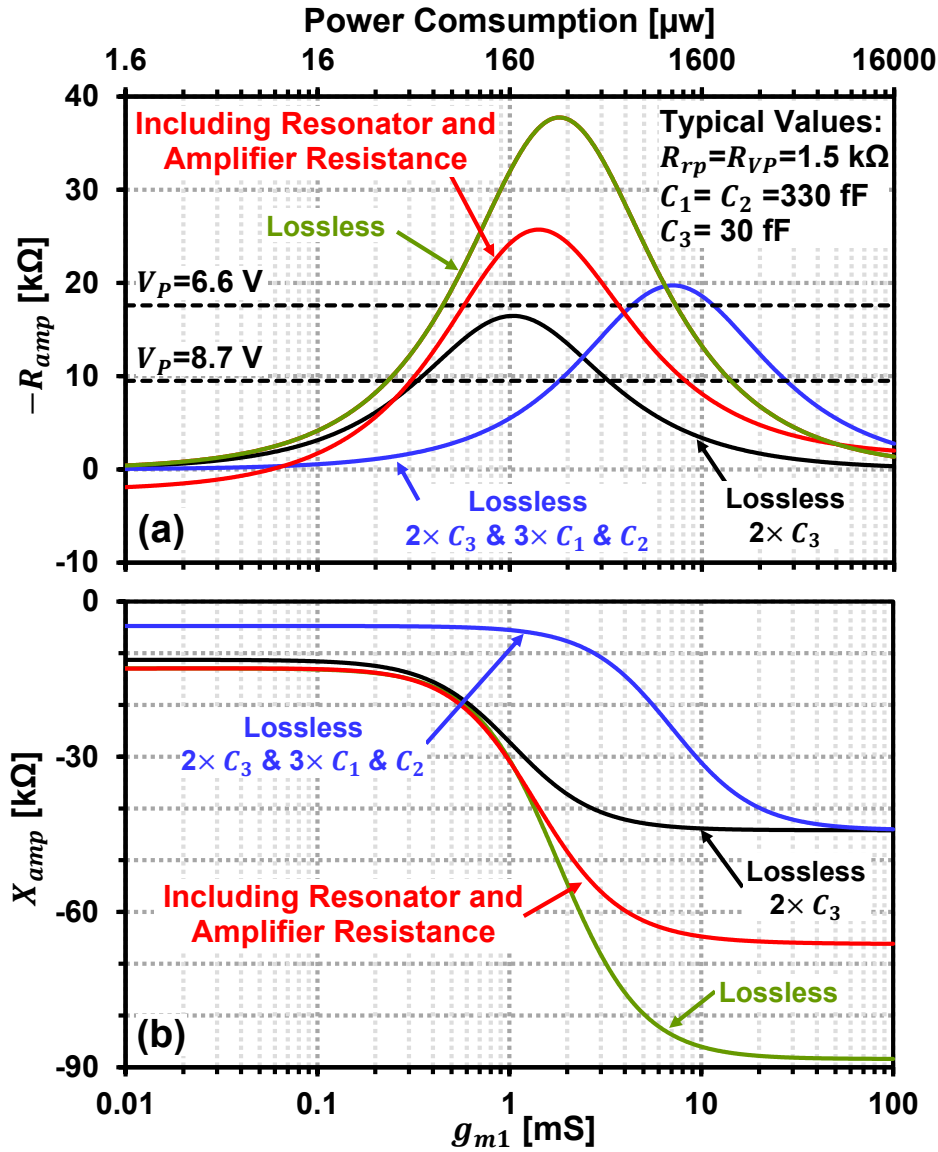


Figure 3.5: (a) Theoretical plots of amplifier gain,  $-R_{amp}$ , vs. transconductance,  $g_{m1}$ , of the  $M_1$  transistor, together with the required power consumption to achieve this  $g_{m1}$ , and (b) corresponding plots of amplifier reactance,  $X_{amp}$ . The black dashed lines correspond to calculated motional resistances of the resonator for different  $V_P$ 's. The green line represents a lossless oscillator with typical values for  $C_{1-3}$  that easily generates sufficient gain for oscillation, while the black curve illustrates the detriment of increasing  $C_3$  by two times, resulting in no oscillation for  $V_P$  of 6.6 V. Increasing  $C_1$  and  $C_2$  by three times allows the oscillation for  $V_P = 6.6$  V case at the cost of burning significantly larger power as shown by the blue curve. The red curve includes typical parasitic loss/resistance of the amplifier and resonator.  $V_{DD} = 2$  V and  $V^* = 0.16$  V are used. Here,  $V^* = 2I_{D1}/g_{m1}$  where  $I_{D1}$  is the drain current of  $M_1$ .

therefore, no oscillation can occur even with increased power consumption. To overcome this limit,  $C_1$  and  $C_2$  may be increased by a factor of 3 as in the blue curve, providing an increase in  $|R_{amp}|_{max}$  and thus allowing oscillation, though at a significant cost in power. Clearly, the goal of low-power oscillators is best achieved through minimizing  $C_3$ .

This strong dependence on  $C_3$  reveals why self-sustained oscillation of a micromechanical resonator is possible using a Pierce circuit, despite the resonator's large motional resistance  $R_x$ . Indeed, the  $C_3$  of a 61-MHz Wine-Glass disk resonator is on the order of 30-50 fF, many times smaller than the 4 pF [48], [49] in a typical 60-MHz quartz crystal, allowing  $|R_{amp}|_{max}$  to exceed the disks  $R_x$  of 18.2 k $\Omega$  for  $V_P$  of 6.6 V. In comparison, with  $C_3 = 4$  pF, a typical quartz crystal cannot muster a  $|R_{amp}|_{max}$  more than 157  $\Omega$ , even with  $C_1$  and  $C_2$  as large as 7 pF. Of course, the much smaller  $R_x = 70$   $\Omega$  of a typical 60-MHz quartz crystal does not require that  $|R_{amp}|_{max}$  be so large, but the needed  $C_1$  and  $C_2$  values are still on the order of 10 pF. Since larger  $C_1$  and  $C_2$  demand higher transistor drive power, a MEMS-based Pierce oscillator circuit with a relatively small  $C_3$  that in turn allows small  $C_1$  and  $C_2$  should permit much lower power consumption. If the resonator  $R_x$  can be further lowered, e.g., by increasing its dc-bias voltage  $V_P$ , as illustrated in Fig. 3.5(a), the power consumption of a MEMS-based Pierce oscillator should shrink. Indeed, the intersection of the green curve of Fig. 3.5(a) with the  $V_P = 8.7$  V line shows that indeed an increase in  $V_P$  by  $\sim 2$  V decreases the oscillation power requirement from  $\sim 72$   $\mu$ W to  $\sim 37$   $\mu$ W.

### 3.2.2 Lossy Analysis

Though the lossless analysis gives a good general understanding of the oscillator system, it neglects real-world parasitic losses from the resonator trace resistances ( $R_{rp}$  and  $R_{VP}$ ) and the amplifier's intrinsic resistance and leakage, both of which lead to increased gain requirements and hence increased power consumption. Here, amplifier loss is dominated by  $M_1$ , and can be approximated for long channel-length as follows:

$$r_{o1} \approx \frac{2}{\lambda g_{m1} (V_{GS1} - V_{th1})} \quad (3.11)$$

where  $\lambda$  is the channel-length modulation constant,  $V_{th1}$  is the threshold voltage of  $M_1$ , and  $V_{GS1}$  is the bias gate-to-source voltage of  $M_1$ . Including these typical losses produces the red curves in Fig. 3.5, where the amplifier needs to burn  $\sim 30\%$  more power to produce oscillation compared to the lossless case.

### 3.2.3 Minimizing Power Consumption

For low-power operation, parasitic capacitances constituting  $C_1$  and  $C_2$  are approximately the same. Rewriting  $C_1$  and  $C_2$  as  $(C_o + C_{p1,2})$  where  $C_{p1,2}$  is the sum of all the parasitic capacitance at either the input or the output allows a simplified form of Eqn. (3.10):

$$g_{m1,crit} = \frac{\omega_{oc}}{QC_x} (C_o + C_{p1,2} + 2C_3)^2 \quad (3.12)$$

Equation (3.12) suggests that low power operation necessitates the smallest possible stray capacitance. Here, it can be seen that the required  $g_{m1,crit}$ , and thus the required power to oscillate is inversely proportional to  $(C_x/C_{ptot}^2)$ , where  $C_{ptot}^2$  is the sum of the parasitic capacitances by the amplifier and the resonator. In the case of an integrated (ie., single-chip) system, the  $C_o$  term typically dominates, producing a simple performance metric of  $(C_x/C_o^2)$ .

Further reduction in power consumption necessitates maximizing  $C_x$  (or equivalently, decreasing resonator  $R_x$ ) while maintaining low parasitic capacitance. One approach, increasing  $V_P$ , quadratically reduces  $R_x$  as seen in Eqn. (2.26), but can be limited by available supply voltages in mobile applications. Instead, reducing the sidewall gap spacing,  $d_o$ , provides a marked 4th-order decrease in resonator  $R_x$ , while  $C_o$  increases only linearly, providing an overall decrease in operating power if these smaller gaps can be realized.

As the gap is made smaller,  $C_o$  dominates over  $(C_{p1,2} + 2C_3)$ , allowing Eqn. (3.12) to be approximated as:

$$g_{m1,crit} \cong \frac{\omega_{oe}}{QC_x} C_o^2 \rightarrow g_{m1,crit} \propto d_o^2 \quad (3.13)$$

In principle power requirements may thus be scaled downwards entirely through reduction in this gap size, subject to only fabrication limitations, at least when resistive losses are small.

Illustrating this, Fig. 3.6(a) presents theoretical plots of  $g_{m1,crit}$  and power consumption versus resonator sidewall gap. For gap sizes above 100 nm,  $R_x > |R_{amp}|_{max}$  and no solution to (3.9) exists. As gap is reduced, power consumption reduces with the fourth power of gap size. In the lossless case, represented by the green curve, this power reduction has no limit. If instead intrinsic amplifier loss is considered as in the blue curve, power consumption plateaus at a minimum value of  $\sim 9$  nW, representing the lowest power design possible. The red curves additionally add typical resonator trace resistances of 200  $\Omega$  (dotted line) and 1.5 k $\Omega$  (solid line), showing increased minimum power consumption of  $\sim 1$   $\mu$ W and  $\sim 10$   $\mu$ W, respectively. Clearly, achieving the lowest possible power requires minimizing both stray capacitance and trace resistance.

### 3.3 TransImpedance Amplifier Design

The TransImpedance Amplifier (TIA) topology offers an alternative MEMS oscillator configuration. The design presented here combines a two-port frequency-selective MEMS resonator wired in closed-loop feedback with a TIA amplifier. Similar to previous work [11], [13], Fig. 3.7 presents the CMOS circuit, where MOS transistor  $M_1 - M_4$  acts as a differential transconductance gain stage, while  $M_{RF}$  provides a shunt-shunt feedback to set transimpedance gain. The two differential pairs on the right in Fig. 3.7 is the common-mode feedback to provide a proper biasing of the amplifier. The bandwidth of this common-mode feedback needs to be larger than the oscillation frequency for this feedback to work properly.  $V_{CM}$  voltage provides the common-mode voltage level at the output of the amplifier. The differential amplifier with the output taken from one side, with the other side connected in

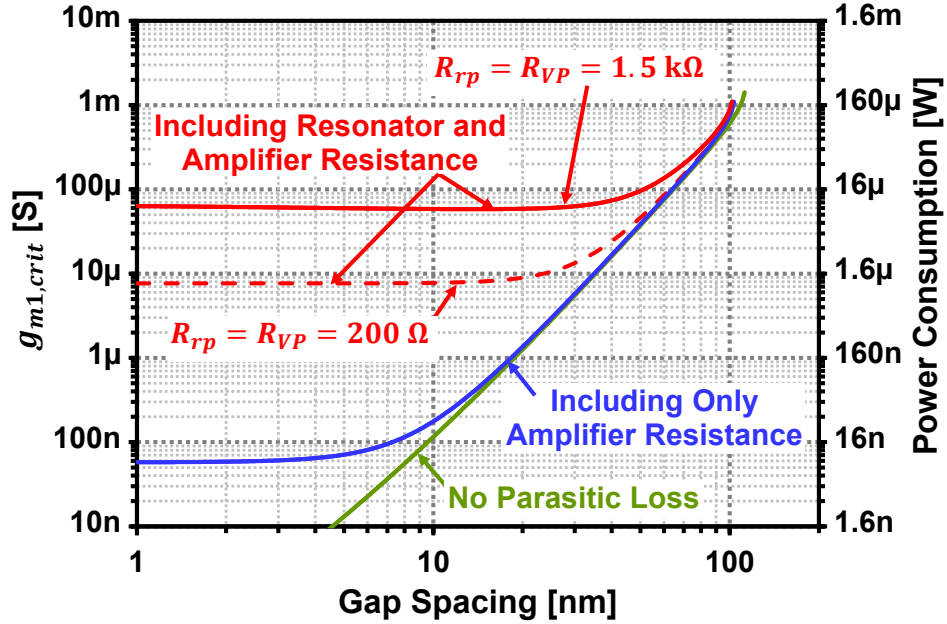


Figure 3.6: (a) Theoretical predictions of  $g_{m1,crit}$  and power consumption requirements to achieve oscillation vs. resonator capacitive-gap spacing. The green curve assumes the lossless case of Eqn. (3.9), where power consumption decreases without limit as gap is shrunk. The blue curve includes amplifier loss/resistance while the red curves also include additional resonator parasitic resistance, showing a minimum power plateau regardless of decreased gap spacing. Here,  $V_{DD}=2\text{ V}$ ,  $V^* = 0.16\text{ V}$ , and  $V_P = 8.7\text{ V}$  with the same capacitor values as in Fig. 3.5.

shunt-shunt feedback gives a  $0^\circ$  phase shift from input to output. At resonance, the phase shift across the Wine-Glass mode disk resonator is  $0^\circ$ , satisfying oscillation criterion. Lowering  $V_{GAIN}$  increases the gain of the amplifier: when this gain is larger than the resonator's loss, oscillation starts. The impedance looking into the input and output can be modeled using the small signal equivalent circuits of Fig. 3.2(b). Here, capacitance  $C_1$  and  $C_2$  comprise the total parasitic capacitance from the resonator, the amplifier, and surrounding structures (e.g., bond pads) at the input and output nodes.  $R_F$  is the shunt-shunt feedback resistor and is implemented by the MOS transistor,  $M_{RF}$ , in Fig. 3.7.

To describe oscillator operation first requires a small-signal analysis of the complete amplifier-resonator system. Continuing to follow the impedance-based approach, the amplifier topology of Fig. 3.7 with equivalent small-signal model of Fig. 3.2(b), produces an impedance looking into the amplifier of

$$Z'_{amp} = \frac{v_{out}}{i_{in}} = \frac{-R_F A_v \omega_1 \omega_2}{s^2 + (\omega_1 + \omega_2) s + \omega_1 \omega_2 (1 + A_v)} \quad (3.14)$$

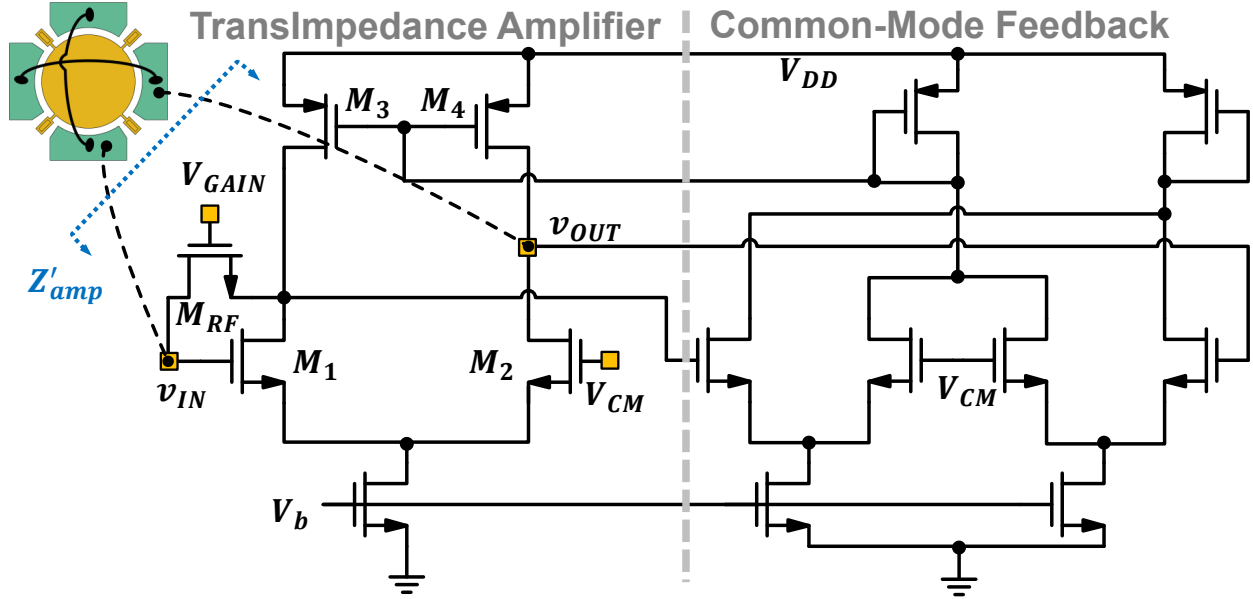


Figure 3.7: Schematic of the CMOS amplifier used in the TIA-based oscillator.

where

$$\omega_1 = \frac{1}{R_F C_1}; \quad \omega_2 = \frac{1}{(R_F // R_2) C_2}; \quad A_v = G_m (R_F // R_2); \quad G_m = \frac{1}{2} g_{m1}; \quad (3.15)$$

To achieve Eqn. (3.14) and (3.15), three assumptions have been made:

1. The bandwidth of the common-mode feedback is large such that the TIA amplifier can be analyzed using the half-circuit method.
2. Only parasitic capacitance shunt to the ground from the input and output dominate the system. This means the feedthrough capacitance from the input to output is negligible.
3. Parasitic resistances are negligible except transistors'  $r_o$ .

These assumptions are reasonable for the 61MHz TIA oscillator presented in this work.

Further combining the complete small-signal model for the resonator (*cf.* Fig. 2.3) with this amplifier model (*cf.* Fig. 3.2(b)) gives the resultant complete model of the oscillator shown in Fig. 3.8. Here, the additional resonator parasitics  $C_{1,r}$  and  $C_{2,r}$  are included in  $C_1$  and  $C_2$ .  $C_{3,r}$  is neglected per the assumptions. Analyzing the impedance  $Z_{amp}$  seen by the resonator tank, which includes the impedances of the amplifier circuit and all parasitic elements, provides the requirements for oscillation from Eqns. (3.1), (3.2):

$$-R_{amp} = \text{Re}[Z_x] = R_x; \quad -X_{amp} = \text{Im}[Z_x] = \omega L_x - \frac{1}{\omega C'_x} \quad (3.16)$$

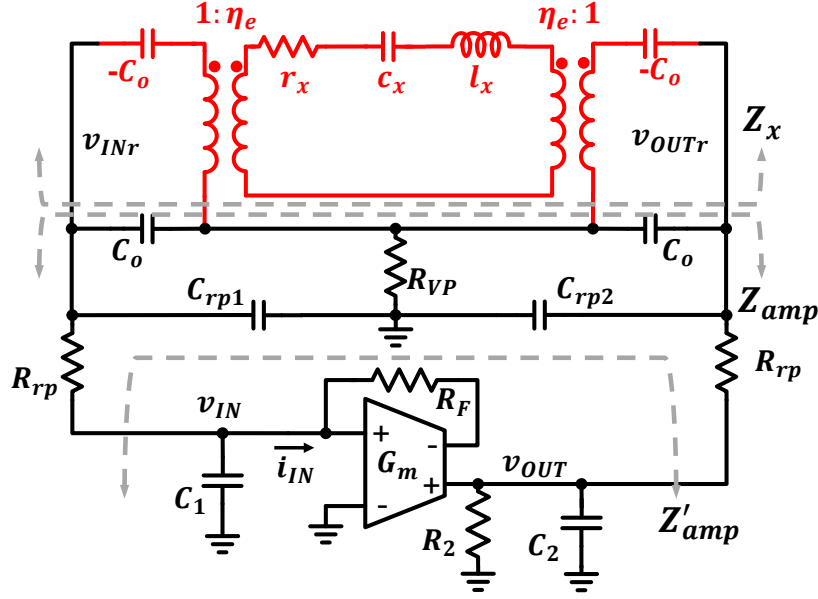


Figure 3.8: Complete small-signal oscillator circuit model indicating the division between amplifier and resonator used for impedance modeling. Here,  $C_{1,r}$  and  $C_{2,r}$ , and  $C_{3,r}$  in Fig. 2.3 are combined with  $C_1$  and  $C_2$ .

To simplify the analysis, all resonator's resistance elements are assumed to be zero; i.e. trace resistance is zero ( $R_{rp} = 0$  and  $R_{VP} = 0$ ). This assumption is only valid when  $R_x$  is larger than trace resistance. Combining capacitors,  $C_{rp1}$ ,  $C_{rp2}$ , and  $C_o$  from the resonator into  $C_1$  and  $C_2$ , the real and imaginary components of  $Z_{amp}$  can be found:

$$R_{amp} = \frac{-R_F A_v \omega_1 \omega_2 [(1 + A_v) \omega_1 \omega_2 - \omega^2]}{[\omega_1 \omega_2 (1 + A_v) - \omega^2]^2 + \omega^2 (\omega_1 + \omega_2)^2} \quad (3.17)$$

$$X_{amp} = \frac{R_F A_v \omega_1 \omega_2 \omega (\omega_1 + \omega_2)}{[\omega_1 \omega_2 (1 + A_v) - \omega^2]^2 + \omega^2 (\omega_1 + \omega_2)^2} \quad (3.18)$$

Similar to the Pierce oscillator,  $-R_{amp}$  must be larger than the motional resistance  $R_x$  for oscillation to start.  $-R_{amp}$  can be increased by increasing  $R_F$  through the voltage control signal  $V_{GAIN}$ . However,  $C_1$  and  $C_2$  constrain the achievable  $-R_{amp}$  to a maximum value. To illustrate, Fig. 3.9(a) plots  $R_{amp}$  and  $X_{amp}$ , as the feedback resistor  $R_F$  of the TIA changes (Note: Fig. 3.9(a) is plotting  $R_{amp}$  and should not be confused with the convention  $-R_{amp}$  used through out this Chapter). The maximum  $-R_{amp}$  occurs at point A in Fig. 3.9(a). This is the optimal bias condition of  $R_F$  for an oscillator. Point B and C are not important for an oscillator but they are crucial for an active- $Q$  boosted resonator systems in Section 7.2. In such system, point A corresponds for the maximum  $Q_{eff}$  and point B corresponds for the transition of  $Q$  boosting to  $Q$  loading while point C corresponds for the minimum  $Q_{eff}$ . Section 7.2 will present the detail analysis. Refocusing to the oscillator application,

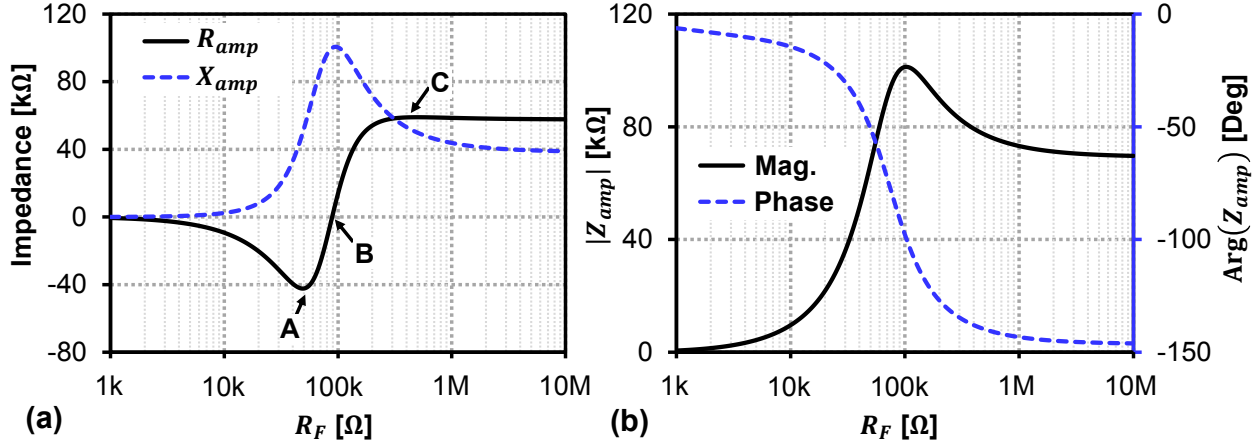


Figure 3.9: (a) Theoretical prediction of resistance (black) and reactance (dotted blue) parts of the impedance,  $Z_{amp}$ , looking into the TIA amplifier as the feedback resistor,  $R_F$ , increases. Here, resistance and capacitance values used are given in Fig. 3.10. (b) Theoretical prediction of magnitude (black) and phase (dotted blue) of  $Z_{amp}$ . Note: the operating frequency simulated here is 61 MHz.

Fig. 3.9(b) shows the magnitude and phase of  $Z_{amp}$ . Comparing Fig. 3.9 (a) and (b), it is important to note that the magnitude of  $Z_{amp}$  continues to increase for  $R_F$  between point A and 100 k $\Omega$ , but, due to sufficient phase shift,  $-R_{amp}$  goes down.

If  $A_v \gg 1$  and substituting Eqn. (3.15) into Eqn. (3.17), the corresponding  $R_F$ 's for point A, B, and C become:

$$R_{FA} = \frac{G_m R_2}{C_1 \omega \left[ C_2 R_2 \omega + \sqrt{\frac{(G_m + C_2 [C_1 + C_2] R_2 \omega^2)^2}{G_m^2 + [C_1 + C_2]^2 \omega^2}} \right]} \quad (3.19)$$

$$R_{FB} = \frac{G_m}{C_1 C_2 \omega^2} \quad (3.20)$$

$$R_{FC} = \frac{G_m R_2}{C_1 \omega \left[ C_2 R_2 \omega - \sqrt{\frac{(G_m + C_2 [C_1 + C_2] R_2 \omega^2)^2}{G_m^2 + [C_1 + C_2]^2 \omega^2}} \right]} \quad (3.21)$$

Substitute Eqn. (3.19) into Eqn. (3.17) and (3.18),  $R_{amp}$  and  $X_{amp}$  becomes:

$$R_{ampA} = \frac{-G_m R_2 \left[ \sqrt{G_m^2 + (C_1 + C_2)^2 \omega^2} - (C_1 + C_2) \omega \right]}{2C_1 \omega [G_m + R_2 C_2 (C_1 + C_2) \omega^2]} \quad (3.22)$$

$$X_{ampA} = \frac{G_m^2 R_2}{2C_1 \omega [G_m + R_2 C_2 (C_1 + C_2) \omega^2]} \quad (3.23)$$

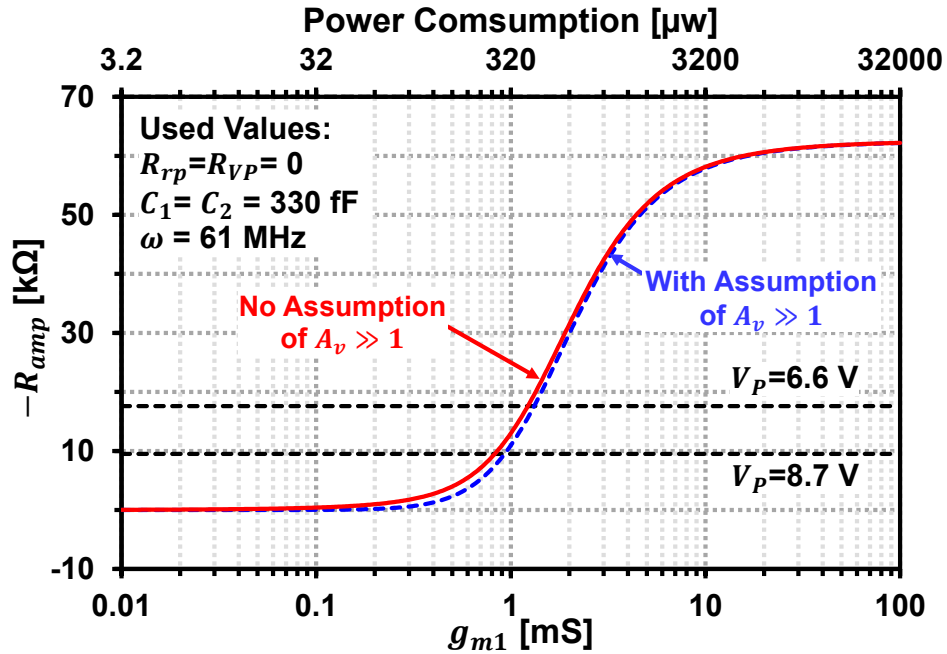


Figure 3.10: Theoretical plots of amplifier gain,  $-R_{amp}$ , vs.  $g_{m1}$  of the  $M_1$  transistor, together with the required power consumption to achieve this  $g_{m1}$ . Here,  $V_{DD} = 2$  V and  $V^* = 0.16$  V are used to calculate power numbers. The black dashed lines corresponds to calculated motional resistances of the resonator for different  $V_P$ 's. The red line represents an oscillator with typical values of  $C_1$  and  $C_2$  that easily generates sufficient gain for oscillation for  $V_P$  of both 6.6 V and 8.7 V. The dotted blue line is generated using Eqn. (3.22) and illustrates that the approximation of ( $A_v \gg 1$ ) gives similar values for  $-R_{amp}$ .

The dotted blue curve in Fig. 3.10 illustrates the effect of  $-R_{amp}$  versus  $g_{m1}$  using Eqn. (3.22) for typical device values, together with typical resonator  $R_x$  values for two different bias voltages,  $V_P$  (cf. Table 3.1). Here,  $R_2$  approximately equals  $r_{o1}/r_{o3}$  where  $r_o$  is output resistance of a transistor, determined by the  $g_m$  of the transistor (Eqn. (3.11)).  $-R_{amp}$  asymptotically approaches a max value as  $g_{m1}$  increases. The red line in Fig. 3.10 similarly shows the theoretical plot of  $-R_{amp}$  without the  $A_v \gg 1$  assumption: this verifies that Eqn. (3.22) is a reasonable approximation to understand the TIA oscillator design. Furthermore, the intersection of the two black dashed lines with  $-R_{amp}$  lines in Fig. 3.10 informs that the oscillation power requirement decreases by 34% for increasing  $V_P$  from 6.6 V to 8.7 V.

### 3.4 Pierce vs. Transimpedance Amplifier Oscillators

The TIA comprised a fully differential CMOS amplifier biased by a common-mode feedback circuit that effectively canceled common-mode noise, especially low-frequency noise caused by vibration [50]. The Pierce oscillator, however, with its single-ended Pierce topol-

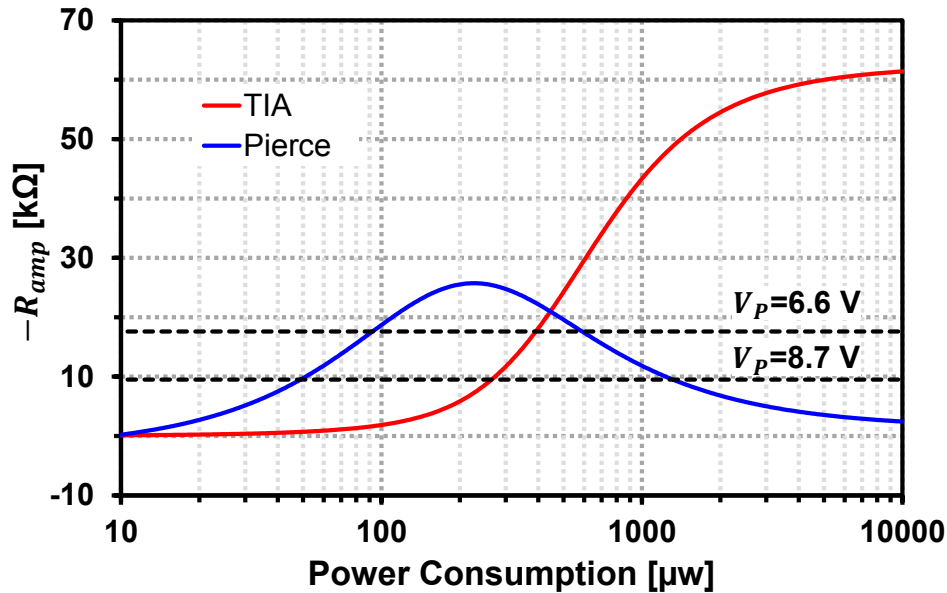


Figure 3.11: Theoretical plots of amplifier gain,  $-R_{amp}$ , vs. the required power consumption. The black dashed lines correspond to calculated motional resistances of the resonator for different  $V_P$ 's. The red line and the blue line represents the TIA-based oscillator and the Pierce oscillator with typical values for parasitic capacitance and resistance given in Fig. 3.5 and Fig. 3.9.  $V_{DD} = 2$  V is used.

ogy, sacrifices this common-mode feedback to achieve lower noise-figure, hence lower phase noise, than TIA-based oscillators. This is made possible by 1) using only two active transistors compared to a minimum of four in the TIA; 2) using a very large shunt-shunt feedback MOS resistor,  $M_3$ , for biasing compared to the much smaller gain-setting resistor required by the TIA, where the larger the resistance, the smaller the current noise; and 3) using  $C_{BP}$ , at the cost of some area increase, between the gate of  $M_2$  and  $V_{DD}$ , as shown in Fig. 3.3, to filter noise from bias transistors  $M_{b1} - M_{b3}$  and from  $V_{DD}$ .

Figure 3.11 presents  $-R_{amp}$  of the TIA-based oscillator (red) and the Pierce oscillator (blue) versus the required power consumption. The TIA-based oscillator requires 260  $\mu$ W and 395  $\mu$ W for the resonator's  $R_x$  corresponding to  $V_P$  of 8.7 V and 6.6 V, respectively. By comparison, the Pierce oscillator only needs 50  $\mu$ W and 92  $\mu$ W, 4-5 times smaller power consumption than the TIA. Fig. 3.11 further indicates that the TIA topology can generate larger  $-R_{amp}$  by burning more power, but of course for low power applications, burning extra power is not desirable. Finally, the smaller transistor stack of the Pierce oscillator circuit allows it to operate at a lower supply voltage  $V_{DD}$  without driving the two transistors into their triode regions, and hence allows even further power reduction. Together these design changes enable a pierce oscillator with not only lower power, but also reduced noise when compared to the more complicated TIA configurations. This will be verified experimentally in Section 5.2.

### 3.5 Amplifier-Derived Frequency-Pulling

Though oscillation frequency is determined primarily by the mechanical resonance, stray capacitance and amplifier reactance produce a slight shift of oscillation frequency to meet the requirement of Eqn. (3.4) and (3.16). Solving this for frequency yields:

$$f_o = f_{nom} \sqrt{\left[ 1 - \eta_e^2 \left( \frac{2}{C_o} + \omega_{oe} X_{amp} \right) \frac{1}{k_{mre}} \right]} \quad (3.24)$$

where  $X_{amp}$  is the amplifier reactance as defined in Eqn. (3.6) and (3.18). This can be recognized as a correction to total resonator stiffness consisting of both the usual electrical stiffness,  $2\eta_e^2/C_o$ , as well as a second term,  $\eta_e^2\omega_{oe}X_{amp}$ , representing electrical pulling due to amplifier loading. The resultant total electrical stiffness can then be written as:

$$k_{eL} = \eta_e^2 \left( \frac{2}{C_o} + \omega_{oe} X_{amp} \right) \quad (3.25)$$

For the Pierce amplifiers here,  $X_{amp}$  has a negative value (*cf.* Fig. 3.5(b)), leading to a reduction in total electrical stiffness. This permits an oscillator designed such that amplifier loading cancels the electrical stiffness. On the other hand,  $X_{amp}$  has a positive value (*cf.* Fig. 3.9) for the TIA amplifier, leading to an increases in total electrical stiffness. By way of illustration, the electrical stiffness for the resonator described in Table 3.1 with  $V_P = 6.6V$  is -168 N/m while the Pierce amplifier effective stiffness is 31 N/m corresponding to a mere 7.26 ppm frequency shift. Such precise resonator-defined frequencies is a strong advantage of this MEMS-based oscillator compared typical on-chip LC oscillators, where amplifier loading can be a design challenge that must be expressly compensated for.

### 3.6 Oscillation Start-up

Upon amplifier turn-on, a loop gain of greater than unity produces oscillation growth, modeled in the small-signal regime by an exponential with time constant [51]:

$$\tau = -\frac{2L_x}{R_{amp} + R_x} = -\frac{2L_x}{R_x(1 - T)} \quad (3.26)$$

where  $T = R_{amp}/R_x$  is the loop gain. As oscillator turn-on time is an important performance metric for applications requiring cycled oscillator use to save power, it is instructive to examine the total time required to reach a desired steady-state amplitude. Neglecting nonlinear effects, this time can be given by

$$t_{su} = \tau \ln \left( \frac{V_{osc}}{v_{res}(0)} \right) \quad (3.27)$$

where  $V_{osc}$  is the steady-state oscillation voltage across the resonator, and  $v_{res}(0)$  is the initial voltage across the resonator at  $t = 0$ . For the mechanical circuit presented in Chapter 2, it is

more intuitive to look into the current (or velocity in mechanical domain) going through the resonance tank. At resonance, the initial voltage  $v_C(0)$  across the capacitance equivalently defines the initial current,  $i_x(0)$ , going through the resonator based on energy conservation principles

$$\frac{L_x i_x^2(0)}{2} = \frac{C_{tot} v_C^2(0)}{2} \quad (3.28)$$

where  $C_{tot}$  is the total loop capacitance of the tank  $C'_x$  and  $C_{amp}$  in series:

$$\frac{1}{C_{tot}} = \frac{1}{C'_x} + \frac{1}{C_{amp}} \quad (3.29)$$

$C_{amp}$  is the equivalent capacitance of the amplifier and can be defined as  $C_{amp} = 1/(\omega_{oe} X_{amp})$ . Relating  $v_C(0)$  to  $v_{res}(0)$  as

$$v_{res}(0) = \frac{C_{amp}}{C'_x + C_{amp}} v_C(0) \quad (3.30)$$

Equations (3.27), (3.28), and (3.30) are combined to yield the total start-up time for the oscillator:

$$t_{su} = \tau \ln \left[ \frac{V_{osc}}{i_x(0)} \sqrt{\frac{(C'_x + C_{amp}) C_{amp}}{L_x C'_x}} \right] = \tau \ln \left[ \frac{V_{osc} \omega C_{amp}}{i_x(0)} \right] \quad (3.31)$$

Fast oscillator turn-on time can be an important performance metric for applications requiring cycled oscillator startup for power savings, or super-regenerative receivers [23], [52] that identify RF transmitted data by measuring the rate at which oscillation grows. Two approaches are thus suggested to reduce oscillator startup time: 1) increasing the initial starting current,  $i_x(0)$ , and 2) decreasing the time constant ( $\tau$ ). Typically,  $i_x(0)$  derives from thermal noise, which in the case of a mechanical system takes the form of Brownian motion, but may also be tailored by an appropriate switch-on procedure or injection of resonance current at start-up. The oscillator time constant is seen to depend primarily on the loop gain, which may be increased via either increasing amplifier gain or via a reduction of resonator  $R_x$ . As an increase in  $R_{amp}$  comes at the cost of increased  $g_{m1}$  requirements and thus higher power consumption, the lowest power and fastest startup is achieved via minimizing  $R_x$  by increasing DC-bias  $V_P$  or reducing gap spacing  $d_o$ .

## Chapter 4

# Device Fabrication and Measurement Methods

The MEMS resonators of this dissertation were fabricated using surface micro-machining processes in the Berkeley Nanolab. Several fabrication runs offered a diversity of devices designs and resonator materials used in the work of this dissertation. Based on variations of the process presented in [53], these fabrications runs were broadly grouped as a self-aligned stem processes, where the resonator anchor attachment is defined by the resonator structure mask itself (thus ‘self-aligned’ to the resonator structure), and a planarized process, where the planarization steps allow thick polysilicon interconnects, remove overhanging electrodes, and relax lithographical requirements. This chapter presents a detailed accounting of these processes, followed by a description of the methods used to measure the resultant resonators, as well as measurement examples of completed devices.

### 4.1 Self-Aligned Stem Process

The self-aligned stem process described here is similar to the process used in [53]. Figure 4.1 presents cross-sections of the fabrication process that achieves the disk resonators with perfectly-centered, self-aligned stems. The process starts with a heavy phosphorous diffusion via  $\text{POCl}_3$  to serve as the substrate ground plane, followed by sequential depositions of 2  $\mu\text{m}$  of high temperature LPCVD oxide (HTO) at  $950^\circ\text{C}$  and 350 nm of stoichiometric silicon nitride that together serve to isolate devices and interconnects from the conductive silicon substrate. Interconnect polysilicon is then deposited to a thickness of 300-500 nm and doped, again via  $\text{POCl}_3$ . After patterning this polysilicon layer to form interconnects, 300-700 nm of HTO is deposited to act as a sacrificial layer to temporarily support the subsequent structural layer during its deposition and patterning. The 2-3  $\mu\text{m}$ -thick structural film—either  $\text{POCl}_3$ -doped polysilicon or hot-filament boron-doped CVD microcrystalline diamond—is then deposited and capped with a 1.2  $\mu\text{m}$ -thick film of HTO that serves as both a hard mask during etching of the structural film, and later as a spacer layer to sep-

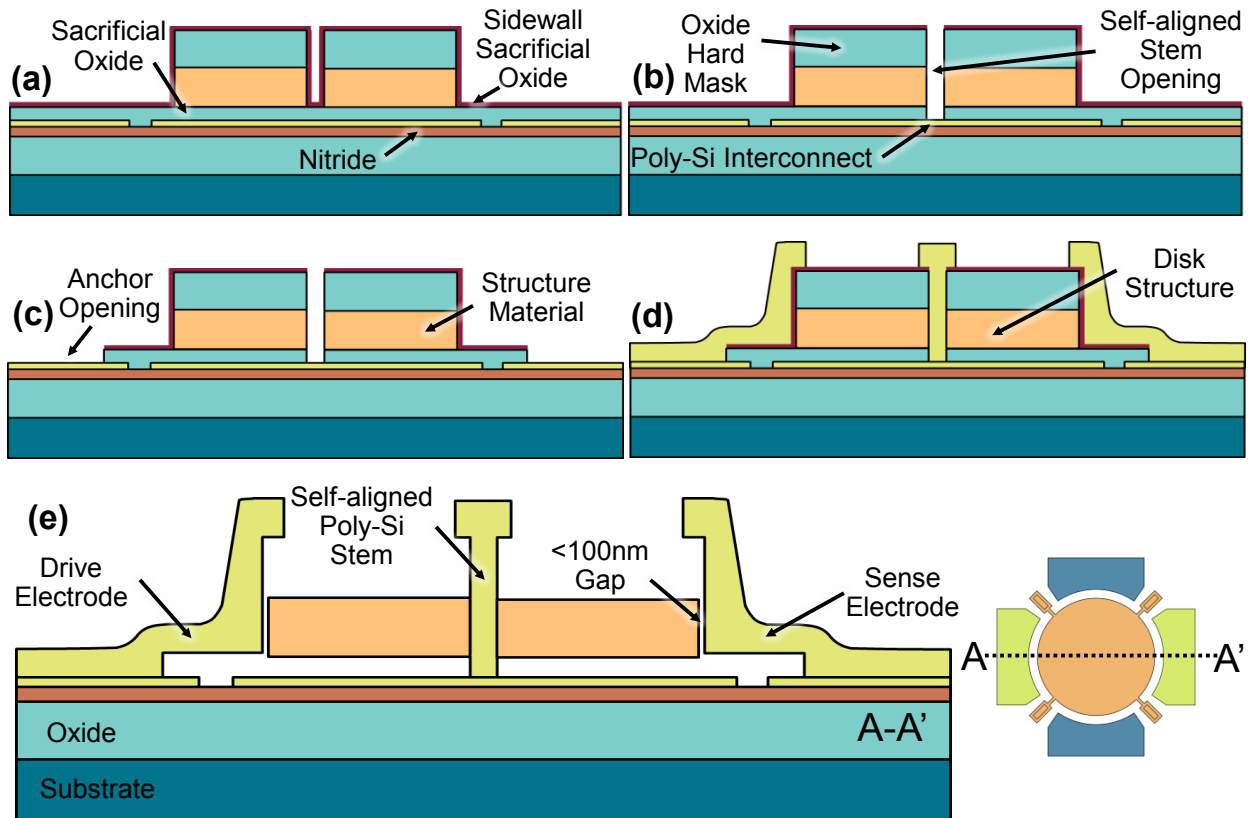


Figure 4.1: Fabrication process flow for polysilicon and microcrystalline diamond disk resonators. (a)-(d) illustrate the resonator construction through repeated LPCVD film depositions, lithography, and plasma etches, followed by a 49% HF wet etch process to remove the sacrificial oxide to yield the final released structure of (e). Note: the Wine-Glass disk resonator normally does not have a center stem. Here, a center stem such as used for a contour-mode disk resonator is included in the process flow to illustrate the self-align feature of this process.

arate the disk from overhanging electrode portions. The composite oxide mask-structural film layer is patterned in a single mask to define not only the disk structure, but also the 0.6-2  $\mu\text{m}$ -diameter stem opening at its center, as shown in Fig. 4.1(a). Definition of the stem location via the same mask as the resonant structure self-aligns the stem to the very center of the disk structure.

An HTO deposition of less than 100 nm conformally coats all surfaces, including structure sidewalls, and defines the ever-important electrode-to-resonator gap spacing. Since this thin oxide film also coats the stem opening, as shown in Fig. 4.1(a), steps are needed to remove it from the stem before stem-refilling to permit electrical contact to the disk. This is done by spinning a thick photoresist and patterning it to expose the stem and the electrode vias,

after which a combination of dry and wet etching removes the sidewall sacrificial spacer oxide in the stem opening (*cf.* Fig. 4.1(b)) and the underlying bottom sacrificial oxide down to interconnect on the substrate, as shown in Fig. 4.1(c). A subsequent 2  $\mu\text{m}$  polysilicon deposition then not only provides the material for electrodes, but also refills the anchor vias to create very rigid, self-aligned, electrically-contacted stems. This last polysilicon layer is then doped and patterned as shown in Fig. 4.1(d) to define the electrodes and stem tops. Finally, structures are released in 48.8 wt. % Hydrofluoric acid (HF) to yield the final cross-section of Fig. 4.1(e). Self-aligned stem process allows the stem to be at the center of the resonator structure minimizing the anchor loss. Devices fabricated with this process are used in the experiments presented in Chapter 5, Chapter 6, and Chapter 9.

## 4.2 Planarized Process

While the self-aligned stem process in the previous section is beneficial for high- $Q$  resonator design with a center stem, it has a few major shortcomings. 1) Adhesion of the stem to the structure material is often poor due to native oxide or polymer formation in the stem during the structure etch step. The native oxide can be removed with a 25:1 HF dip before the electrode polysilicon deposition. Due to tiny stem holes, the time of this HF dip step needs to be longer than the required time to remove the native oxide in large anchor areas, but this is definitely not desirable for the thin ( $< 80$  nm) sidewall sacrificial oxide. 2) Large topologies are not desirable before the deposition of structural material: this limits the interconnect layer thickness. 3) The byproduct electrode overhangs (*cf.* Fig. 4.1(e)) apply an upwards force on the resonator structure. Combined with fabrication non-uniformities, the device can snap-in at relatively low bias voltages. 4) Resolving small features during electrode lithographic step is quite difficult due to large topologies created by lower layers: the hard mask oxide layer, the structure layer, and the sacrificial oxide layer. Moreover, the Wine-Glass disk device shown in Fig. 2.1(a) does not have a center stem and, hence, does not need the self-aligned stem to get high- $Q$ .

Pursuant to resolving the above shortcomings, Fig. 4.2 presents cross-sections of the fabrication process that uses chemical-mechanical polishing (CMP). The process starts with a heavy phosphorous diffusion via  $\text{POCl}_3$  to serve as the substrate ground plane, followed by sequential depositions of 2  $\mu\text{m}$  of high temperature LPCVD oxide (HTO) at  $950^\circ\text{C}$  and 350 nm of stoichiometric silicon nitride that together serve to isolate devices and interconnects from the conductive silicon substrate. Interconnect polysilicon is then deposited to a thickness of 3  $\mu\text{m}$  for the thick interconnects (400-500 nm for the thin interconnects) and doped, again via  $\text{POCl}_3$ . After patterning this polysilicon layer to form interconnects, a layer of HTO is deposited and its thickness is 500 nm thicker than the previous polysilicon interconnect layer. For the thin interconnect process, this HTO layer is 500 nm if the succeeding CMP step is skipped. A CMP step follows to planarize the wafer until the interconnect layer is exposed. Then, 500 nm of HTO is deposited to act as a sacrificial layer to temporarily support the subsequent structural layer during its deposition and patterning, as shown in

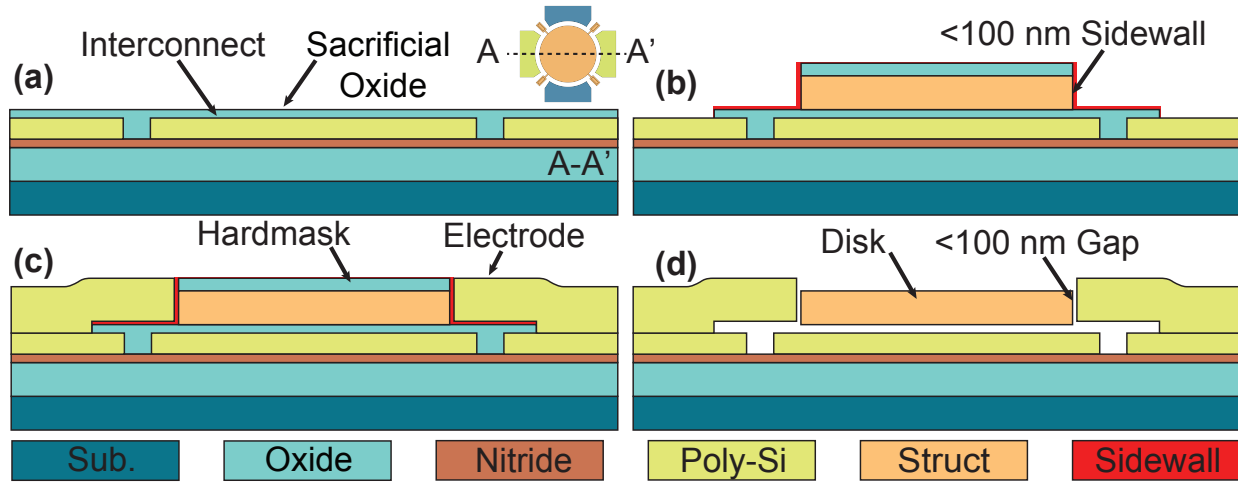


Figure 4.2: Fabrication process flow for polysilicon and microcrystalline diamond disk resonators. (a)-(c) illustrate the resonator construction through repeated LPCVD film depositions, lithography, chemical-mechanical polishing, and plasma etches, followed by a 49% HF wet etch process to remove the sacrificial oxide to yield the final released structure of (d). Note: the process cross sections presented here are for thick polysilicon interconnects.

Fig. 4.2(a). This 500 nm HTO step is not needed for the thin interconnect process skipping the CMP after the first HTO deposition. Next, stem holes or structural anchors (not shown in Fig. 4.2) are defined with a lithographical step. The 2-3  $\mu\text{m}$ -thick structural film— $\text{POCl}_3$ -doped polysilicon—is then deposited and capped with a 1.2  $\mu\text{m}$ -thick film of HTO that serves as a hard mask during etching of the structural film. The composite oxide mask-structural film layer is patterned in a single mask to define the disk structure, as shown in Fig. 4.2(b).

An HTO deposition less than 100 nm-thick that conformally coats all surfaces, including structure sidewalls, then defines the ever-important electrode-to-resonator gap spacing. The electrical contact opening to the interconnect is defined by spinning a thick photoresist and patterning it to expose the electrode vias, after which a dry etching removes the underlying bottom sacrificial oxide down to interconnect in the electrode area, as shown in Fig. 4.2(b). A subsequent  $\sim 5\ \mu\text{m}$  polysilicon deposition then provides the material for electrodes. The thickness of this polysilicon layer is at least 500 nm thicker than the combined thickness of the bottom oxide sacrificial layer, the structural layer, and the oxide hardmask layer. The 5  $\mu\text{m}$  polysilicon is deposited in two steps to make sure the polysilicon contacting with the interconnects is properly doped. The first 2.5  $\mu\text{m}$  layer is deposited and followed by a  $\text{POCl}_3$  doping step. Next, the second 2.5  $\mu\text{m}$  layer is deposited. The second CMP planarize any topologies. It is crucial to make sure that this CMP step does not polish through the oxide hard mask sitting on top of the structural layer as shown in Fig. 4.2(c). This last polysilicon layer is then patterned to define the electrodes. Finally, structures are released in 48.8 wt. %

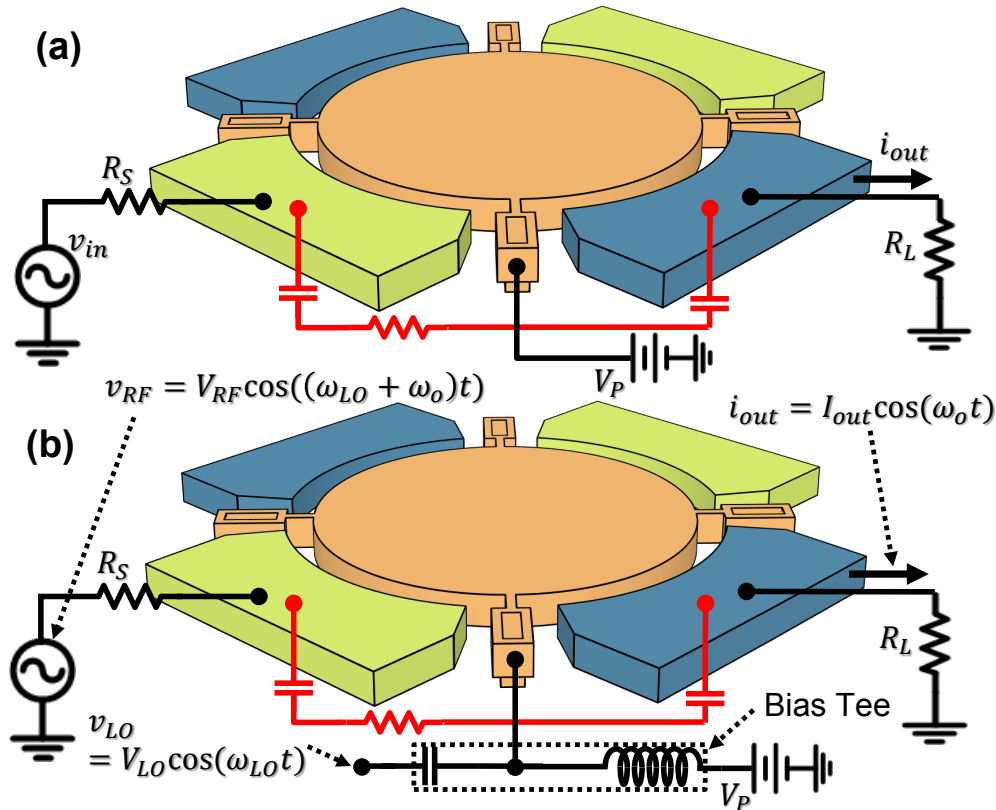


Figure 4.3: Schematics comparing (a) a typical two-port measurement scheme and (b) the mixing measurement scheme used here to bypass the parasitic feedthrough path for the fabricated devices. In both cases, measurements employ a network analyzer with  $R_S = R_L = 50\Omega$ .

HF to yield the final cross-section of Fig. 4.2(d). Appendix B details process steps required to complete a planarized process with  $3\text{-}\mu\text{m}$  polysilicon interconnects. Additionally, the appendix B also gives detail steps required to release a small MEMS die. Devices fabricated with this planarized process are used in the experiments presented in Chapter 5, Chapter 7, and Chapter 8.

## 4.3 Measurement Methods

### 4.3.1 Resonator Measurement Methods

The released MEMS resonators are measured and characterized using two measurements setups. The first of which involved a custom-built bell-jar vacuum chamber (*cf.* Fig. 4.7), which enables characterization of resonators at the mtorr or lower pressures needed to re-

move viscous gas damping. In this apparatus, dies containing devices-under-test were epoxied/taped down to a custom-built printed circuit board (PCB) chip carrier containing isolated ports that connect to on-die devices via bondwires then direct signals through vacuum chamber feedthroughs to external measurement instrumentation. In the second setup, a Lakeshore FWPX vacuum probe station allowed rapid measurement of the very high frequency diamond structural material resonators without the need for wirebonding, which facilitates testing of a large number of device variations. For all vacuum measurements, a turbo molecular pump evacuated the chamber to pressures on the order of 10  $\mu$ torr before testing.

Frequency response measurements were taken using an Agilent E5071B network analyzer using the measurement scheme of Fig. 4.3, where the network analyzer produces an ac drive signal on one port and measures power output on a second port to a 50  $\Omega$  load. Beyond measurement instrument hookups, Fig. 4.3(a) depicts the parasitic capacitive signal path through the substrate layers underlying a disk device. Though not a significant problem at low frequencies, the signal feeding through this path becomes larger as frequencies rise to the GHz range, where it can mask or distort a device's output current, making it difficult to determine important parameters, like  $Q$ .

To prevent inaccurate measurement due to feedthrough, this work employs the mixing measurement [43] setup, shown in Fig. 4.3(b), that separates motional and feedthrough currents in the frequency domain, thereby allowing measurement of motional current without interference. As shown, this setup uses a bias tee to add a local oscillator signal to the dc-bias voltage already applied to the conductive resonator structure. The network analyzer then sources an RF signal at a frequency higher than the expected resonance frequency by the frequency of the local oscillator signal while measuring at the resonance frequency.

Even though none of the applied signals are at the resonance frequency,  $f_o$ , they still generate a mechanical force at resonance via the square-law voltage-to-force transfer function of the input capacitive transducer, where

$$\begin{aligned}
 F_{in} &= \frac{1}{2} \frac{\partial C_{o,in}}{\partial r} [V_P + V_{LO} \cos(\omega_{LO}t) - V_{RF} \cos(\omega_{RF}t)]^2 \\
 F_{in} &= \frac{1}{2} \frac{\partial C_{o,in}}{\partial r} [V_P^2 + (V_{LO} \cos(\omega_{LO}t))^2 + (V_{RF} \cos(\omega_{RF}t))^2 - \\
 &\quad V_{LO}V_{RF} (\cos((\omega_{LO} + \omega_{RF})t) + \cos((\omega_{LO} - \omega_{RF})t) + \dots]
 \end{aligned} \tag{4.1}$$

where the bias dc voltage across the gap ( $V_{PG}$ ) is the same as  $V_P$  for the hock-up shown in Fig. 4.3. Here, multiplication of the LO and RF signals produces sum and difference terms. If frequencies are chosen such that  $\omega_{RF} - \omega_{LO} = \omega_o$ , a force arises at the resonance frequency:

$$\begin{aligned}
 F_{in}@_{\omega_o} &= \frac{1}{2} \cdot \frac{\partial C_{o,in}}{\partial r} \cdot V_{LO} \cdot V_{RF} \cdot \cos((\omega_{RF} - \omega_{LO})t) \rightarrow \\
 F_{in}@_{\omega_o} &= \frac{1}{2} \cdot \frac{\partial C_{o,in}}{\partial r} \cdot V_{LO} \cdot V_{RF} \cdot \cos(\omega_o t)
 \end{aligned} \tag{4.2}$$

The ensuing motion then combines with the resonator bias voltage,  $V_P$ , to produce an output current at  $\omega_o$ . Note that none of the applied signals are at the resonance frequency of the disk under test, so none of them can introduce feedthrough at this frequency. As long as the signal is measured within only a narrow frequency band, as is the case when a network analyzer senses the resonator output, parasitic feedthrough currents at frequencies different from the motional current will not interfere, allowing accurate measurement of the resonator response alone.

### Measurements of Wine-Glass Mode Disk

Using Eqn. (2.9), MEMS resonators were designed for operation at 61 MHz with a disk radius of 32  $\mu\text{m}$ . Figure 4.4(a) presents the scanning electron micrograph (SEM) of a fabricated 61-MHz Wine-Glass disk resonator using the self-aligned stem process described in Section 4.1 while Fig. 4.4(b) shows SEM of a similar device using the planarized process described in Section 4.2. Devices were tested using a Lakeshore model FWPX probe station as described in this section. The coupling of the 61 MHz Wine-Glass devices is much stronger than the background feedthrough. Therefore, using the 2-port measurement described here, Fig. 4.5 shows a typical measured frequency response, where  $Q$ 's of 130,000 in vacuum and motional resistances of 15  $\text{k}\Omega$  at  $V_P = 5$  V were common among devices with 80 nm gaps. The measured motional resistances is in a good agreement with the theoretical prediction using Eqn. (2.26).

### 4.3.2 Oscillator Measurement Methods

To verify the oscillator operation model, amplifiers were designed and fabricated using a 0.35  $\mu\text{m}$  CMOS technology. In the Pierce oscillator,  $C_{BP}$  (*cf.* Fig. 3.3) effectively filters out high-frequency thermal noise. Although the entire die, shown in Fig. 4.6(a), occupies an area of 900  $\mu\text{m} \times 500 \mu\text{m}$ , the actual sustaining amplifier with its biasing circuits only consumes about 60  $\mu\text{m} \times 45 \mu\text{m}$  while the 44 pF  $C_{BP}$  occupies about 200  $\mu\text{m} \times 100 \mu\text{m}$ . The attenuation of noise at node  $V_b$  in Fig. 3.3—50 dB at 60 MHz in this case—depends on the pole,  $g_{m,b2}/C_{BP}$ , where  $g_{m,b2}$  is the transconductance of diode-connected transistor  $M_{b2}$  in Fig. 3.3 and  $1/g_{m,b2}$  is the resistance looking into  $M_{b2}$ . It is important to note that the attenuation at high-frequencies does not help to improve phase noise of the oscillator due to flick noise as explained in Section 5.1. If the area is limited, for the same attenuation, the area of  $C_{BP}$  can be reduced easily by 2 to 4 times by simply decreasing  $g_{m,b2}$ . However, this will increase low-frequency noise and, hence, phase noise of the oscillator. The rest of the IC area is consumed by 1) an on-chip buffer used to drive the 50- $\Omega$  desired for external measurement systems; 2) by-pass capacitors to further reduce noise on DC supply lines; and 3) bond pads. Similarly, Fig. 4.6(b) shows the die photo of a TIA based amplifier. Its bondpad arrangement is the same as that of the Pierce oscillator such that the same PCB can be used for both amplifier. The entire die, hence, occupies an area of 900  $\mu\text{m} \times 500 \mu\text{m}$  while the actual TIA amplifier consumes only about 100  $\mu\text{m} \times 100 \mu\text{m}$ . Using the design

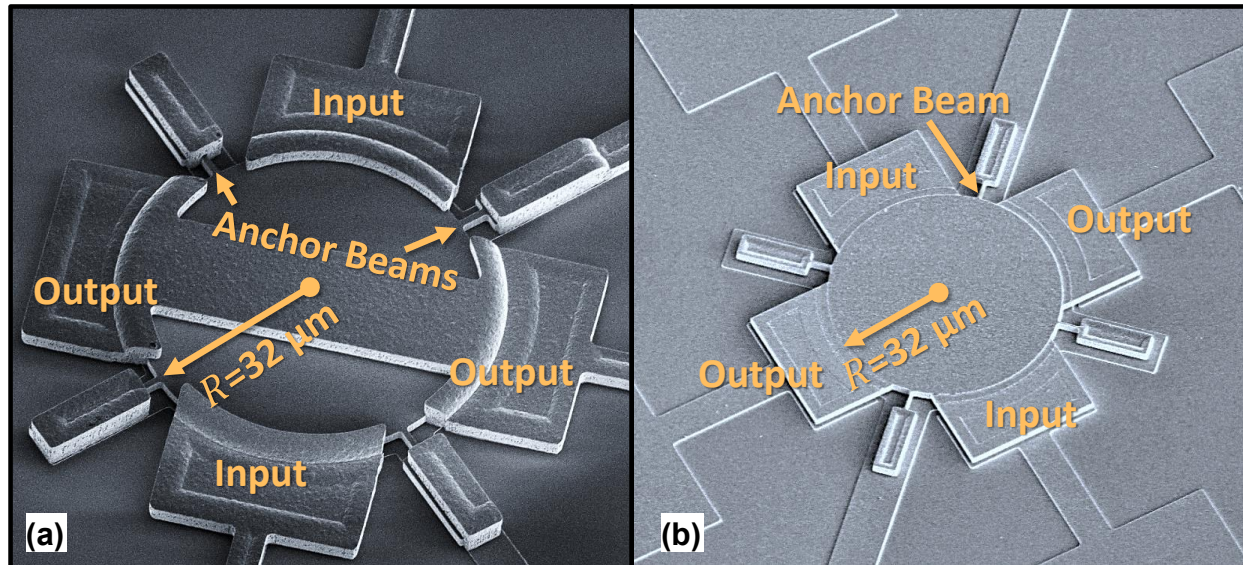


Figure 4.4: SEMs of a fabricated Wine-Glass disk resonator (a) using the self-aligned stem process described in Section 4.1 and (b) using the planarized process described in Section 4.2.

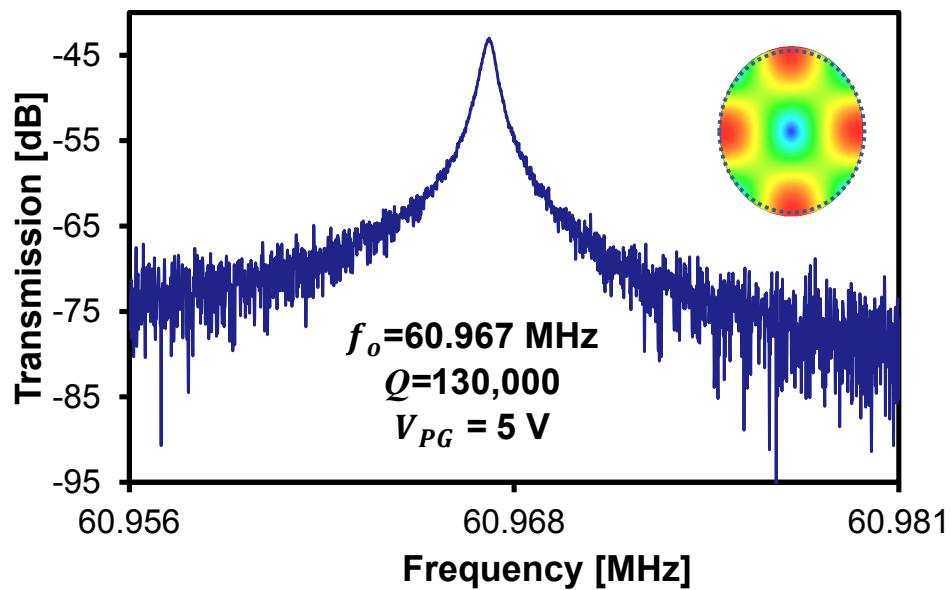


Figure 4.5: The measured frequency response of a typical Wine-Glass disk resonator.

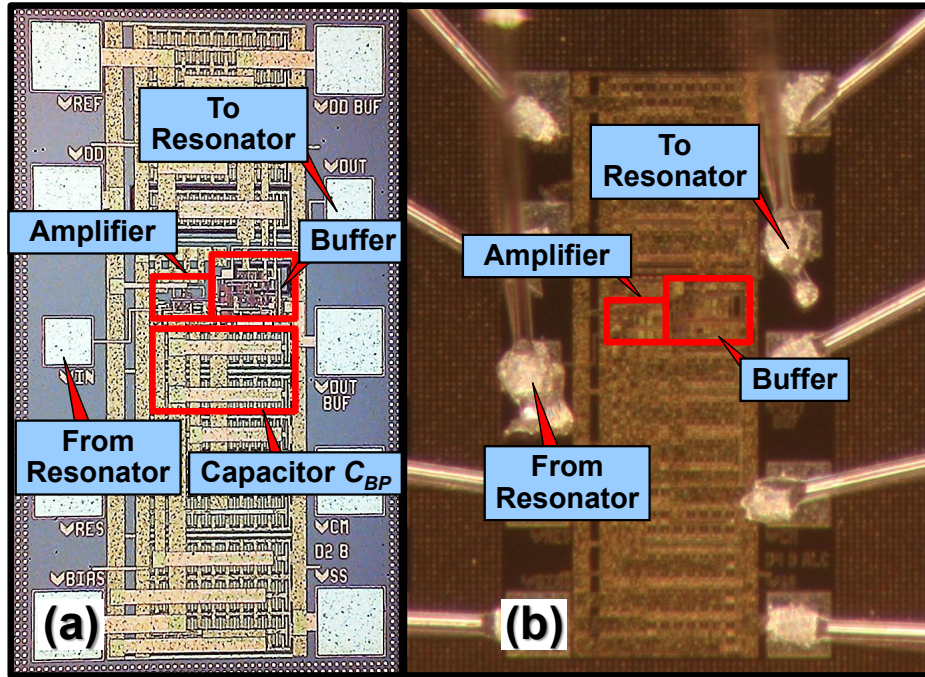


Figure 4.6: (a) IC die photo of the Pierce oscillator. (b) IC die photo of the TIA oscillator.

methodology in Chapter 2, MEMS resonators were designed for operation at 61 MHz with a disk radius of 32  $\mu\text{m}$ . Following fabrication steps in Section 4.1 or 4.2, structures were released in 49% HF to yield the final device imaged in the SEM of Fig. 4.4.

The released MEMS die is wire-bonded to a CMOS amplifier die to form an oscillator. To maintain high (i.e., over 50,000) resonator  $Q$  as needed to minimize phase noise [7] and motional resistance, the MEMS-based oscillator must operate in a stable vacuum environment with less than 10 torr (*cf.* Fig. 6.11). Two measurement setups for oscillators are used in this dissertation:

1. Figure 4.7(a) shows a custom-made miniature vacuum chamber, containing a printed circuit board (PCB) board that houses the MEMS/CMOS device package and provides electrical feed-throughs to allow connection to outside instrumentation. Once sealed, this system provides weeks to months of measurement time under at least a 10 Torr vacuum, which is sufficient to support  $Q$ 's  $> 50,000$  for Wine-Glass disks. The MEMS and CMOS dies are epoxied/glued down on a 24-pin standard dip package, which is held down on the PCB with a socket. Combining this with the compact and steady vacuum chamber makes this setup reliable for measurements such as acceleration sensitivity and low phase noise measurement.
2. The compactness and sturdiness of the custom-made vacuum chamber setup comes with the price of inconvenient usage due to its limited electrical feed-throughs. To

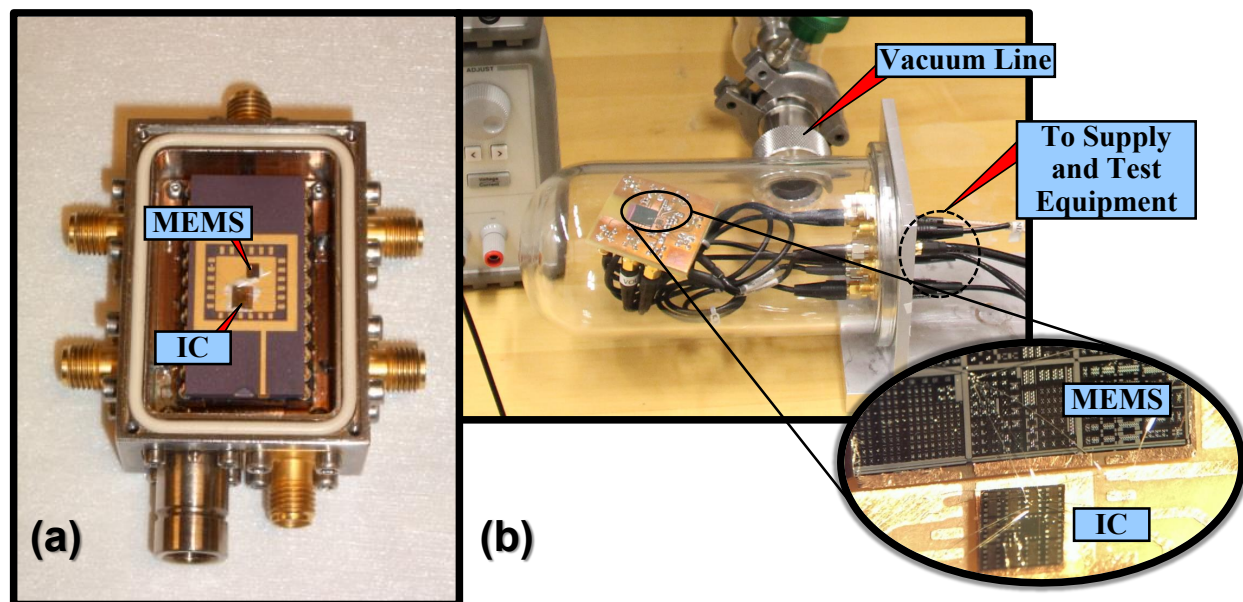


Figure 4.7: (a) Photo of the packaged oscillator in a custom-designed vacuum box. (b) Photo of the wire-bond oscillator on a Printed Circuit Board (PCB) in a bell-jar vacuum environment.

solve this, Figure 4.7(b) presents a custom bell-jar which allows  $\mu\text{torr}$  of vacuum using a continuously operating vacuum pump. The metal plate on the right can house 14 hermetic SMA feed-throughs. To construct an oscillator, the released MEMS resonators are bondwired together with the CMOS IC and affixed to a much larger PCB circuit than the PCB in Fig. 4.7(a) setup. Now, the PCB circuit not only can have simple discrete capacitors and resistors but also can have voltage regulators, an off-chip RF diode detector, and a flip-flop circuit: these are required circuits for the super-regenerative receiver discussed in Chapter 8.

## Chapter 5

# 61-MHz Low-Power Pierce Oscillator

Reference oscillators based on high- $Q$  MEMS resonators are already viable alternatives to traditional quartz-based oscillators, where the exceptional  $Q$ -factors of above 100,000 made possible in these on-chip resonators allow low phase noise in compact packages. However, further reductions in power are still desired for increased battery life. Pursuant to further reducing power and area consumption while retaining the high performance of previous such efforts [11], [13], this chapter presents a Pierce-topology oscillator referenced to a single polysilicon Wine-Glass disk resonator, *cf.* Fig. 2.1(a). Complete phase noise modeling of the full oscillator system is also presented, providing performance predictions incorporating real-world non-linear and cyclostationary noise effects. Combining this with the analytical framework from Chapter 3, several oscillators were designed and fabricated for low power operation. Measurements attained phase noise performance marks of -119 dBc/Hz at a 1-kHz offset and -139 dBc/Hz at far-from-carrier offsets, satisfying even challenging GSM specifications [13] while consuming only 78  $\mu$ W power. Sacrificing the phase noise at far-from-carrier offsets by a just few dB, power consumption may be lowered to just 43  $\mu$ W. For applications where the power requirement is more stringent and a few dB increase in phase noise from GSM specifications is tolerable, reducing gap spacings to 40 nm decreases the power consumption further to 8.8  $\mu$ W, which is a 40 times reduction in power compared to the 350  $\mu$ W quoted in [11], [13].

### 5.1 Phase Noise

Achieving low phase noise in reference oscillators is essential for wireless communications, where close-to-carrier phase noise degrades receiver noise figure by adding noise within the receiver bandwidth and, on the transmit side, risks producing excessive out-of-channel interference. The phase noise of a linear oscillator in the presence of thermal noise sources is often described by Leeson's phase noise model [7]:

$$\mathcal{L}(\Delta\omega) = 10 \cdot \log \left[ \frac{2FkT}{P_{sig}} \left( 1 + \frac{1}{Q^2} \left( \frac{\omega_o}{2\Delta\omega} \right)^2 \right) \right] \quad (5.1)$$

where  $\mathcal{L}(\Delta\omega)$  is single side-band phase noise power in dBc,  $k$  and  $T$  are the Boltzmann constant and temperature in Kelvin, respectively,  $F$  is the amplifier noise correction factor,  $P_{sig}$  is the loop signal power, and  $\Delta\omega$  is the offset frequency. Though this model does not always provide perfect predictive power, it serves as a useful tool in understanding avenues to reducing total phase noise. To design the lowest phase noise oscillator, Eqn. (5.1) suggests minimizing amplifier noise, increasing loop signal power; and maximizing resonator  $Q$ , with the latter having the strongest impact on close-to-carrier phase noise. Indeed, it is the extraordinarily high  $Q$ -factors achievable in capacitive-gap MEMS resonators which make possible the simultaneous low power and low phase noise oscillators here.

However, as Lesson's equation is predicated on a linear model incorporating thermal noise sources alone, it does not capture many important aspects of real-world oscillator operation. In particular, nonlinearity, cyclostationary noise sources, and time varying noise-to-phase transfer processes—all inherently unavoidable aspects of large-signal oscillating systems—are disregarded in this model.

To improve upon this, a complete noise-to-phase transfer function of the linear time varying oscillator system may be derived here using the Hajimiri approach [32]. To characterize the oscillation phase noise induced due to current or voltage noise sources from circuit elements, a set of Impulse Sensitivity Functions (ISFs) are introduced, denoted as  $\Gamma(\theta)$ . Defined as the oscillation phase shift induced per normalized voltage(current) unit impulse applied at a specified oscillation phase,  $\theta$ , to a specified node(branch), ISF is a dimensionless transfer function that relates noise sources to their contribution to oscillator phase noise. Because the ISF is phase-dependent, this allows nonlinear dynamics to be modeled by the noise-to-phase conversion varying with the periodic signal amplitude (ie, oscillator phase). Additionally, summation of multiple independent ISF's allow an arbitrary number of noise sources to be accurately modeled, improving upon the single thermal noise source model of the Leeson equation.

In the Pierce oscillator, three sources of noise contribute to phase noise: 1) current noise due to the gain transistor ( $M_1$ ), 2) current noise due to the bias circuitry, and 3) intrinsic thermal noise of the resonator. Modeling these sources requires an ISF for the resonator noise, along with a single ISF for transistor noise, as both the bias circuit and gain transistor inject current noise at  $v_{OUT}$ .

To simulate the ISF for current noise injected at  $v_{OUT}$ , a transient simulation is run till steady-state oscillation is achieved. Small charge impulses,  $\Delta q$ , are then injected to  $v_{OUT}$  at varying points in the oscillation cycle, and the resultant oscillation phase shift,  $\Delta\phi(\theta) = \omega_o \cdot \Delta t(\theta)$ , is measured. Normalizing these phase shifts by the ratio of injected charge to maximum charge produced by the oscillation itself,  $q_{max}$ , then yields the desired ISF:  $\Gamma(\theta) = \Delta\phi(\theta) (q_{max}/\Delta q(\theta))$ . Figure 5.1(a) presents the simulated ISF  $\Gamma_{OUT}(\theta)$ , in red, for the oscillator bias conditions corresponding to 43  $\mu\text{W}$  operation in Table 5.1, together with the oscillator output,  $v_{OUT}$ , in black. As would be expected, noise injected near oscillator zero-crossings produces the greatest phase shift, while noise near oscillator peak amplitude is largely insignificant. Similarly, Fig. 5.1(b) presents simulated ISF  $\Gamma_{RES}(\theta)$  for voltage noise injected by the resonator (red) together with resonator current  $i_x$  (black).

Table 5.1: Resonator and amplifier design summary.

Parameter	Source	Operating Power				Unit
		110 $\mu$ W	78 $\mu$ W	43 $\mu$ W	8.8 $\mu$ W	
<b>Resonator Design/Parameters</b>						
Structure Material	-	Polysilicon				-
Radius, $R$	layout	32				$\mu$ m
Electrode overlapping angle, $\Delta\theta$	layout	67				deg
Thickness, $h$	layout	3.0		2.0		$\mu$ m
Electrode-to-resonator gap, $d_0$	measured	80		40		nm
Density, $\rho$	[Lin, JSSC'04]	2300				kg/m <sup>3</sup>
Young's modulus, $E$	[Tang, Trans'89]	150				GPa
Poisson ratio, $\sigma$	[Lin, JSSC'04]	0.226				-
Resonator mass, $m_{mre}$	Eqn. (2.16)	$8.06 \times 10^{-12}$		$5.37 \times 10^{-12}$		kg
Resonator stiffness, $k_{mre}$	Eqn. (2.16)	$1.15 \times 10^6$		$7.66 \times 10^5$		N/m
Damping factor, $c_{mre}$	Eqn. (2.17)	$3.8 \times 10^{-8}$		$2.54 \times 10^{-8}$		kg/s
Quality factor in vacuum, $Q$	measured	$\sim 80,000$		$\sim 80,000$		-
Series Resistance, $R_x$	Eqn. (2.26)	18.2	13.8	9.8	0.435	k $\Omega$
Inductance, $L_x$	Eqn. (2.26)	3.85	2.93	2.08	0.092	H
Capacitance, $C_x$	Eqn. (2.26)	1.82	2.39	3.37	76.4	aF
Electromech. coupling, $\eta_e$	Eqn. (2.24)	$1.45 \times 10^{-6}$	$1.66 \times 10^{-6}$	$1.97 \times 10^{-6}$	$7.63 \times 10^{-6}$	C/m
DC-biased voltage, $V_p$	measured	6.6	7.45	8.7	12.3	V
DC-biased voltage across the gap, $V_{pG}$	calculated	5.913	6.778	8.046	11.708	V
Parasitic Trace Resistance, $R_{VP}$ & $R_{rP}$	measured	$\sim 1.5$		$\sim 1.5$		k $\Omega$
Static Overlap Capacitance, $C_o$	Eqn. (2.25)	24.8		33.13		fF
<b>Amplifier Design/Parameters</b>						
Transconductance Gain of $M_1$ , $g_{m1}$	simulation	571	497	410	180	$\mu$ S
Transconductance Gain of $M_2$ , $g_{m2}$	simulation	195	177	153	88	$\mu$ S
Transistor Region of $M_1$	simulation	Strong Inv.	Strong Inv.	Strong Inv.	Weak Inv.	-
Transistor Region of $M_2$	simulation	Strong Inv.	Strong Inv.	Strong Inv.	Strong Inv.	-
Drain Current of $M_1$	simulation	44.9	36.9	28.5	10.4	$\mu$ A
Supply Voltage, $V_{DD}$	measured	2	1.7	1.3	0.9	V
Supply Current, $I_{DD}$	measured	55	45.9	33.1	9.8	$\mu$ A
Input/Output Common-mode Voltage, $V_{CM}$	measured	0.687	0.672	0.654	0.592	V
Feedback Transistor Gate Voltage, $V_{RF}$	measured	1	0.96	1	1.22	V

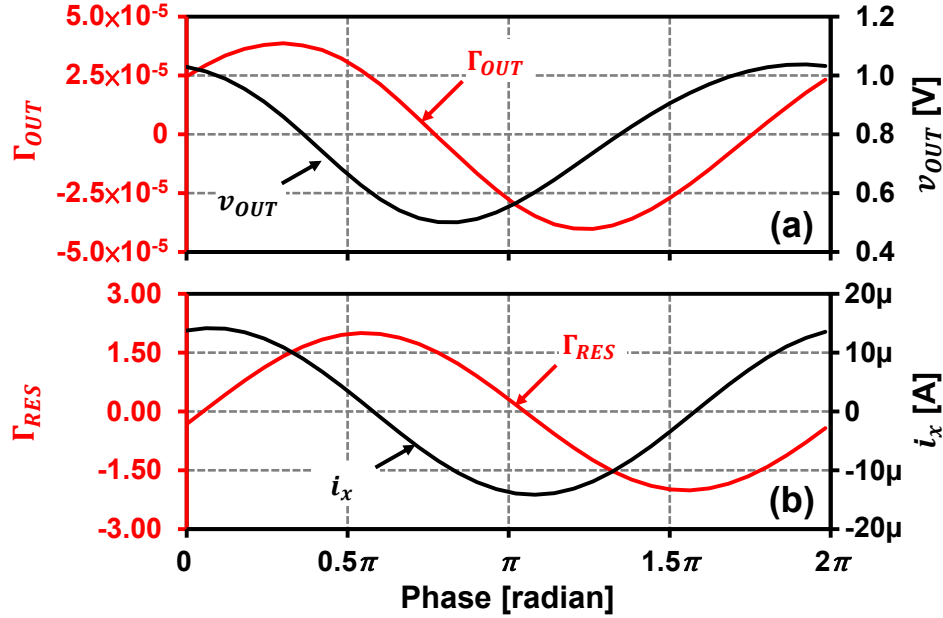


Figure 5.1: (a) impulse sensitivity function  $\Gamma_{OUT}$  (red) for current noise injected at node  $v_{OUT}$ , with oscillator output waveform for reference (black) and, (b)  $\Gamma_{RES}$  (red) for voltage noise injected in series with the resonator, together with resonator current,  $i_x$  (black) as a function of oscillation phase. Here, simulations assume operating conditions of the  $43 \mu\text{W}$  bias in Table 5.1.

With the ISF functions in hand, the phase noise contribution of the equivalent current noise sources at  $v_{OUT}$  may be found. In the Pierce oscillator of Fig. 3.3, the relevant current noise sources comprise  $M_1$  and  $M_2$  drain current noise and the equivalent current noise due to the bias circuit (note that the near-zero current in  $M_3$  renders its noise contribution as negligible). The former can be defined as:

$$\overline{i_{nT,M1,2}^2} = 4kT\gamma g_{m1,2}\Delta f; \quad \overline{i_{nF,M1,2}^2} = \overline{i_{nT,M1,2}^2} \frac{\omega_{c1,2}}{\Delta\omega} \quad (5.2)$$

where  $\overline{i_{nT,M1,2}^2}$  represents the thermal noise of  $M_1$  or  $M_2$ ,  $\overline{i_{nF,M1,2}^2}$  the flicker noise current of  $M_1$  or  $M_2$ , and  $g_{m1,2}$  is the transconductance of  $M_1$  or  $M_2$ ,  $\omega_{c1,2}$  is the flicker noise corner frequency of  $M_1$  or  $M_2$ , and  $\gamma$  is a process dependent parameter equal to  $\sim 0.81$  for the CMOS used in this work. The equivalent current noise due to the bias circuit can be found as  $g_{m2}^2 \overline{v_{n,B}^2}$  where  $\overline{v_{n,B}^2}$  is the equivalent voltage noise of the bias circuit at the gate of  $M_2$ . Here,  $C_{BP}$  and the diode-connected transistor  $M_{b2}$  filter out high frequency thermal noise, leaving only flicker noise components of  $\overline{v_{n,B}^2}$ . Meanwhile, voltage noise in series with the resonator is dominated by the resonator's thermal noise, given by  $\overline{v_{nT,RES}^2} = 4kTR_x\Delta f$ .

Because the transistor noise sources depend on the drain current of the transistor, the resultant noise amplitude must vary periodically with the oscillation cycle. The contribution from such cyclostationary noise sources may be modeled using a second set of phase-

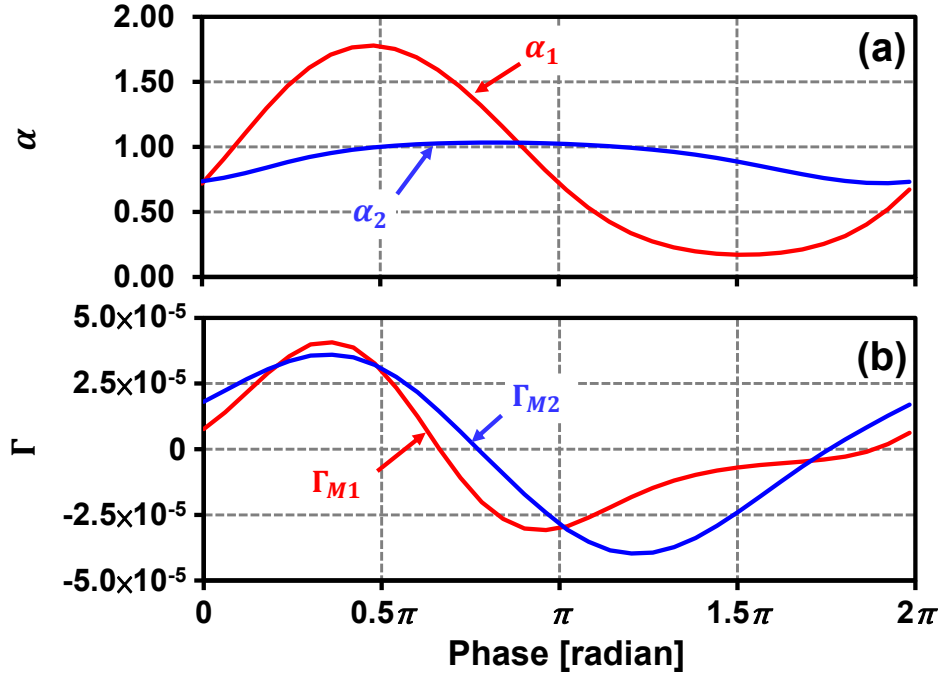


Figure 5.2: (a) Phase-dependent shaping functions,  $\alpha$ , and (b) effective  $\Gamma(\theta)$  functions of transistor  $M_1$  (red) and  $M_2$  (blue) operating at the  $43 \mu\text{W}$  bias condition in Table 5.1. Here, the corresponding rms and  $c_0$  values are found:  $\Gamma_{rms,M1} = 2.13 \times 10^{-5}$ ,  $\Gamma_{rms,M2} = 2.58 \times 10^{-5}$ ,  $c_{0,M1} = 8.46 \times 10^{-7}$ , and  $c_{0,M2} = -9.25 \times 10^{-7}$ .

dependent functions,  $\alpha_1(\theta)$  and  $\alpha_2(\theta)$ , which capture the instantaneous  $G_m$  of the transistor normalized to the small signal bias  $g_m$ . Figure 5.2(a) illustrates the simulated  $\alpha_1(\theta)$  and  $\alpha_2(\theta)$  here. To model both these changing noise sources and the phase-dependent noise-source to phase noise conversion, a new set of effective  $\Gamma(\theta)$  are defined as the product of  $\alpha(\theta)$  functions and  $\Gamma_{OUT}(\theta)$ :

$$\Gamma_{M1}(\theta) = \Gamma_{OUT}(\theta) \cdot \alpha_1(\theta); \quad \Gamma_{M2}(\theta) = \Gamma_{OUT}(\theta) \cdot \alpha_2(\theta) \quad (5.3)$$

In contrast, resonator thermal noise is essentially constant throughout the oscillation cycle, allowing it to be treated as a stationary source.

The phase noise power spectrum density due to current noise from  $M_1$ ,  $M_2$ , and the bias circuit can then be found [32]:

$$\begin{aligned}
S_{\phi,M1}(\Delta\omega) &= \left( \Gamma_{rms,M1}^2 + \frac{c_{0,M1}^2}{4} \cdot \frac{\omega_{c1}}{\Delta\omega} \right) \frac{\overline{i_{nT,M1}^2}/\Delta f}{2(C_{OUT}V_{OUT,sw}\Delta\omega)^2} \\
S_{\phi,M2}(\Delta\omega) &= \left( \Gamma_{rms,M2}^2 + \frac{c_{0,M2}^2}{4} \cdot \frac{\omega_{c2}}{\Delta\omega} \right) \frac{\overline{i_{nT,M2}^2}/\Delta f}{2(C_{OUT}V_{OUT,sw}\Delta\omega)^2} \\
S_{\phi,B}(\Delta\omega) &= \frac{c_{0,M2}^2}{4} \cdot \frac{\overline{g_{m2}^2 v_{n,B}^2}/\Delta f}{2(C_{OUT}V_{OUT,sw}\Delta\omega)^2}
\end{aligned} \tag{5.4}$$

where  $\Gamma_{rms,M1}$  and  $\Gamma_{rms,M2}$  are the rms values and  $c_{0,M1}$  and  $c_{0,M2}$  are the 1st term ( $n=0$ ) in the Fourier series coefficients of  $\Gamma_{M1}(\theta)$  and  $\Gamma_{M2}(\theta)$  respectively, and  $V_{OUT,sw}$  is the maximum voltage swing across the effective total capacitance at the output:  $C_{OUT} = C_2 + C_1 C_3 / (C_1 + C_3)$ . The rms values of  $\Gamma(\theta)$  may be seen as converting the high frequency thermal noise into phase noise while the Fourier components,  $c_0$ , capture the conversion of the flicker noise. Since  $\overline{v_{n,B}^2}$  comprises only flicker noise,  $S_{\phi,B}(\Delta\omega)$  has only the  $c_0$  term. Similarly, the phase noise power spectrum density due to the resonator voltage noise can be written as:

$$S_{\phi,RES}(\Delta\omega) = \frac{\Gamma_{rms,RES}^2 \overline{v_{nT,RES}^2}/\Delta f}{2(L_x I_{x,sw} \Delta\omega)^2} \tag{5.5}$$

where  $I_{x,sw}$  is the maximum current swing going through the effective inductor of the resonator,  $L_x$ . The total single sideband phase noise spectrum density normalized to the carrier power (in dBc/Hz) can then be trivially found as the sum of these individual sources:

$$\mathcal{L}(\Delta\omega) = 10 \cdot \log \left[ S_{\phi,M1}(\Delta\omega) + S_{\phi,M2}(\Delta\omega) + S_{\phi,B}(\Delta\omega) + S_{\phi,RES}(\Delta\omega) + S_{\phi,fl}(\Delta\omega) \right] \tag{5.6}$$

where the final term represents the far-from-carrier (thermal) noise floor of the amplifier.

Figure 5.3 presents the phase noise curve predicted by Eqn. (5.6) using the extracted  $\alpha(\theta)$  and  $\Gamma(\theta)$  functions of Fig. 5.1 and Fig. 5.2, overlaid on top of measured data for the physically realized oscillator (discussed further in Section 5.2). Additionally, the dotted curve models the same oscillator circuit with an equivalent resonator having a  $Q$ -factor of only 800. As expected, this reduced  $Q$  produces a marked reduction in the predicted phase noise performance, replicating the phenomenological behavior of Leeson's model and further emphasizing the importance of high  $Q$  to achieving low phase noise performance on small power budgets.

For low power applications, both phase noise performance and power consumption are important. For fair comparison of such oscillators, a figure of merit ( $FOM$ ) that accounts for the total power consumption required to achieve a given phase noise can be used:

$$FOM = 10 \cdot \log \left[ \mathcal{L}(\Delta\omega) \cdot \frac{P_{diss}}{1mW} \cdot \left( \frac{\Delta\omega}{\omega_o} \right)^2 \right] \tag{5.7}$$

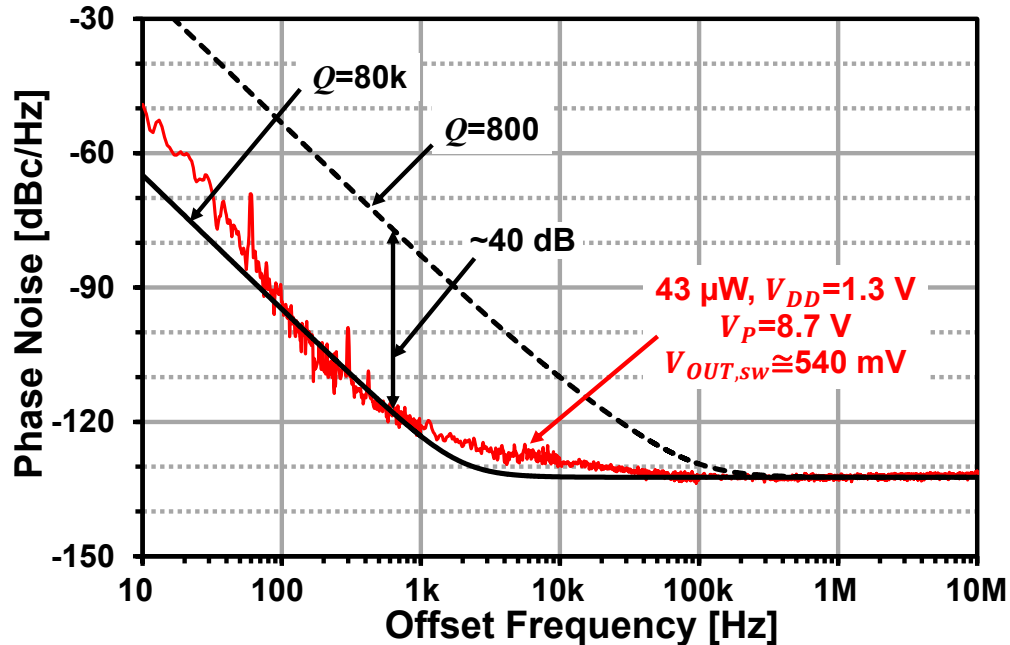


Figure 5.3: The predicted phase noise plot (solid black) generated using Eqn. (5.6) and the simulated functions of Fig. 5.1 and Fig. 5.2 overlaid on top of the measured phase noise (red). The dashed black line predicts phase noise performance when resonator  $Q$  is reduced to 800 while maintaining constant motional resistance. Here, the flicker noise corner frequencies of  $M_1$  and  $M_2$  are found in simulation  $\overline{v_{n,B}^2}$  to be 16.6 MHz and 1.6 MHz, respectively, while the flicker noise corner frequency of  $\overline{v_{n,B}^2}$  is 648 kHz with noise floor of  $1.29 \times 10^{-15} \text{ V}^2/\text{Hz}$ .

where  $P_{diss}$  is oscillator power consumption. Use of this  $FOM$  then allows even comparison of oscillators designed with differing power budgets and operating at different frequencies.

## 5.2 Experimental Verification

To verify the oscillator operation model, a low power amplifier IC was designed and fabricated using a 0.35  $\mu\text{m}$  CMOS technology. Table 5.1 presents design and operating information for the constructed amplifiers. Here, the operation of  $M_2$  with significantly reduced  $g_m$  compared to  $M_1$  minimizes the noise contribution from the bias circuit, while  $C_{BP}$  effectively filters out high-frequency thermal noise. MEMS resonators were designed for operation at 61 MHz with a disk radius of 32  $\mu\text{m}$ . The 80 nm gap device in Table 5.1 is fabricated using the self-aligned stem process described in Section 4.1.

A completed oscillator is constructed from amplifier die (*cf.* Fig. 4.6(a)) bond-wired to the resonator and package leads. To maintain high (*i.e.*, over 50,000) resonator  $Q$  as needed to minimize phase noise required loop gain [7], [32], the MEMS-based oscillator must

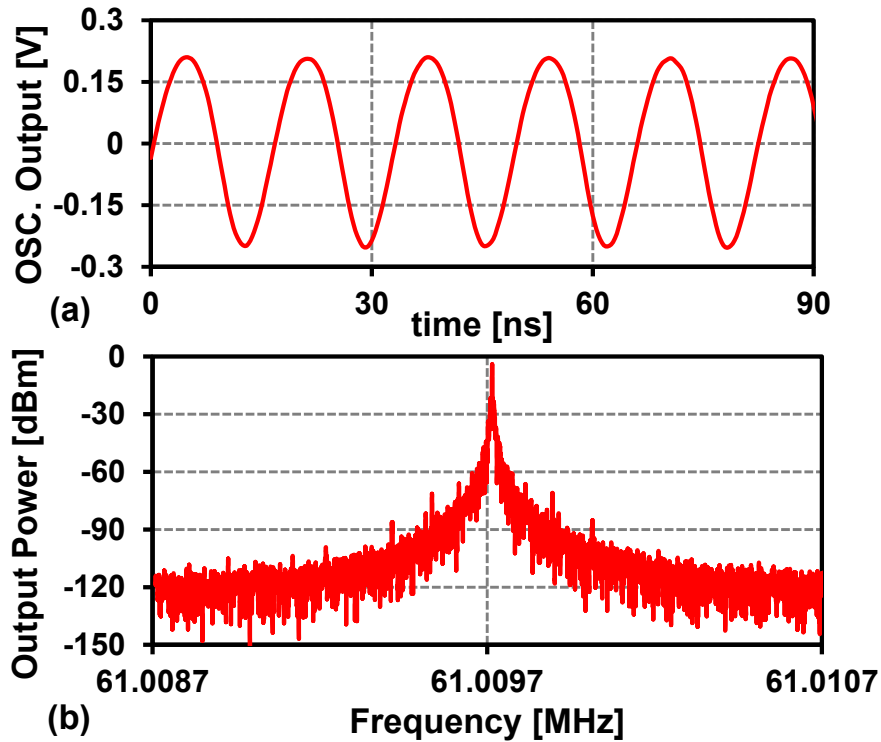


Figure 5.4: (a) Pierce oscillator output waveform measured on an oscilloscope and (b) output spectrum as measured on a spectrum analyzer.

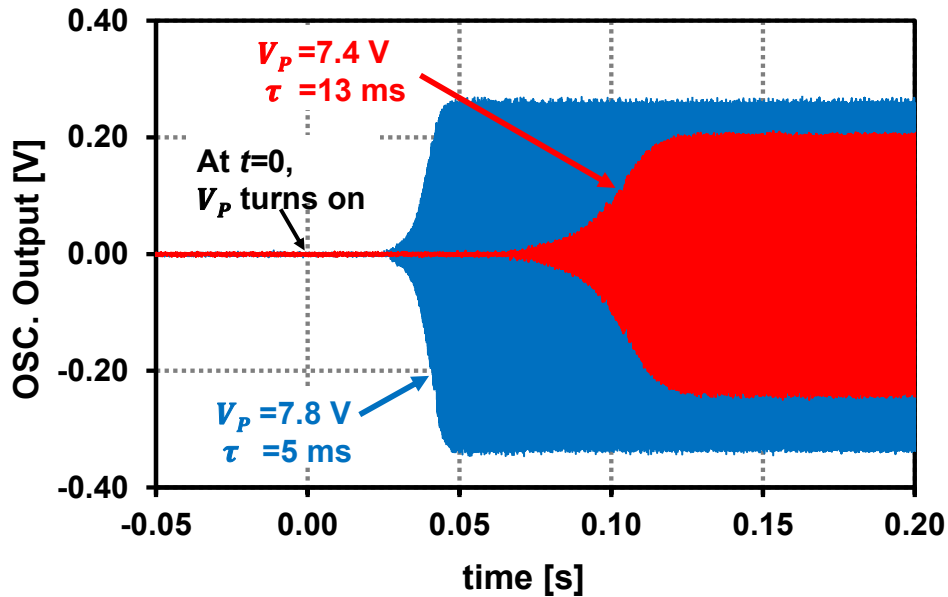


Figure 5.5: Measured start-up time response of the oscillator when  $V_P$  of the resonator is turned on at  $t=0$ . An increased resonator bias voltage increases total loop gain, and hence speeds start-up time of the blue curve compared to the red as expected from Eqn. (3.31).

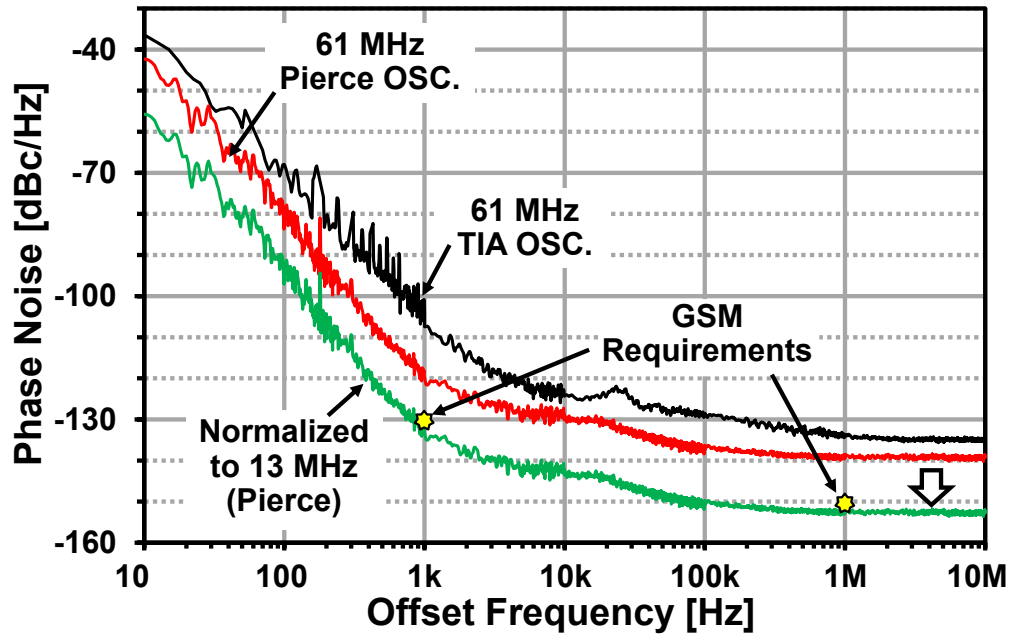


Figure 5.6: Measured phase noise of 61-MHz oscillators comparing the new Pierce topology and an TIA topology similar to [13], as well as the Pierce oscillator phase noise divided down to 13 MHz for comparison to the GSM spec.

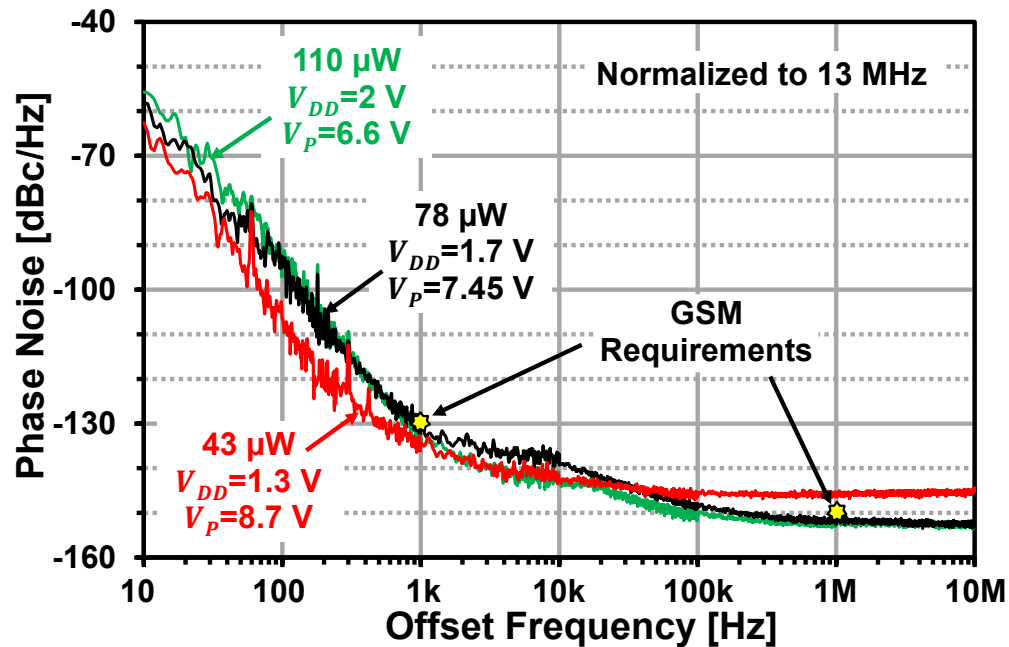


Figure 5.7: Measured phase noise of the oscillator operating on varying supply voltages. A reduction in  $V_{DD}$  and  $I_{BIAS}$  can be seen to decrease power consumption by 61% with only a modest decrease in phase noise performance.

operate in a stable vacuum environment, provided here via a custom-made miniature vacuum chamber, depicted in Fig. 4.7(a), that encloses a printed circuit board (PCB) board housing the MEMS/CMOS device package and provides electrical feedthroughs to allow connection to outside instrumentation. The output of the oscillator was measured using an Agilent E5500 phase noise test setup configured to use a low-noise PLL-based measurement.

When biased with  $V_P$  used to “turn on” the MEMS resonator and provide positive loop gain, the oscillator generates the typical output waveform shown in Fig. 5.4(a), with equivalent output spectra in Fig. 5.4(b). Figure 5.5 gauges oscillator startup time, with the red curve demonstrating startup at bias points just above that needed to produce oscillation and showing a modest 13 ms time constant. Slightly increasing resonator bias voltage from 7.4 V to 7.8 V increases total loop gain, producing the blue curve with a much smaller 5 ms time constant, as is predicted by Eqn. (3.31).

Figure 5.6 presents measured phase noise data for the Pierce oscillator alongside comparison data for a TIA-based oscillator [13] employing the same MEMS resonator design. Here, the Pierce oscillator achieves -117 dBc/Hz at 1-kHz offset and -139 dBc/Hz at far-from-carrier offsets from its 61-MHz oscillation frequency. Comparing this phase noise performance with that predicted by the analysis of Section 5.1 in Fig. 5.3 yields excellent agreement with theory. The slight increase in phase noise at offset frequencies below 50 Hz from that predicted is likely due to additional random-walk variations from thermal or other factors that are not captured in the phase noise model [54].

When divided down to GSM’s 13 MHz, these phase noise marks corresponds to -130 dBc/Hz at 1-kHz and -152 dBc/Hz far-from-carrier, both of which satisfy GSM reference oscillator phase noise requirements. This Pierce oscillator not only provides phase noise improvements of 7 dB at 1-kHz offset and 7 dB far-from carrier versus the TIA version of [13] using a similar single disk; it also reduces power consumption down to 78  $\mu$ W, a factor of 4.5 smaller.

Figure 5.7 presents phase noise measurements for the Pierce oscillator that investigate the degree to which increases in resonator dc-bias  $V_P$  allow lower supply voltages, hence, lower power consumption. Here, a 0.85 V increase in  $V_P$  allows  $V_{DD}$  and  $I_{BIAS}$  reductions that decrease overall power consumption from 110  $\mu$ W to 78  $\mu$ W, with very little degradation of phase noise. A further increase in  $V_P$  to 8.7 V allows yet lower power consumption of 43  $\mu$ W, though at the cost of slight increases in far-from-carrier phase noise due to the resultant decrease in oscillator swing.

Figure 3.6 predicts that the power consumption of the oscillator can further be reduced using smaller gap spacings. To verify this, new devices with 40-nm gap spacings were fabricated using the 500-nm thick interconnect CMP process presented in Section 4.2. Table 5.1 presents design and operating information for the constructed device and amplifier. The black line in Fig. 5.8 presents the normalized phase noise measurement of the oscillator using the 40-nm gap device. The red line in Fig. 5.8 is the phase noise measurement of the 43  $\mu$ W operating oscillator using the 80-nm gap device. Combined with a slight decrease in  $V_{DD}$  and a slight increase in  $V_P$ , a decrease in gaps from 80 nm to 40 nm reduces the power consumption from 43  $\mu$ W to 8.8  $\mu$ W, which is  $4.9 \times$  reduction in power. This reduction

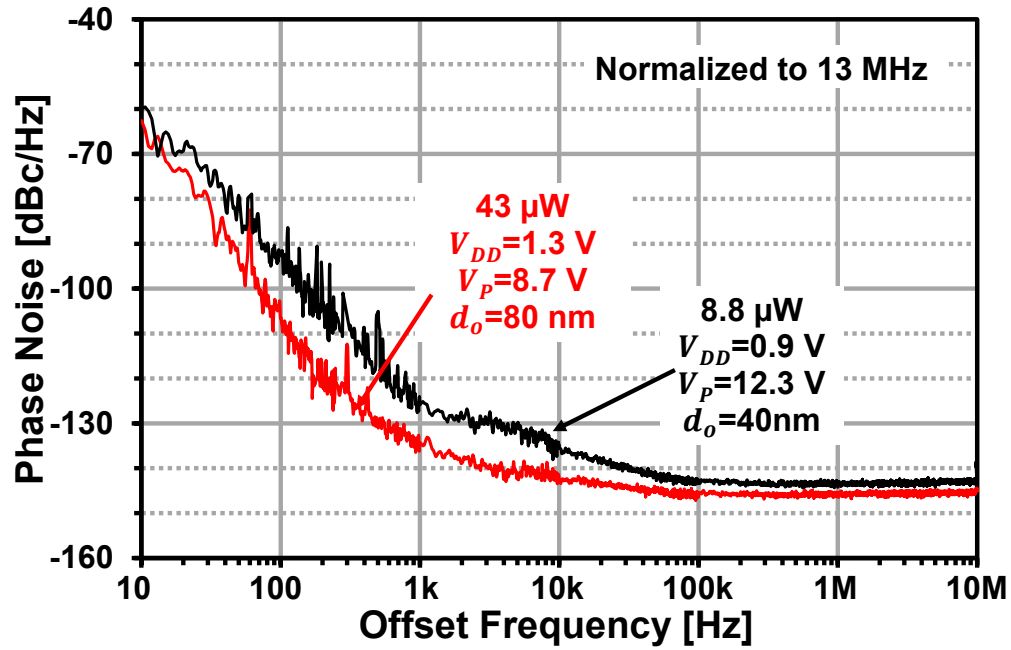


Figure 5.8: Measured phase noise of oscillators using two resonators with two different gaps. A reduction in gaps from 80 nm to 40 nm can be seen to decrease power consumption by  $4.9 \times$ . Note: the phase noise plots are divided down to 13 MHz oscillation frequency.

Table 5.2: Oscillator performance comparison

DEVICE TYPE	This work			WG array	AlN	AlN	FBAR	Quartz
	8.8 $\mu$ W	43 $\mu$ W	78 $\mu$ W	[Lin, IEDM'05]	[Wu, Trans'13]	[Wu, ISCAS'13]	[Nelson, RFIC'11]	[Beek, JMM'12]
$f_o$ [MHz]	61	61	61	61	4.9	204	2000	10
Power [ $\mu$ W]	8.8	43	78	350	120	47	25	$\sim$ 1500
COMOS Process	0.35 $\mu$ m			0.35 $\mu$ m	0.18 $\mu$ m	65nm	0.18 $\mu$ m	N/A
$V_{DD}$ [V]	0.9	1.3	1.7	3.3	1	0.55	0.35	N/A
$\mathcal{L}(\Delta\omega)$ @1kHz [dBc/Hz] <sup>1</sup>	-126	-135	-130	-136	-130	-101	-122	-135
$\mathcal{L}(\Delta\omega)$ Noise Floor[dBc/Hz] <sup>1</sup>	-142	-144	-152	-150	-147	-141	-183	-150
Meet GSM Spec.?	No	No	Yes	Yes	No	No	No	Yes
FOM @1kHz [dB]	-229	-231	-225	-223	-221	-202	-220	-211

<sup>1</sup>Normalized to 13 MHz.

comes with the cost of 2 dB increase in far-from-carrier phase noise and 9 dB increase in 1-kHz offset frequency phase noise. The increase in Far-from-carrier phase noise is due to the resultant decrease in the oscillator swing. The causes of the 9 dB increase at 1-kHz offset frequency could be 1) an increase in the resonator's non-linearity due to smaller gaps and 2) a significant  $Q$  loading by the parasitic trace resistance which is larger than the resonator motional resistance in the 40 nm gap device, *cf.* Table 5.1. Additionally, the parasitic trace resistance limits the minimum achievable power consumption in this measurement as predicted in Section 3.2.3. This motivates to fabricate new devices using the 3- $\mu\text{m}$  thick polysilicon interconnects, but this is a topic for future work.

Nevertheless, compared to previous work [13] using a single disk resonator, the measured phase noise here, -126 dBc/Hz at 1-kHz and -142 dBc/Hz far-from-carrier when divided down to 13 MHz, is  $\sim 3$  dB better at 1-kHz and  $\sim 3$  dB worse far-from-carrier while only consuming 8.8  $\mu\text{W}$ , which is a whopping 40 times reduction in power compared to 350  $\mu\text{W}$  quoted in [13]. Use of Eqn. (5.7) yields Table 5.2, where the present Pierce oscillators achieve the top  $FOM$ 's at 1 kHz amongst published on-chip oscillators [8], [11], [45], [47], [55] to date.

## Chapter 6

# Oscillator Frequency Stability

The performance of electronic circuits and systems used in wireless communications depends strongly on the accuracy and stability of timing and frequency reference oscillators. For example, communication between a wireless receiver and a far-away transmitter can often be masked by the noise, i.e., short-term instability, of another transmitter closer to the receiver. The phase noise of such oscillators, studied in the last chapter, forms a key limitation of such transmitters—however, other stability limitations also exist. This chapter investigates two additional stability criteria, that of short-term acceleration-induced frequency shift and long-term drift.

### 6.1 Acceleration Sensitivity

Unfortunately, for many applications simply lowering electronics-induced phase noise is only half the battle. In particular, phase noise degrades dramatically when an oscillator experiences vibration. Vibration, of course, is everywhere, from buildings with typical accelerations of  $0.02g$ , to missiles with accelerations up to  $100g$ . Figure 6.1 illustrates the influence on the output power spectrum typically seen for an oscillator experiencing vibration. Here, vibration induces spikes at frequencies offset from the carrier by the vibration frequency,  $f_v$ . Normally, vibration occurs randomly at all frequencies up to a few kHz, so instead of spikes of added noise, a broad spectrum of increased phase noise often ensues, as illustrated by the red curve in Fig. 6.1. In traditional quartz-based oscillators, the primary cause of this acceleration sensitivity is often changes in stress at the mounting points of the crystal.

In this work, a low phase noise oscillator referenced to a 61-MHz vibrating Wine-Glass disk resonator is presented that posts a measured acceleration sensitivity at least as good as  $\Gamma \sim 0.2$  ppb/g for vibration frequencies up to 2 kHz and in all directions, yielding a vector magnitude  $|\bar{\Gamma}|$  less than 0.5 ppb/g. This result is the best mark to date among MEMS-based oscillators, including those aided by feedback compensation circuits; is more than an order of magnitude better than an off-the-shelf crystal oscillator; and is now comparable with

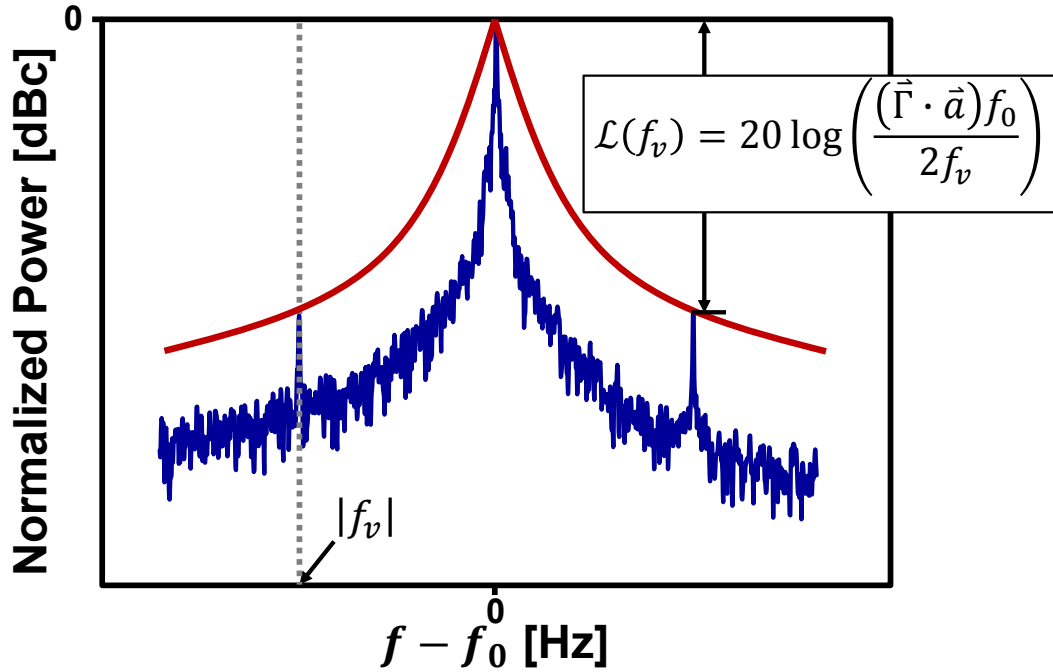


Figure 6.1: A typical oscillator output power spectrum in the presence of vibration with frequency  $f_v$ . The ratio between the sidebands and output characterizes the acceleration sensitivity of the oscillator. The red curve illustrates a broad spectrum of increased phase noise under random vibration.

low acceleration sensitivity oven-controlled crystal oscillators (OCXO's). Unlike quartz, the MEMS resonators used here do not suffer much from stress-induced frequency shifts, but are instead limited more by an electrical stiffness effect.

### 6.1.1 Acceleration–Induced Oscillator Frequency Instability

The procedure for measurement of oscillator acceleration sensitivity essentially entails vibrating the oscillator at frequency  $f_v$ , while measuring its output spectrum. In such a scheme the ratio between the induced sideband and carrier powers shown in Fig. 6.1 can be expressed as [56]

$$\mathcal{L}(f_v) = 20 \log \left( \frac{(\vec{\Gamma} \cdot \vec{a}) \cdot f_o}{2 f_v} \right) \quad \text{with} \quad \frac{\Delta f}{f_o} = \vec{\Gamma} \cdot \vec{a} \quad (6.1)$$

where  $f_o$  is the oscillation frequency,  $\vec{a}$  is the peak amplitude of the acceleration vector, and  $\vec{\Gamma}$  is the acceleration sensitivity vector of the oscillator gauging fractional changes in oscillation

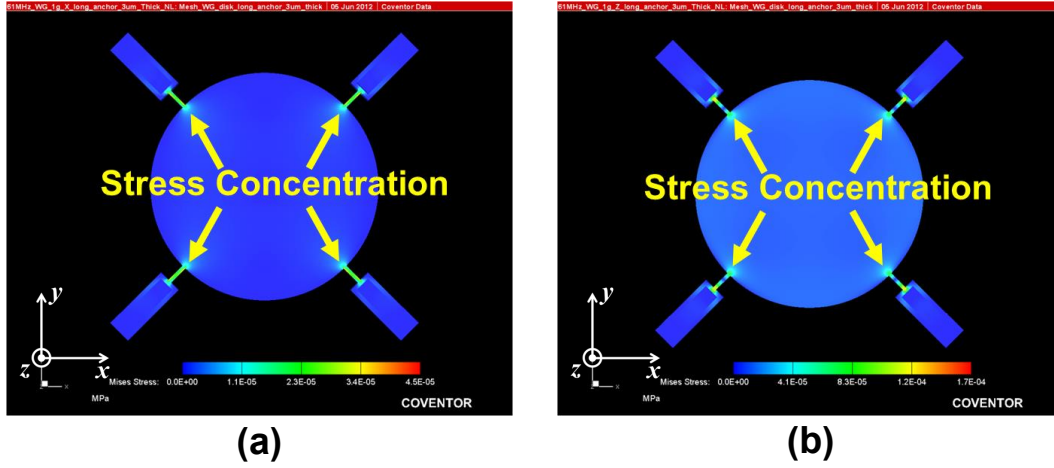


Figure 6.2: Finite Element Simulation (FEM) of the resonator subjected to (a) lateral acceleration and (b) vertical acceleration, showing stress concentrations in the structure.

frequency due to a unit  $g$  acceleration. In the presence of random vibration, this noise would appear as  $1/f^2$  phase noise.

The acceleration sensitivity vector can be described in a Cartesian coordinate system fixed to the resonator by

$$\vec{\Gamma} = \Gamma_x \vec{a}_x + \Gamma_y \vec{a}_y + \Gamma_z \vec{a}_z \quad \text{and} \quad |\vec{\Gamma}| = \sqrt{\Gamma_x^2 + \Gamma_y^2 + \Gamma_z^2} \quad (6.2)$$

where  $\vec{a}_x$ ,  $\vec{a}_y$ , and  $\vec{a}_z$  are peak acceleration vectors in different directions, and  $|\vec{\Gamma}|$  is the magnitude of their vector sum. It is this vector sum that is normally used to compare oscillator performance. For quartz crystal oscillators,  $|\vec{\Gamma}|$  may vary from  $5 \times 10^{-11}/g$  [57] to  $10^{-7}/g$  [58] depending on crystal design, cut, mounting, and whether or not feedback compensation circuits (that normally use accelerometers) are employed. As might be expected, the lower the acceleration sensitivity, the more expensive the oscillator.

### 6.1.2 Resonator Acceleration Sensitivity

Among possible mechanisms that give rise to acceleration-induced resonance frequency shifts in the Wine-Glass disk of this work, two stand out: 1) acceleration-induced mechanical stress, which is historically the main mechanism in quartz crystals; and 2) acceleration-induced changes in electrical stiffness, which is somewhat new and unique to capacitive-gap transduced MEMS-based resonators.

#### Mechanical Stress-Induced Frequency Instability

When the disk undergoes acceleration, its anchored support beams introduce stresses into its structure that then change its resonance frequency. Because the Wine-Glass disk

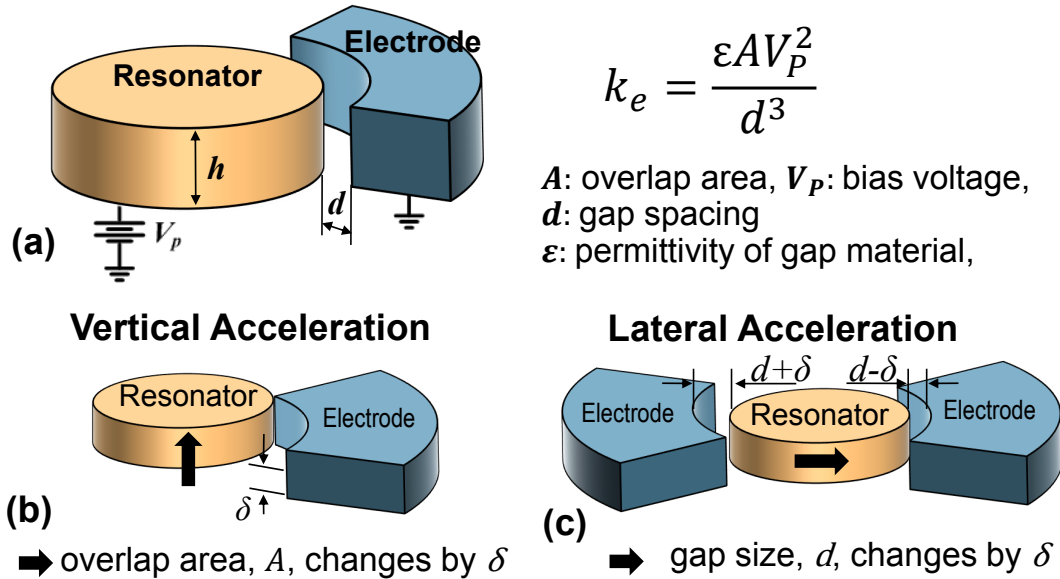


Figure 6.3: (a) Schematic of the resonator along with the electrical stiffness formula. (b) Overlapping area and (c) gap spacing change when the resonator experiences vertical and lateral acceleration, respectively.

is orders of magnitude smaller than a typical quartz crystal, its inertia is also many times smaller. Moreover, its support beams are strategically designed to attach to the disk at nodal points of the Wine-Glass mode shape. As shown in Fig. 6.2, this concentrates any acceleration-induced stress to nodal points in the vibration mode shape, where their influence on the resonance frequency of the disk is minimal. Finite element simulation using nonlinear models in Coventorware predicts  $|\vec{\Gamma}| = 5 \times 10^{-14}/g$ . Of course, since computer simulation is not infallible when it comes to predicting values this small, these specific numbers are perhaps best taken with a grain of salt, with the main take-away being not the specific numbers, but that mechanical-stress induced acceleration sensitivity is very small for the anchor-isolated MEMS-based resonator used here.

### Electrical Stiffness-Induced Frequency Instability

If mechanical stresses are too small for this device on this scale, then perhaps the dominant mechanism for acceleration sensitivity involves the electrical stiffnesses generated across the tiny electrode-to-resonator gaps in Fig. 6.1. In particular, when the disk vibrates (*cf.* Fig. 6.3(a)) the gap spacing between it and its electrode changes, which in turn means the electric field in the gap varies. It follows that the electrostatic force in the gap must also change, and it does so in phase with the disk edge displacement and with a magnitude that is proportional to it. Since any mechanism that generates a force in phase with and proportional to displacement fits the definition of stiffness, this electrical field-dependent

phenomenon is popularly termed the electrical stiffness and can be expressed as [26]

$$k_e = \frac{\varepsilon AV_P^2}{d^3} \quad (6.3)$$

where  $\varepsilon$  is permittivity of the gap material (i.e., vacuum in this case),  $A$  is the overlap area between the resonator and its electrodes, and  $d$  is the gap spacing between them.

Since the electrostatic force aids the motion of the resonator, this electrical stiffness actually softens the total stiffness of the structure and therefore reduces the resonance frequency as described by

$$f_o = f_{nom} \sqrt{1 - \left\langle \frac{k_e}{k_m} \right\rangle} \quad (6.4)$$

where  $f_{nom}$  is the nominal resonance frequency defined purely by geometry (with no applied voltages), and  $\langle k_e/k_m \rangle$  is the integrated ratio of electrical stiffness to mechanical stiffness  $k_m$  [13]. If external vibration induces a change in  $k_e$ , the corresponding change in resonance frequency can be approximated (when the change is small) as

$$\frac{\Delta f}{f_o} \approx -\frac{1}{2} \frac{\Delta k_e}{k_m} \quad (6.5)$$

For the case where the disk experiences a vertical acceleration, the height of its electrode-to-resonator overlap area changes by  $\delta$ , as shown in Fig. 6.3(b). According to Eqn. (6.3), the change in  $k_e$  due to a change in overlap area,  $\Delta A$ , can be expressed as

$$\Delta k_{e,z} = k_e \frac{\Delta A}{A} \quad (6.6)$$

Coventorware finite element simulation predicts for the 61-MHz Wine-Glass disk used in this work a change in overlap area per unit acceleration,  $g$ , in the z-direction of  $\Delta A = 3.722 \times 10^{-6} \mu\text{m}^2/g$ . Substituting this number into Eqn. (6.6), and combining with Eqns (6.1) and (6.5), the corresponding z-direction acceleration sensitivity  $\Gamma_{z,ke}$  component is

$$\Gamma_{z,ke} = 5.76 \times 10^{-13} /g \quad (6.7)$$

For the case where the disk experiences a lateral acceleration, its electrode-to-resonator gap spacings change. Similar to the vertical case, the change in  $k_e$  due to a change in gap,  $\Delta d$ , can be approximated using the first two terms of the Taylor series expansion of Eqn. (6.3) as follows

$$\Delta k_{e,x} = \Delta k_{e,y} \approx k_e \left( -3 \frac{\Delta d}{d} + 6 \left( \frac{\Delta d}{d} \right)^2 \right) \quad (6.8)$$

If the disk of Fig. 2.1 had only one electrode covering one quadrant of its sidewall area, then the frequency shift imposed by Eqn. (6.5) could actually be significant. However, the

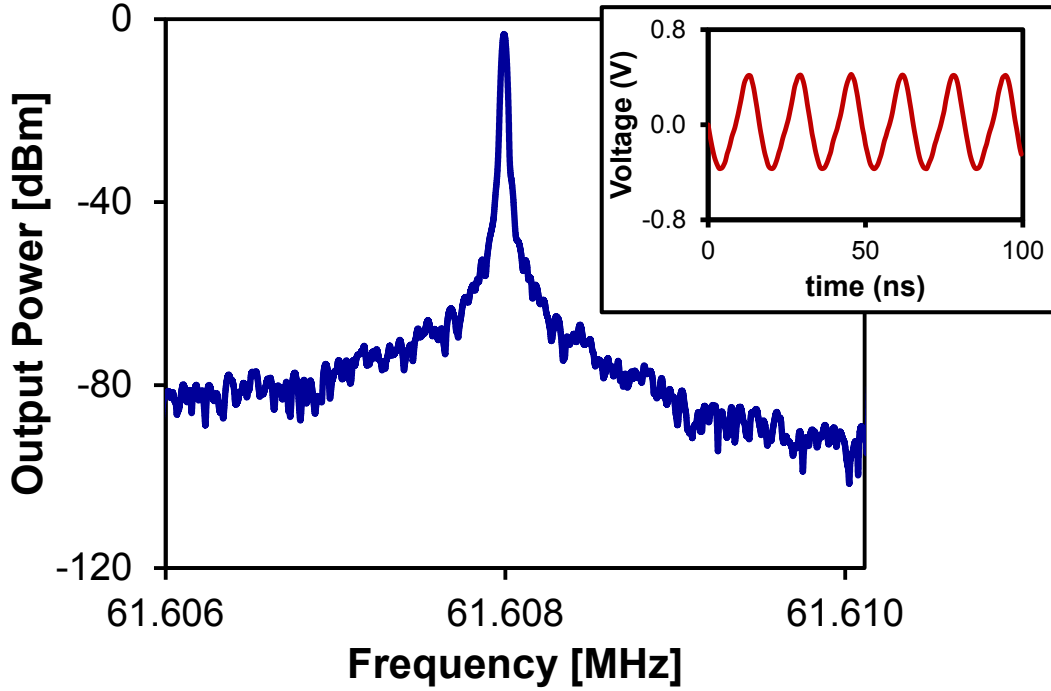


Figure 6.4: The measured output power spectrum of the Wine-Glass disk oscillator. Inset: its measured output waveform.

disk of Fig. 2.1 sports not just one, but four electrodes placed symmetrically around its perimeter. In this scheme, if the gap decreases by  $\delta$  on the right side of the disk, as shown in Fig. 6.3(c), a corresponding gap increase by  $\delta$  ensues on the left side. The total change in  $\Delta k_e$  is the sum of  $\Delta k_e^+$  due to a gap decrease and  $\Delta k_e^-$  due to a gap increase:

$$\Delta k_{e,x} = \Delta k_{e,y} = \Delta k_e^+ + \Delta k_e^- \approx \frac{k_e}{4} \left( 12 \cdot \left( \frac{\Delta d}{d} \right)^2 \right) \quad (6.9)$$

where  $k_e$  is divided by 4 because the Wine-Glass disk resonator has four electrodes. Coventorware simulation gives  $\Delta d = 2.3285 \times 10^{-6}$  nm/g, which then yields

$$\Gamma_{x,ke} = \Gamma_{y,ke} = 1.4978 \times 10^{-19}/g \quad (6.10)$$

This is far smaller than the already very small acceleration sensitivity due to electrical stiffness in the  $z$ -direction.

### 6.1.3 Measurement Setup

The Wine-Glass disk resonators used for testing are fabricated via the self-aligned stem process in Section 4.1. Figure 4.4(a) presents the scanning electron micrograph (SEM)

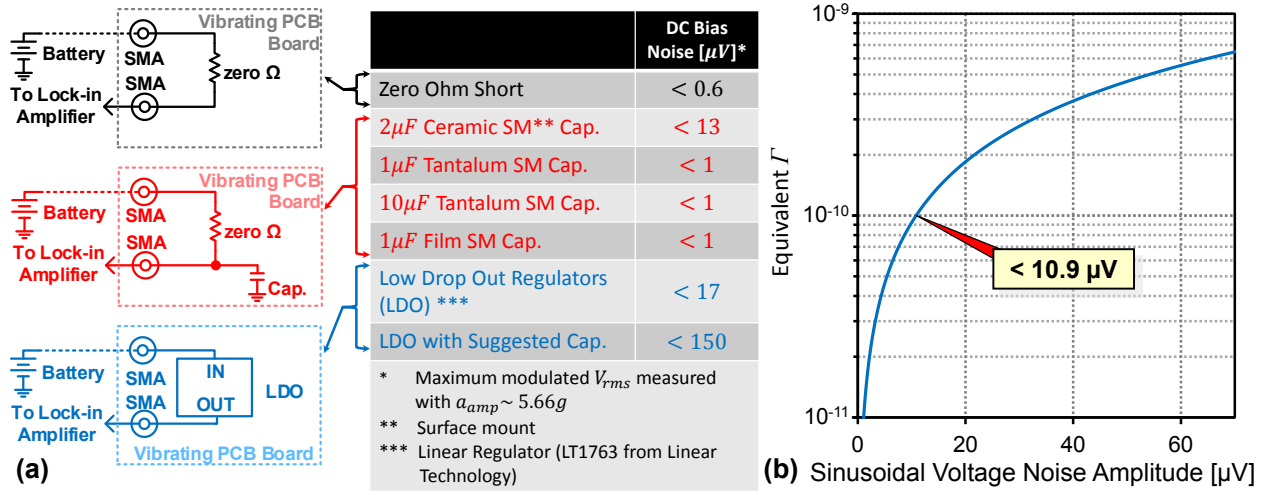


Figure 6.5: (a) Schematics of measurement setups used to measure the voltage noise induced by various electronic components under acceleration. The table summarizes the measured  $rms$  voltage noise caused by various electronic components under a sinusoidal acceleration with 5.66g amplitude. (b) Theoretical prediction of the required sinusoidal noise voltage amplitude to be applied on the  $V_P$  line to produce the same equivalent  $\Gamma$ -factor for the 61-MHz Wine-Glass disk resonator under 5.66g amplitude of sinusoidal acceleration. Here, the resonator's thickness is 3  $\mu m$ , its gap is 80 nm, and its  $Q$  is 100k. The frequency pull-in due to amplifier is assumed to be zero.

of a fabricated 61-MHz Wine-Glass disk resonator used in this measurement. To see the acceleration effect of these oscillator, it requires an oscillator with low phase noise. This requires the high resonator's  $Q$  (i.e., over 50,000 loaded) and, therefore, requires the operation in vacuum. The custom-made miniature vacuum chamber in Fig. 4.7(a) is used in this measurement for its compactness and sturdiness. An TIA amplifier (*cf.* Fig. 3.7 is used in this measurement for the interest of versatility. Figure 6.4 presents the measured output power spectrum of the MEMS-based oscillator operating inside this chamber and the inset shows the measured output waveform of the oscillator.

### Parasitic Acceleration Sensitivity

Unfortunately, the device of interest is often not the only component in an acceleration sensitivity test setup that responds to acceleration. Indeed, the electronic components, the PCB, and the wires and solder joints, are all also sensitive to acceleration due to stress, as well as to charge distribution and electromagnetic interference. Therefore, understanding noise contributors of electronic components in the system is very important to do good measurements: particularly, the amount of voltage noise induced by electronic components under acceleration is measured. The first test includes two SMAs connected with a printed

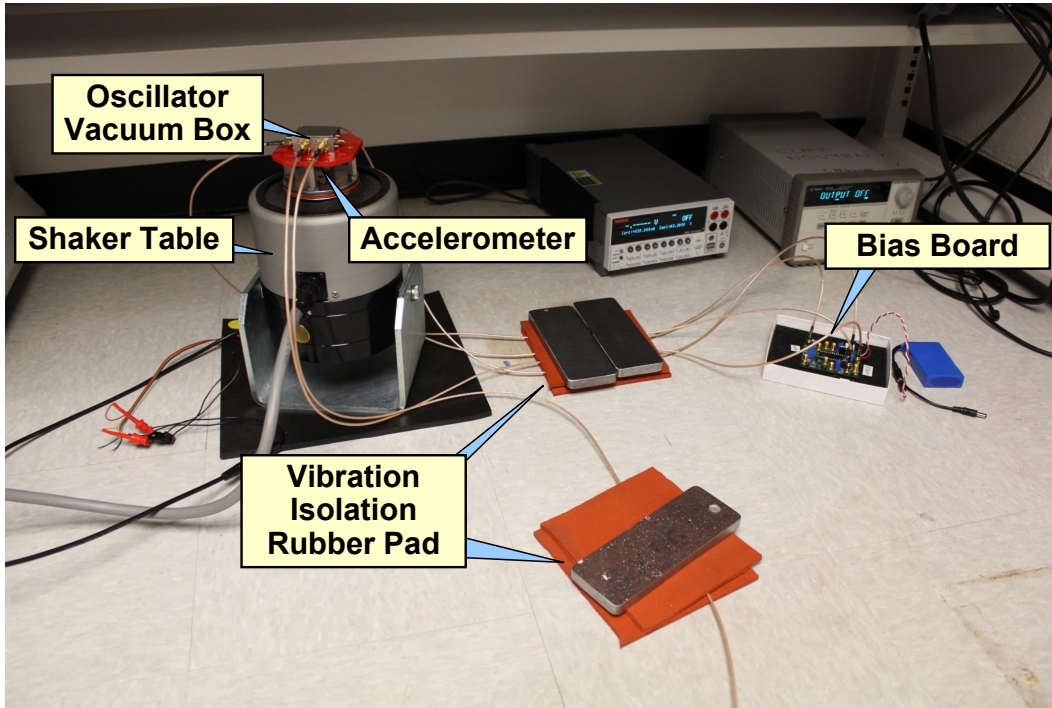


Figure 6.6: Acceleration sensitivity measurement setup.

circuit board (PCB) trace through a zero- $\Omega$  resistor as shown in the black schematic of Fig. 6.5(a). The PCB is then screwed down on the ET-139 shaker table, which generates a sinusoidal vibration. One of the SMA is hooked up to a battery and another one is connected to a lock-in amplifier to precisely measure the *rms* voltage noise generated by the zero- $\Omega$  resistor component. The second test (as shown the red schematic of Fig. 6.5(a)) is similar to the first test except different kinds of capacitors were shunted to the ground in order to measure noise produced by capacitors. In the last text, low drop out regulators (LDO) are investigated using a similar test setup as shown in the blue schematic of Fig. 6.5(a).

Table in Fig. 6.5(a) summarizes measured voltage noise ( $V_{\text{rms}}$ ) of different electronic components. It shows that SMAs, PCB traces, and zero- $\Omega$  resistors introduce noise smaller than  $0.6 \mu\text{V}_{\text{rms}}$ . A typical  $2 \mu\text{F}$  ceramic capacitor can produce up to  $13 \mu\text{V}_{\text{rms}}$  noise while tantalum and film capacitors introduce much less noise. On the other hand, the LDO can introduce large noise from  $17\text{-}150 \mu\text{V}_{\text{rms}}$ . This means electronic components such as ceramic capacitors and LDO have to be off the shaker table while electronic components such as tantalum and film capacitor can be on the shaker table only when needed. To illustrate the importance of minimizing voltage noise in the measurement system, Fig. 6.5(b) predicts that measuring acceleration sensitivity  $\Gamma$  factor of  $10^{-10}$  using  $5.66g$  acceleration amplitude requires the voltage noise amplitude to be less than  $10.9 \mu\text{V}$ .

To measure the acceleration sensitivity of the MEMS oscillator, the measurement system

shown in Fig. 6.6 constructed around an ET-139 shaker table from Labworks Inc. pays careful attention to minimize the parasitic voltage noise. In this setup, the vacuum box housing the MEMS-based oscillator is securely bolted onto the shaker table in one of the three orthogonal orientations. A low-noise analog voltage regulator board supplies all needed bias and supply voltages to the amplifier via shielded coaxial cables routed through weighed foam pads for vibration isolation and away from the power amplifier driving the shaker table. A single coax line carries the oscillator output waveform for capture of output spectra on a N9030A Agilent spectrum analyzer. This setup incorporates many improvements over that used in [59], including removal of acceleration sensitive components from the accelerated PCB and simplification of the feedback loop from large PCB-level wires to short die-level bondwires.

To apply acceleration, the shaker table is driven by a variable-amplitude sine wave at frequencies from 100 Hz to 2 kHz. An ADXL326Z accelerometer from Analog devices mounted directly beneath the oscillator senses the amplitude of acceleration, converting it to an electrical signal that then feeds a Stanford Research Systems SR830 lock-in amplifier. This setup provides a highly accurate and noise-free measure of acceleration amplitude at the frequency of interest.

### 6.1.4 Measurement Results

Using the refined experimental setup, the acceleration sensitivity of the packaged oscillator of Fig. 4.7 was measured in all three orthogonal directions up to 2 kHz. Figure 6.7 presents all measured gamma components and demonstrates a remarkable sensitivity  $\Gamma \sim 0.2$  ppb/ $g$  in all directions at all measured frequencies. This value is at least a factor of  $\sim 30\times$  better than the work of [59] (*cf.* Fig. 6.8) and marks the best performance posted to date for a MEMS-based oscillator (*cf.* Fig. 6.9) outperforming even those enhanced by accelerometer-based feedback compensation circuits [60], [61].

To provide a comparison to commercial quartz devices and as an additional qualification of the measurement system, several “off-the-shelf” 66.67MHz quartz oscillators were measured as direct drop-in replacements for the bondwired MEMS oscillator inside the hermetic vacuum box. Figure 6.8 compares the measured  $\Gamma$ -vector sum of one of these oscillators with that of the MEMS oscillator, as well as with the work of [59]. As shown, the MEMS oscillator measured via the improved system displays more than an order of magnitude reduction in sensitivity over the commercial quartz. While this is not the best quartz can do—bulky, high-cost quartz oscillators built explicitly for acceleration insensitivity are significantly better—this does represent a fair comparison to a low-price, high-volume product. Even though the MEMS oscillator is not as good as one of the best crystal oscillators measured [57] shown in Fig. 6.9, it certainly outperforms generic quartz and is even on par with most (expensive) low sensitivity OCXO’s, laying to rest, and in fact reversing, concerns that MEMS-based oscillators are intrinsically worse than quartz alternatives.

Despite these impressive performance numbers, measured sensitivities still fall short of that predicted by the theory of Section 6.1.2 for the MEMS device itself. Indeed, although

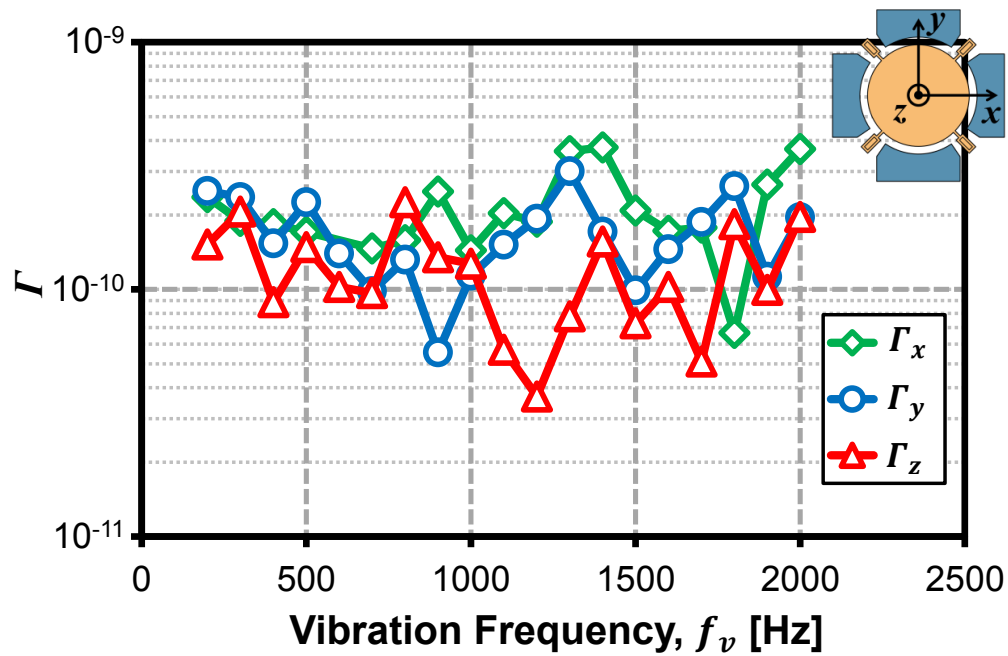


Figure 6.7: Plot of measured  $\Gamma$  components versus vibration frequency.

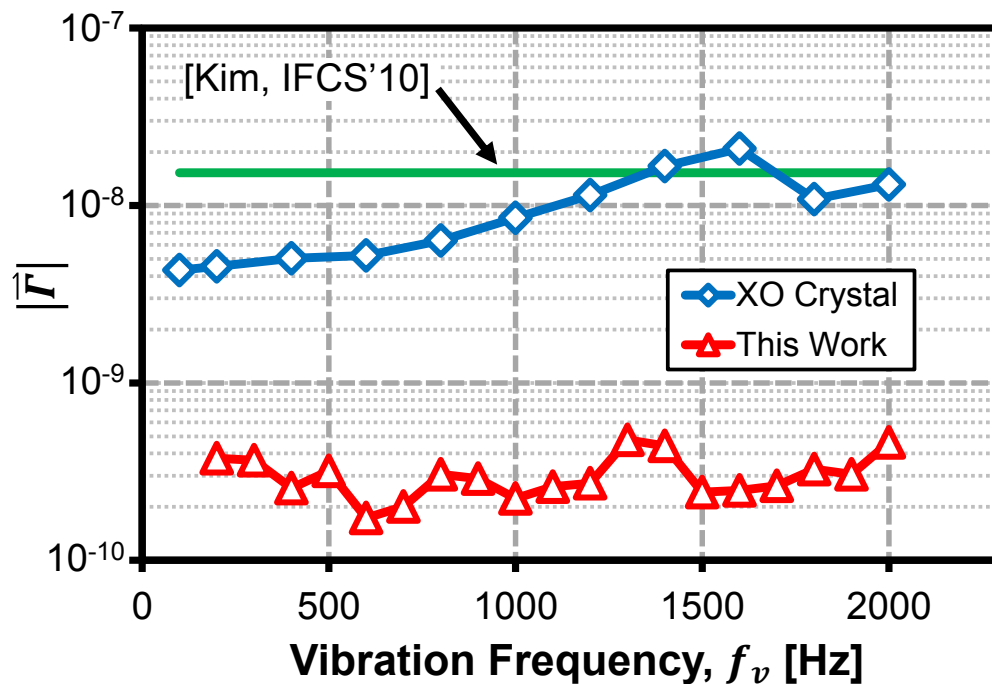


Figure 6.8: Plot of measured  $\Gamma$  vector sum versus vibration frequency for the 61-MHz micro-mechanical disk oscillator alongside similar plots for previous work using a similar resonator device and a measured 66.67-MHz off-the-shelf crystal oscillator.

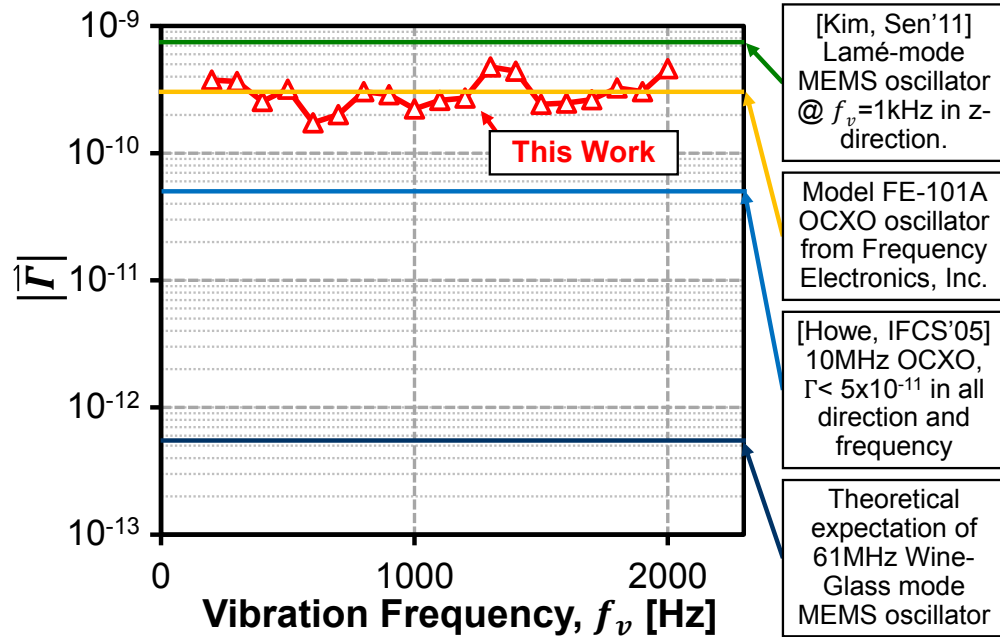


Figure 6.9: Plot of  $\Gamma$  vector sum versus vibration frequency for the 61-MHz micromechanical disk oscillator alongside lines indicating the performance of oscillators in the literature and that of the theoretical expectation.

many precautions were taken to eliminate extraneous sources of vibration noise, some still remain, particularly bondwires. The influence of bondwires was further explored by constructing and measuring an additional oscillator with intentionally lengthened bondwires, particularly those within the oscillation loop linking the amplifier to the MEMS resonator, and one connected to the resonator dc-bias voltage  $V_P$ . Figure 6.10(a) and (b) present close-up photos of both oscillators, showing the much longer bondwires of design (b). Figure 6.10(c) presents the measured data, showing close to an order of magnitude decrease in z-direction sensitivity for the device with short versus long bondwires at all frequencies measured.

These results strongly suggest that flexing wires on sensitive nodes constitute a primary limitation on past, and possibly present, measurements. While the exact nature of the coupling of bondwire motion to the oscillation frequency is not precisely known, inductive and capacitive effects could easily explain it. Additionally, the spikes seen in the measured acceleration sensitivity versus frequency curve of Fig. 6.10(c) can be well understood as weak mechanical resonances in the bondwires themselves.

To summarize, the acceleration sensitivity of a 61-MHz vibrating Wine-Glass disk resonator is measured to be at least as good as  $\Gamma \sim 0.2$  ppb/ $g$  for vibration frequencies up to 2 kHz and in all directions, yielding a vector-sum magnitude  $|\vec{\Gamma}|$  less than 0.5 ppb/ $g$ . This remarkable number is achieved without any compensation and marks the best among

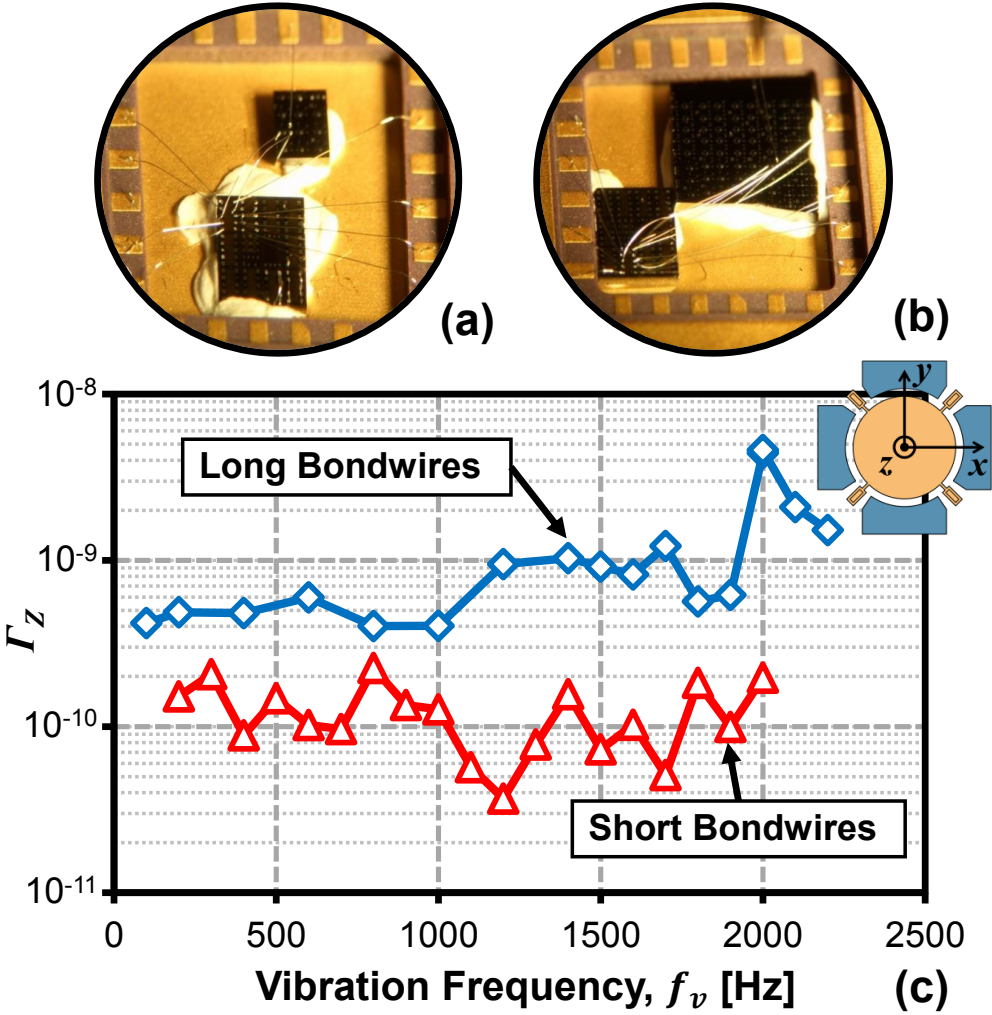


Figure 6.10: Plot of measured  $\Gamma$  components versus vibration frequency.

MEMS-based oscillators, including those aided by accelerometer-based feedback compensation circuits. It is more than an order of magnitude better than an off-the-shelf crystal oscillator and is now comparable with some low sensitivity OCXO's.

## 6.2 Long-Term Stability

While short-term stability of MEMS-based oscillators has proven to be quite good, where even the challenging GSM phase noise specifications were met some time ago [13], the long-term reliability and stability of these resonators has been largely unstudied. Long-term frequency stability of reference oscillators is essential to maintain reliable radio communication without signals drifting into nearby bands. Typical frequency stability requirements are application-dependent and can range from tens of ppm per year to less than one ppm [15]. Cell phone requirements, for instance, remain one of the most challenging, with GSM requiring  $\pm 0.1$  ppm reference oscillator stability [16]. Requirements for local-area wireless standards are much more lenient, however, with typical stability requirements of  $\pm 40$  ppm [17]. Although the small size of MEMS resonators make them an exciting alternative to traditional quartz, they at the same time raise concerns of increased aging effects due to mass loading, package leaks, or stress fatiguing [18].

Wine-Glass disk oscillators have shown to exhibit exceptional short-term stability, with demonstrated phase noise below the GSM spec. [11], [62] and superior insensitivity to vibration versus typical quartz counterparts [50]. But studies of long-term stability have until now been unpublished. To remedy this, this Chapter presents a first measurement of the MEMS oscillator of Fig. 3.7, comprised of a Wine-Glass disk resonator bond-wired to an ASIC transimpedance amplifier and hermetically packaged in a custom-built vacuum-packaging system capable of maintaining torr pressures. A double-oven system maintains a constant oscillator temperature at  $34^\circ\text{C}$  with less than  $0.001^\circ\text{C}$  deviation, a key improvement over previous studies.

The long-term frequency drift of this MEMS oscillator is measured over 10 months and found to stabilize to within the short-term measurement variation of  $\pm 300$  ppb over a period of months after an initial burn-in period. This marks a significant improvement from previous studies on other MEMS resonator types, where frequency fluctuations were  $\pm 3.1$  ppm [19] and  $\pm 1.2$  ppm [20] over similar time scales. Including burn-in, the total observed aging of 10 ppm over 10 months is now on par with many consumer quartz oscillators designed for timing applications [15].

### 6.2.1 Stable Measurement Environment

#### Packaging

Of central import in MEMS oscillator stability is packaging. For example, exposure to air is known to produce frequency shifts due to oxidation or moisture absorption even in quartz oscillators [15]. The tiny size of MEMS resonators makes environmental control even more important. For the typical resonator used here, even a single additional monolayer of atoms, from sources such as contamination or package leakage, would correspond to a frequency change of over 30 ppm.

Beyond material aging concerns, a good vacuum environment is also needed to reduce air

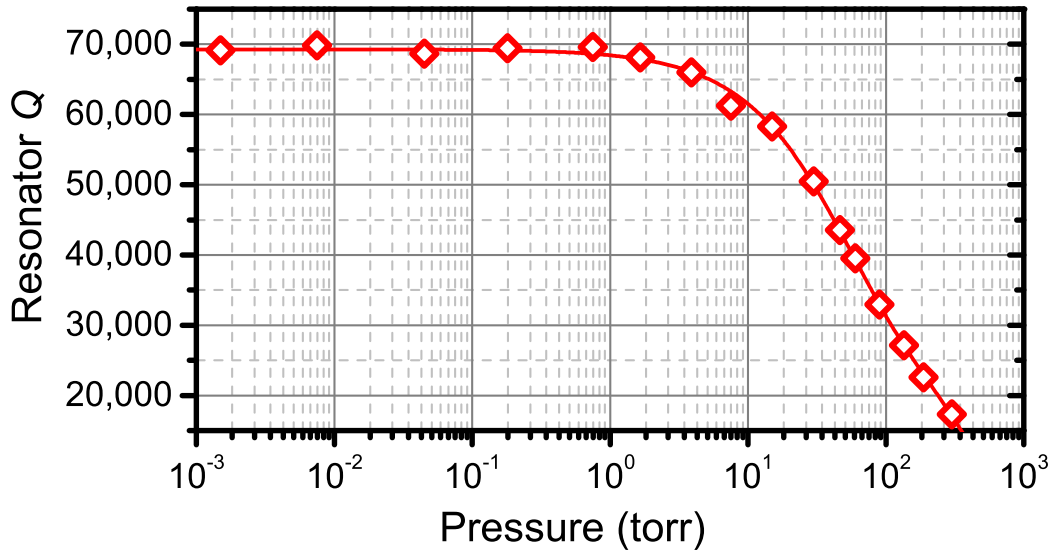


Figure 6.11: Measured Wine-Glass disk MEMS resonator  $Q$  as a function of ambient air pressure.

damping and enhance resonator  $Q$ . Figure 6.11 gauges the degree to which air damping affects a typical Wine-Glass disk resonator used in this study with a measured plot of  $Q$  versus pressure that indicates a required operating pressure of below 1mtorr to remove air damping as a relevant loss mechanism. Achieving reliable hermetic packaging at such pressures is a challenge in a laboratory environment, and a chief obstacle in past long-term studies.

Pursuant to this goal, the vacuum packaging system of Fig. 6.12 was constructed to facilitate hermetic sealing using AuSn solder seals with a variety of conventional ceramic packages in a vacuum environment. In this system, a heated chuck holds the ceramic package containing the bond-wired MEMS resonator and ASIC while the package lid and magnetically attach to a linear motional feedthrough.

To package an oscillator, the ASIC and MEMS die, along with Ti meta shavings used as a getter, are first glued within the package using Ceramabond 552 high-vacuum ceramic adhesive. The package is mounted in the packaging chamber and pumped to torr vacuum. Following a 2 hour bakeout at 220°C, the package lid with AuSn preform is pressed with ~10 lbs. of force against the package and heated to 350°C for 1 minute. The package and chuck are allowed to cool to room temperature before venting and unloading. For the oscillators in this study, Kyocera KD-78382-01 24-pin dual in-line packages (DIP) and HRC-2578 lids were used.

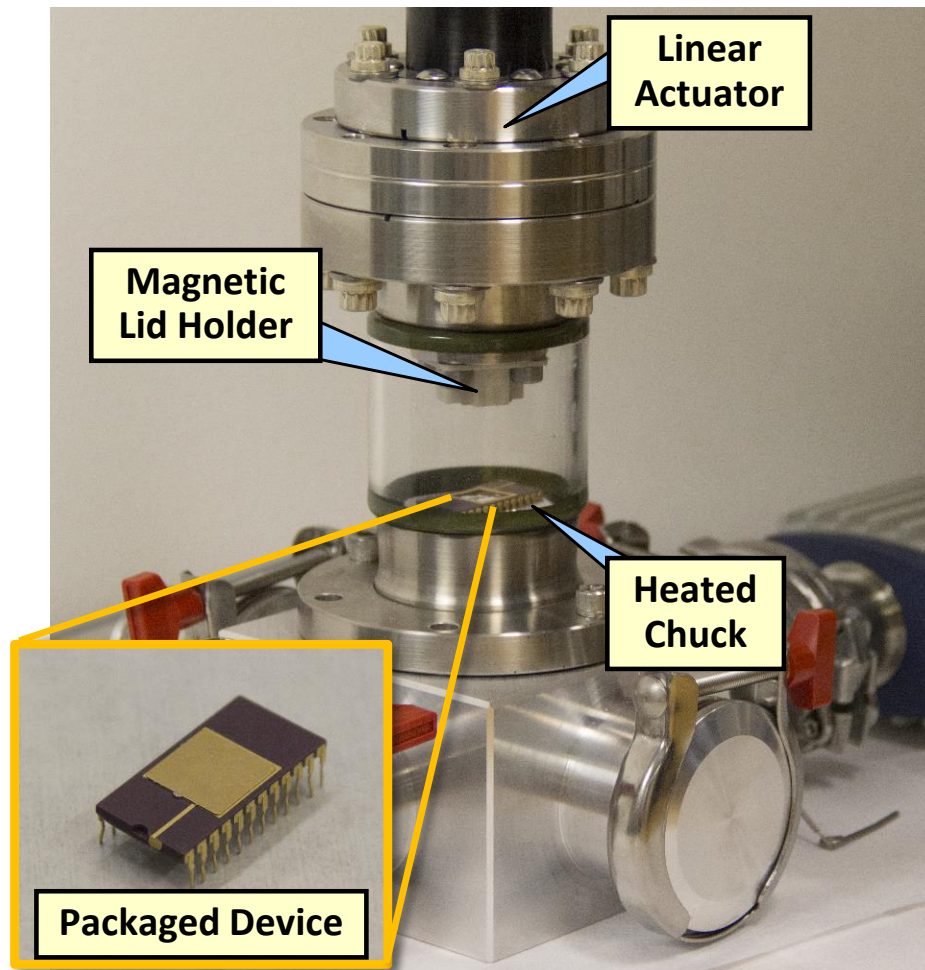


Figure 6.12: Hemermetic vacuum packaging tool with zoom-in (inset) on a DIP package sealed via the tool.

### Temperature Control

In order to accurately measure true aging-induced frequency drifts, the oscillator temperature environment must be very tightly controlled or compensated. For the polysilicon devices used here, the measured temperature coefficient of frequency is on the order of  $T_{CF} = 21$  ppm/ $^{\circ}\text{C}$ , which allows excessive frequency shifts when ambient temperature fluctuations are not compensated. In the past, two methods of temperature compensation have been applied to MEMS oscillators. Passive compensation seems to be limited to  $\pm 40$  ppm total frequency shift over commercial temperature ranges [20]. On the other hand, active temperature compensation is widely used in production MEMS oscillators to provide full temperature range stability to better than  $\pm 10$  ppm [4]. But to accurately observe true frequency drift in the absence of thermal variations, an even more stable temperature environment is needed.

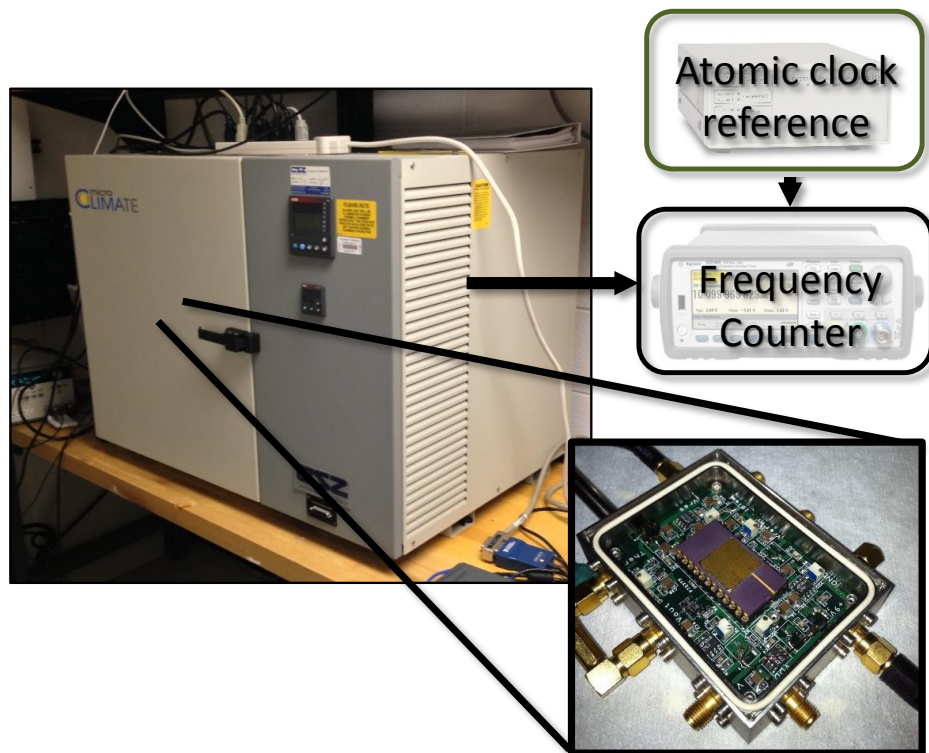


Figure 6.13: Experimental measurement setup showing the oscillator mounted in the first temperature controlled oven (inset) and placed in a second environmental chamber oven for further temperature stability. The oscillator frequency is measured via a zero dead-time counter referenced to an atomic clock.

To this end, the work presented here employs the double-oven setup of Fig. 6.13 to house the measured oscillators. The outer oven consists of a Cincinnati Sub-Zero MCB-1.2 chamber which keeps the internal temperature within  $\pm 0.1^\circ\text{C}$ . To further stabilize temperature, a second internal oven combines a computer controlled heating element and temperature sensor incorporated into the box used to mount the oscillator. An ultra-stable Measurement-Specialties 46007 glass-encapsulated thermistor serves as the temperature monitor and control, measured using an Agilent 34420A micro-ohm meter. This double oven was observed to hold temperature to within  $\sim 200\mu\text{K}$  in the face of typical daily external temperature fluctuations.

### Frequency Measurement

When placed in the temperature-stable double-oven system, the oscillator output is measured using an Agilent 53230A frequency counter which allows high-resolution measurement with no dead time, i.e., no gap between measurements. For highly-stable measurements

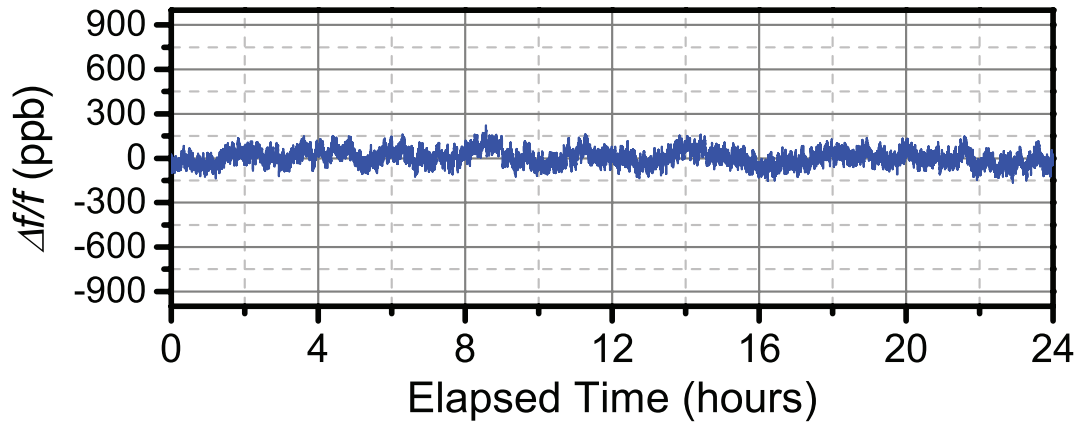


Figure 6.14: Typical oscillator stability over 24 hours with a 1 s averaging time.

over long periods, a Stanford Research Systems FS725 atomic clock provides a frequency reference specified with  $\pm 5$  ppb aging over a 20 year lifespan.

## 6.2.2 Measurement Results

Figure 6.14 presents typical 1 day data for the oscillator mounted in the double-oven stabilization system and demonstrates frequency stability down to  $\pm 150$  ppb. Figure 6.15 presents measured oscillator frequency versus time data over a 10 month aging period, exhibiting the same logarithmic decay behavior typical of quartz oscillators [15]. The increasing frequency suggests possible stress relaxation or changes to the resonator material properties over mass loading or package leaks as the aging mechanism. Stress relaxation in particular would be expected to contribute as both bond-wires and high-temp glue adhering the die to package would be expected to produce strain and have been observed to produce over 100 ppm/week drift in flexural mode devices [63]. Despite this, performance is good, on par even with low-cost quartz oscillators. This is not unexpected for such Wine-Glass devices, for which supports attached to quasi-nodal points on the resonant disk structure greatly isolate the disk from the substrate and its associated stress changes.

Interestingly, Fig. 6.16 presents oscillation amplitude data taken from this same time range, and shows an unexpected increase closely following the frequency drift seen. As the amplifier gain is kept fixed, this points to a surprising decrease in the  $R_x$  of the resonator over time. This again suggests that increased mass loading or air damping is not a factor here and further confirms a reliable package over the measured time span.

To better gauge the performance of this oscillator, Allan Deviation,  $\sigma_y$ , can be calculated from the fractional frequency shift  $y_n = \Delta f/f_o$  using

$$\sigma_y^2(\tau) = \frac{1}{2} \langle (\bar{y}_{n+1} + \bar{y}_n)^2 \rangle \quad (6.11)$$

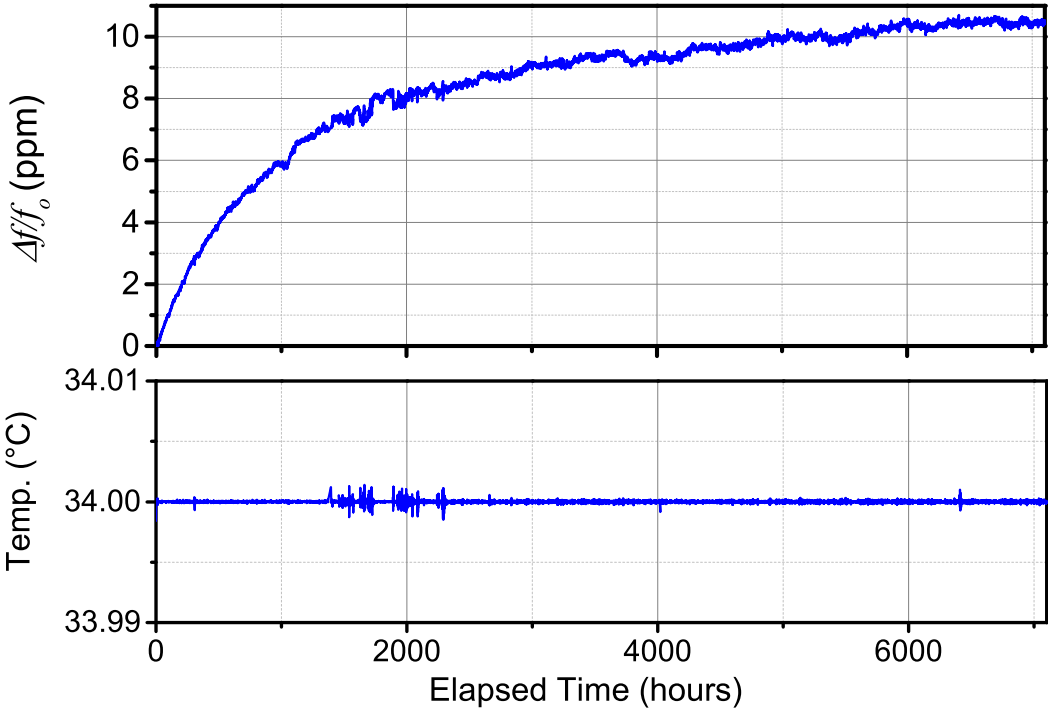


Figure 6.15: Measured frequency drift and temperature stability of the MEMS oscillator. Frequency measurements were made using an Agilent 53230A frequency counter and shown here with a 100s measurement time.

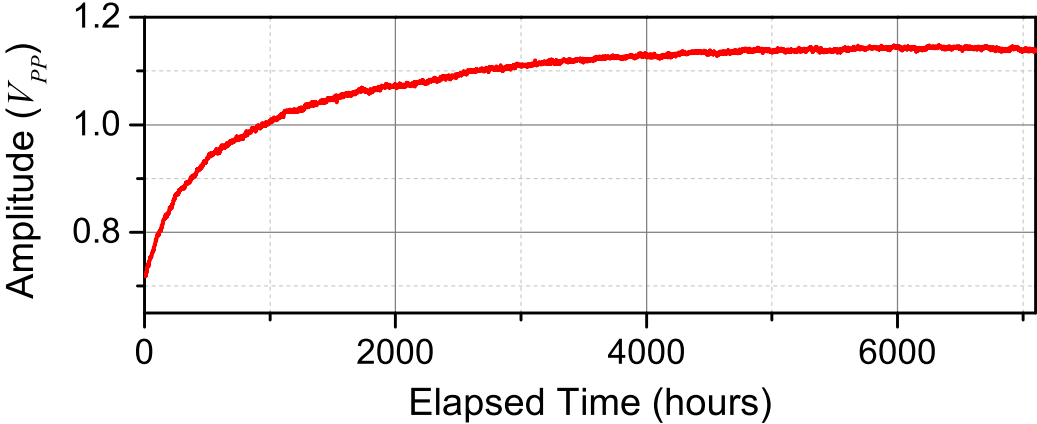


Figure 6.16: Amplitude of oscillation during a long-term measurement.



# Chapter 7

## Oscillator Systems for Signal Processing

Chapter 5 demonstrated a 61-MHz capacitive-gap transduced Wine-Glass disk Pierce oscillator capable of meeting the challenging GSM specifications while using only 78  $\mu\text{W}$  of power consumption. By reducing the gaps from 80 nm to 40 nm, the power consumption can further be reduced to 8.8  $\mu\text{W}$  at the cost of a few dB increase in phase noise. Chapter 6 further studied the acceleration sensitivity and the long-term stability showing excellent frequency stability in these oscillators. Applications of such oscillators are not limited to reference oscillators. Using their multi-electrodes capability, electrical stiffness based frequency tuning, and regenerative amplification effect, these oscillators can be used as signal processors to improve current wireless technologies to have lower power and more spectrum efficient communications. This chapter and the following chapter present efforts towards these goals.

### 7.1 Simultaneous Multi-Frequency Switchable Oscillator and FSK Modulator

Pursuant to expanding the range and capability of MEMS oscillator transmitters, this work presents an oscillator (*cf.* Fig. 7.1) that combines a single amplifier with a plurality of MEMS resonators capable of not only outputting multiple independent frequencies in the vicinity of 61 MHz; but also, by exercising voltage-controlled electrical stiffness tuning [26] of individual resonator array-composites, Frequency Shift Key (FSK) modulating each frequency to generate waveforms suitable for simultaneous wireless transmission in multiple channels. The chosen frequency is ideal for long-range unlicensed operation in the 52-74 MHz band white-space [30] and ISM bands at 27.12 MHz and 40.68 MHz [31].

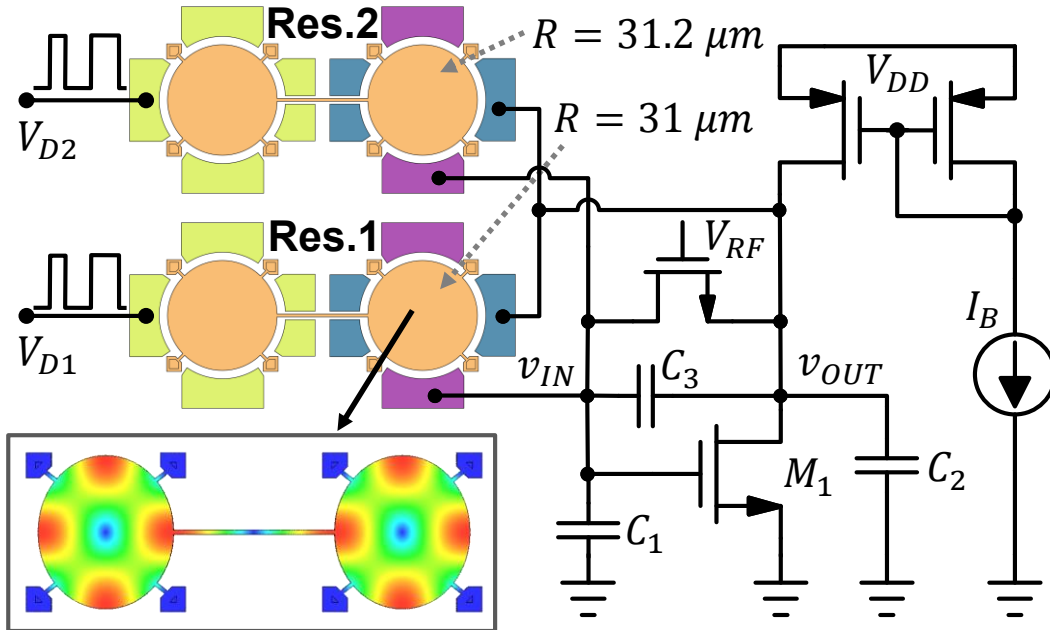


Figure 7.1: Schematic of the Pierce topology multi-oscillator circuit used in this work. Independent tuning voltages and input bit streams are applied to Res. 1 and Res. 2. In each array-composite resonator, electrodes with the same color are electrically connected together. Inset shows FEM mode shape simulation of the two-disk array.

### 7.1.1 Device Design and Operation

The multi-oscillator system here comprises two main parts: a sustaining amplifier circuit and a multi-frequency MEMS array-composite resonator circuit. The ability to use only one amplifier with multiple resonators saves considerable power and derives from the ability of MEMS resonators to limit the oscillation amplitude [64]. In particular, unlike the vast majority of oscillators in which the sustaining amplifier rails out to limit the oscillation amplitude, thereby desensitizing it to any other frequency; the multiple oscillation amplitudes (at different frequencies) of this MEMS oscillator limit via spring softening and damping nonlinearities in the MEMS resonators. This then allows the amplifier to remain linear and provide gain at multiple frequencies.

The use of array-composites like that of Fig. 7.2, rather than just single resonators, allows for additional electrodes through which more control of the total array-composite resonator is obtained, e.g., for frequency pulling, strong input/output (I/O), “on/off” switching, etc. The array-composite of Fig. 7.2 specifically uses Wine-Glass-mode disk resonators to take advantage of their ability to attain the needed frequencies while allowing accurate specification via CAD layout of multiple unique frequencies on the same die. Each resonator comprises a 2  $\mu\text{m}$ -thick,  $\sim 31 \mu\text{m}$ -radius polysilicon disk supported by beams at quasi nodal points and electrically coupled along their sidewalls to input-output electrodes by tiny 50

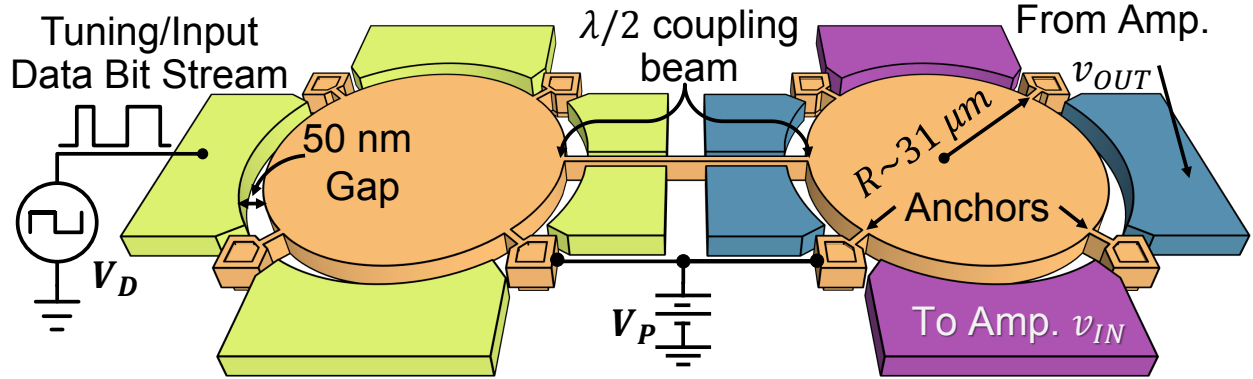


Figure 7.2: Perspective view of a single MEMS two-disk array-composite comprising two suspended, mechanically-coupled disk resonators (orange) anchored at their 4 nodal points. Tuning electrodes (green) on one disk allow for electronic frequency control while input (blue) and output electrodes (purple) on the second one connect to bus bars to provide a multi-port multi-resonator device.

nm capacitive gaps.

In each two-disk array-composite, a half-wavelength beam mechanically couples the disks, where sizing to half the acoustic wavelength forces the individual resonator disks to move in-phase at a single resonance frequency. Effectively, the array of disks behaves as one disk with twice the sidewall surface area with which to electrically interrogate or control it. To excite the composite resonator into motion, a bias voltage  $V_P$  on the disk structure combines with an ac drive voltage applied to the input electrodes (blue and labeled “From Amp”) around the right-hand disk to produce forces across the input electrode-to-resonator gaps that, at resonance, excite the Wine-Glass (i.e., compound (2, 1)) mode shape, shown in the inset of Fig. 7.1. Here, disk radius  $R$  primarily sets the resonance frequency [33], [35]. A 0.2  $\mu\text{m}$  difference in disk radii separates the Fig. 7.1 resonator frequencies by 300 kHz around 61 MHz.

While the disk on the right provides the I/O interface (to the sustaining amplifier), the disk on the left enables control of frequency via the voltage-controllable electrical stiffness, which influences the frequency via [26], [35]:

$$f_{ot} = f_{nom} \sqrt{1 - \frac{k_e}{k_{mre}}}; \quad f_{nom} = \frac{1}{2\pi} \sqrt{\frac{k_{mre}}{m_{mre}}}; \quad k_e = \frac{\alpha^2 C_o}{d_o^2} V_{PG}^2 \quad (7.1)$$

where  $k_{mre}$  and  $m_{mre}$  are the effective dynamic mechanical stiffness and mass at the highest displacement location,  $k_e$  is electrical stiffness, the  $C_o$  is the total electrode-to-resonator overlap capacitance of a disk,  $d_o$  is the gap spacing, and  $V_{PG}$  is the bias voltage across the gap.  $k_{mre}$  and  $m_{mre}$  are two times larger than a single disk resonator given by Eqn. (2.16).  $\alpha$  is a dimensionless constant based on mode and electrode shape, equal to 0.787 for the design used here and takes the form:

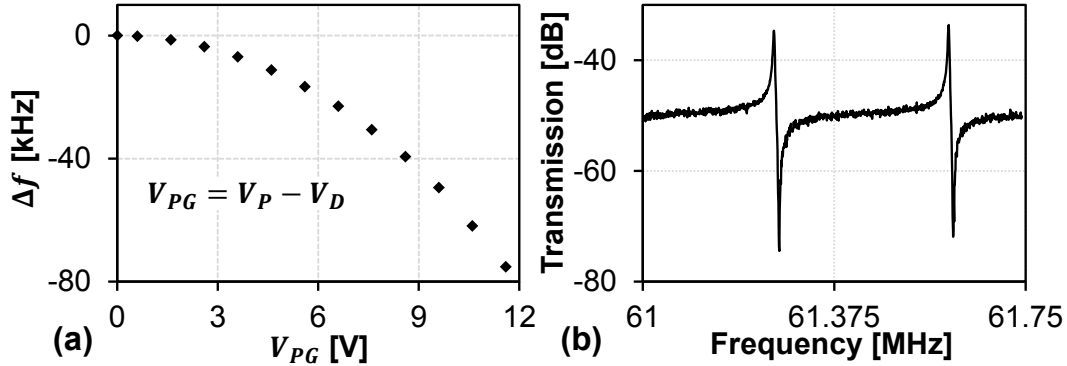


Figure 7.3: (a) Oscillation frequency tuning vs. applied voltage across the capacitance gap of the tuning resonator. (b) Frequency response as measured by an Agilent E5071C network analyzer for a two-disk array-composite with both resonators turned ‘on’ via applied bias voltage.

$$\alpha = \left[ \frac{1}{\Delta\theta} \int_{\theta_1}^{\theta_2} \frac{\Re(R, \theta')}{\Re(R, 0)} d\theta' \right]^2 \quad (7.2)$$

where  $\Re(r, \theta)$  is defined in Eqn. (2.12) and  $\Delta\theta$  is the subtended angle of an electrode. This effect enables both frequency tuning via adjustment of the voltage on tuning electrodes (green in Fig. 7.2) producing the typical tuning response shown in Fig. 7.3(a), as well as a simple FSK modulation of the steady-state oscillation to be discussed.

To shut an array-composite off, its  $V_P$  is simply set to zero.

### 7.1.2 Oscillator Design and Limiting

Upon connection of the I/O electrodes of two or more Fig. 7.2-like array-composites to a suitable sustaining amplifier, oscillation ensues for those devices given sufficiently large dc-bias voltages  $V_P$ 's. Whether or not the  $V_P$  is large enough depends on the relative magnitude of the resulting motional resistance  $R_x$  of the array-composite in question versus the effective transresistance gain  $R_{amp}$  of the sustaining amplifier. If  $R_{amp} > R_x$ , oscillations start up and continue to grow until some form of nonlinearity reduces the loop gain to 1, at which point growth stops and steady-state oscillation ensues with a constant amplitude. In the vast majority of cases, including quartz crystal oscillators, electronic amplifier nonlinearity is responsible for limiting. However, unlike macroscopic resonators, the MEMS-based frequency setting element in the present oscillator can actually go nonlinear before the amplifier, at which point it ends up limiting the steady-state oscillation amplitude. Whether or not this happens depends upon the type and linearity of the amplifier itself.

### Amplifier Limiting

Among MEMS-based oscillator types, series resonant and Pierce topologies have been most popular and successful. Series resonant oscillators often employ TransImpedance Amplifiers (TIA's) [52], such as shown in Fig. 3.7, that amplify an input current to an output voltage by a gain factor set by the value of resistance simulated by the shunt-shunt feedback transistor  $M_{RF}$ . While the ability of this topology to cancel common-mode noise is beneficial [13], it exhibits stronger nonlinearity than alternative circuits, because: 1) it uses three stacked transistors between the supply and ground, which sacrifices output voltage swing; and 2) the resistance of the feedback transistor  $M_{RF}$  can vary significantly as the output voltage changes. As a result, a TIA-based series resonant oscillator generally limits oscillation at amplitudes smaller than required to incite sufficient resonator nonlinearity, i.e., the amplifier limits the oscillation, not the resonator.

Conversely, the simpler Pierce topology [62] of Fig. 7.1 allows larger output swings, as it has only two stacked transistors between the supply and ground and does not employ feedback. By staying linear under larger voltage swings, a Pierce topology makes possible the resonator-limited operation needed to achieve a multi-oscillator.

### Resonator Limiting

The disk resonator nonlinearity responsible for limiting oscillator amplitude generally manifests as a combination of stiffness nonlinearity that generates the well-known Duffing response [65]; and damping nonlinearity that increases resonator loss at large displacement amplitudes. In MEMS-based resonators, Duffing nonlinearity appears as either a hardening nonlinearity typically caused by stress, where the frequency response bends forwards, i.e., towards higher frequencies; or a softening nonlinearity, caused in capacitive-gap transduced resonators by higher-order components of electrical stiffness that bend the frequency response backwards, i.e., towards lower frequencies.

For the tiny-gap disks of this work, the softening nonlinearity dominates. Pursuant to modeling this nonlinearity, the differential equation governing resonator motion is

$$\begin{aligned} m_{mre} \frac{\partial^2 x}{\partial t^2} + (\gamma_0 + \eta x^2) \frac{\partial x}{\partial t} + kx + k_1 x^2 + k_2 x^3 \\ = \frac{\alpha C_o}{2d_o} V_{PG} v_{IN} \cos(\omega t) = F_\omega \cos(\omega t) \end{aligned} \quad (7.3)$$

where  $F_\omega$  is the magnitude of the drive force acting on the resonator,  $k_1$  and  $k_2$  model the softening nonlinearity derived from capacitive-gap interactions,  $\eta$  is an empirically-determined term describing non-linear damping [66], and

$$k = k_{mre} - 2k_e; \quad k_1 = \frac{6k_e}{2d_o}; \quad k_2 = -\frac{4k_e}{d_o^2}; \quad \gamma_0 = \frac{\omega_o m_{mre}}{Q} \quad (7.4)$$

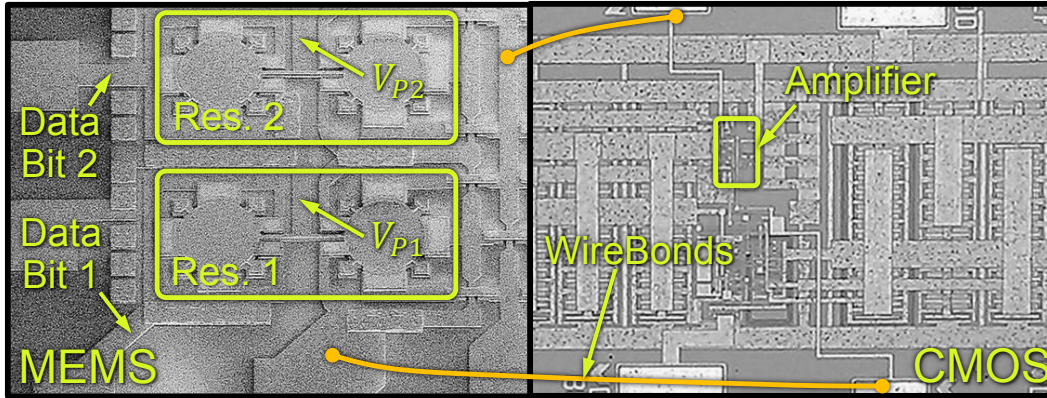


Figure 7.4: SEMs of the fabricated MEMS circuit and die photo of the custom-made CMOS amplifier IC. Wirebond connections shown in orange.

where  $Q$  is the resonator's unloaded quality factor, and  $\omega_o = \sqrt{(k/m_{mre})}$ . Using the perturbation method of [66], this nonlinear system yields an approximate displacement amplitude as a function of frequency given by

$$X_0 = \frac{F_\omega/m_{mre}}{\sqrt{(\omega^2 - \omega_o'^2)^2 + (\omega\omega_o'/Q')^2}} \quad (7.5)$$

$$Q' = \frac{2\omega_o m_{mre}}{2\gamma_0 + \eta X_0^2}; \quad \omega_o' = \omega_o + \kappa \cdot X_0^2; \quad \kappa = \left[ \frac{3k_2}{8k} - \frac{5k_1^2}{12k^2} \right] \omega_o$$

Equation (7.5) captures the drive amplitude-induced bending and peak lowering of the frequency response responsible for oscillator amplitude limiting.

### 7.1.3 Experimental Results

Pursuant to demonstrating a multi-frequency oscillator and FSK-generator, two-disk array-composites like that of Fig. 7.2 were designed to operate around 61 MHz and fabricated using a planarized process with 3- $\mu\text{m}$  thick polysilicon interconnects as described in Section 4.2 to achieve the final cross-section shown in Fig. 4.2. Here,  $\text{POCl}_3$ -doped polysilicon deposited via low-pressure chemical-vapor deposition (LPCVD) at 615  $^\circ\text{C}$  provided all resonator structure, electrode, and electrical interconnect material. A high-temperature oxide (HTO) sidewall sacrificial deposition defined the 50-nm resonator-to-electrode gaps. Structures were released in 49% HF to yield the final test devices.

Amplifier ICs were designed and fabricated using a 0.35  $\mu\text{m}$  CMOS technology. To construct a complete multi-frequency oscillator, wire bonds connect released two-disk array-composites with the CMOS ASIC shown in Fig. 7.4, both of which are then mounted on a circuit board to provide needed bias and signal voltages.

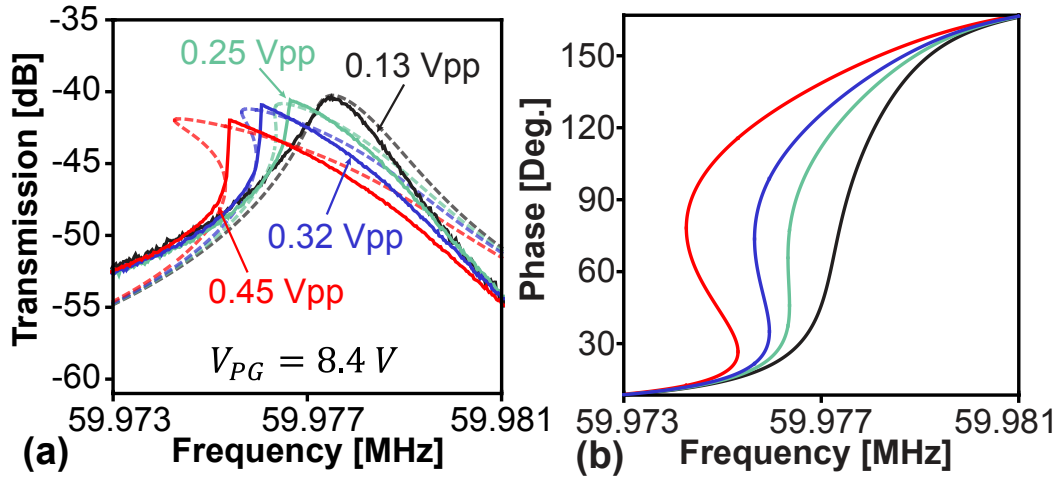


Figure 7.5: (a) Measured (solid lines) and theoretical (dashed lines) spring softening and damping nonlinear response as a function of increasing drive voltage. (b) The phase response for a modeled resonator at the same frequency and drive levels as the experimental data.

Table 7.1: Design and extracted parameters of the fabricated MEMS array-composite.

$Q$	40k	$\alpha$	0.787	$k_{mre}[\text{N/m}]$	$1.61 \times 10^6$
$d_0[\text{nm}]$	50	$m_{mre}[\text{pg}]$	11.33	$k_e[\text{N/m}]$	$9.73 \times 10^2$
$V_{PG}[\text{V}]$	8.4	$\gamma_0[\text{N.s/m}]$	$1.07 \times 10^{-7}$	$k_1[\text{N/m}^2]$	$5.84 \times 10^{10}$
$C_o[\text{fF}]$	55.66	$\eta[\text{N.s/m}^3]$	$4 \times 10^8$	$k_2[\text{N/m}^3]$	$-1.56 \times 10^{18}$

Figure 7.3(b) presents the frequency response of a two-disk array-composite under 10 V dc-bias and in vacuum. Figure 7.5(a) presents the measured (solid lines) and theoretical (dotted lines, using Eqn. (7.5)) the frequency response behavior of a single such disk with increasing drive voltage measured with forward going frequency, showing both spring softening (generating the saw-tooth shape) and damping (causing a decrease in peak height) nonlinearities. Again, the latter damping nonlinearity limits the oscillation amplitude. Here, the model can be seen to closely match measurement, verifying that capacitive-gap derived phenomena govern the stiffness non-linearity and that significant amplitude-limiting loss manifests when the drive voltage surpasses  $\sim 130$  mVpp. Figure 7.5(b) additionally shows the theoretical phase response of the device when it is driven by the voltage amplitudes shown in Fig. 7.5(a).

Figure 7.6(a,b) present measured output spectra from a Pierce-based multi-oscillator like that of Fig. 7.1, where application or removal of  $V_P$ 's  $\sim 10$  V on/off switch the MEMS array-composites sequentially. Figure 7.6(c) and 7.7 demonstrate operation with bias applied to both resonators, showing two simultaneous oscillation frequencies, each indepen-

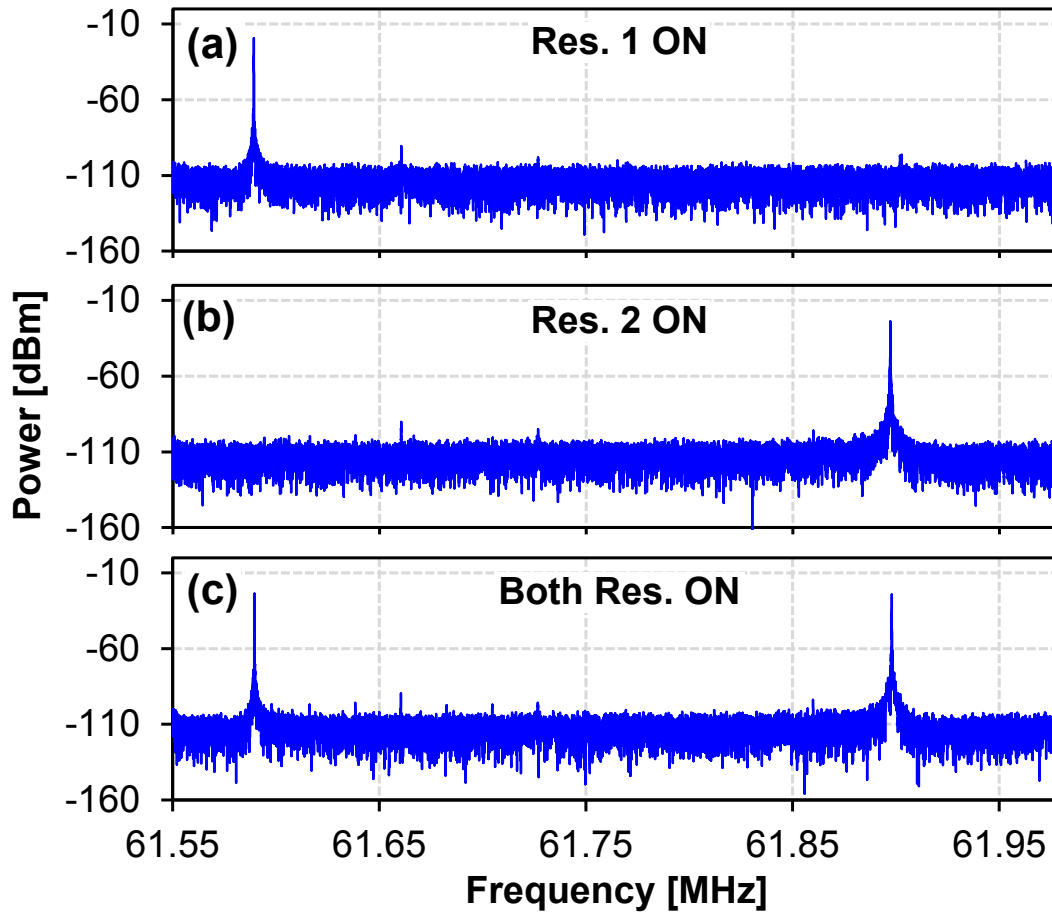


Figure 7.6: Pierce oscillator output spectra measured on an Agilent N9030A spectrum analyzer. (a) shows oscillator output with resonator 1 turned on via an applied bias of 9.35 V, (b) with 11.6 V applied to resonator 2, and (c) simultaneous oscillation with bias voltages applied to both.

dently amplitude-limited as expected when using the linear sustaining amplifier of a Pierce oscillators. Here, the ASIC operates off a 2.8 V supply drawing  $\sim 49 \mu\text{A}$ . To verify the need for MEMS-based amplitude limiting, Fig. 7.8 presents the output of another such oscillator built instead using the TIA of Fig. 3.7 designed to limit at drive amplitudes above 10 mVpp. Unlike the Pierce design, when both resonators are “on”, one of them grows in amplitude faster than the other and causes amplifier-induced (rather than resonator-induced) limiting, desensitizing the amplifier to other frequencies, and making it impossible to achieve the desired multi-frequency output.

Finally, to gauge the efficacy of this mechanical circuit as a multi-channel transmitter, Fig. 7.9 presents the output with one oscillator active with a binary FSK input signal applied to the tuning electrode of its array-composite. This realizes electrical stiffness-induced

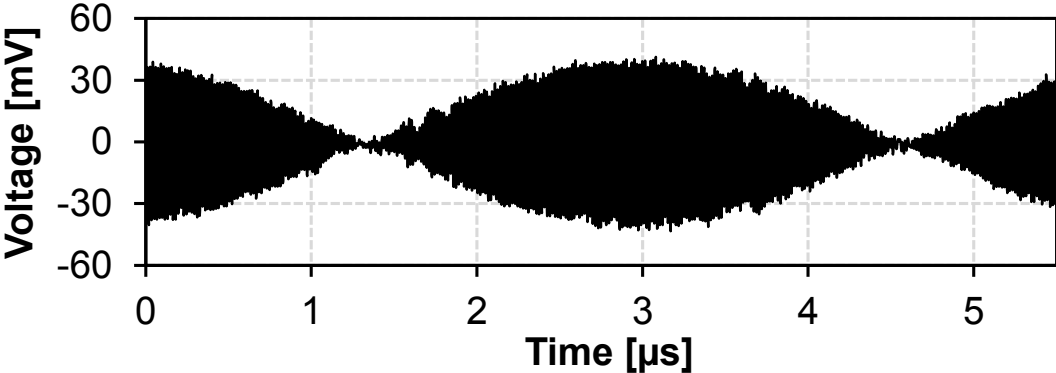


Figure 7.7: Measured oscillator output waveform of the Pierce-based circuit with two resonators active.

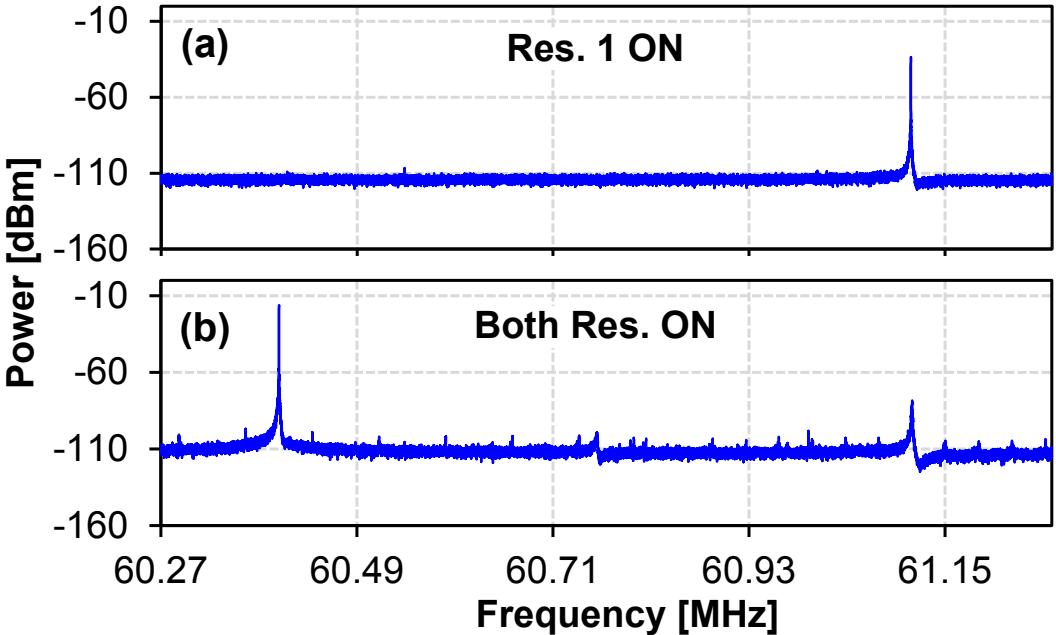


Figure 7.8: TIA-based oscillator output spectra with (a) one resonator turned on and (b) both resonators on and loop gain increased by  $\sim 30\%$  in an attempt to produce simultaneous oscillation. Oscillation at one frequency desensitizes the TIA, suppressing output at the other.

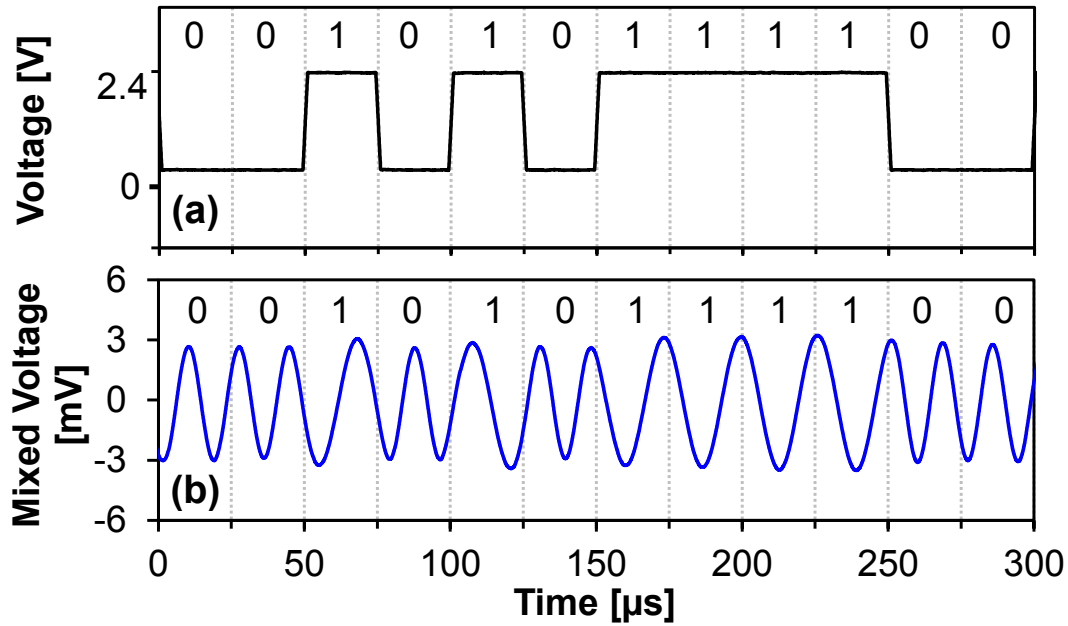


Figure 7.9: Applying the 40 kbps modulation bit stream of (a) to the tuning electrodes on one disk array-composite generates the measured FSK modulated waveform of (b), shown mixed down to  $\sim 20$  kHz to facilitate visualization.

switching of the oscillator frequency, thereby producing the fast-response, continuous-phase FSK modulation shown, at a minimum-shift keyed bitrate of 40 kbps. The multi-frequency oscillator in this work is the first of its kind to generate simultaneous oscillation outputs around 61 MHz using capacitive-gap MEMS resonator array-composites while employing only a single amplifier. This MEMS-based circuit provides not only independently switchable and tunable oscillation outputs at multiple frequencies, but also a multi-channel FSK transmitter, all in a power- and space-saving package.

## 7.2 Active $Q$ -Control for Improved Insertion Loss Micromechanical Filters

Among components in a typical radio receiver, the front-end filters play a pivotal role in reducing power consumption. In particular, by removing unwanted blockers before they reach front-end electronics, these filters allow said electronics to operate with substantially lower dynamic range than would otherwise be needed, hence, substantially lower power consumption. If possible, a capability to select single channels out of a band would allow removal of not only out-of-band interferers, but also in-band ones. This would then provide reduction in power consumption. Unfortunately, the resonator  $Q$  required for such a channel-selecting filter is quite daunting. For example, a 400-kHz bandwidth filter designed to select a single 200-kHz wide GSM-850 channel (and reject all others) would need constituent resonators with  $Q$ 's greater than 15,000 to maintain less than 2 dB of insertion loss (I.L) [24]. Along similar lines, sensor network nodes with much smaller data transfer needs might benefit from even smaller channel bandwidths, on the order of only a few kHz, which at 433 MHz would represent only 0.002% bandwidth, for which resonator  $Q$ 's on the order of 370,000 would be required!

To achieve such  $Q$ 's for filters, this work explores the use of active positive feedback to boost the  $Q$ 's of the constituent passive resonators in a parallel-class filter and thereby make possible sub-0.01% bandwidth and its associated radio power savings for sensor network nodes [25]. Specifically, the use of active feedback in closed-loop with two electrodes of a four-electrode capacitive-gap transduced Wine-Glass disk resonator has enabled boosting of the effective resonator  $Q$  and independent control of insertion loss across the two other electrodes. As a first demonstration of the capability of this approach, two such  $Q$ -boosted resonators wired in the parallel-type micromechanical filter [67] of Fig. 7.10, achieve a tiny 0.001% bandwidth passband centered around 61 MHz with only 2.7 dB of insertion loss something not possible with the intrinsic resonator  $Q$  of 60,000, but quite possible with  $Q$ 's actively boosted to 670,000. Unlike past efforts [27], [28] operating at kHz-frequencies, the split electrode design used here removes the amplifier feedback loop from the signal path allowing independent control of input-output coupling,  $Q$ , and frequency.

### 7.2.1 $Q$ and Insertion Loss Adjustable Resonator

Figure 7.11 presents details of the  $Q$ -boosted resonator sub-circuit used twice in the filter circuit of Fig. 7.10. This sub-circuit essentially combines a Wine-Glass disk resonator with a gain and phase-controllable Trans-Impedance Amplifier (TIA). The Wine-Glass disk comprises a 2  $\mu\text{m}$ -thick, 32  $\mu\text{m}$ -radius polysilicon disk supported at quasi nodal points by four beams and surrounded by electrodes spaced only 65 nm from its edges. Chapter 2 details the resonator design. Once vibration ensues, voltages across the electrode-to-resonator gaps generate currents that then serve as electrical input/output (I/O) signals at ports 1 and 2 respectively; and as feedback control signals at ports 3 and 4 conditioned by the TIA

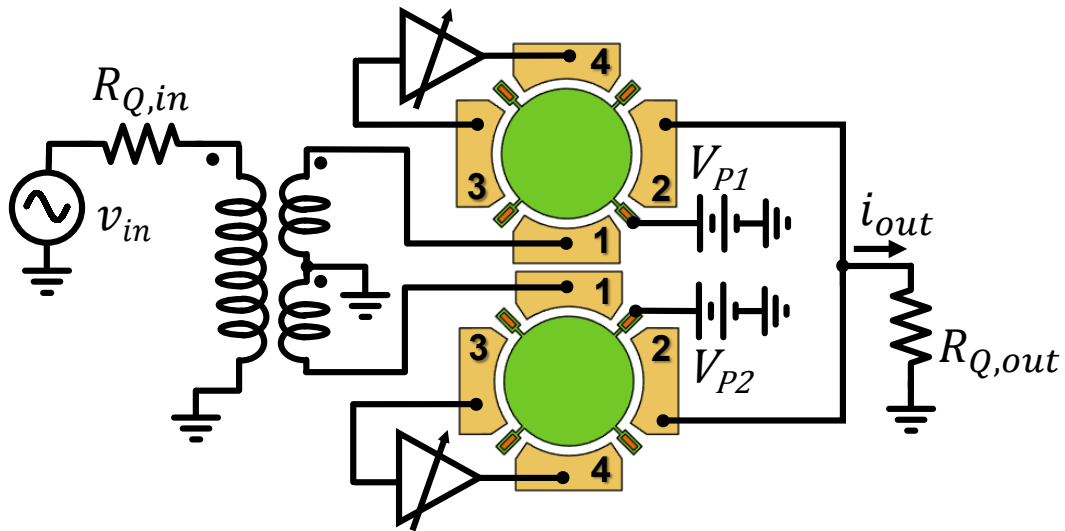


Figure 7.10:  $Q$ -boosted parallel filter comprised of two independent Wine-Glass disk resonator and amplifier circuits, all in a typical measurement circuit. Here, the filter input is driven differentially while output currents are combined to generate the response of Fig. 7.14.

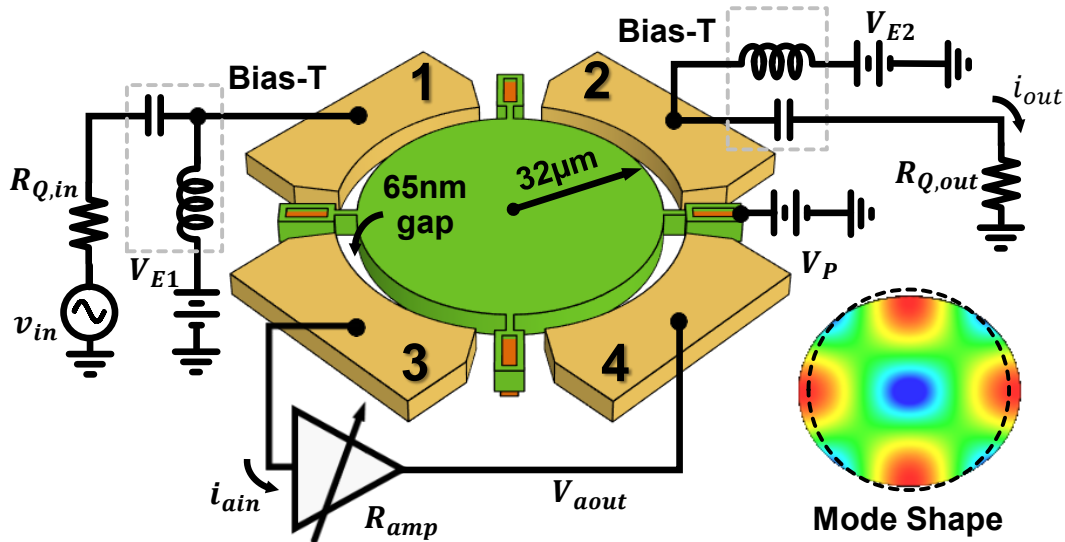


Figure 7.11: Circuit schematic of an active  $Q$ -controlled resonator. A transimpedance amplifier provides closed-loop feedback using two electrodes of a Wine-Glass resonator, while the remaining two electrodes serve as input/output.

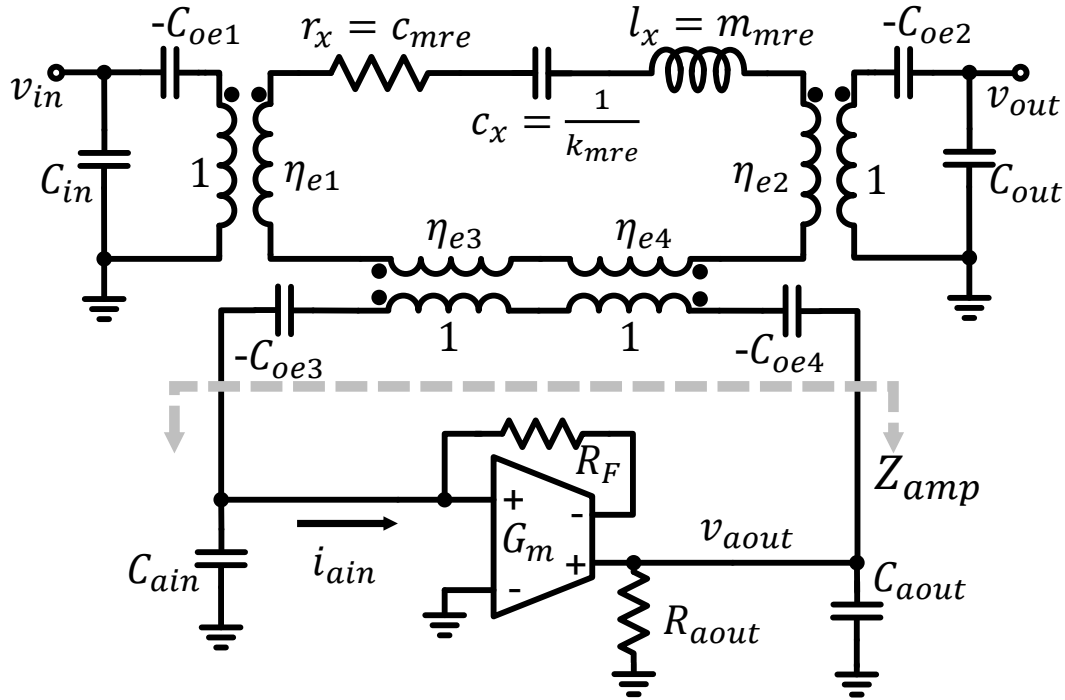


Figure 7.12: Equivalent small signal circuit model for the  $Q$  and insertion loss adjustable resonator of Fig. 7.11, with electrodes 1-2 used for input and output and electrodes 3-4 embedded in a feedback loop with the amplifier to enable control of  $Q$ .

connected to these ports.

In the hookup of Fig. 7.11, the transresistance gain of the TIA adds or subtracts from the damping of the resonator to yield a total effective damping (and thus,  $Q$ ) controllable up or down via the gain and phase of the TIA. If the TIA gain and phase are configured to realize positive feedback with loop gain less than unity, then from I/O terminals 1 and 2 the device looks like an electrical resonator sporting a bandpass biquad transfer function like any other electrical resonator, except with extremely high  $Q$  on the order of millions. As such, its small-signal circuit model derives principally from a core  $LCR$  tank.

### Resonator-Amplifier Electrical Model

To help quantify the  $Q$  attainable, Fig. 7.12 shows the complete small signal model of the Fig. 7.11 hookup, using the multi-port negative capacitance resonator equivalent circuit from [35]. The small signal equivalent circuit shown in Fig. 7.11 is the same as in Fig. 2.2(a) except redraw it in a way to facilitate the analysis. Here,  $C_{in}$ ,  $C_{out}$ ,  $C_{ain}$ , and  $C_{aout}$  represent capacitance derived from both intrinsic electrode-to-resonator capacitors; and from parasitic capacitors surrounding the resonator structure, e.g., from bond pads. In the resonator model,

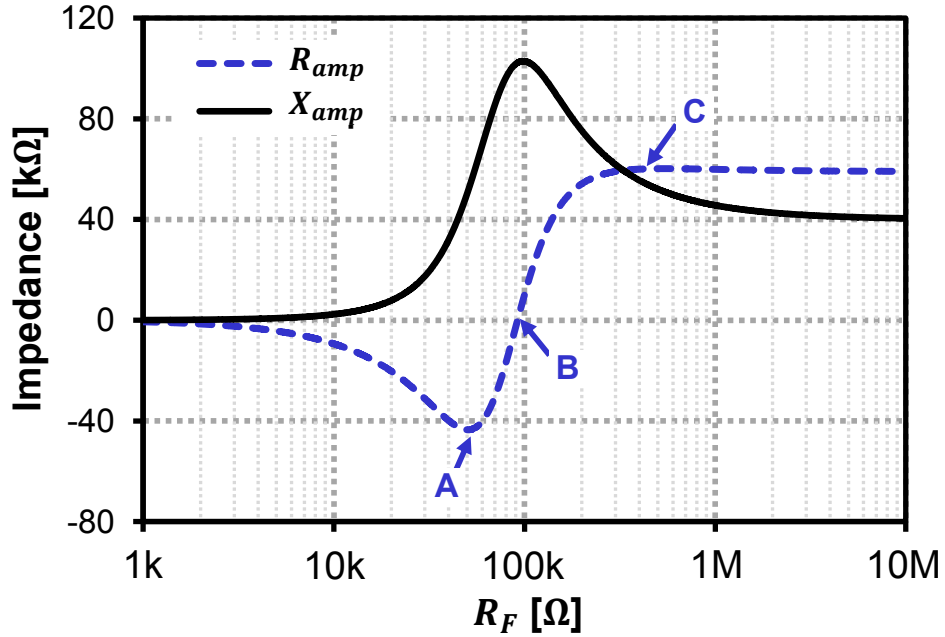


Figure 7.13: Theoretical prediction of resistance (dotted blue) and reactance (black) parts of the impedance,  $Z_{amp}$ , looking into the TIA amplifier as the feedback resistor,  $R_F$ , increases. Here, approximate resistance and capacitance values for the amplifier in this work are used for simulation.

the values of the core  $rlc$  are given in Equations (2.16) and (2.17).  $\eta_{e1}$  to  $\eta_{e4}$  and  $C_{oe1}$  to  $C_{oe2}$  are defined in Eqn. (2.19).

Although the circuit analysis here is the same as that in Section 3.3, the analysis is repeated here due to the subtle difference between the oscillator and the active- $Q$  boosted resonator system. Connecting a Trans-Impedance Amplifier (TIA) with transconductance  $G_m$  and output resistance  $R_{aout}$ , in negative shunt-shunt feedback through  $R_F$  gives a total impedance looking into the amplifier of

$$Z_{amp} = \frac{v_{aout}}{i_{ain}} = \frac{-R_F A_v \omega_{in} \omega_{out}}{s^2 + (\omega_{in} + \omega_{out})s + \omega_{in} \omega_{out} (1 + A_v)} \quad (7.6)$$

where

$$\omega_{in} = \frac{1}{R_F C_{ain}}; \quad \omega_{out} = \frac{1}{(R_F // R_{aout}) C_{aout}}; \quad A_v = G_m (R_F // R_{aout}) \quad (7.7)$$

Figure 7.13 plots  $Z_{amp}$ 's resistance,  $R_{amp}$ , and its reactance,  $X_{amp}$ , as the feedback resistor  $R_F$  of the TIA changes. Only the real (resistive) part of  $Z_{amp}$  influences the total effective damping of the resonator, which with this influence becomes

$$c_{eff} = c_{mre} + R_{amp} \eta_{e3} \eta_{e4} \quad (7.8)$$

The resultant effective  $Q$  then takes the form

$$Q_{eff} = \frac{k_{mre}}{\omega_o c_{eff}} \quad (7.9)$$

which is directly controllable (up or down) via  $R_F$ . Clearly,  $Q_{eff}$  is larger than the intrinsic  $Q$  of the device when  $R_{amp}$  is negative and  $Q_{eff}$  is smaller when  $R_{amp}$  is positive, and the transition occurs (point B in Fig. 7.13) when

$$R_F = \frac{G_m}{C_{in} C_{out} \omega_o^2} \quad (7.10)$$

The maximum  $Q_{eff}$  occurs at point A in Fig. 7.13, while the minimum occurs at point C. It is important to note that  $c_{eff}$  must be greater than zero for the system to be stable. This means that the loop gain,  $T$ , of the feedback loop must satisfy:

$$T = \frac{-R_{amp,min}}{R_{x34}} = \frac{-R_{amp,min}}{c_{mre}/\eta_{e3}\eta_{e4}} = 1 - \frac{Q_{int}}{Q_{eff}} < 1 \quad (7.11)$$

where  $R_{x34}$  is the motional impedance looking into electrodes 3 and 4, and  $Q_{int}$  is the intrinsic  $Q$  of the resonator. In practice, the loop gain  $T$  should not be too close to unity, lest some unexpected variation, e.g., noise, acceleration, bumps it past 1, after which oscillation ensues. Thus, stability considerations will likely limit the amount of  $Q$ -boost in practical design to less than 100 times.

### Amplifier-Derived Frequency-Pulling

During operation, the gap spacing between resonator and electrode changes, which in turn generates a changing electric field, and hence varying electrostatic force in the gap. In a small-signal model, this force is in phase and proportional to disk edge displacement, and thus meets the definition of stiffness. Popularly termed electrical stiffness, this “softens” the equivalent stiffness of the resonator resulting in a negative shift in the resonance frequency [26]. The resultant electrical stiffness generated from the gaps at electrodes 3-4 is:

$$k_{e34} = \eta_{e3}\eta_{e4} \left[ \frac{1}{C_{oe3}} + \frac{1}{C_{oe4}} + \omega_o X_{amp} \right] \quad (7.12)$$

which subtracts from the resonators mechanical stiffness to yield a resonance frequency given by

$$f_o = f_{nom} \sqrt{\left[ 1 - \frac{k_{e1} + k_{e2} + k_{e34}}{k_{mre}} \right]} \quad (7.13)$$

where  $k_{e1}$  and  $k_{e2}$  are the effective electrical stiffnesses from the gap at electrode 1 and 2, respectively.

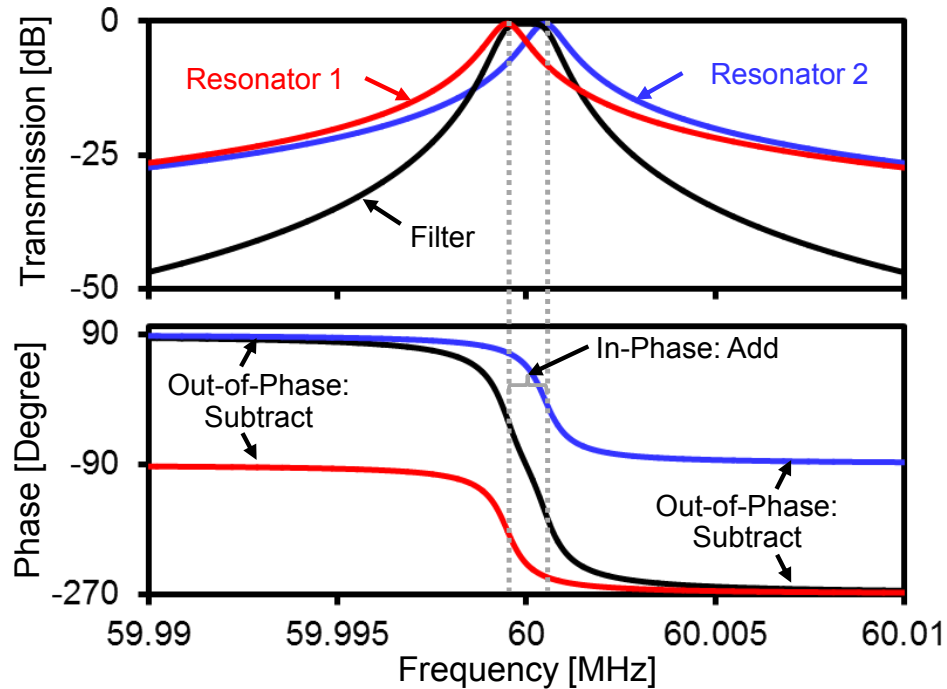


Figure 7.14: Description of parallel filter operation, where two differentially driven bandpass biquad responses add to form a flat passband (between the peaks) and subtract in the stopband (outside the peaks) to provide greater stopband rejection.

## 7.2.2 Active $Q$ -Boosted Filter Implementation

To create a filter response, the circuit of Fig. 7.10 combines into a parallel-class filter similar to that of [67]: two Fig. 7.11 electromechanical circuits with resonance frequencies spaced from one another by the desired passband bandwidth. A balun converts a single ended input at the left into a differential drive signal with plus end applied to one resonator input and minus to the other, so that each resonator receives oppositely phased inputs. The output terminals of each device are then tied together so that their output currents add.

This filter operates as illustrated in Fig. 7.14, which plots the individual resonator spectra together with the resulting filter spectrum. As shown, differential drive of the resonators produces a relative phase shift of approximately  $0^\circ$  between the resonator peaks, which allows their outputs to add to form a flat filter passband between these peaks. Meanwhile, outside the passband the resonators vibrate  $180^\circ$  out-of-phase, giving rise to subtraction that steepens the roll-off to the stopband.

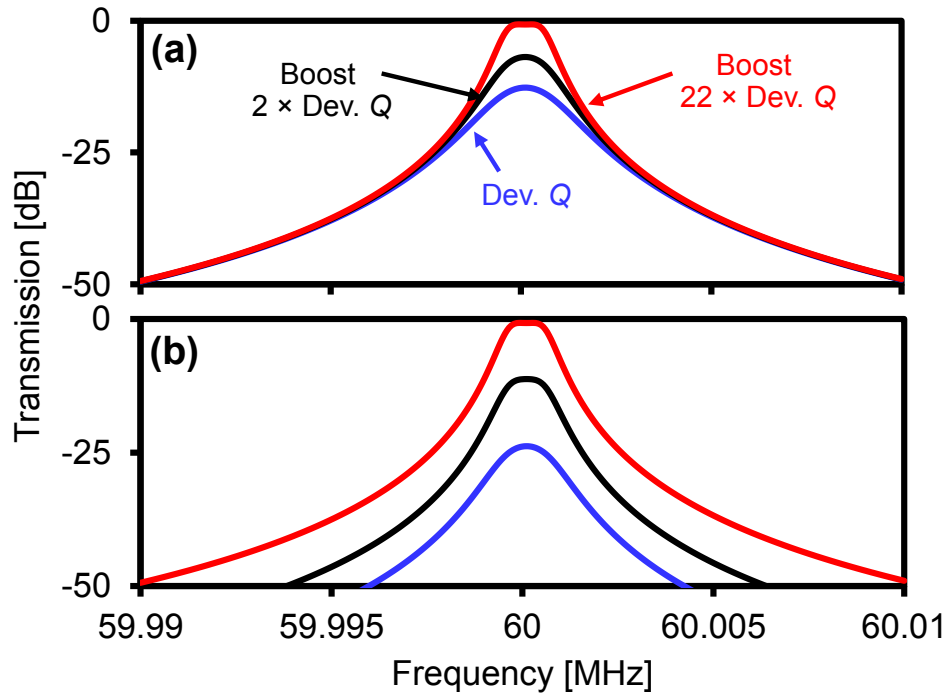


Figure 7.15: Simulated parallel filter responses for a narrow 0.002% bandwidth filter with low  $Q$  (intrinsic device's  $Q$ ) equivalent to  $1.36 \times BW_{fil}$  (blue),  $Q$ -boosted by two times (black), and  $Q$ -boosted by 22 times (red). (a) shows responses for constant  $R_Q$  (its value is the needed  $R_Q$  for highest  $Q$  case) and  $IL$  improvement of 12 dB. (b) illustrates that the filter can be terminated properly by adjusting the bias voltage across input and output gaps while  $R_Q$  is kept constant. Boosting  $Q$  by 22 times improves  $IL$  by 23 dB. Note that the  $Q$  equivalent to  $1.36 \times BW_{fil}$  (blue case) is too small for the filter to be terminated properly.

### Adjustable Dynamic Range

As with any bandpass filter, the higher the  $Q$  of the constituent resonators, the lower the insertion loss. This means the insertion loss of the filter should be fully controllable by merely adjusting the gain of the  $Q$ -controlling amplifiers placed in feedback between terminals 3 and 4 of each resonator. Doing so when simulating the Fig. 7.10 equivalent circuit for a 60-MHz, 0.002%-bandwidth two-resonator filter for a constant termination impedance, without adjusting dc-bias to re-match the terminations, yields the curves of Fig. 7.15(a), which clearly show the dependence of insertion loss on  $Q$ -controlling amplifier gain. In effect, active  $Q$ -control not only makes possible low insertion loss even for 0.002% bandwidth filters that would not be feasible otherwise; but also enables variable gain filters, as opposed to the variable gain LNA's commonly used in RF front-ends.

The curves in Fig. 7.15(a) lose their passband shape as  $Q$  is lowered, mainly because the motional resistance of the constituent resonators changes with their  $Q$ , so the  $R_Q$ 's no

longer present the needed termination. To remedy this, the electrode-to-resonator dc-bias voltages  $V_{PE1}$  and  $V_{PE2}$  can be adjusted to compensate, which then yields the curves of Fig. 7.15(b), where the filter frequency response retains its shape as insertion loss increases.

The ability to tune insertion loss essentially amounts to an ability to adjust dynamic range. In particular, if the input to the filter receives a signal hot enough to drive it into nonlinear behavior, one need only tune the  $Q$ -controlling amplifier gain to increase insertion loss, thereby allowing reception of the signal without desensitization. In effect, this adjustable insertion loss provides an effective bias shift for dynamic range—a very useful function for any transceiver front-end.

### Power Consumption Considerations

The use of active circuits in an otherwise passive filter implementation does introduce power consumption, where there was none before. The extra active circuits are justified only if their presence offers performance benefits beyond what might be achieved by raising power consumption elsewhere in the system, e.g., in the LNA and/or IF channel-select filter (if realized using transistors). In fact, a typical LNA power consumption is on the order of 5 mW [68], which is needed mainly to insure adequate noise figure. Recent developments in passive transformer coupled front-ends have successfully reduced the power consumption in the LNA and mixer close to zero, but due to the lack of RF channel-select filtering in traditional technologies, power on the order of 10 mW is still needed to maintain adequate linearity in the active IF channel-select filter [69].

Meanwhile, the power required for the active circuits in the  $Q$ -boosting loop of Fig. 7.11 can be sub-100  $\mu$ W [45], [62], making the  $Q$ -boosted MEMS approach more desirable. This point amplifies with the recognition that the loss of an RF front-end filter directly adds to the noise figure of a receiver, so lowering RF filter insertion loss by several dB is often a better investment of consumed power than lowering the noise figure of an LNA by a smaller dB number.

### 7.2.3 Experimental Results

To experimentally verify the utility of active  $Q$ -boosting, Wine-Glass disks were designed and fabricated using the planarized process with 500-nm thick interconnects as described in Section 4.2. Here, doped polysilicon serves as the structural material for resonator and electrodes, alike, and the gaps between them were set to 65 nm by a sacrificial high-temperature oxide spacer that is removed in the final release step. With a radius of 32  $\mu$ m, electrode-to-resonator gap spacing of 65 nm, and dc-bias voltage  $V_P$  of 10 V, this fabricated device provides a coupling strength of  $(C_x/C_o) \sim 0.04\%$  at an operating frequency of 61 MHz, sufficient for the 0.001% bandwidth filter demonstrated here.

Figure 7.16 presents measured electrical transmission plots for a 50  $\Omega$ -terminated single disk in a  $Q$ -controlling hookup (*cf.* Fig. 7.11) as a function of TIA gain and phase shift. Here, insertion loss and  $Q$  are quite tunable, with effective  $Q$  adjustable anywhere from 24k

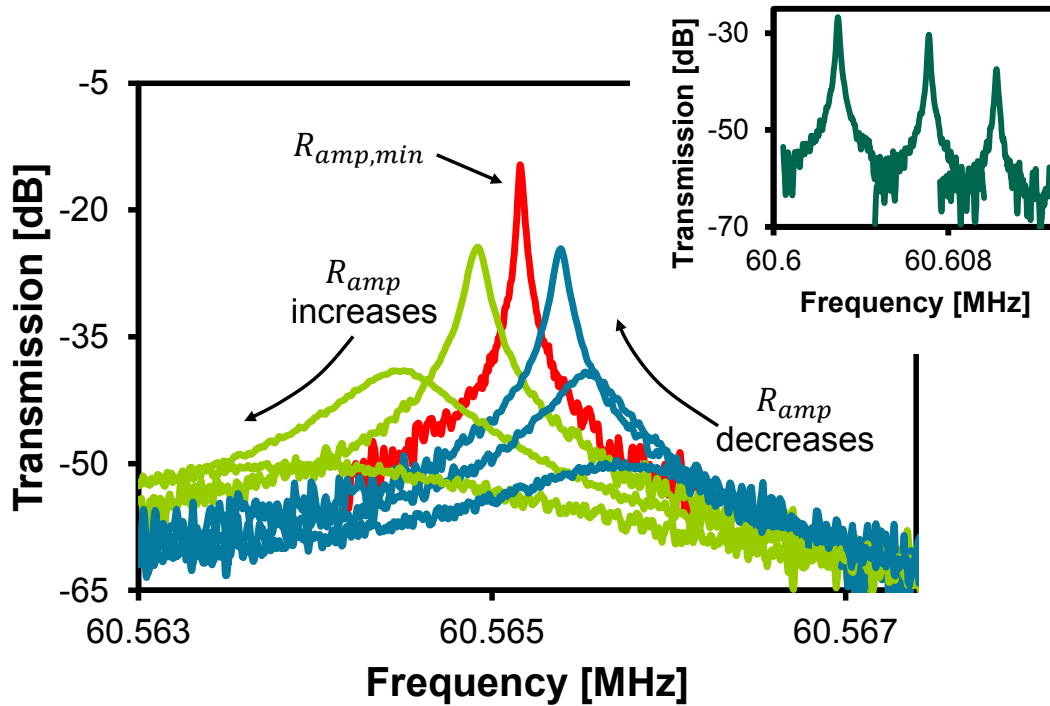


Figure 7.16: Single resonator  $Q$ -boosting as a function of amplifier gain with constant  $V_P = 8.5$  V. As  $V_{GAIN}$  is decreased amplifier gain increases, boosting effective resonator  $Q$  (blue curves) from an initial intrinsic  $Q=57,000$  to a maximum boosted  $Q$  of 2.3 million (red). On the other hand, decreasing  $V_{GAIN}$  further allows control of amplifier phase shift, leading to negative feedback and allowing controlled loading of  $Q$  (green curves). The inset demonstrates independent tuning of frequency and insertion loss via control of the voltage across input-output electrode-disk gap, all while holding  $Q$  constant by holding  $V_{GAIN}$  constant.

to 2.3M. Even operating at the maximum boosted  $Q$  of 2.3M, the active resonator remained stable for hours of measurement time with no evidence of oscillation, likely a result of compact implementation made possible by die-level ASIC and MEMS resonator connections. Figure 7.16 also confirms that the resonance frequency shifts to the left with decreasing  $V_{GAIN}$ , as predicted by Eqn. (7.13). The inset figure further demonstrates insertion loss tuning while maintaining constant  $Q$  (by keeping  $V_{GAIN}$  constant) via independent tuning of the input-output electrode to disk bias voltage, i.e., tuning  $V_{E1}$  and  $V_{E2}$ .

To verify the theoretical predictions of Fig. 7.13, Fig. 7.17 additionally demonstrates the  $Q$  enhancement and subsequent improvement in insertion loss when measured with  $50 \Omega$  terminations as a function of  $V_{GAIN}$  applied to the amplifier. As  $V_{GAIN}$  decreases, the shunt-shunt feedback resistance  $R_F$  in the TIA increases. As depicted in Fig. 7.13, with increasing  $R_F$ ,  $R_{amp}$  (initially a negative value and hence boosting  $Q$ ) decreases to a minimum value

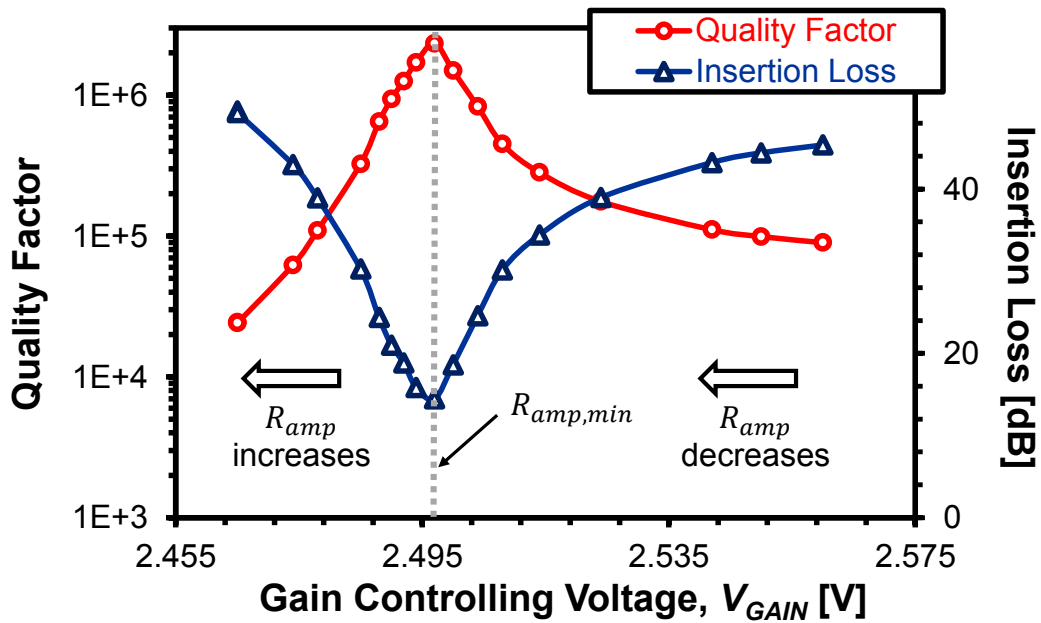


Figure 7.17: Measured effective quality factor (red) and insertion loss (blue) of the resonator with constant  $V_P = 8.5 \text{ V}$  as  $V_{GAIN}$  of the amplifier changes.

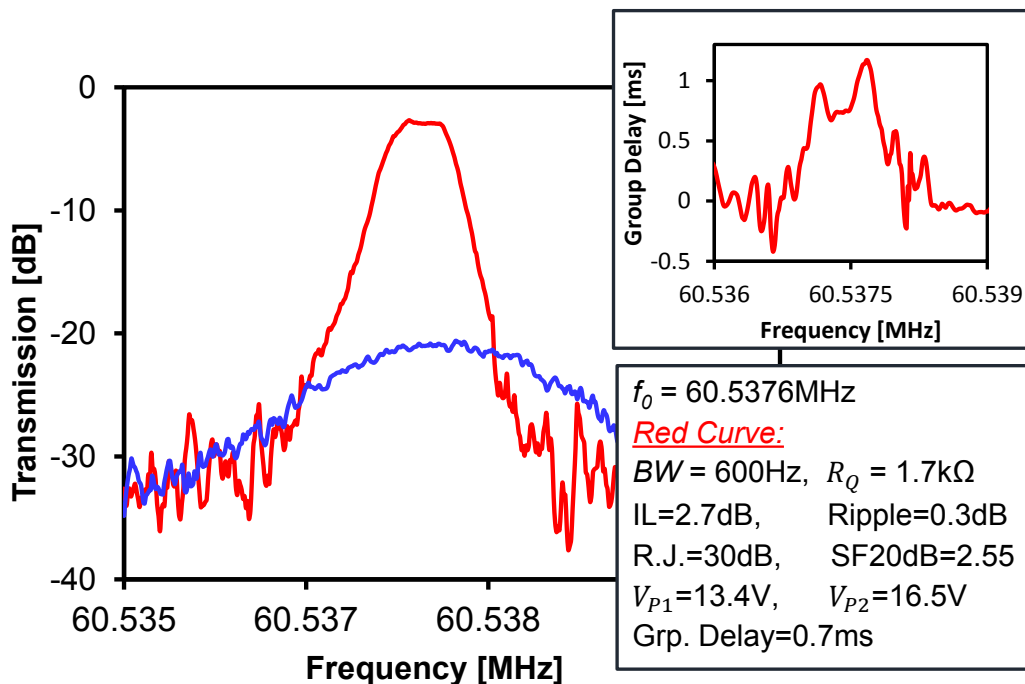


Figure 7.18: Measured transmission for a two-resonator filter hooked up as in Fig. 7.10 and terminated by the designed (i.e., required) value of  $1.7 \text{ k}\Omega$  at both input and output for the cases with (red) and without (blue)  $Q$ -boosting TIA's.

for the maximum  $Q$  of 2.3M and the maximum loop gain of 0.975. Decreasing  $V_{GAIN}$  further decreases  $Q$  (or increases  $R_{amp}$ ) until it becomes smaller than devices' intrinsic  $Q$  at which point  $R_{amp}$  is greater than zero.

Figure 7.18 finally presents the measured transmission for a two-resonator parallel filter hooked up as in Fig. 7.10 and terminated by the designed (i.e., required) value of 1.7 k $\Omega$  at input and output for the cases with and without  $Q$ -boosting TIA's. As expected, the insertion loss is a dismal 21 dB without  $Q$ -boosting of the constituent resonators; compared with only 2.7 dB when the TIA's boost  $Q$ 's. Indeed, 2.7 dB is quite impressive for a percent bandwidth this small.

On the other hand, the stopband rejection of only 30 dB seen in Fig. 7.18 is less than expected. The insufficient stopband rejection actually derives from the measurement apparatus and scheme, not the device itself. In particular, the current measurement simulates the needed filter terminations using network analyzer-based load simulation, rather than a real 1.7 k $\Omega$  termination impedance, and this compromises the noise floor of the instrument. An improved measurement effort using real terminations is expected to greatly improve the noise floor of the measurement, and thus significantly increase the measurement noise-limited rejection currently seen.

# Chapter 8

## Super-Regenerative Transceiver

### 8.1 Background

The field of RF-MEMS has thus far improved many aspects of wireless communication, with commercially available products ranging from on-chip MEMS devices providing compact and low phase-noise reference oscillators [2], [62], to band-selecting RF front-end duplexers [3]. Greater potential remains, however, if the high quality factor and CAD-definable frequency possible in capacitive-gap MEMS can be harnessed to achieve a true channel-selection scheme. Combined the low-power operation shown in Chapter 5 with the regenerative amplification in an oscillator loop, this chapter presents a FSK super-regenerative transceiver targeted for low-power applications. Such electromechanical circuit comprising a capacitive-gap RF MEMS resonator (*cf.* Fig. 8.1) embedded in a positive feedback loop with an Application-Specific Integrated Circuit (ASIC) Trans-Impedance Amplifier (TIA) has demonstrated a fully-functional MEMS-based tunable RF channel-selecting radio transceiver employing a super-regenerative reception scheme. Unlike previous super-regenerative receivers [23], [29], this rendition harnesses the high  $Q$  filtering and voltage-controlled frequency tuning [26] of its capacitive-gap transduced disk resonator to enable selection of 1-kHz-wide RF channels across a 80-kHz range, as in Fig. 8.1(c,d). Furthermore, the split electrode resonator design made possible here isolates the loop amplifier from the antenna, greatly relaxing circuit linearity requirements and eliminating the need for an isolation amplifier, thus saving considerable power.

This electrical stiffness-based tuning additionally allows the same MEMS-ASIC system to operate as an FSK transmitter, enabling a complete transceiver in one simple device. Operated as a closed-loop oscillator with FSK modulation enabled via an applied voltage on the MEMS input electrodes, this transmitter offers direct carrier generation at the RF frequency of interest without the power-hungry complexity of previous PLL-based MEMS transmitters [70].

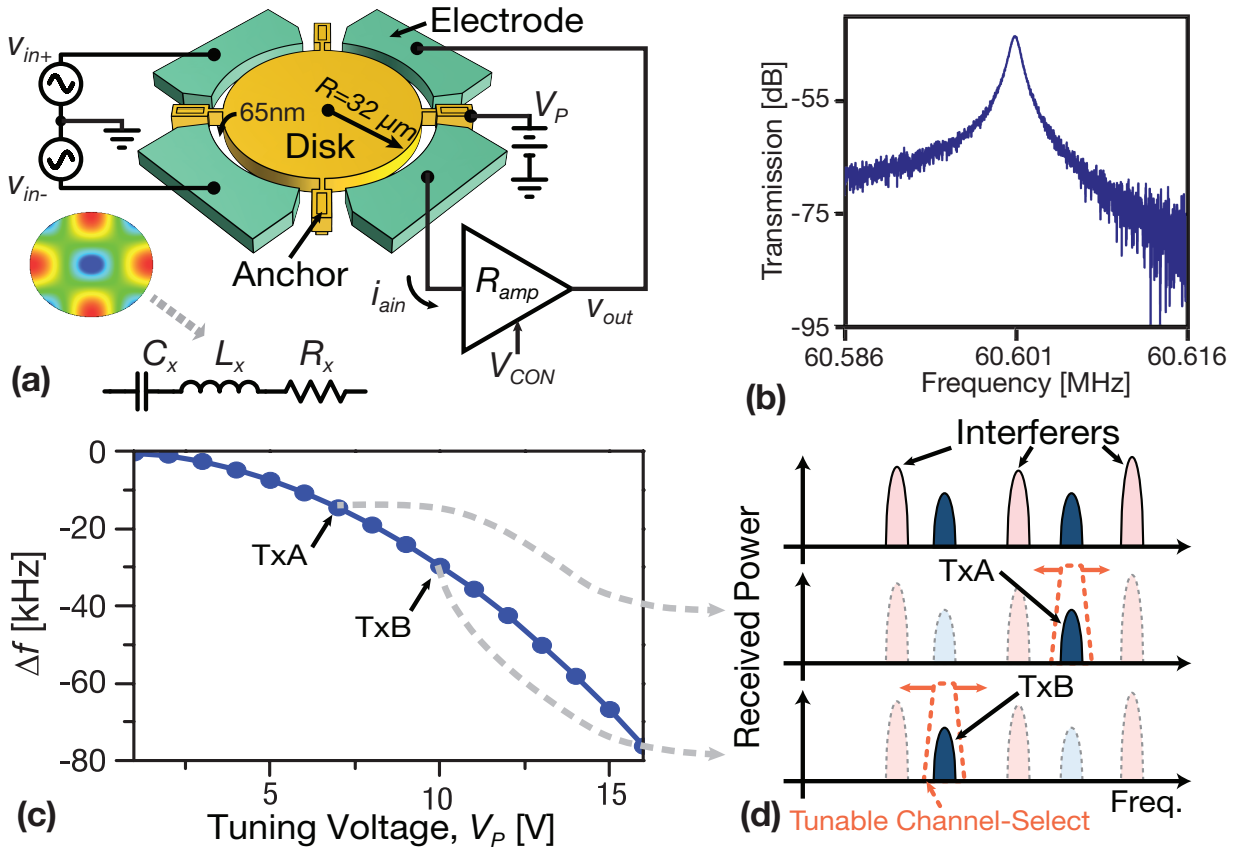


Figure 8.1: Perspective-view schematic (a) of the micromechanical disk resonator circuit used in this work. (b) presents the high  $Q \sim 100,000$  resonator frequency response, which may be tuned as in (c) via negative electrical stiffness with applied voltage to select one of several communication channels as illustrated in (d).

## 8.2 The Regenerative Transceiver

Figure 8.2 presents the system-level design used for the super-regenerative receiver in this work, while Fig. 8.3 illustrates typical operation. This super-regenerative system identifies an incoming ‘1’ or ‘0’ by measuring the rate at which oscillation grows in a positive feedback circuit. In this rendition, the absence of received antenna signal power in the resonance passband results in a slow rise in oscillation amplitude, which indicates a ‘0’. On the other hand, with received power on resonance, signal couples into the positive feedback loop, speeding up rise time to indicate a ‘1’. Operated in such a fashion, this regenerative receiver forms a Binary Frequency-Shift Keying (BFSK) demodulator, where the FSK ‘mark’ and ‘space’ correspond to on and off-resonance signals, respectively.

To generate a stream of received bits, a periodic quench signal  $V_{CON}$  restarts oscillation,

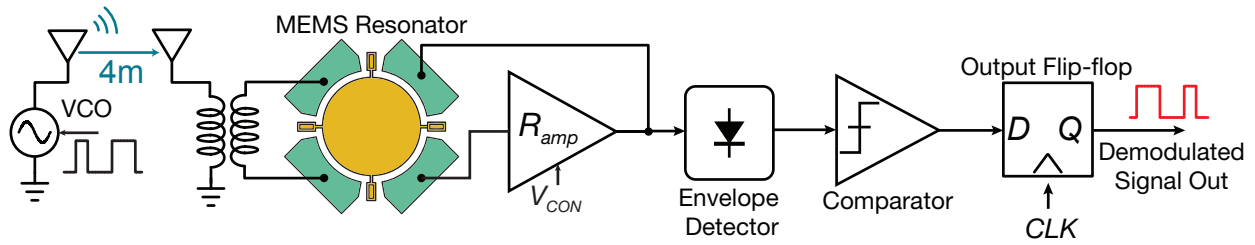


Figure 8.2: Schematic of the regenerative MEMS radio transceiver configured in receive-mode. Here, the MEMS resonator applies the needed channel-selecting filter to RF signals picked up by the antenna. The ASIC amplifier regeneratively amplifies this weak received in-band signal to produce a growing oscillation output, periodically quenched via  $V_{CON}$ . An envelope detector, comparator and flop-flop latch recovers the original transmitted digital data.

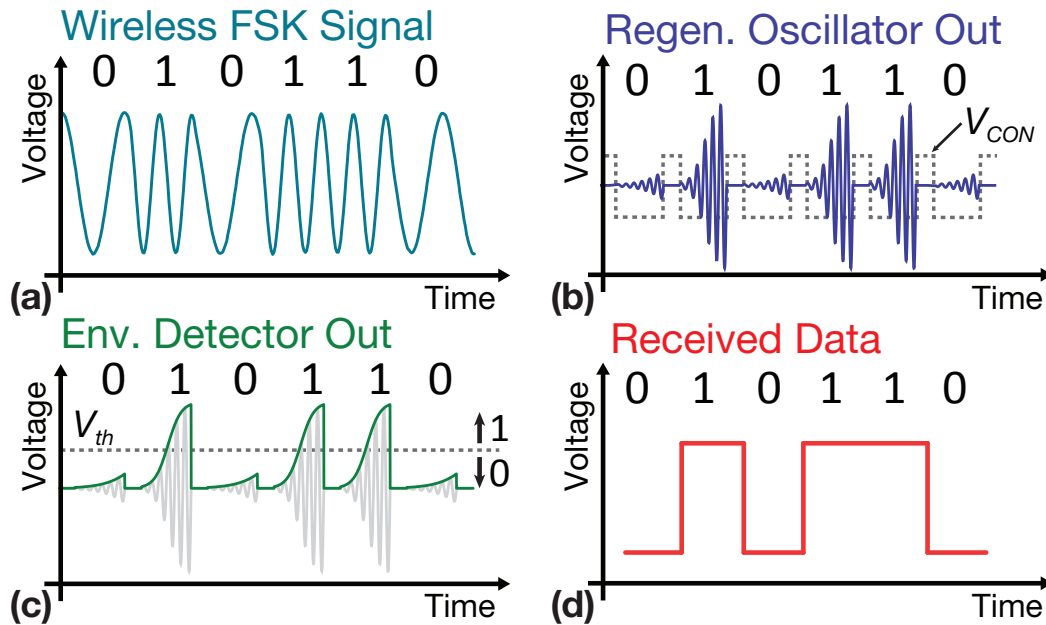


Figure 8.3: Conceptual operation of the regenerative receiver. The BFSK modulated and transmitted waveform of (a) gives rise to the periodically restarted oscillation of (b), where the on-resonance signal generates faster oscillation growth. Here, amplifier output drops to zero when  $V_{con}$  is raised, though resonator motion decays with a time constant based on resonator  $Q$ . Finally, envelope amplitudes which exceed  $V_{th}$  in (c) allow discrimination of 0s and 1s, recovering the original data in (d).

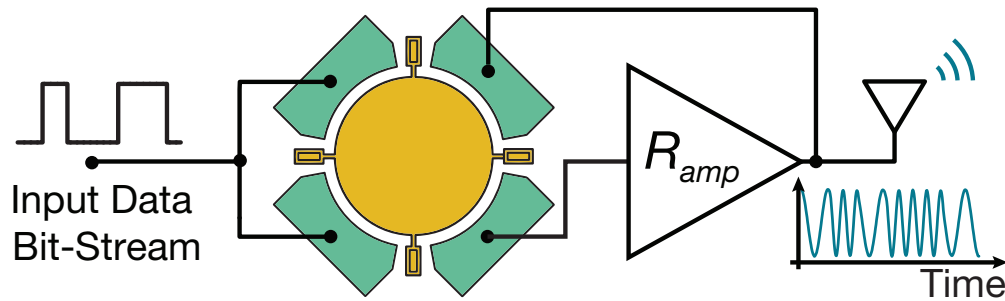


Figure 8.4: Schematic of the MEMS radio transceiver configured in transmit-mode where demodulating circuitry is switched out for an FSK modulating input to the capacitive-gap disk. With TIA gain no longer quenched, a continuous RF carrier is generated.

allowing each bit to be decoded in a separate, short oscillation growth as seen in Fig. 8.3(b). Figure 8.3(c) presents the envelope of the periodic oscillation growth produced by the envelope detector of Fig. 8.2. The output of this envelope detector feeds a comparator, the output of which in turn is latched into a flip-flop to recover the original transmitted data (Fig. 8.3(d)).

With the high  $Q$  of the MEMS resonators, this receiver isolates a single narrow channel while rejecting signals in nearby channels, spaced here at 4 kHz apart. Because the amplifier in such a design is isolated from the input antenna with only on-resonance signals passed through the MEMS resonator, out-of-channel interferers are blocked. This marks a significant improvement over previous regenerative receiver architectures [23], where loop amplifiers must handle any spurious signal received by the antenna without causing excess intermodulation. Here, the filtering of any such interferers greatly relaxes the linearity, and hence power consumption, of the amplifier.

Meanwhile, with voltage tunable via electrical-stiffness, such MEMS oscillators may also be configured as frequency-modulated elements, offering a uniquely simple, continuous-phase Frequency-Shift Keying transmitter. Such operation can be enabled using the same circuit as used for receive-mode, but with amplifier gain held constant to generate a continuous RF carrier as shown in Fig. 8.4. Data to be transmitted may be applied to the input MEMS electrodes to generate FSK modulation, while the output of the amplifier is wired to the antenna.

The transimpedance amplifier ASIC (as described in Section 3.3) is used to achieve regenerative amplification (in receive mode, *cf.* Fig. 8.2) and the FSK modulated carrier (in transmit mode, *cf.* Fig. 8.2). In Fig. 3.7, transistors  $M_1 - M_4$  comprise the basic differential pair biased by a Common-Mode Feedback (CMFB) circuit;  $M_{RF}$  serves as the voltage controllable feedback resistor to allow control of the total transimpedance gain via input bias voltage  $V_{CON}$  (which is  $V_{GAIN}$  in Fig. 3.7). With transresistance gain  $R_{amp}$  sufficient to overcome resonator losses, the oscillator loop amplitude rises exponentially with

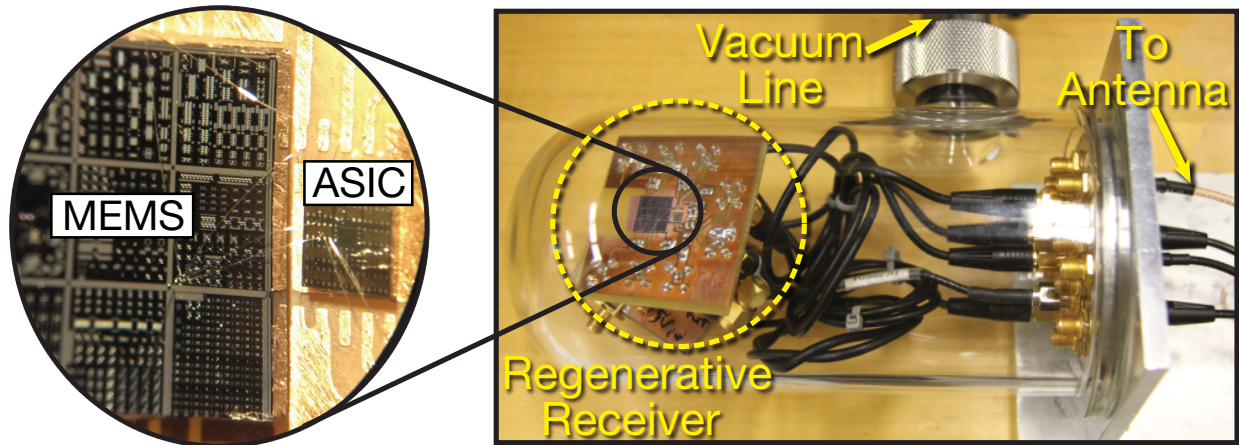


Figure 8.5: Measurement setup consisting of the regenerative transceiver dies mounted on a Printed Circuit Board (PCB) and measured in a bell-jar vacuum environment. The inset displays the MEMS and ASIC dies, both fabricated with many devices on a single die, one each of which is bondwired to the PCB.

time constant given by Eqn. (3.26). An on-resonance signal reduces the time required to rise to the ‘1’-bit threshold amplitude in two ways: first, the drive signal is resonantly enhanced to produce a resonator starting amplitude at the beginning of each oscillation cycle much larger than the background thermal noise, and second, this input signal continues to drive the resonator to increased amplitude during oscillation startup.

As with any filter, the bandwidth of the filter limits the possible data transmission rate. Here, such a limit is enacted by the decay time required for the resonator to reach a low amplitude of motion following a ‘1’. If the amplifier quench time falls short of the decay time of the resonator (here a long 0.5 ms due the high resonator  $Q$ ), oscillation will restart quickly even in the absence of an input signal, preventing detection of subsequent ‘0’s.

To meet the filtering requirements of channel-select radio applications, the MEMS resonators used must possess both a useful RF operating frequency and sufficient  $Q$  to achieve the narrow  $\sim 1$  kHz bandwidths desired for the sensor node application. To this end, the disk resonators depicted in Fig. 8.1(a) and Fig. 8.2 are quite suitable, with the added capability to accurately define multiple unique frequencies on the same die via only CAD layout, thus expanding possible operating frequency beyond that achievable from electrical stiffness tuning alone.

### 8.3 Experimental Realization

Using the design methodology in Chapter 2, MEMS resonators were designed for operation at 60.6 MHz with a disk radius of 32  $\mu\text{m}$ . Following the fabrication steps for the

planarized process with 500-nm thick interconnects in Section 4.2, structures were released in 49% HF to yield the final device imaged in the SEM of Fig. 4.4(b). To construct a complete radio transceiver, released MEMS resonators are bondwired together with the CMOS ASIC described above and affixed to PCB circuits that provided all needed bias voltages as well as the simple off-chip RF diode detector and flip-flop circuit used for data recovery. Figure 8.5 presents this assembled MEMS transceiver mounted in a custom bell-jar setup to allow measurement in a  $\mu$ torr vacuum. The hermetic feedthroughs seen on the right connect the radio to a simple antenna formed from  $\sim 20$  cm of wire. A bench-top frequency-synthesizer connected to a 2<sup>nd</sup> antenna positioned 4 m from the receive antenna provided wirelessly transmitted test signals.

### 8.3.1 Measurements

Figure 8.6 presents measured time-traces illustrating operation of the receiver circuit of Fig. 8.2. Here, a frequency synthesizer transmits the -17 dBm (20  $\mu$ W) test signal modulated with the bit-stream of Fig. 8.6(a) using 1-kHz mark-space separation FSK at a data rate of 1 kbps. Gating the regenerative amplifier gain control  $V_{CON}$  at the receive data rate to periodically grow and quench oscillation produces the oscillation envelope of Fig. 8.6(c), generated from a receive antenna located at a distance of 4 m from the transmitter. Here, small in-band signals are regeneratively amplified to create the observed speed-up in oscillation amplitude growth, clearly distinguishing mark vs. space frequency of the transmitted signal. Figure 8.6(d) presents the output of the comparator following the envelope detector, while Fig. 8.6(e) shows the final data latched into the output flip-flop, clearly recovering the original transmitted data from Fig. 8.6(a).

Despite the use of make-shift antennas, the performance is remarkable and demonstrates the sensitivity and selectivity of this capacitive-gap MEMS-based receiver, even in the face of typical interferers in an unshielded environment. To further gauge this ability to reject interference, Fig. 8.7 presents the measured receiver output with the transmitter detuned by 4 kHz to a nearby channel and increased by 30 dB, showing no detected signal, as it should.

Meanwhile, Fig. 8.8 demonstrates the BFSK-modulated output of the transmit-mode configuration in Fig. 8.4, where the TIA gain is no longer gated and the transmit data-stream is applied to the input electrodes. With the input data encoded in the 200 mV swing seen in Fig. 8.8(a), the oscillation output (Fig. 8.8(b)) is seen to undergo a fast-response, continuous-phase FSK modulation, well-suited to the desired transmit function.

Using a periodically quenched transimpedance amplifier ASIC, the demonstrated MEMS-based circuit provides not only reliable selection and detection of individual narrow-band channels, but also FSK generation for transmission, and marks a first demonstration of an RF channel-select-capable MEMS radio transceiver. Additionally, a separate set of MEMS resonator electrodes for the antenna input and the amplifier loop shield the amplifier from out of band interferers.

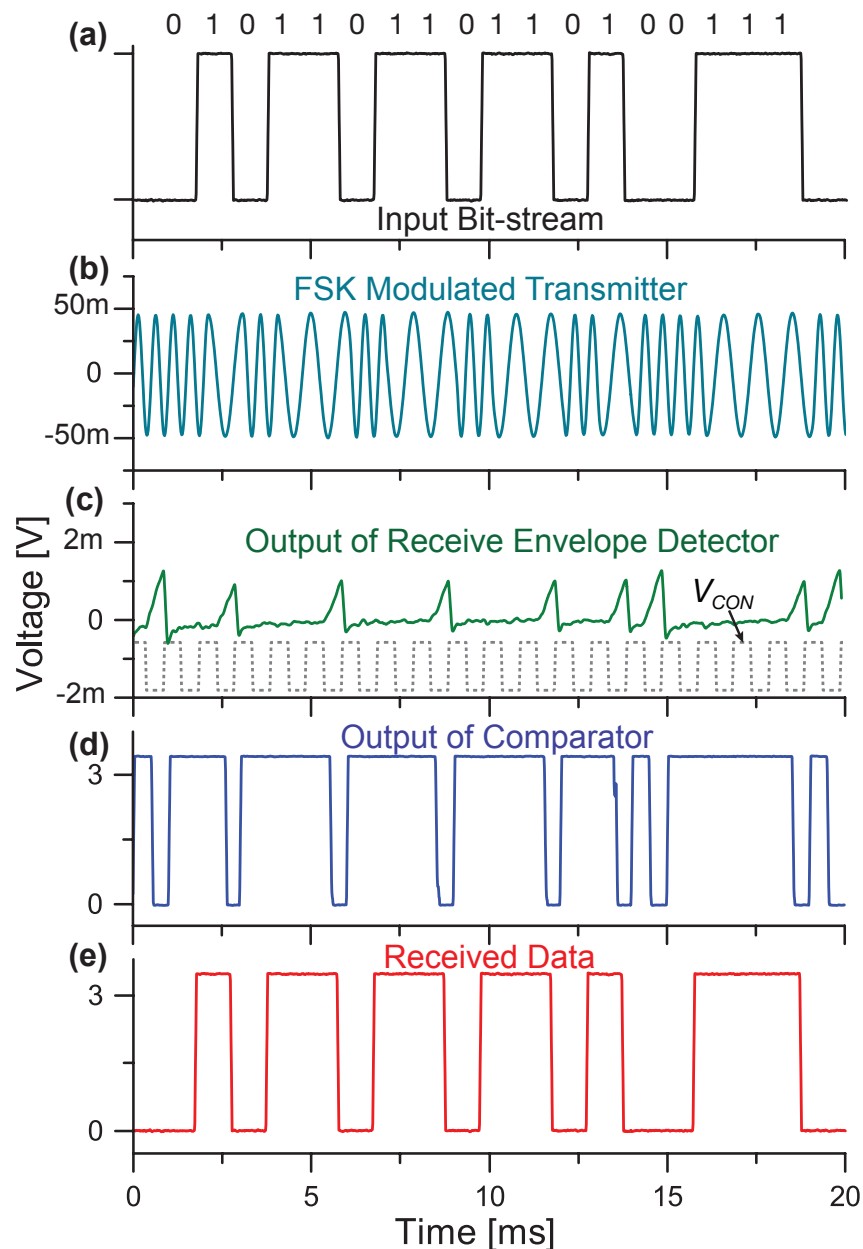


Figure 8.6: Measured receiver operation for a 1 kbps bit-stream transmitted across a distance of 4 m as in Fig. 8.2 using a Binary-FSK modulated transmitter with 1kHz shift and output power of -17 dBm ( $20 \mu\text{W}$ ). The transmitted data-stream (a) is BFSK encoded and transmitted on a 60.6 MHz RF carrier (b) using a bench-top signal generator (shown mixed down to 2 kHz). Regenerative detection yields (c) amplitude following envelope detection; (d) shows resultant signal following comparator; and (e) presents the final recovered data-stream clocked by the output flip-flop. Here, the MEMS resonator is biased with 10.3 V, and the ASIC is operated on a 2.1 V supply drawing  $\sim 233 \mu\text{A}$ .

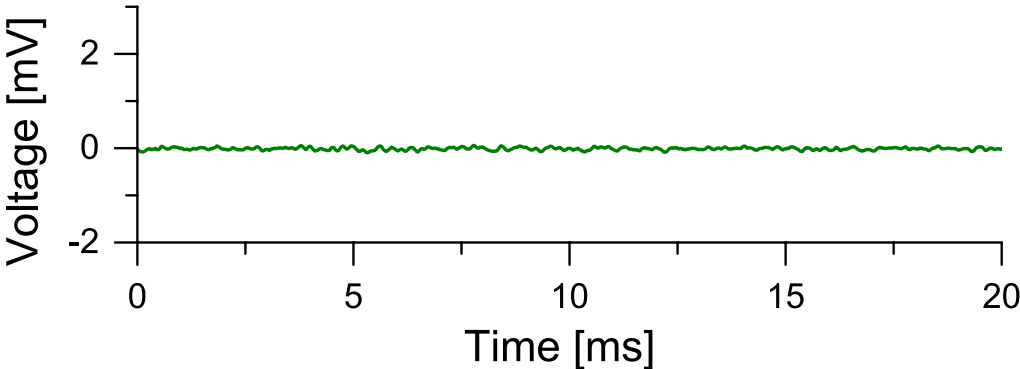


Figure 8.7: Measured regenerative receiver signal when transmitter is shifted by 4 kHz to a near-by channel and increased 30dB in power.

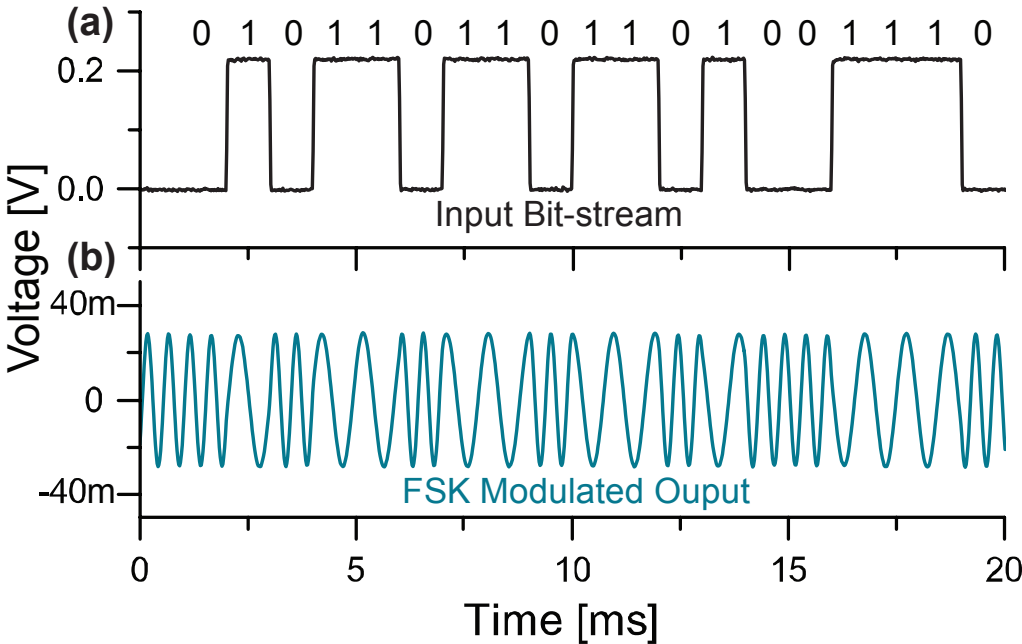


Figure 8.8: Measured FSK modulation at a 1kHz mark-space frequency separation generated using the transmit-mode configuration of Fig. 8.4. With the applied modulation signal (a), a continuous-phase output modulation is produced (b), shown here mixed down to  $\sim 2$  kHz for presentation.

## Chapter 9

# Avenues Towards Higher Frequency Operation

The past chapters have demonstrated the capability of MEMS resonators as references for high quality oscillators and oscillator systems. With the demonstrated performance, these devices are already sufficient for wireless sensor node networks targeted for long-range unlicensed operation in the 52-74 MHz band white-space [30] and ISM bands at 27.12 MHz and 40.68 MHz [31]. However, many applications would greatly benefit from similar systems operating at higher frequency, in particular radios designed to interoperate with existing wireless standards. Pursuant to this push to provide high frequency operation, this chapter introduces two new resonator designs that make possible frequency to GHz and above without sacrificing the high quality factors possible in capacitive-gap devices.

### 9.1 Whispering-Gallery Mode Disk Resonators

The name “Whispering Gallery mode” was first coined by Lord Rayleigh in the early 1900’s while describing acoustic resonances in St. Paul’s Cathedral [71]. The original term as applied to building-sized phenomena eventually became the term of choice to describe similar phenomena in micro-optical devices [72], and more recently, in high-order optically excited acoustic microspheres [73]. Low-order acoustic WGMs were in fact first used at the micro-scale in the device of [53], which was dubbed the “Wine-Glass Disk, but was functionally a 2nd order WGM. Therefore, the modeling and design analysis of Whispering-Gallery mode disk device is the same as that of Chapter 2 with a minor difference in the small signal equivalent circuit in Fig. 2.2 (a). In the Whispering-Gallery mode disk device, the number of electrodes increases with the order of the Whispering-Gallery mode.

Figure 9.1(a) presents the perspective-view schematic of a 3<sup>rd</sup> Whispering-Gallery Mode (WGM) disk resonator under a two-port bias, excitation, and measurement scheme, identifying key features to be used later for analysis. As shown, this device consists of a disk structure constructed in doped polysilicon or diamond, with thickness  $h$  and radius  $R$ , supported by

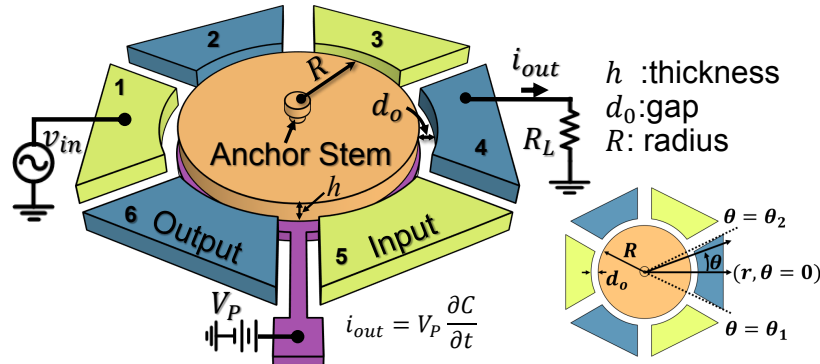


Figure 9.1: Perspective views of disk resonators in typical two-port bias schemes for 3<sup>rd</sup> Whisping-Gallery Mode. Note: electrodes with the same color are electrically connected together.

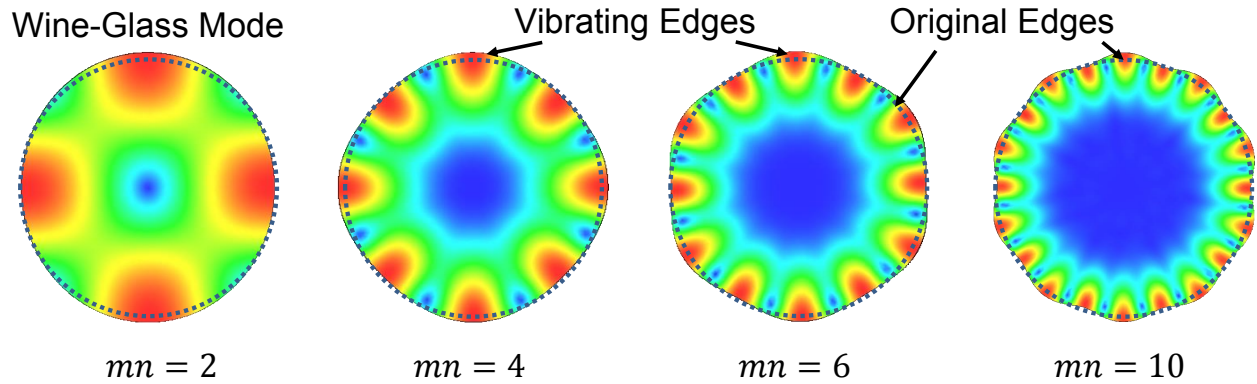


Figure 9.2: Finite element simulated modes for the 2<sup>nd</sup>, 4<sup>th</sup>, 6<sup>th</sup>, and 10<sup>th</sup> Whisping-Gallery Modes. It shows that the movement of the disk moves to the edge as the mode number increases.

a stem self-aligned to the very center of the disk [74].

The disk is surrounded by doped polysilicon capacitive transducer electrodes spaced less than 100 nm from its outer edge. To excite the device of Fig. 9.1(a) in its two-port configuration, a dc-bias voltage  $V_P$  is applied to the conductive disk and an ac signal  $v_{in}$  to its drive or input electrodes. When the frequency of  $v_{in}$  matches that of one of the resonance modes, the resulting force applied to the disk drives it into the vibration mode shape of that mode. Figure 9.2 presents the 2<sup>nd</sup>, 4<sup>th</sup>, 6<sup>th</sup>, and 10<sup>th</sup> WGM modes. Additionally, Fig. 9.2 confirms that Whisping-Gallery modes with multiple lobe maxima along the circumference of a disk produce much smaller motions at the center of the stem-supported disk as the mode number increases (indicated by the blue color), and so should allow higher  $Q$  for higher mode number (assuming the stem dominates the loss). As shown, one of the location where the maximum displacement occurs is  $(R, 0)$ , which is taken as a reference point for  $rlc$  core elements in Fig. 2.2(a).

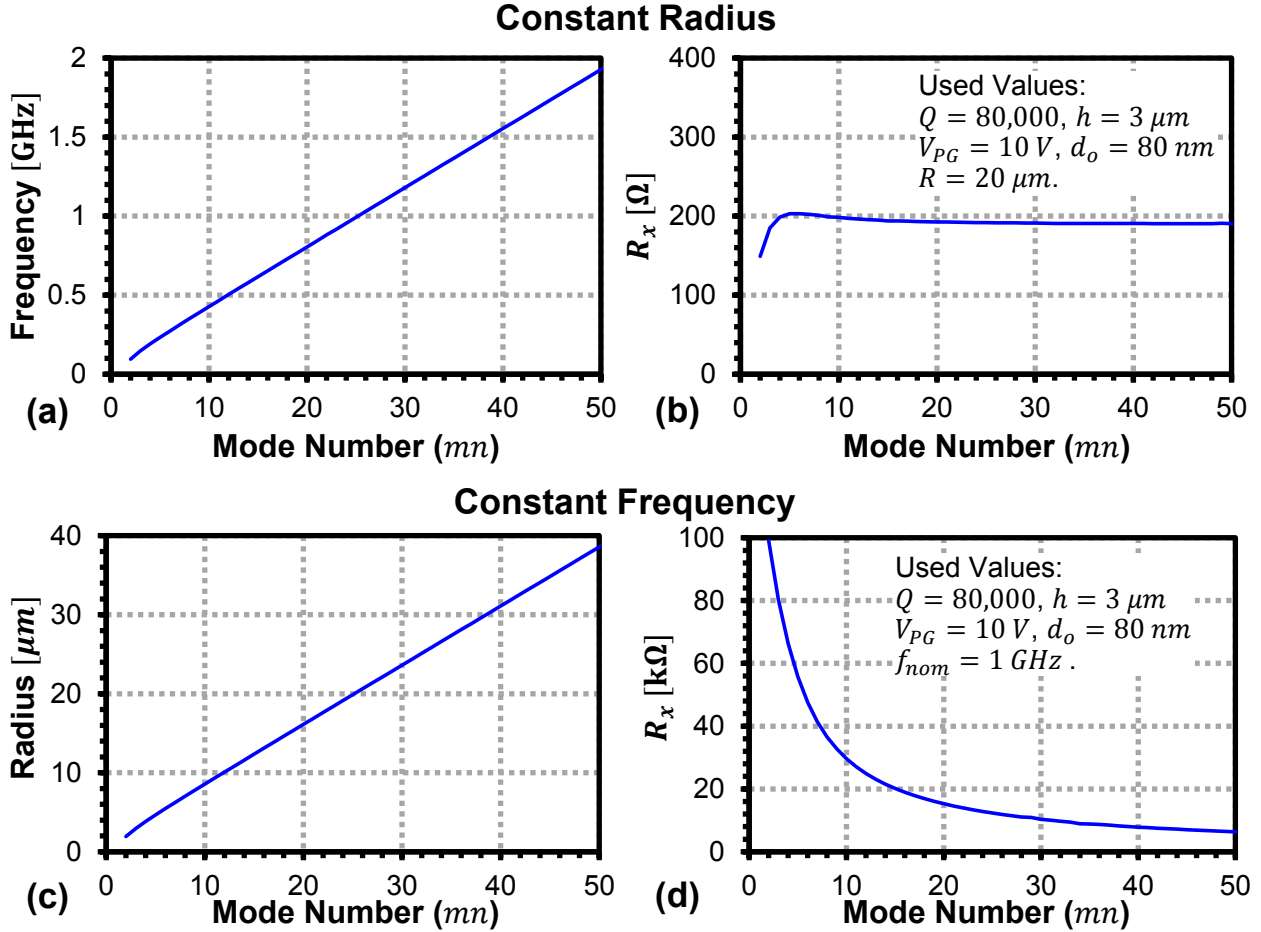


Figure 9.3: Plots of (a) the resonance frequency and (b) the motional resistance,  $R_x$ , of the disk with  $R = 20 \mu\text{m}$  versus the mode number. Plots of (c) the disk radius and (b) the motional resistance,  $R_x$ , of the disk for the 1 GHz resonance frequency design versus the mode number.

The frequency of the resonance can be found by solving for  $\zeta$  in Eqn. (2.7) and substituting  $\zeta$  in to Eqn. (2.9). The 4<sup>th</sup> Whispering-Gallery mode corresponds to  $(mn, m) = (4, 1)$ , denoting the first solution of Eqn. (2.7) for  $mn = 4$ . The 6<sup>th</sup> Whispering-Gallery mode corresponds to  $(mn, m) = (6, 1)$  and so forth. Figure 9.3(a) plots the WGM resonance frequencies for a  $3\mu\text{m}$ -thick ring with  $20 \mu\text{m}$  radius as a function of the mode number ( $mn$ ). Figure 9.3(c) further presents the disk radius versus the mode number for 1 GHz frequency design. Both the resonance frequency and radius have a linear dependence to the mode number. To capture this, Eqn. (2.9) can be approximated:

$$f_{nom/approx.} = \frac{K_1 \cdot mn + K_0}{R} \sqrt{\frac{E}{\rho(2 + 2\sigma)}}, \quad \text{for } mn \geq 2 \quad (9.1)$$

where  $K_1$  and  $K_0$  are unitless material parameter and their values for microcrystalline diamond are 0.1414 and 0.2174, respectively. To maximize the disk's  $Q$ , loss must be minimized. Among loss mechanisms that influence  $Q$ , material and anchor loss are often the most important at GHz frequencies. Material loss is generally governed by phonon-phonon interactions [75], [76], which in turn depend upon acoustic velocity and thermal conductivity, where diamond's values of  $18,500 \text{ ms}^{-1}$  and  $2000 \text{ Wm}^{-1}\text{K}^{-1}$ , respectively, give it a (theoretical) advantage over many other materials at GHz frequencies. At least theoretically, with some dependence on what values are used for material constants, diamond is predicted to allow a maximum  $Q$  of 380,000 at 3 GHz, to be compared with the 36,000 and 3,400 predicted for silicon and AlN, respectively [37]. Provided material loss theory can be trusted, anchor losses will likely govern the ultimate  $Q$  of this device. From this perspective, a high mode number Whispering-Gallery design is desirable.

The small signal equivalent circuit analysis in Section 2.3 can be use to model the Whispering-Gallery mode disk. In the reduced 2-port circuit as shown Fig. 2.2(c), the  $\eta_e$  and  $C_o$  are redefined as follows:

$$\begin{aligned}\eta_{e,in} &= \eta_{e1} + \eta_{e3} + \dots + \eta_{e(2mn-3)} + \eta_{e(2mn-1)} = mn \cdot \eta_{en} \\ \eta_{e,out} &= \eta_{e2} + \eta_{e4} + \dots + \eta_{e(2mn-2)} + \eta_{e(2mn)} = mn \cdot \eta_{en} \\ \eta_e &= \eta_{e,in} = \eta_{e,out} = mn \cdot \eta_{en}\end{aligned}\tag{9.2}$$

where  $\eta_{e1}$  to  $\eta_{e(2mn)}$  and  $\eta_{en}$  are defined in Eqn. (2.19). Similarly, the equivalent input and output electrode-to-resonator overlap capacitances become

$$\begin{aligned}C_{o,in} &= C_{oe1} + C_{oe3} + \dots + C_{oe(2mn-3)} + C_{oe(2mn-1)} = mn \cdot C_{oen} \\ C_{o,out} &= C_{oe2} + C_{oe4} + \dots + C_{oe(2mn-2)} + C_{oe(2mn)} = mn \cdot C_{oen} \\ C_o &= C_{o,in} = C_{o,out} = mn \cdot C_{oen}\end{aligned}\tag{9.3}$$

where  $C_{oe1}$  to  $C_{oe(2mn)}$  and  $C_{oen}$  are defined in Eqn. (2.19). By substituting Eqn. (9.2) and (9.3) into Eqn. (2.26), the motional resistance,  $R_x$ , is plotted versus the mode number in Fig. 9.3 (b) and (d) showing:

1. For a fixed radius disk, using higher mode number increases the operation frequency without sacrificing the motional resistance.
2. For a desired frequency of operation, using higher mode number decreases the motional resistance.

However, for the fixed radius case, the electrode area becomes smaller with increasing mode numbers. For the fixed frequency case, the disk becomes larger with increasing mode numbers. Therefore, there are practical limitations on using higher mode numbers.

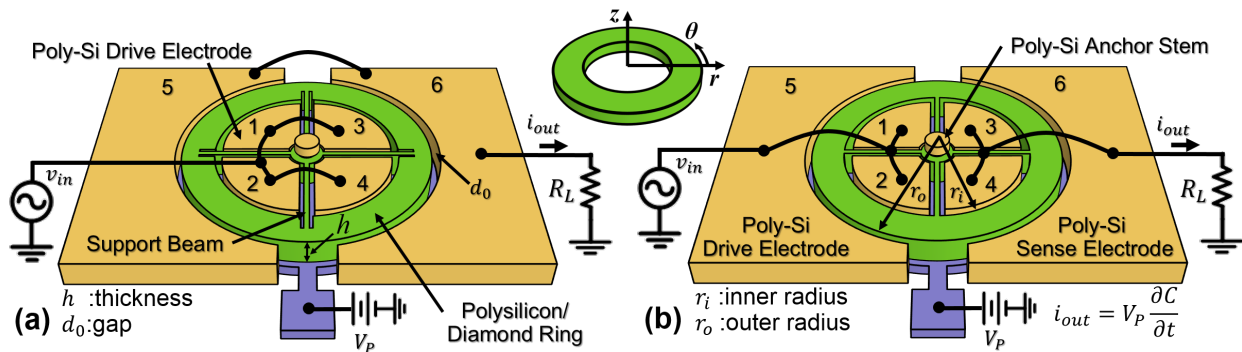


Figure 9.4: Perspective views of ring resonators in typical two-port bias schemes for (a) electrode configuration A; and (b) electrode configuration B.

## 9.2 Spoke-Supported Ring Resonators

Pursuant to achieving high  $Q$  values, [77] introduced the first radial ring resonator that utilized a centralized spoke-supported structure to greatly reduce support loss towards pure polysilicon ring resonator  $Q$ 's in excess of 10,000 at frequencies past 1 GHz. The specific design, shown in Fig. 9.4(a), was previously dubbed the hollow-disk ring resonator in [77], since it was conceived of by removing quadrants of material from a solid disk resonator, but purposely leaving intact beams of material to non-intrusively support the ring structure. Similar devices when constructed in diamond [78] have now pushed performance even further, with  $Q$ 's above 40,000 at frequencies approaching 3 GHz. Specifically, the design of Fig. 9.4(b) constructed in microcrystalline diamond achieves a  $Q$  of 42,900 at 2.97 GHz, which is now high enough to make possible RF channel-select filters with less than 1 dB of insertion loss. With electrodes both inside and outside the spoke-supported ring structure, this design attains electrode overlap advantages similar to that of a previously published annular ring [79] and extensional Wine-Glass mode ring designs [80], while offering a much less intrusive support structure that not only enables substantially higher  $Q$ , but also enables measured impedances as low as 81 k $\Omega$  with 75-nm electrode-to-resonator gaps. This marks a 30X reduction in impedance from previous surface-micromachined, pure polysilicon, solid disk resonators operating past 1 GHz [74], with similar gap spacing.

Figure 9.4(a) presents the perspective-view schematic of a spoke-supported ring under a two-port bias, excitation, and measurement scheme, identifying key features to be used later for analysis. As shown, this device consists of a ring structure constructed in diamond, with thickness  $h$ , inner radius  $r_i$ , and outer radius  $r_o$ , suspended by spokes emanating from an anchored stem self-aligned to the very center of the structure [74]. Here, the use of a centrally-located anchor with radially emanating longitudinal-mode, quarter-wavelength support beams provides a degree of balance and isolation that greatly suppresses anchor losses to the substrate, allowing this annular ring-type resonator to achieve  $Q$ 's much higher than versions where the ring vibrating in radial-contour modes is directly anchored to the

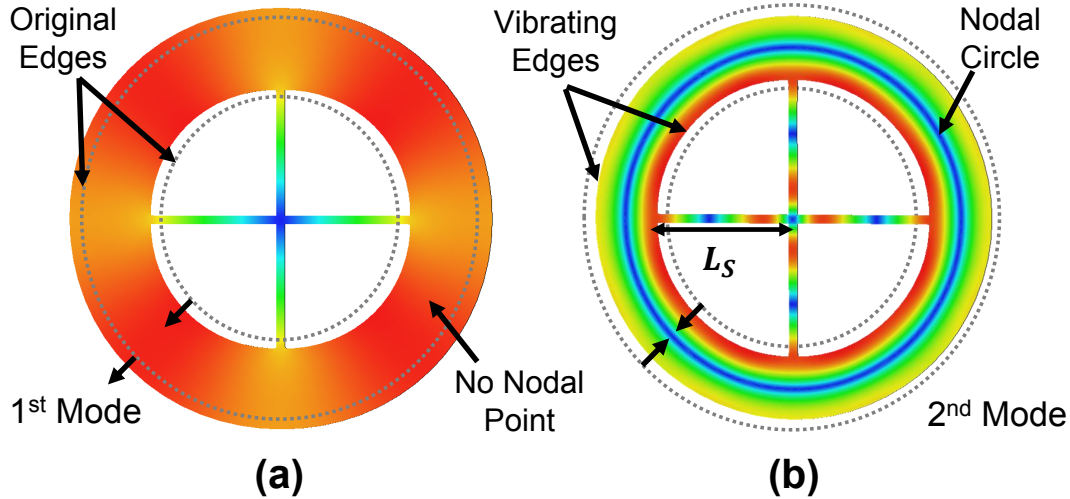


Figure 9.5: Finite element simulated modes for the spoke-supported ring resonator and longitudinal supporting beam of Fig. 9.4(a). (a) 1<sup>st</sup> contour mode (symmetric). (b) 2<sup>nd</sup> contour mode (anti-symmetric).

substrate from underneath [79]; or where the ring vibrating in extensional Wine-Glass modes is supported by tethers (i.e., support beams) at its quasi-nodal points [80]. As will be detailed later, the support beams are designed with geometries that isolate the resonator structure from its anchors in order to minimize energy losses to the substrate, allowing the structure to maintain exceptionally high  $Q$ .

A complete modeling and design of the ring resonators are in Appendix A. This Chapter presents a brief description of the device operation of the ring resonators and the support design along with measurement results. The spoke-supported ring is surrounded by inner and outer doped polysilicon capacitive transducer electrodes spaced less than 100 nm from its inner and outer edges, respectively. To excite the device in either one of the two port configurations of Fig. 9.4, a bias voltage  $V_P$  is applied to the ring and an ac signal  $v_{in}$  to drive electrodes. These voltages produce an ac force between the electrode and the ring at the frequency of  $v_{in}$ , which if applied at the resonance frequency of the ring structure excites a resonant motion, with displacement amplitude amplified by the  $Q$ .

Figure 9.5(a) presents a finite element simulation (FEM) of the fundamental radial contour mode shape in which red and blue represent maximum and minimum modal displacements, respectively. In this mode, the ring inner and outer radii expand and contract in phase, much like a disk with its center hollowed-out. Figure 9.5(b) presents the second radial mode in which the inner and outer edges of the ring move in opposite directions, creating a so-called “breathing” mode that sports a nodal line between the ring edges. The support beams are made symmetric and balanced (*cf.* Fig. 9.5), to cancel forces at the center of the ring thus minimizing transfer of motion to the stem and substrate. This work focuses on the second radial mode as it is most amenable to simultaneous high frequency and  $Q$ .

After solving Eqn. (A.14) to obtain frequency parameter  $p$ , the mechanical resonance

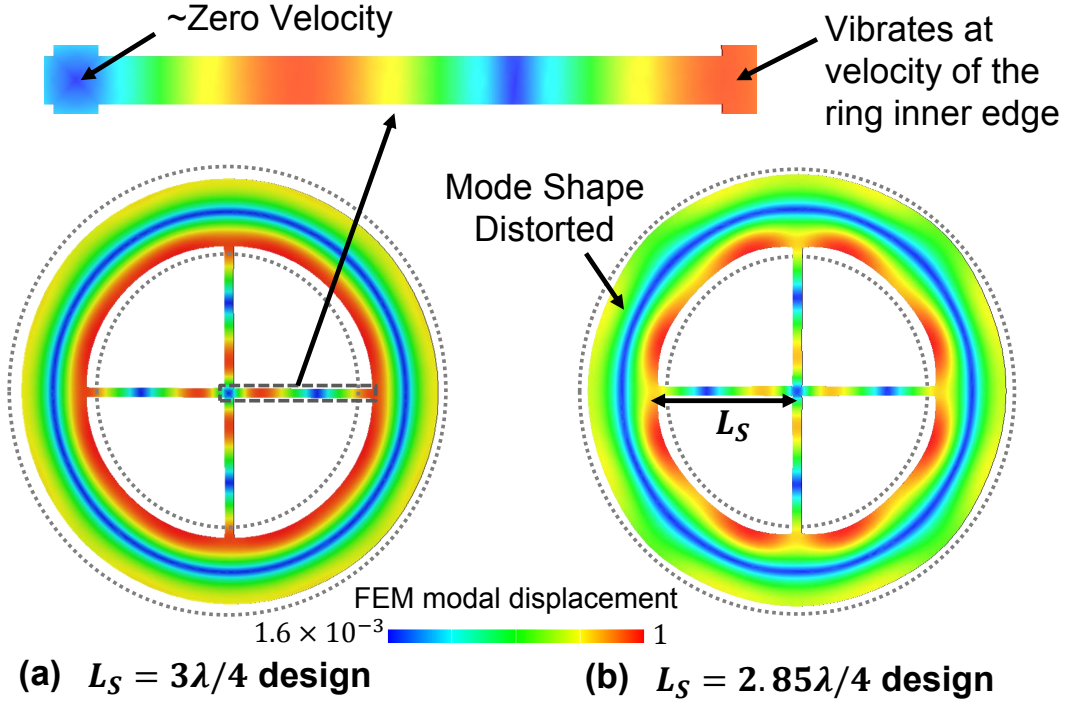


Figure 9.6: FEM simulations comparing modal displacements when the supports are (a) quarter-wavelength and (b) non-quarter-wavelength.

frequency of the ring structure,  $f_{nom}$ , readily follows via

$$f_{nom} = \frac{\omega_{nom}}{2\pi} = \frac{p}{2\pi} \sqrt{\frac{E}{\rho(1-\sigma^2)}} \quad (9.4)$$

where  $\omega_{nom}$  is the radian nominal mechanical resonance frequency, and  $E$  is the Young's modulus of the structural material. The first solution of Eqn. (A.14) gives the first mode resonance of Fig. 9.5(a), and the second solution gives the second mode resonance of Fig. 9.5(b), and so forth.

Provided material loss theory [75], [76] can be trusted, anchor losses will likely govern the ultimate  $Q$  of this device. Like the design of [77], the ring of this work employs quarter-wavelength support beams to minimize escape of energy to the substrate. To illustrate the importance of quarter-wavelength design, Fig. 9.6 presents FEM images generated using Coventorware for spoke-supported rings equipped with (a) quarter-wavelength ( $3\lambda/4$  in this case) support beams and (b) non-quarter-wavelength ( $2.85\lambda/4$ ) ones. As shown, the quarter-wavelength design of (a) clearly exhibits less mode distortion, so is freer to vibrate in the desired ring breathing mode and should yield higher  $Q$  in an actual implementation. Note that both designs benefit from the balanced symmetrical spoke-support structure, where the blue color of their anchors indicates minimal motion at the anchor, and thus, minimum loss to the substrate.

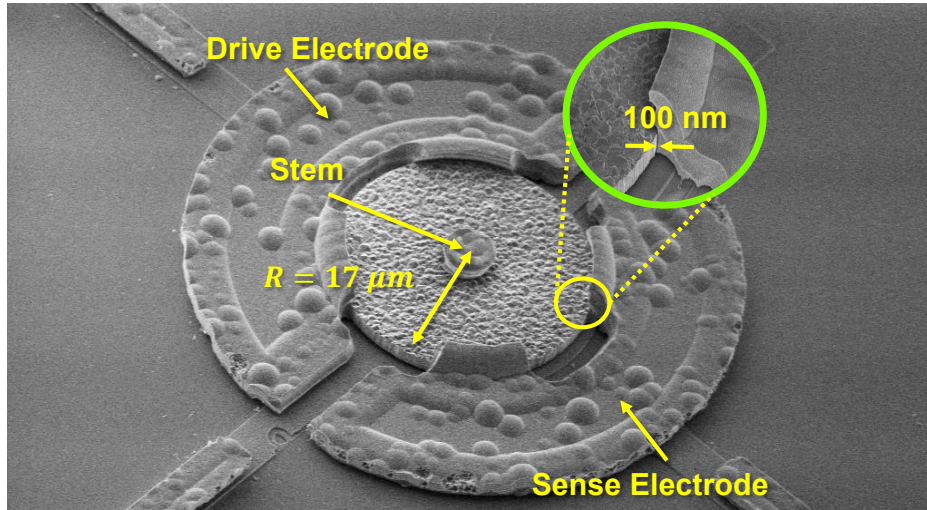


Figure 9.7: SEM showing the fabricated disk device. The micromechanical resonator consists of a  $17\mu\text{m}$ -radius,  $2\mu\text{m}$ -thick micro-crystalline HF CVD diamond disk. The inset zooms in on the tiny 100 nm capacitive gap between disk

## 9.3 Measurement Results

### 9.3.1 Whispering-Gallery Mode Disk Resonator Results

Using the fabrication process of Section 4.1,  $17\mu\text{m}$  diameter diamond disk devices with 100 nm capacitive gaps were constructed using electrodes designed to couple to the fourth mode. Figure 9.7 presents the SEM of one such device: note that, due to the limitation of a single interconnect later, the electrodes configuration is different from the device shown in Fig. 9.1. Despite its segmented geometry, the electrodes are capable of exciting not only the 4th WGM, but also the radial contour mode (the mode shape is shown in Fig. 9.8(a)). This then allows direct comparison of  $Q$ 's for these modes.

Devices were tested using a Lakeshore model FWPX probe station as described in Section 4.3.1. To overcome smaller-than-expected output currents caused by the lack of ideal electrodes described earlier, and to maximize the accuracy of extracted  $Q$ -values, measurements employed the mixing technique presented in Section 4.3.1 to separate desired motional currents from competing parasitics.

Figure 9.8 presents the measured responses in vacuum for a  $17\mu\text{m}$ -radius disk operating in (a) its radial-contour mode at 309 MHz with a  $Q \sim 17,300$ ; and (b) in the 4<sup>th</sup> WGM, at a higher frequency of 511 MHz with a higher  $Q \sim 47,900$ —an overall  $f \cdot Q$  increase of  $4.6\times$ . This data, measured on the same device, confirms the expectation that anchor losses indeed dominate among loss mechanisms at high frequency, allowing the WGM device with its smaller stem motion to attain significantly higher  $Q$ .

From the measured curves, the motional resistances of the devices were extracted using the methods of [43] and were found to be 770 k $\Omega$  and 560 k $\Omega$  for the contour and whispering

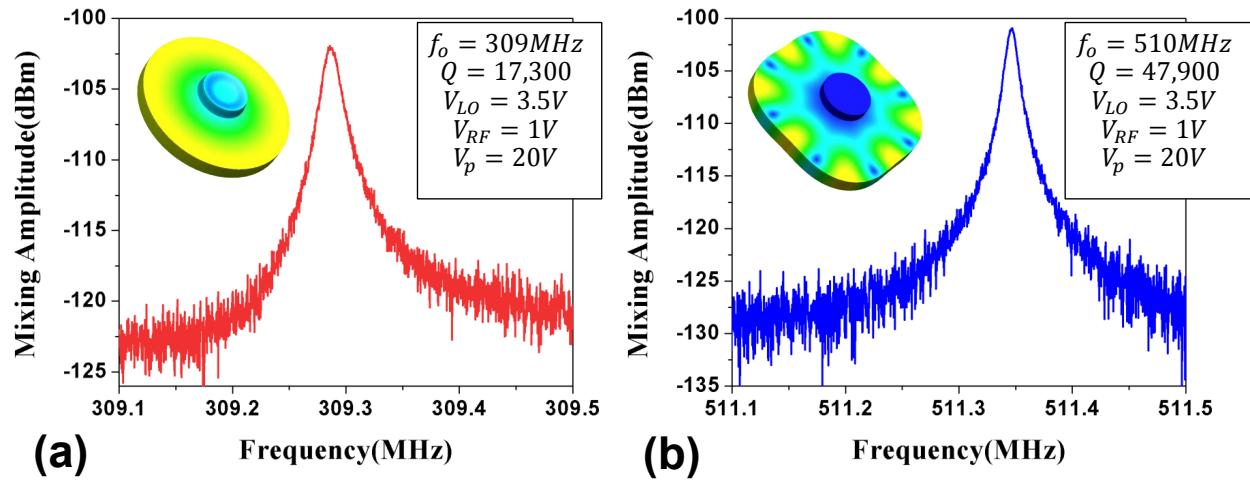


Figure 9.8: Measured responses for diamond disk resonators operating (a) in the radial contour mode with  $Q=17.3\text{k}$  at 309 MHz; and (b) in the 4<sup>th</sup> Whispering-Gallery mode for the same device with  $Q = 47.9\text{k}$  at 510 MHz, which constitutes a  $4.6\times$  improvement in  $f \cdot Q$  product.

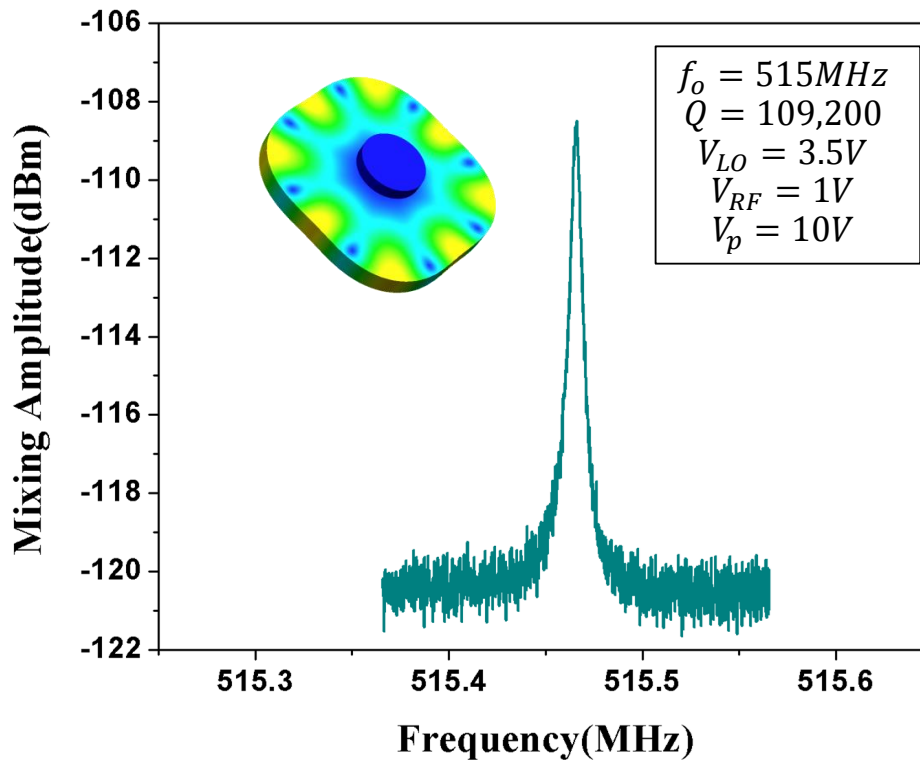


Figure 9.9: Measured frequency characteristic for a second diamond disk device with a remarkable  $Q = 109.2\text{k}$  at 515 MHz. While of the same diamond resonator design, this device did not have fully notched electrodes, so had significantly less coupling.

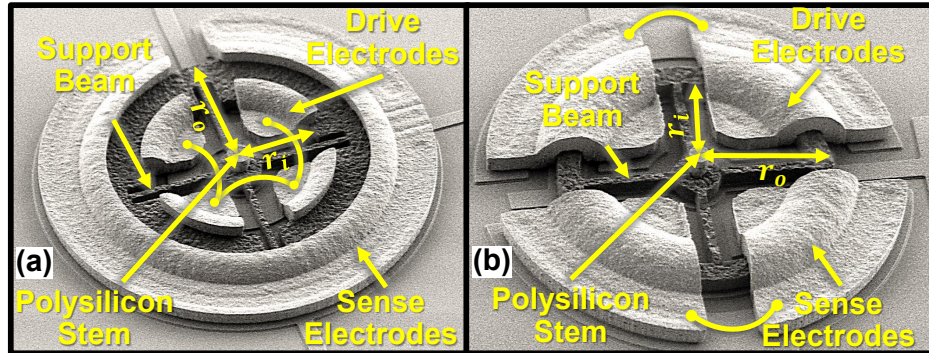


Figure 9.10: SEM's of fabricated ring resonators: (a) a 900-MHz diamond ring with polysilicon stem using electrode configuration B; and (b) a 3-GHz diamond ring with polysilicon stem using electrode configuration A

gallery modes, respectively. These agree, within the uncertainty of the measurement, with theoretical calculations using Eqn. (2.26) and (9.2) on this electrode shape together with measured  $Q$  values and a 100 nm electrode-to-resonator gap spacing.

One remaining question is whether or not the stem isolation provided by the WGM device is enough to eliminate anchor losses to the point of revealing the maximum  $Q$  value permitted by structural material losses. To shed some light on this, Fig. 9.9 presents the measured frequency characteristic for another of the same WGM disk devices, this one exhibiting the best performance among  $\sim 60$  measured devices, with a startlingly high  $Q = 109,000$  at 515 MHz. This is the highest  $Q$  measured to date at  $\sim 500$  MHz for any on-chip room temperature resonator, yielding an  $f \cdot Q$  product of  $5.6 \times 10^{13}$ .

### 9.3.2 Spoke-Supported Ring Resonator Results

Several self-aligned, radial-contour mode micromechanical spoke-supported ring resonators with frequencies at 900MHz and 2.97 GHz were designed in diamond structural materials using the methods of Section A.2-A.3, then fabricated using the process flow in Section 4.1. Figure 9.10(a)-(b) present ring devices in diamond structural material and designed to resonate in the 2<sup>nd</sup>-mode at 900-MHz and 2.97-GHz, respectively. In addition, an ensemble of 900-MHz diamond devices were fabricated with varying support beam lengths in 50 nm steps in order to map out resonator performance due to deviations from perfect quarter-wavelength operation. Table 9.1 summarizes the dimensions used for each design along with measured and predicted performance data.

Figure 9.11 presents the frequency response of a ring design fabricated in microcrystalline diamond. The low-loss and high acoustic velocity of the diamond material increases the frequency of the 2<sup>nd</sup> mode to 900 MHz while simultaneously boosting  $Q$  to an exceptional 77,400. Reducing ring width further, the resonator operating frequency increases to 2.97 GHz in Fig. 9.12, while still retaining a remarkable series resonant  $Q$  of 42,900—a record high at these frequencies. The 8-10% decrease in frequency of these devices as compared

Table 9.1: Spoke-supported ring resonator design and performance summary.

Parameter	Source	Operating Frequency		Unit
		900 MHz	3 GHz	
<i>Design/Given</i>				
Structure Material	-	Diamond	Diamond	-
Inner radius, $r_i$	layout	19.4	13.8	$\mu\text{m}$
Outer radius, $r_o$	layout	29.1	16.6	$\mu\text{m}$
Thickness, $h$	layout	2.0	2.0	$\mu\text{m}$
Electrode-to-resonator gap, $d_o$	measured	75	75	nm
Density, $\rho$	[Akgul, IFCS'11]	3500	3500	$\text{kg/m}^3$
Young's modulus, $E$	[Akgul, IFCS'11]	1198	1198	GPa
Poisson ratio, $\sigma$	[Akgul, IFCS'11]	0.07	0.07	-
RF input amplitude, $v_{RF}$	measured	2	2	V
LO carrier amplitude, $v_{LO}$	measured	1.12	2	V
DC-biased voltage, $V_p$	measured	6	8	V
Resonator mass, $m_{mre}$	Eqn. (A.30)	$4.18 \times 10^{-12}$	$8.52 \times 10^{-13}$	kg
Resonator stiffness, $k_{mre}$	Eqn. (A.30)	$1.55 \times 10^8$	$3.71 \times 10^8$	N/m
Damping factor, $c_{mre}$	Eqn.(A.31)	$3.29 \times 10^{-7}$	$4.44 \times 10^{-7}$	kg/s
Inner-to-outer coupling ratio $\eta_c = \eta_{c5} = \eta_{c6}$	Eqn. (A.36)	-0.816	-0.912	-
Electromech. coupling, $\eta_{e,in}$	Eqn. (A.37)(A.38)	$1.77 \times 10^{-6}$	$1.81 \times 10^{-6}$	C/m
Electromech. coupling, $\eta_{e,out}$	Eqn. (A.37)(A.38)	$2.71 \times 10^{-6}$	$1.81 \times 10^{-6}$	C/m
Static Overlap Capacitance, $C_{o,in}$	Eqn. (A.39)(A.40)	$2.21 \times 10^{-14}$	$1.78 \times 10^{-14}$	F
Static Overlap Capacitance, $C_{o,out}$	Eqn. (A.39)(A.40)	$4.15 \times 10^{-14}$	$1.78 \times 10^{-14}$	F
<i>Performance</i>				
Quality factor in vacuum, $Q$	Measured	77,400	42,900	-
Resonant frequency, $f_o$	Measured	899.6	2970	MHz
	Eqn. (9.4)	969	3321	
Series resistance, $R_x$	Measured	51	81	k $\Omega$
	Eqn. (A.41)	69	136	
Inductance, $L_x$	Eqn. (A.41)	0.873	0.261	H
Capacitance, $C_x$	Eqn. (A.41)	$3.09 \times 10^{-20}$	$8.79 \times 10^{-21}$	F
Coupling Efficiency, $C_x/C_{o,in}$	calculated	$1.4 \times 10^{-4}$	$4.94 \times 10^{-5}$	%
Coupling Efficiency, $C_x/C_{o,out}$	calculated	$7.44 \times 10^{-5}$	$4.94 \times 10^{-5}$	%

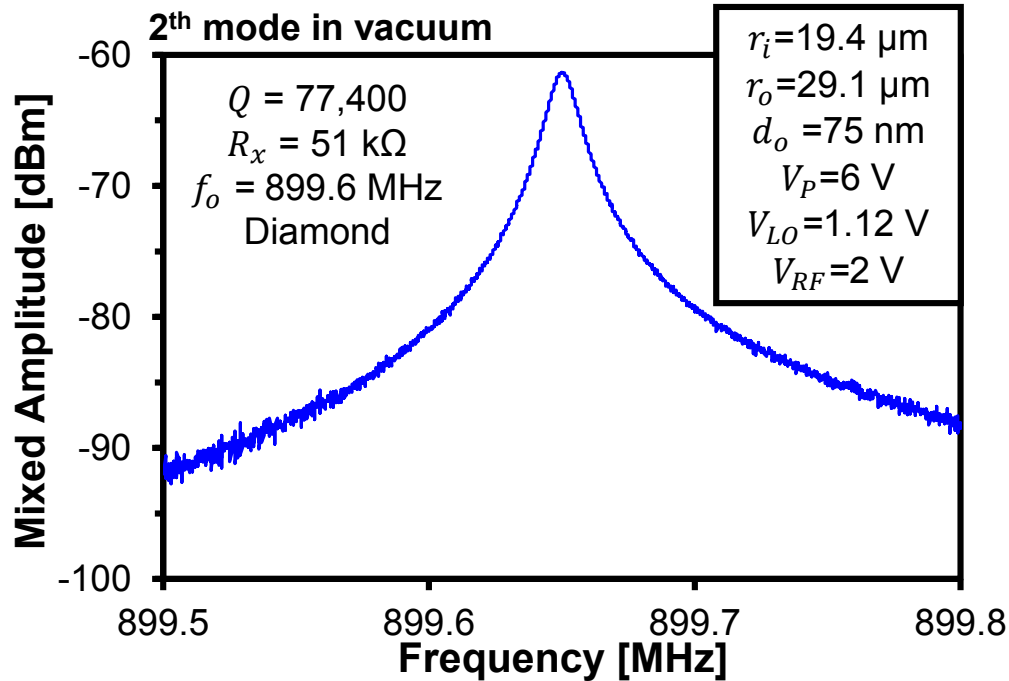


Figure 9.11: Mixing-measured frequency response of a 2<sup>nd</sup> mode 900-MHz diamond spoke-supported ring with polysilicon stem.

with prediction, *cf.* Table 9.1, likely results from slight differences in the material properties of the diamond used here compared with [37].

The frequency response data demonstrate operation at the designed mode frequency for these ring resonators. However, these resonators display many additional unwanted mechanical modes that can interfere with desired operation in real-world applications. Fortunately, lateral and symmetric placement of electrodes suppresses electrical detection of the out-of-plane spurious modes and of the modes that do not match the electrode symmetry. Despite this, two primary symmetric resonances near the 2<sup>nd</sup> mode frequency remain observable.

Figure 9.13 presents measured frequency data for the designed mode as well as the measured spurious mode for a large ensemble of 900 MHz 2<sup>nd</sup> mode diamond rings with varying support beam lengths. Black dots plot out measured frequencies of the two resonator modes most coupled by the electrode geometry, corresponding to the desired 2<sup>nd</sup> ring mode (top curve) as well as an additional hybrid mode (bottom curve). This reveals a clear trend as support beam lengths deviate from perfect quarter-wavelength. Overlaid blue and red curves represent calculated frequencies from FEM simulation showing excellent agreement with measured data.

Changes in support beam length further affect loading of the mechanical mode, where mode shape distortion ensues when the vibrating ring sees non-zero impedances from the supports, as illustrated in the simulations of Fig. 9.13. Here, the amount of loading depends on the deviation of support beam length from the  $\lambda/4$  condition described in Section A.3

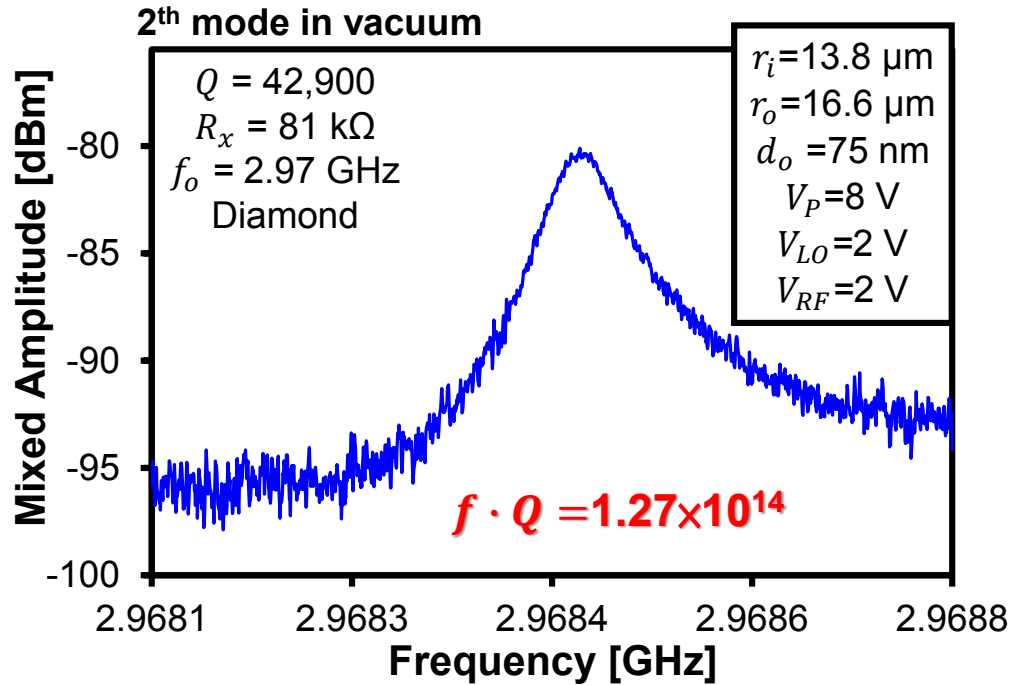


Figure 9.12: Mixing-measured frequency response of the 2<sup>nd</sup> mode 2.97-GHz ring demonstrating the highest to-date  $f \cdot Q$  product of  $1.27 \times 10^{14}$ .

needed to present an effective zero impedance to the inner ring edge. Figure 9.14 presents the difference in insertion loss in two-port network analyzer measurements of the two dominant modes in the 900 MHz ring resonators as support beam length changes. Note that measurement of this insertion loss provides a direct gauge of support beam loading changes independent of intrinsic loss variations among the many devices measured.

The observed difference in relative coupling of the two measured modes of greater than 30 dB as beam length is swept confirms the dependence of support beam loading on beam length deviations from the optimal  $\lambda/4$  condition. Here, the correctly designed support length provides 20 dB suppression of the undesired hybrid mode, which is sufficient for many oscillator and filter applications. This not only emphasizes the importance of proper design to maximize resonator  $Q$ , but also offers the potential to enhance the designed mode while further suppressing undesired spurious modes.

The record high  $Q$  of 42,900 at 2.97 GHz for the microcrystalline diamond device measured under vacuum correspond to a frequency- $Q$  product of  $1.27 \times 10^{14}$ , which is the highest measured value yet seen for micromechanical resonators operating at the room temperature. Comparison with previous high frequency- $Q$  product acoustic resonators [77], [81]–[84] in Fig. 9.15 reveals that the result of this work exceeds even that of macroscopic BAW resonators, setting a new high-water mark for frequency- $Q$  product of any acoustic resonator.

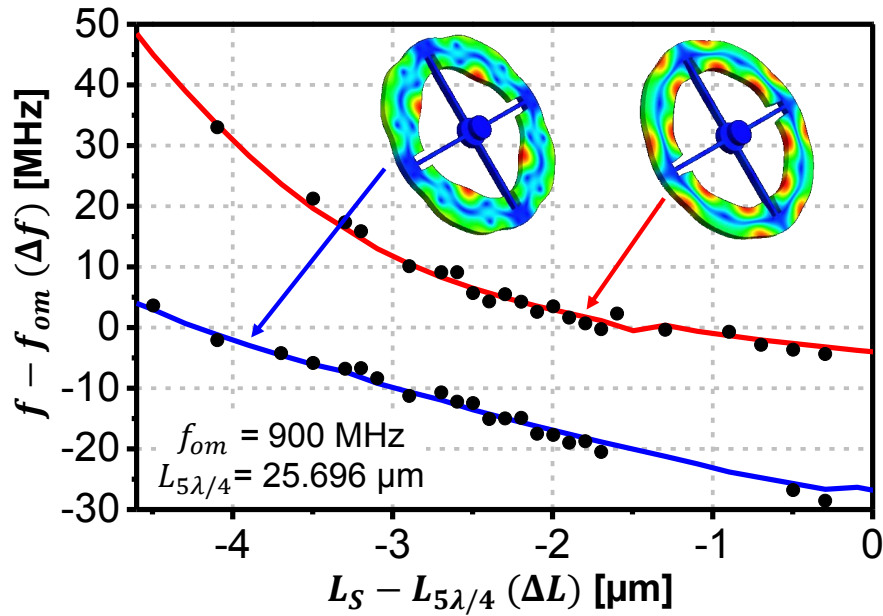


Figure 9.13: Measured frequency response (black dots) of the two strongest modes of several 900 MHz ring resonators as their support beam lengths change. The data matches well the FEM-simulated blue and red curves.

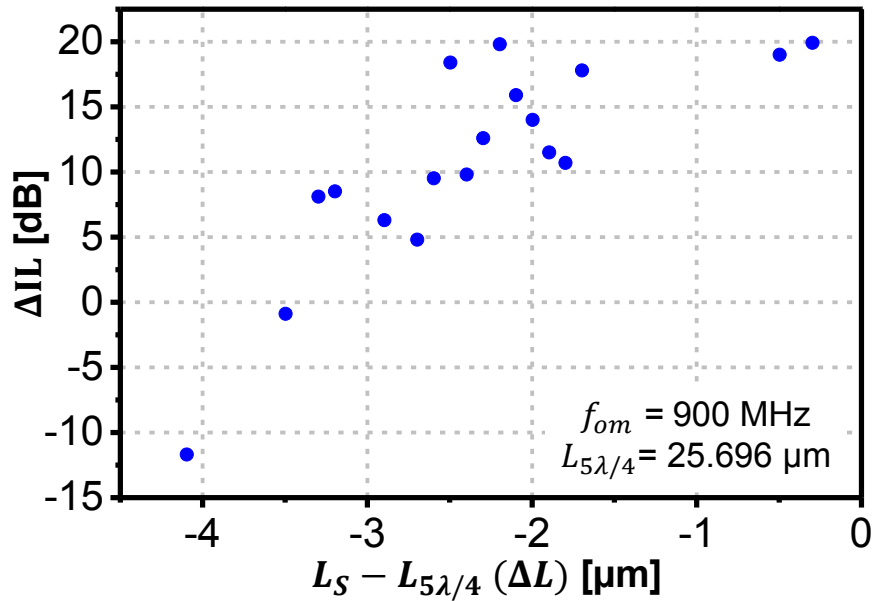


Figure 9.14: Measured difference in resonator insertion loss (blue dots) of the two strongly coupled modes shown in Fig. 9.13 as support beam length changes. When the beam length approaches  $\lambda/4$ , the ring is virtually “levitated”, so behaves as if it had no supports. This enhances its motional amplitude and lowers its insertion loss, all while suppressing the 2<sup>nd</sup> hybrid mode.

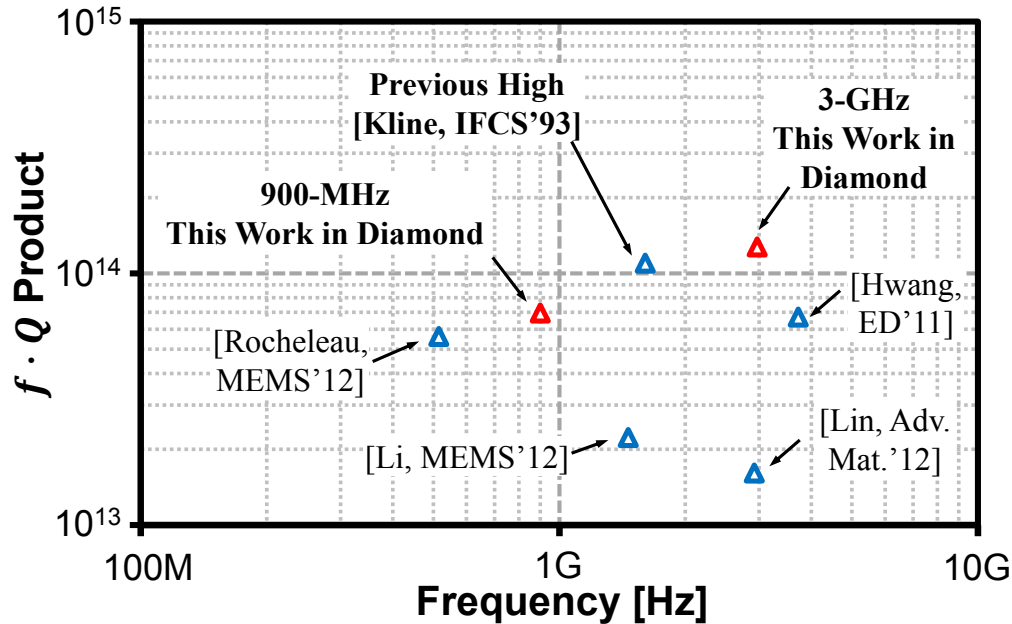


Figure 9.15: The  $f \cdot Q$  products of previously published high  $f \cdot Q$  acoustic resonators along with the ring resonators presented here.

## 9.4 Device Design Insights

For filter applications, there are two regimes to consider: 1) narrow bandwidth filters such as the tiny 0.03% bandwidth required for direct RF channel-selection [25] and 2) wide bandwidth filters covering 0.2% bandwidth or greater and suitable for full band selection. Focusing first on narrowband operation, high  $Q$  resonators are required to achieve such filters without large insertion loss. For this type of application, resonators made with diamond materials are preferred as they have higher  $Q$  than polysilicon counterparts. In addition, materials with higher acoustic velocity (such as diamond) enable higher frequencies with larger resonator dimensions, which in turn relaxes fabrication tolerances. For a 3-GHz resonator design, for example, the width of the ring is approximately 3  $\mu\text{m}$  in diamond while only 1.4  $\mu\text{m}$  in polysilicon.

In contrast, for wide bandwidth filter applications, the limiting factor is the electromechanical coupling ( $C_x/C_o$ ), defined in Eqn. (2.30) and (A.42). This term sets limits on the ability to terminate a given filter bandwidth without undue passband distortion, where ( $C_x/C_o$ ) must be at least comparable to the % bandwidth [24].

By inspection of Eqn. (2.30) and (A.42), ( $C_x/C_o$ ) increases quickly with decreasing gap spacing  $d_0$  or increasing dc-bias voltage  $V_P$ , but decreases with increasing resonance frequency. From a design perspective, reducing gap size offers the fastest path to increasing ( $C_x/C_o$ ). For example, decreasing gap size from the 80 nm used here to 10 nm improves ( $C_x/C_o$ ) by 512 times. For the 3-GHz diamond resonator, this 10 nm gap corresponds to a ( $C_x/C_o$ ) of approximately 0.08% with  $V_P$  of 15 V, while an equivalent polysilicon device

with  $(E \cdot \rho)$  product of 1/12 that of diamond has  $(C_x/C_o)$  of 0.28%. If other materials are considered, additional improvement is available through material properties. Aluminum, for example, has an exceptional  $(E \cdot \rho)$  product, 22 times smaller than diamond's, and would yield a  $(C_x/C_o)$  of 0.37% with the same  $V_P$  and gap. To achieve 3-GHz operation, however, aluminum's small acoustic velocity necessitates a design width of only 0.9  $\mu\text{m}$ , which introduces additional process challenges. As a general rule of thumb for GHz capacitive-gap resonators, it is desirable to use a material that has, in addition to low material loss, high acoustic velocity  $\sqrt{E/\rho}$  and small  $(E \cdot \rho)$  product.

While the motional impedances here of tens of  $\text{k}\Omega$  at GHz are sufficient for many sensor applications, use of these devices in oscillators or filters motivates reduction of  $R_x$  to the  $\text{k}\Omega$ -range or less to allow matching to external components, either directly or via matching networks. Inspection of equations (2.19) and (2.26) ((A.33) and (A.41) for the ring) indicate that the capacitive gap offers the most straightforward path towards reduced  $R_x$ , which is inversely proportional to the fourth power of gap size. Additionally, mechanically-coupled arrays of resonators allows further reduction in  $R_x$  without a significant reduction in  $Q$  [11], [85]. As illustration, an example design suitable for oscillator construction might use modest 30 nm gaps with a coupled array of seven 3-GHz diamond rings to achieve a motional resistance of 300  $\Omega$  with a  $V_P$  of only 8 V, all within the capabilities of demonstrated fabrication technology [85]. Here, all the seven ring resonators in the array are assumed to be perfectly matched. Often,  $R_x$  of the  $N$ -disks array resonator does not decrease by  $N$  due to non-ideality associated with process variation. Nevertheless, the results in [11], [85] show that arraying 7 of similar resonators approximately improves the motional resistance linearly with the number of resonators. Note that using a planarized process in [52],  $V_P$  is not limited at a low voltage (such as 8 V) since the planarized electrodes will not create an upward force on the resonator structure. Using a higher bias voltage will allow a smaller number of ring resonators in the array. Showing these resonators work in oscillator based signal processors is a PhD dissertation on its own.

# Chapter 10

## Conclusions

This dissertation has provided a complete model and analysis required to design low-power oscillators using capacitive-gap MEMS devices. Using this design methodology, the demonstrated 61-MHz capacitive-gap transduced Wine-Glass disk Pierce oscillator capable of meeting GSM specifications while using only 78  $\mu\text{W}$  of power marks a milestone for MEMS-based frequency control technology. Compared with previous TIA-based renditions, this oscillator reduces power and area consumption by 4.5 times and 10 times, respectively. Increasing the bias voltage of the resonator by just 1.25 V allows operation at a still lower 43  $\mu\text{W}$  of power, at the cost of only a few dB in far-from-carrier offset phase noise. The power consumption can further reduced to 8.8  $\mu\text{W}$  by decreasing the gaps of the resonator from 80 nm to 40 nm. When power consumption is considered, to best of the author's knowledge, oscillators presented in this work post the highest *FOM*'s of any published on-chip oscillator to date for 1kHz offset frequency.

Additionally, the acceleration sensitivity of an oscillator referenced to a 61-MHz vibrating Wine-Glass disk was measured to be at least as good as  $\Gamma \sim 0.2$  ppb/*g* for vibration frequencies up to 2 kHz and in all directions, yielding a vector-sum magnitude  $|\vec{\Gamma}|$  less than 0.5 ppb/*g*. This remarkable number is achieved without any compensation and marks the best among MEMS-based oscillators, including those aided by accelerometer-based feedback compensation circuits. It is more than an order of magnitude better than an off-the-shelf crystal oscillator and is now comparable with some low sensitivity OCXO's.

This work also presents a first study of long-term frequency drift in micromechanical Wine-Glass disk oscillators. Performance was seen to be quite good, achieving stability within  $\pm 300$  ppb over a month after a burn-in period. With burn-in, the total drift is only 10 ppm over 10 months, well within required limits for many short-distance wireless communication specifications despite concerns that the small size of such MEMS resonators would lead to drift and reliability issues. Moreover, the increasing amplitude of oscillation over time suggests actual improvement in resonator quality factor and demonstrates that even simple in-house vacuum packaging is sufficient to achieve reliable operation of these MEMS devices. With these performance marks in both long- and short-term stability, such oscillators are excellent candidates for tomorrow's low-power radio systems.

However, the measured acceleration sensitivity is still about two orders of magnitude worse than the theoretical expectation for the MEMS device itself, and there is evidence that in the current measurement setup bondwires are a primary limitation. Additionally, the circuit analysis presented here predicts the power consumption can be further lower merely by reducing parasitic capacitance and trace resistance. This motivates the use of more fully integrated systems, such as flip-chip, to achieve even better results. Whether or not such further improvements are achieved, the power reduction already demonstrated while achieving GSM-compliant phase noise marks and remarkable frequency stability makes a compelling case for application to future low power wireless applications. Certainly, the demonstrated oscillator bests traditional crystal oscillator technologies and their battery-unfriendly mW's of power, while offering the single-chip form-factor desired for mobile electronics.

Moving beyond simple oscillators, devices such as these are good candidates for low-power signal processing. The multi-frequency oscillator in Chapter 7 showed a first effort to produce simultaneous oscillation outputs around 61 MHz using capacitive-gap MEMS resonator array-composites while employing only a single amplifier. This MEMS-based circuit provides not only independently switchable and tunable oscillation outputs at multiple frequencies, but also a multi-channel FSK transmitter, all in a power- and space-saving package commensurate with the needs of long-term mobile applications, such as wireless sensor nodes. The ability to simultaneously transmit on multiple channels using only one amplifier enables a high degree of wireless multiplexing while saving the power needed to operate additional amplifiers used in competing approaches—clearly desirable for tomorrow's autonomous wireless networks.

Furthermore, the demonstration in Chapter 7 of a 0.001% bandwidth micromechanical filter comprised of actively  $Q$ -boosted passive resonators with only 2.7 dB of insertion loss is the first of its kind on the micro-scale and presents opportunities for implementing some very unique and desired capabilities in the near future. Opportunities to realize RF channel-selecting radios were the focus of this work, and the demonstrated  $Q$ 's up to 2.3 million should prove useful towards greatly lowering power consumption for the low data rate wireless communications needed for network sensors. Bandwidths as small as 0.001% might further enable noise shaping for oscillators and other applications to unprecedented performance marks. Although this work focused on very small percent bandwidth filters, it is worthwhile to take a step back and consider use of these techniques in more mainstream applications, like cellular communications, for which RF channel-selection still offers substantial reductions in power consumption. As mentioned, existing resonator technologies do not yet possess the simultaneous  $Q$  and coupling to realize such a front-end. As described in this section, as long as the small additional power consumption is acceptable, active  $Q$ -boosting might be the answer for resonators that possess adequate coupling, but insufficient  $Q$ . In other words, RF channel-selection using piezoelectric resonators such as [86], or composite material structures [84] may indeed just be a few more electrodes and some active circuits away from reality. This is a topic for future work.

Finally, using a periodically quenched amplifier ASIC, the demonstrated MEMS-based circuit in Chapter 8 provides not only reliable selection and detection of individual narrow-

band channels, but also FSK generation for transmission, and marks a first demonstration of an RF channel-select-capable MEMS radio transceiver. Additionally, a separate set of MEMS resonator electrodes for the antenna input and the amplifier loop shield the amplifier from out of band interferers. This greatly relaxes the amplifier linearity spec, which lowers its power consumption to enable a significant improvement over previous regenerative MEMS receiver topologies.

Even though all the oscillator-based signal processors demonstrated in this dissertation are using 61-MHz capacitive-gap disk resonator, they are not limited to either 61-MHz carrier frequency or a capacitive-gap disk resonator. These methods can be applied to any high- $Q$  resonators [78], [87]–[90] with frequency tunability and multi-electrodes feature. Showing these systems work at GHz frequencies with  $< 100 \mu\text{W}$  power consuming is not too far away from reality.

This dissertation has presented the design methodology along with measurement results to achieve low-power capacitive-gap MEMS based oscillators. Combined with their low-power operation, the small acceleration sensitivity and the decent long-term stability of these oscillators shown in this dissertation not only make them compelling alternatives to the available oscillator products on the market but also provide new kinds of signal processors. Exploiting their frequency tunability, high- $Q$  multi-electrodes resonator, and regenerative amplification, the oscillator-based signal processors introduced in this dissertation pave a path towards realization of future low-power sensor networks.

# Bibliography

- [1] (). Facts and forecasts: Billions of things, trillions of dollars, [Online]. Available: <http://www.siemens.com/innovation/en/home/pictures-of-the-future/digitalization-and-software/internet-of-things-facts-and-forecasts.html> (visited on 11/14/2014).
- [2] H. Lee, A. Partridge, and F. Assaderaghi, “Low jitter and temperature stable MEMS oscillators,” in *Frequency Control Symposium (FCS), 2012 IEEE International*, May 2012, pp. 1–5.
- [3] *LTE Band 7 Duplexer*, ACMD-6007, Avago Technologies.
- [4] *Low-jitter precision CMOS oscillator*, DSC1121, Discera Corporation.
- [5] *LVC MOS/LVTTL compatible oscillators*, SiT8208, SiTime Corporation.
- [6] *Ultra-Small, 1 to 26 MHz oscillator*, SiT8021, SiTime Corporation.
- [7] D. B. Leeson, “A simple model of feedback oscillator noise spectrum,” *Proceedings of the IEEE*, vol. 54, no. 2, pp. 329–330, Feb. 1966.
- [8] J. T. M. van Beek and R. Puers, “A review of MEMS oscillators for frequency reference and timing applications,” *Journal of Micromechanics and Microengineering*, vol. 22, no. 1, p. 013001, 2012.
- [9] C. T.-C. Nguyen, “MEMS technology for timing and frequency control,” *Ultrasonics, Ferroelectrics, and Frequency Control, IEEE Transactions on*, vol. 54, no. 2, pp. 251–270, Feb. 2007.
- [10] *High performance MEMS VCXOs*, MV-9300A, Vectron International.
- [11] Y.-W. Lin, S.-S. Li, Z. Ren, and C. T.-C. Nguyen, “Low phase noise array-composite micromechanical wine-glass disk oscillator,” in *Electron Devices Meeting, 2005. IEDM Technical Digest. IEEE International*, Dec. 2005, 4 pp.–281.
- [12] J. M. Rabaey, J. Ammer, T. Karalar, S. Li, B. Otis, M. Sheets, and T. Tuan, “Pico-Radios for wireless sensor networks: The next challenge in ultra-low power design,” in *Solid-State Circuits Conference, 2002. Digest of Technical Papers. ISSCC. 2002 IEEE International*, vol. 1, Feb. 2002, pp. 200–201.

- [13] Y.-W. Lin, S. Lee, S.-S. Li, Y. Xie, Z. Ren, and C. T.-C. Nguyen, "Series-resonant VHF micromechanical resonator reference oscillators," *Solid-State Circuits, IEEE Journal of*, vol. 39, no. 12, pp. 2477–2491, Dec. 2004.
- [14] G. W. Pierce, "Piezoelectric crystal resonators and crystal oscillators applied to the precision calibration of wavemeters," *Proceedings of the American Academy of Arts and Sciences*, vol. 59, no. 4, pp. 81–106, Oct. 1923.
- [15] J. R. Vig and T. Meeker, "The aging of bulk acoustic wave resonators, filters and oscillators," in *Frequency Control, 1991., Proceedings of the 45th Annual Symposium on*, May 1991, pp. 77–101.
- [16] "Digital cellular telecommunications system," European Telecommunications Standards Institute (ETSI), Technical Specification ETSI TS 100 912, Feb. 2003.
- [17] "Part 15.4: Low-rate wireless personal area networks (LR-WPANs)," IEEE Computer Society, IEEE Std. 802.15.4<sup>TM</sup>-2011, 2011.
- [18] C. L. Muhlstein, S. B. Brown, and R. O. Ritchie, "High-cycle fatigue of single-crystal silicon thin films," *Microelectromechanical Systems, Journal of*, vol. 10, no. 4, pp. 593–600, Dec. 2001.
- [19] B. Kim, R. N. Candler, M. Hopcroft, M. Agarwal, W.-T. Park, and T. W. Kenny, "Frequency stability of wafer-scale encapsulated MEMS resonators," in *Solid-State Sensors, Actuators and Microsystems, 2005. Digest of Technical Papers. TRANSDUCERS '05. The 13th International Conference on*, vol. 2, Jun. 2005, pp. 1965–1968.
- [20] R. Tabrizian, M. Pardo, and F. Ayazi, "A 27 MHz temperature compensated MEMS oscillator with sub-ppm instability," in *Micro Electro Mechanical Systems (MEMS), 2012 IEEE 25th International Conference on*, Jan. 2012, pp. 23–26.
- [21] E. J. Ng, H. K. Lee, C. H. Ahn, R. Melamud, and T. W. Kenny, "Stability of silicon microelectromechanical systems resonant thermometers," *Sensors Journal, IEEE*, vol. 13, no. 3, pp. 987–993, Mar. 2013.
- [22] J. M. Rabaey, M. J. Ammer, J. da Silva J. L., D. Patel, and S. Roundy, "PicoRadio supports ad hoc ultra-low power wireless networking," *Computer*, vol. 33, no. 7, pp. 42–48, Jul. 2000.
- [23] B. Otis, Y. H. Chee, and J. Rabaey, "A 400  $\mu$ W-RX, 1.6mW-TX super-regenerative transceiver for wireless sensor networks," in *Solid-State Circuits Conference. Digest of Technical Papers. ISSCC. 2005 IEEE International*, Feb. 2005, pp. 396–606.
- [24] A. I. Zverev, *Handbook of Filter Synthesis*. New York: Wiley, 1967.
- [25] C. T.-C. Nguyen, "MEMS-based RF channel selection for true software-defined cognitive radio and low-power sensor communications," *Communications Magazine, IEEE*, vol. 51, no. 4, pp. 110–119, Apr. 2013.

- [26] H. C. Nathanson, W. E. Newell, R. A. Wickstrom, and J. Davis J. R., “The resonant gate transistor,” *Electron Devices, IEEE Transactions on*, vol. 14, no. 3, pp. 117–133, Mar. 1967.
- [27] C. Jeong, S. Seok, B. Lee, H. Kim, and K. Chun, “A study on resonant frequency and  $Q$  factor tunings for MEMS vibratory gyroscopes,” *Journal of Micromechanics and Microengineering*, vol. 14, no. 11, p. 1530, 2004.
- [28] C. T.-C. Nguyen and R. T. Howe, “Quality factor control for micromechanical resonators,” in *Electron Devices Meeting (IEDM '92.)*, *Technical Digest, International*, Dec. 1992, pp. 505–508.
- [29] A. Vouilloz, M. Declercq, and C. Dehollaini, “A low-power CMOS super-regenerative receiver at 1 GHz,” *Solid-State Circuits, IEEE Journal of*, vol. 36, no. 3, pp. 440–451, Mar. 2001.
- [30] “Second report and order and memorandum opinion and order,” Federal Communications Commission, ET Docket No. 08-260, Nov. 2008. [Online]. Available: [https://apps.fcc.gov/edocs\\_public/attachmatch/FCC-08-260A1.pdf](https://apps.fcc.gov/edocs_public/attachmatch/FCC-08-260A1.pdf) (visited on 07/13/2015).
- [31] “FCC online table of frequency allocations,” Federal Communications Commission, 47 C.F.R. § 2.106, May 2015. [Online]. Available: <https://transition.fcc.gov/oet/spectrum/table/fcctable.pdf> (visited on 07/13/2015).
- [32] A. Hajimiri and T. H. Lee, “A general theory of phase noise in electrical oscillators,” *Solid-State Circuits, IEEE Journal of*, vol. 33, no. 2, pp. 179–194, Feb. 1998.
- [33] M. Onoe, “Contour vibrations of isotropic circular plates,” *The Journal of the Acoustical Society of America*, vol. 28, no. 6, pp. 1158–1162, 1956.
- [34] R. A. Johnson, *Mechanical Filters in Electronics*. New York: John Wiley & Sons, Inc., 1983.
- [35] M. Akgul, L. Wu, Z. Ren, and C. T.-C. Nguyen, “A negative-capacitance equivalent circuit model for parallel-plate capacitive-gap-transduced micromechanical resonators,” *Ultrasonics, Ferroelectrics, and Frequency Control, IEEE Transactions on*, vol. 61, no. 5, pp. 849–869, May 2014.
- [36] S.-S. Li, Y.-W. Lin, Z. Ren, and C. T.-C. Nguyen, “Self-switching vibrating micromechanical filter bank,” in *Frequency Control Symposium and Exposition, 2005. Proceedings of the 2005 IEEE International*, Aug. 2005, pp. 135–141.
- [37] M. Akgul, R. Schneider, Z. Ren, G. Chandler, V. Yeh, and C. T.-C. Nguyen, “Hot filament CVD conductive microcrystalline diamond for high  $Q$ , high acoustic velocity micromechanical resonators,” in *Frequency Control and the European Frequency and Time Forum (FCS), 2011 Joint Conference of the IEEE International*, San Francisco, USA, May 2011, pp. 1–6.

- [38] W. C. Tang, T.-C. H. Nguyen, M. W. Judy, and R. T. Howe, "Electrostatic-comb drive of lateral polysilicon resonators," in *Solid-State Sensors, Actuators and Microsystems (Transducers'89), the 5th International Conference on*, Montreux, Switzerland, Jun. 1989.
- [39] F. Bannon, J. R. Clark, and C. T.-C. Nguyen, "High- $Q$  HF microelectromechanical filters," *Solid-State Circuits, IEEE Journal of*, vol. 35, no. 4, pp. 512–526, Apr. 2000.
- [40] K. Wang and C.-C. Nguyen, "High-order medium frequency micromechanical electronic filters," *Microelectromechanical Systems, Journal of*, vol. 8, no. 4, pp. 534–556, Dec. 1999.
- [41] W.-T. Hsu, J. R. Clark, and C. T.-C. Nguyen, " $Q$ -optimized lateral free-free beam micromechanical resonators," in *Solid-State Sensors, Actuators and Microsystems (Transducers'01), the 11th International Conference on*, Jun. 2001, pp. 1110–1113.
- [42] L. W. Nagel and D. O. Pederson, "SPICE (Simulation Program with Integrated Circuit Emphasis)," University of California, Berkeley, Memorandum ERL-M382, Apr. 1973.
- [43] A.-C. Wong and C.-C. Nguyen, "Micromechanical mixer-filters ("mixlers")," *Microelectromechanical Systems, Journal of*, vol. 13, no. 1, pp. 100–112, Feb. 2004.
- [44] E. A. Vittoz, M. G. Degrauwe, and S. Bitz, "High-performance crystal oscillator circuits: Theory and application," *Solid-State Circuits, IEEE Journal of*, vol. 23, no. 3, pp. 774–783, Jun. 1988.
- [45] A. Nelson, J. Hu, J. Kaitila, R. Ruby, and B. Otis, "A 22  $\mu$ W, 2.0GHz FBAR oscillator," in *Radio Frequency Integrated Circuits Symposium (RFIC), 2011 IEEE*, Jun. 2011, pp. 1–4.
- [46] M. Rinaldi, C. Zuo, J. Van der Spiegel, and G. Piazza, "Reconfigurable CMOS oscillator based on multifrequency AlN contour-mode MEMS resonators," *Electron Devices, IEEE Transactions on*, vol. 58, no. 5, pp. 1281–1286, May 2011.
- [47] Z. Z. Wu, V. A. Thakar, A. Peczalski, and M. Rais-Zadeh, "A low phase-noise Pierce oscillator using a piezoelectric-on-silica micromechanical resonator," in *Solid-State Sensors, Actuators and Microsystems, The 17th International Conference on*, Jun. 2013, pp. 490–493.
- [48] *Mhz range crystal unit*, MA-506, Seiko Epson Corporation.
- [49] *SMD glass sealing crystals*, 7S Series, TXC Corporation.
- [50] T. L. Naing, T. O. Rocheleau, Z. Ren, E. Alon, and C. T.-C. Nguyen, "Vibration-insensitive 61-MHz micromechanical disk reference oscillator," in *Frequency Control Symposium (FCS), 2012 IEEE International*, May 2012, pp. 1–6.
- [51] A. Rusznyak, "Start-up time of CMOS oscillators," *Circuits and Systems, IEEE Transactions on*, vol. 34, no. 3, pp. 259–268, Mar. 1987.

- [52] T. O. Rocheleau, T. L. Naing, J. Naghsh Nilchi, and C. T.-C. Nguyen, "A MEMS-based tunable RFchannel-selecting super-regenerative transceiver for wireless sensor nodes," in *Digest of Technical Papers, the 2014 Solid-State Sensors, Actuators and Microsystems Workshop*, Hilton Head Island, South Carolina, USA, Jun. 2014.
- [53] M. A. Abdelmoneum, M. U. Demirci, and C. T.-C. Nguyen, "Stemless wine-glass-mode disk micromechanical resonators," in *Micro Electro Mechanical Systems, 2003, IEEE The 16th Annual International Conference on*, Jan. 2003, pp. 698–701.
- [54] D. W. Allan, "Time and frequency (time-domain) characterization, estimation, and prediction of precision clocks and oscillators," *Ultrasonics, Ferroelectrics, and Frequency Control, IEEE Transactions on*, vol. 34, no. 6, pp. 647–654, Nov. 1987.
- [55] X. Wu, C. Zuo, M. Zhang, J. Van der Spiegel, and G. Piazza, "A 47  $\mu$ W 204MHz AlN contour-mode MEMS based tunable oscillator in 65nm CMOS," in *Circuits and Systems (ISCAS), 2013 IEEE International Symposium on*, May 2013, pp. 1757–1760.
- [56] R. L. Filler, "The acceleration sensitivity of quartz crystal oscillators: A review," *Ultrasonics, Ferroelectrics, and Frequency Control, IEEE Transactions on*, vol. 35, no. 3, pp. 297–305, May 1988.
- [57] D. A. Howe, J. L. LanFranchi, L. Cutsinger, A. Hati, and C. Nelson, "Vibration-induced pm noise in oscillators and measurements of correlation with vibration sensors," in *Frequency Control Symposium and Exposition, 2005. Proceedings of the 2005 IEEE International*, Aug. 2005, pp. 494–498.
- [58] J. R. Vig, *Quartz crystal resonators and oscillators for frequency control and timing applications a tutorial*, Open Tutorial, Aug. 2014.
- [59] B. Kim, M. Akgul, Y. Lin, W.-C. Li, Z. Ren, and C. T.-C. Nguyen, "Acceleration sensitivity of small-gap capacitive micromechanical resonator oscillators," in *Frequency Control Symposium (FCS), 2010 IEEE International*, Jun. 2010, pp. 273–278.
- [60] B. Kim, R. H. Olsson, K. Smart, and K. E. Wojciechowski, "Mems resonators with extremely low vibration and shock sensitivity," in *Sensors, 2011 IEEE*, Oct. 2011, pp. 606–609.
- [61] S. Yoneoka, J. C. Salvia, G. Bahl, R. Melamud, S. A. Chandorkar, and T. W. Kenny, "Active electrostatic compensation of micromechanical resonators under random vibrations," *Microelectromechanical Systems, Journal of*, vol. 19, no. 5, pp. 1270–1272, Oct. 2010.
- [62] T. L. Naing, T. O. Rocheleau, E. Alon, and C. T.-C. Nguyen, "A 78-microwatt GSM phase noise-compliant pierce oscillator referenced to a 61-MHz wine-glass disk resonator," in *European Frequency and Time Forum International Frequency Control Symposium (EFTF/IFC), 2013 Joint*, Jul. 2013, pp. 562–565.

- [63] V. Kaajakari, J. Kiihamaki, A. Oja, H. Seppa, S. Pietikainen, V. Kokkala, and H. Kuisma, "Stability of wafer level vacuum encapsulated single-crystal silicon resonators," in *Solid-State Sensors, Actuators and Microsystems, 2005. Digest of Technical Papers. TRANSDUCERS '05. The 13th International Conference on*, vol. 1, Jun. 2005, pp. 916–919.
- [64] S. Lee and C. T.-C. Nguyen, "Phase noise amplitude dependence in self-limiting wine-glass disk oscillators," in *Digest of Technical Papers, the 2004 Solid-State Sensors, Actuators and Microsystems Workshop*, Hilton Head Island, South Carolina, USA, Jun. 2004, pp. 33–36.
- [65] G. Duffing, *Erzwungene Schwingungen bei veranderlicher Eigenfrequenz und ihre technische Bedeutung*. Braunschweig: Vieweg & Sohn, 1918.
- [66] R. Lifshitz and M. C. Cross, "Nonlinear dynamics of nanomechanical and micromechanical resonators," in *Reviews of Nonlinear Dynamics and Complexity*, Weinheim: John Wiley & Sons, Ltd, 2009, pp. 1–52.
- [67] J. R. Clark, F. D. Bannon, A.-C. Wong, and C. T.-C. Nguyen, "Parallel-resonator HF micromechanical bandpass filters," in *Solid State Sensors and Actuator (Transducers'97), the 1997 International Conference on*, vol. 2, Jun. 1997, pp. 1161–1164.
- [68] H. Samavati, H. R. Rategh, and T. H. Lee, "A 5-GHz CMOS wireless LAN receiver front end," *Solid-State Circuits, IEEE Journal of*, vol. 35, no. 5, pp. 765–772, May 2000.
- [69] A. Homayoun and B. Razavi, "A 5-GHz 11.6-mW CMOS receiver for IEEE 802.11a applications," in *Custom Integrated Circuits Conference (CICC), 2013 IEEE*, Sep. 2013, pp. 1–4.
- [70] W.-T. Hsu, A. R. Brown, and K. R. Cioffi, "A programmable MEMS FSK transmitter," in *Solid-State Circuits Conference. ISSCC 2006. Digest of Technical Papers. IEEE International*, Feb. 2006, pp. 1111–1120.
- [71] L. R. O. F.R.S., "CXII. The problem of the whispering gallery," *Philosophical Magazine Series 6*, vol. 20, no. 120, pp. 1001–1004, 1910.
- [72] C. G. B. Garrett, W. Kaiser, and W. L. Bond, "Stimulated emission into optical whispering modes of spheres," *Phys. Rev.*, vol. 124, pp. 1807–1809, 6 Dec. 1961.
- [73] M. Tomes and T. Carmon, "Photonic micro-electromechanical systems vibrating at x-band (11-GHz) rates," *Phys. Rev. Lett.*, vol. 102, p. 113 601, 11 Mar. 2009.
- [74] J. Wang, Z. Ren, and C. T.-C. Nguyen, "1.156-GHz self-aligned vibrating micromechanical disk resonator," *Ultrasonics, Ferroelectrics, and Frequency Control, IEEE Transactions on*, vol. 51, no. 12, pp. 1607–1628, Dec. 2004.

- [75] R. Tabrizian, M. Rais-Zadeh, and F. Ayazi, "Effect of phonon interactions on limiting the  $f \cdot Q$  product of micromechanical resonators," in *Solid-State Sensors, Actuators and Microsystems Conference. TRANSDUCERS 2009. International*, Jun. 2009, pp. 2131–2134.
- [76] V. B. Braginsky, V. P. Mitrofanov, and V. I. Panov, *Systems with Small Dissipation*. Chicago: University Of Chicago Press, 1986.
- [77] S.-S. Li, Y.-W. Lin, Y. Xie, Z. Ren, and C. T.-C. Nguyen, "Micromechanical "hollow-disk" ring resonators," in *Micro Electro Mechanical Systems, 2004. 17th IEEE International Conference on. (MEMS)*, 2004, pp. 821–824.
- [78] T. L. Naing, T. Beyazoglu, L. Wu, M. Akgul, Z. Ren, T. O. Rocheleau, and C. T.-C. Nguyen, "2.97-GHz CVD diamond ring resonator with  $Q > 40,000$ ," in *Frequency Control Symposium (FCS), 2012 IEEE International*, Baltimore, USA, May 2012, pp. 570–575.
- [79] B. Bircumshaw, G. Liu, H. Takeuchi, T.-J. King, R. Howe, O. O'Reilly, and A. Pisano, "The radial bulk annular resonator: Towards a 50 $\Omega$  RF MEMS filter," in *Solid-State Sensors, Actuators and Microsystems (Transducers'03), the 12th International Conference on*, vol. 1, Jun. 2003, pp. 875–878.
- [80] Y. Xie, S.-S. Li, Y.-W. Lin, Z. Ren, and C. T.-C. Nguyen, "1.52-GHz micromechanical extensional wine-glass mode ring resonators," *Ultrasonics, Ferroelectrics, and Frequency Control, IEEE Transactions on*, vol. 55, no. 4, pp. 890–907, Apr. 2008.
- [81] G. R. Kline, K. M. Lakin, and K. T. McCarron, "Overmoded high  $Q$  resonators for microwave oscillators," in *Frequency Control Symposium, 1993. 47th., Proceedings of the 1993 IEEE International*, Jun. 1993, pp. 718–721.
- [82] E. Hwang and S. Bhave, "Transduction of high-frequency micromechanical resonators using depletion forces in p-n diodes," *Electron Devices, IEEE Transactions on*, vol. 58, no. 8, pp. 2770–2776, Aug. 2011.
- [83] T. O. Rocheleau, T. L. Naing, Z. Ren, and C. T.-C. Nguyen, "Acoustic whispering gallery mode resonator with  $Q > 109,000$  at 515MHz," in *Micro Electro Mechanical Systems (MEMS), 2012 IEEE 25th International Conference on*, Jan. 2012, pp. 672–675.
- [84] C.-M. Lin, Y.-Y. Chen, V. V. Felmetger, D. G. Senesky, and A. P. Pisano, "AlN/3C-SiC composite plate enabling high-frequency and high- $Q$  micromechanical resonators," *Advanced Materials*, vol. 24, no. 20, pp. 2722–2727, 2012.
- [85] M. Akgul and C. T.-C. Nguyen, "A passband-corrected high rejection channel-select micromechanical disk filter," in *Frequency Control Symposium (FCS), 2014 IEEE International*, May 2014, pp. 1–6.
- [86] R. A. Schneider and C. T.-C. Nguyen, "On/off switchable high- $Q$  capacitive-piezoelectric AlN resonators," in *Micro Electro Mechanical Systems (MEMS), 2014 IEEE 27th International Conference on*, Jan. 2014, pp. 1265–1268.

- [87] T. J. Cheng and S. A. Bhave, "High- $Q$ , low impedance polysilicon resonators with 10 nm air gaps," in *Micro Electro Mechanical Systems (MEMS), 2010 IEEE 23rd International Conference on*, Jan. 2010, pp. 695–698.
- [88] F. Ayazi, S. Pourkamali, G. Ho, and R. Abdolvand, "High-aspect-ratio SOI vibrating micromechanical resonators and filters," in *Microwave Symposium Digest, 2006. IEEE MTT-S International*, Jun. 2006, pp. 676–679.
- [89] D. Weinstein and S. A. Bhave, "Internal dielectric transduction in bulk-mode resonators," *Microelectromechanical Systems, Journal of*, vol. 18, no. 6, pp. 1401–1408, Dec. 2009.
- [90] G. Piazza, P. J. Stephanou, and A. P. Pisano, "Piezoelectric aluminum nitride vibrating contour-mode MEMS resonators," *Microelectromechanical Systems, Journal of*, vol. 15, no. 6, pp. 1406–1418, Dec. 2006.
- [91] A. Iula, N. Lamberti, and M. Pappalardo, "A model for the theoretical characterization of thin piezoceramic rings," *Ultrasonics, Ferroelectrics, and Frequency Control, IEEE Transactions on*, vol. 43, no. 3, pp. 370–375, May 1996.
- [92] K. Wang, A.-C. Wong, and C.-C. Nguyen, "VHF free-free beam high- $Q$  micromechanical resonators," *Microelectromechanical Systems, Journal of*, vol. 9, no. 3, pp. 347–360, Sep. 2000.
- [93] V. Tas, S. Olcum, M. Aksoy, and A. Atalar, "Reducing anchor loss in micromechanical extensional mode resonators," *Ultrasonics, Ferroelectrics, and Frequency Control, IEEE Transactions on*, vol. 57, no. 2, pp. 448–454, Feb. 2010.
- [94] M. Demirci and C. T.-C. Nguyen, "Higher-mode free-free beam micromechanical resonators," in *Frequency Control Symposium and PDA Exhibition Jointly with the 17th European Frequency and Time Forum, 2003. Proceedings of the 2003 IEEE International*, May 2003, pp. 810–818.

# Appendix A

## Spoke-Supported Ring Resonator Design Details

### A.1 Device Structure and Operation

To excite the device of Fig. 9.4(a) in its two-port configuration, a dc-bias voltage  $V_P$  is applied to the conductive ring and an ac signal  $v_{in}$  to its inner (i.e., drive or input) electrodes. Note that the application of the dc-bias  $V_P$  serves only to charge the electrode-to-resonator capacitance. No dc current flows, so no dc power is consumed. Together, these voltages applied across the small inner capacitive gaps generate a radial electrostatic input force  $F_{in}$  at the frequency of  $v_{in}$  given by

$$F_{in} = \frac{1}{2} \left( \frac{\partial C_{o,in}}{\partial r} \right) (V_P - v_{in})^2 \cong -V_P \left( \frac{\partial C_{o,in}}{\partial r} \right) v_{in} \quad (\text{A.1})$$

where the rightmost form retains only the ac term at the frequency of  $v_{in}$ .  $\partial C_{o,in}/\partial r$  is the change in electrode-to-resonator overlap capacitance per unit radial displacement at the input port, given under a small-signal parallel-plate approximation as

$$\frac{\partial C_{o,in}}{\partial r} = \frac{\varepsilon_0 A_{in}}{d_o^2} \quad (\text{A.2})$$

where  $A_{in}$  is the combined static electrode-to-resonator overlap area of all input ports in the hookup of Fig. 9.4(a), and  $d_o$  is the electrode-to-resonator gap spacing. When the frequency of  $v_{in}$  matches that of one of the resonance modes, the resulting force applied to the inner perimeter drives the ring into the vibration mode shape of that mode. Figure 9.5 presents the first two radial-contour mode shapes, the second of which is of most interest here, since it offers a balanced shape with a nodal circle that helps to maximize  $Q$ . As shown, this mode shape expands and contracts radially around a nodal circle within the ring, with the ring's inner and outer perimeters moving in phase and in opposite directions, with a zero-to-peak resonance radial displacement amplitude at the inner perimeter given by

$$\Re(r_i) = \frac{QF_{in}}{k_{rei}} = \frac{Q}{k_{rei}} V_P \frac{\partial C_{o,in}}{\partial r} v_{in} \quad (\text{A.3})$$

where  $k_{rei}$  is the equivalent dynamic stiffness at a location along the inner perimeter of the ring (for force on the inner edge of the ring as in Fig. 9.4(a) a force on the outer perimeter would require stiffness evaluated on the outer edge) that includes both mechanical and electrical [26] components. Assuming a radial-contour mode shape, e.g., no  $\theta$  dependence, the corresponding resonance displacement amplitude at the outer perimeter is then given by

$$\Re(r_o) = \frac{\Re_{mode}(r_o)}{\Re_{mode}(r_i)} \Re(r_i) = \frac{\Re_{mode}(r_o)}{\Re_{mode}(r_i)} \frac{QV_P}{k_{rei}} \frac{\partial C_{o,in}}{\partial r} v_{in} \quad (\text{A.4})$$

where  $\Re_{mode}(r)$  is a function describing the relative radial displacement in the mode shape of the ring at radial location  $r$ , given later in Section A.2.

The radial vibration of the spoke-supported ring at the outer perimeter in turn creates a dc-biased (by  $V_P$ ) time-varying capacitance between the outer edge of the ring and its output (i.e., sense) electrode. This varying capacitance then sources an output current  $i_{out}$  proportional to the amplitude of vibration at the outer perimeter of the ring, with resonance magnitude given in phasor form by

$$\begin{aligned} i_{out} &= V_P \frac{\partial C_{o,out}}{\partial r} \frac{\partial \Re(r_o)}{\partial t} \\ &= \frac{\Re_{mode}(r_o)}{\Re_{mode}(r_i)} \frac{Q\omega_o}{k_{rei}} \frac{\partial C_{o,in}}{\partial r} \frac{\partial C_{o,out}}{\partial r} V_P^2 v_{in} \end{aligned} \quad (\text{A.5})$$

where Eqn. (A.4) has been used;  $\partial C_{o,out}/\partial r$  is the change in electrode-to-resonator overlap capacitance per unit radial displacement at the output port; and where the output electrode is assumed grounded. The output current is proportional to the change in electrode-to-resonator overlap capacitance per unit radial displacement at both the input and output ports, and inversely proportional to the equivalent dynamic stiffness.

As derived, Eqn. (A.5) corresponds to the case where the input force is applied at precisely the resonance frequency of the spoke-supported ring. This can be further simplified through the introduction of the equivalent series motional resistance of the device,  $R_x$ , given by

$$R_x = \frac{v_{in}}{i_{out}} = \frac{k_{rei}}{Q\omega_o} \frac{\partial C_{o,in}}{\partial r} \frac{\partial C_{o,out}}{\partial r} \frac{\Re_{mode}(r_i)}{\Re_{mode}(r_o)} \quad (\text{A.6})$$

With this substitution and incorporating the standard Lorentzian frequency response of any resonator, the overall transfer function from input voltage to output current becomes

$$\frac{i_{out}}{v_{in}} = \frac{1}{R_x} \frac{(\omega_o/Q) s}{s^2 + (\omega_o/Q) s + \omega_o^2} \quad (\text{A.7})$$

Recognizing Eqn. (A.7) as the transfer function for a classic bandpass biquad, the electrical response of the micromechanical resonator in the hook-up of Fig. 9.4(a) equates to that of a single *LCR* electrical circuit. In short, via action of the spoke-supported ring resonator, the electrical input signal  $v_{in}$  is converted to a mechanical signal at the input port, filtered (with high  $Q$ ) in the mechanical domain, then re-converted to an electrical signal at the output port, ready for further processing by subsequent stages.

## A.2 Resonator Frequency Design

Having described the qualitative operational aspects of the spoke-supported ring, analytical formulations governing the precise frequency design of this device are now in order. Pursuant to maintaining a practical formulation, this analysis assumes that the ring thickness is thin compared to its lateral dimensions ( $h \ll r_i$ )—a very reasonable assumption for the surface-micromachined devices of this work, where thicknesses on the order of 2 or 3  $\mu\text{m}$  are indeed small compared to lateral dimensions of tens of microns. The analysis further assumes that the top and bottom faces of the ring are free of intrinsic stress; and since the structure is thin and forces are applied in only the lateral directions, the vertical stress components also vanish throughout its bulk.

With these assumptions, and given axial-symmetry, i.e.,  $\partial u_r / \partial \theta = 0$ , and  $u_\theta = 0$ , the constitutive equations for the stress tensor  $T_{ij}$  of an ideal ring, such as depicted in inset of Fig. 9.4(a), reduce to [91]

$$\begin{aligned} T_{rr} &= c_{11}^E \frac{\partial u_r}{\partial r} + c_{12}^E \frac{u_r}{r} \\ T_{\theta\theta} &= c_{12}^E \frac{\partial u_r}{\partial r} + c_{11}^E \frac{u_r}{r} \\ T_{r\theta} &= 0 \end{aligned} \quad (\text{A.8})$$

where  $u_r$  is the displacement along the radial direction.  $c_{11}^E$  and  $c_{12}^E$  are elastic stiffness constants to be defined in detail later. Substituting the stress components of Eqn. (A.8) into the radial form of the wave equation given by [91] yields

$$c_{11}^E \left[ \frac{\partial^2 u_r}{\partial r^2} + \frac{1}{r} \frac{\partial u_r}{\partial r} - \frac{u_r}{r} \right] = \rho \ddot{u}_r \quad (\text{A.9})$$

where  $\rho$  is the mass density of the ring structural material. Assuming that the ring is driven by an ac voltage  $v_{in} = V_{in} e^{j\omega t}$ , it follows that

$$\frac{\partial^2 U_r}{\partial r^2} + \frac{1}{r} \frac{\partial U_r}{\partial r} + \left[ \frac{\omega^2}{(v^p)^2} - \frac{1}{r^2} \right] U_r = 0 \quad (\text{A.10})$$

where  $v^p = \sqrt{c_{11}^E / \rho}$  is the acoustic velocity of the material and  $c_{11}^E$  can now be interpreted as its Young's modulus. The general solution of Eqn. (A.10) for contour modes becomes

$$U_r = \Re(r) \cdot e^{j\omega t} = [MJ_1(\rho r) + NY_1(\rho r)] e^{j\omega t} \quad (\text{A.11})$$

which represents the mode shape of the ring at its different resonance frequencies under the assumption that the effect of the support beams on ring motion is negligible, as can be achieved using the quarter-wavelength strategy discussed later in section A.3. Here,  $\rho = \omega_o/v^p$  is a frequency parameter, and  $J_n$  and  $Y_n$  represent  $n^{\text{th}}$  order Bessel functions of the first and second kind, respectively. The constants  $M$  and  $N$  are chosen to satisfy the stress-free boundary conditions at the inner and outer edges of the ring

$$T_{rr} = 0 \quad \text{at} \quad r = r_i \text{ and } r = r_o \quad (\text{A.12})$$

Combining Eqns. (A.8), (A.11), and (A.12), the ratio of constants  $N$  over  $M$  can be written

$$\begin{aligned} \frac{N}{M} &= -\frac{r_i G_J(r_o) - r_o G_J(r_i)}{r_i G_Y(r_o) - r_o G_Y(r_i)} \\ G_J(r) &= pr J_0(pr) - J_1(pr) (1 - \sigma) \\ G_Y(r) &= pr Y_0(pr) - Y_1(pr) (1 - \sigma) \end{aligned} \quad (\text{A.13})$$

where  $\rho = c_{12}^E/c_{11}^E$  can be interpreted as a planar Poisson ratio. This is especially the case for the devices of this work, since their structural materials are isotropic in the plane normal to the  $z$  axis.

Use of Eqns. (A.11) and (A.12) now yields the frequency equation

$$\begin{aligned} &[J_1(pr_i)\sigma - J_1(pr_i) + r_i p J_0(pr_i)] \times [Y_1(pr_o)\sigma - Y_1(pr_o) + r_o p Y_0(pr_o)] \\ &- [Y_1(pr_i)\sigma - Y_1(pr_i) + r_i p Y_0(pr_i)] \times [J_1(pr_o)\sigma - J_1(pr_o) + r_o p J_0(pr_o)] = 0 \end{aligned} \quad (\text{A.14})$$

After solving Eqn. (A.14) to obtain frequency parameter  $p$ , the mechanical resonance frequency of the ring structure,  $f_{nom}$ , readily follows via

$$f_{nom} = \frac{\omega_{nom}}{2\pi} = \frac{p}{2\pi} \sqrt{\frac{E}{\rho(1-\sigma^2)}} \quad (\text{A.15})$$

where  $\omega_{nom}$  is the radian nominal mechanical resonance frequency, and  $E$  is the Young's modulus of the structural material. The first solution of Eqn. (A.14) gives the first mode resonance of Fig. 9.5(a), and the second solution gives the second mode resonance of Fig. 9.5(b), and so forth.

Using Eqn. (A.15), Fig. A.1 plots (using dotted curves) the in-plane extensional resonance frequencies for a 2 $\mu\text{m}$ -thick ring with 20  $\mu\text{m}$  outer radius normalized to the fundamental mode frequency of a 20- $\mu\text{m}$ -radius solid disk as a function of the ratio of inner radius-to-outer radius  $r_i/r_o$  and as a function of mode. Figure A.2 further presents several simulated curves describing the shapes associated with these modes. As expected, the resonance frequency of the first mode equals that of a thin disk [74] when  $r_i/r_o=0$ , then decreases

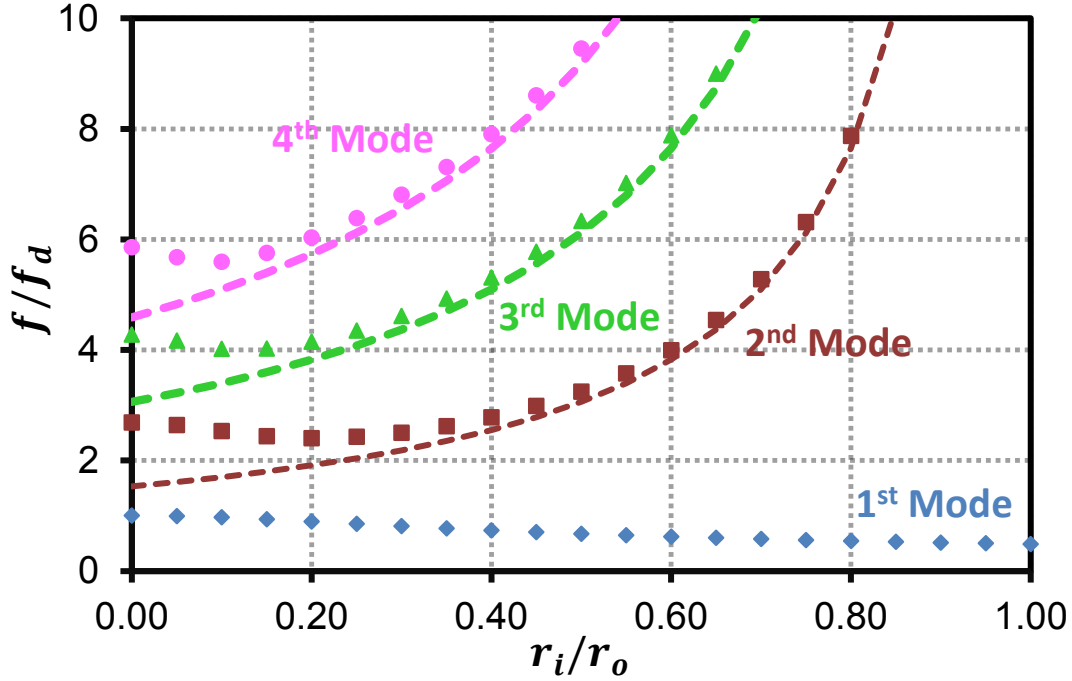


Figure A.1: Plot of the resonance frequency of a spoke-supported ring with  $r_o=20\ \mu\text{m}$  and variable  $r_i$  in its 1<sup>st</sup>, 2<sup>nd</sup>, 3<sup>rd</sup>, and 4<sup>th</sup> modes. The dotted lines show the behavior using Eqn. (A.16).  $f_d$  is the fundamental resonance frequency of a solid disk with radius  $r_o$ .

as  $r_i/r_o$  rises to a lowest point of 0.4867 times that of a disk when  $r_i/r_o=1$ . Here, the first mode frequency approximately varies as the reciprocal of the average of the inner and outer radii of the structure and can be thought of as extensional around the contour of a “hollowed out” disk.

The higher radial-contour modes differ in that they are extensional around the width of the annulus, rather than the contour of the hollow disk. Their frequencies thus vary as the reciprocal of the annulus width ( $r_o - r_i$ ), rather than average radius as for a disk resonator, effectively decoupling design criteria for frequency and impedance. Specifically, frequency depends mainly on ring width, and not average radius, while impedance depends mainly on average radius. This decoupling of frequency and impedance design opens the door for a capacitively-transduced resonator that simultaneously achieves GHz frequency and low impedance.

To capture the strong dependence of higher mode frequency on ring width, rather than average radius, Eqn. (A.15) can be approximated by an expression for the higher extensional modes

$$f_{nom/approx.} = \frac{n-1}{2W_r} \sqrt{\frac{E}{\rho}}, n = 2, 3, 4, \dots \quad \text{for } \frac{r_i}{r_o} > \frac{1}{n} \quad (\text{A.16})$$

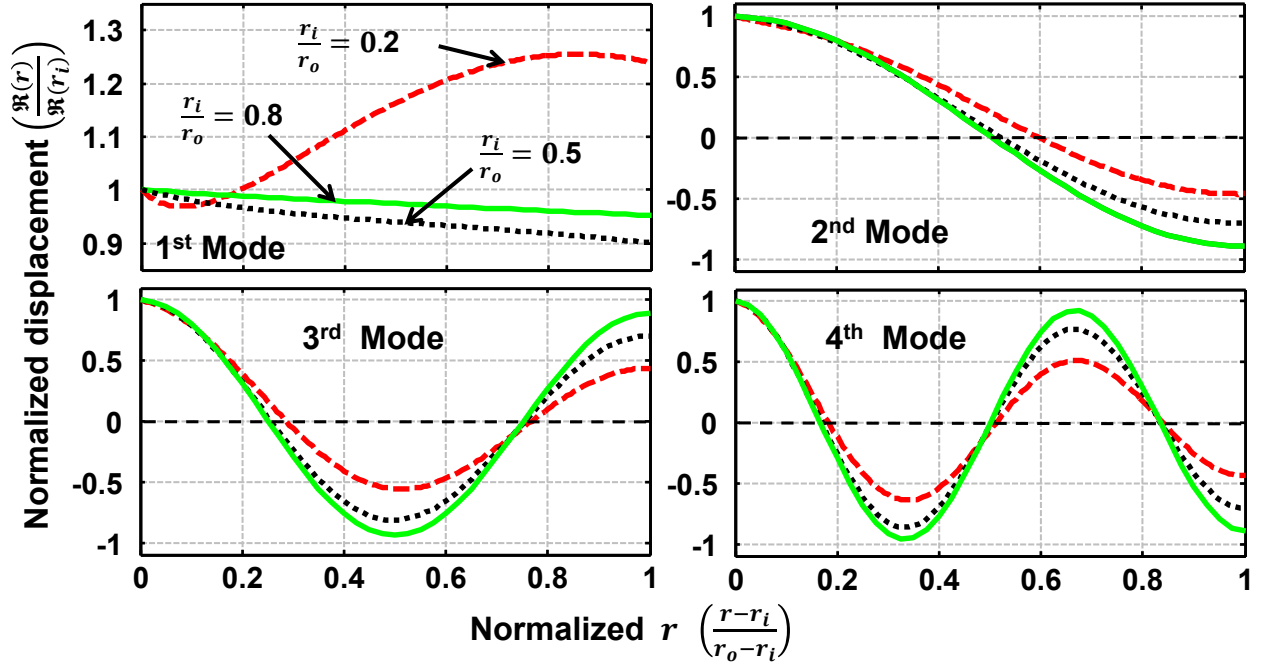


Figure A.2: The first, second, third, and fourth mode shapes for spoke-supported rings with  $r_i/r_o=0.2$ ,  $r_i/r_o=0.5$ , and  $r_i/r_o=0.8$ , all with  $r_o=20\ \mu\text{m}$ .

where  $W_r = (r_o - r_i)$  is the radial ring width, and  $n$  is the order of the vibration mode. The dashed curves in Fig. A.1 are those generated by Eqn. (A.16), which are seen to be accurate for  $r_i/r_o > 1/n$ . This expression is similar to the approximate expression for the extensional Wine-Glass ring (i.e., Eqn. (6) in [80]), except that the spoke-supported ring allows mode shapes for any integer value of  $n$ , rather than the solely odd values permitted by the extensional Wine-Glass ring solutions.

### A.3 Support Design

The preceding analysis assumed negligible effect of the support beams on resonator motion. If not properly designed, however, the support beams can influence not only the  $Q$  of the ring resonator, but also mode shape and resonance frequency. The key to maximizing practically all aspects of a resonator’s performance is to minimize the influence of its support beams. Ultimately, the design that optimizes  $Q$  in fact also sets the resonance frequency equal to the value expected for an ideal ring with no supports and sets the mode shape to that expected for an unsupported (i.e., levitated) ring. The spoke support used in this work attempts to achieve “virtual levitation” [92] to provide a degree of anchor isolation far superior to its predecessors.

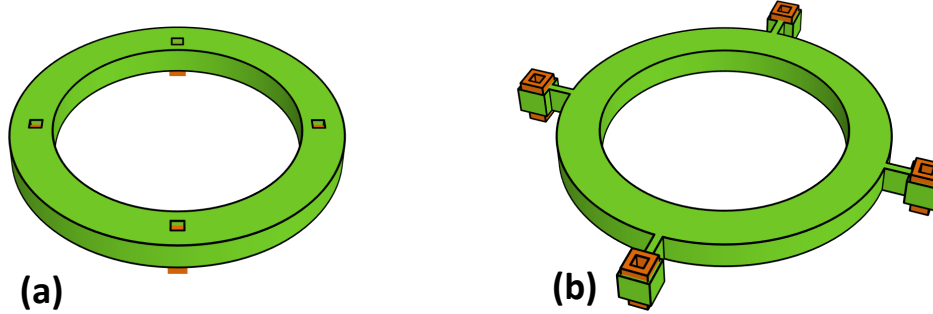


Figure A.3: Perspective-views of (a) a radial ring resonator in [79] and (b) an extensional Wine-Glass mode ring resonator of [80].

### A.3.1 Maximizing Resonator $Q$

To highlight the advantages of the spoke support used in this work, Fig. A.3 presents two previous ring resonator support designs for comparison with the present design of Fig. 9.4. The first of these, in Fig. A.3(a) locates anchors on the nodal line (actually, circle) of the second contour mode, i.e., of the mode in Fig. 9.5(b). Although locating anchors at nodal points—as done in [74] and some versions of [13], [80]—does reduce energy transfer from a vibrating resonator to its anchors by virtue of the very little (ideally no) motion occurring at the nodes, some energy is still lost since the anchors are inevitably finite in size, and thus, still attach to non-nodal (i.e., moving) locations immediately around the nodal points.

The suspension design of Fig. A.3(b) solves this problem by taking advantage of the transmission line-like behavior of its support beams at high frequency and dimensions them to correspond to effective quarter-wavelengths that then generate acoustic impedance-mismatches between the ring resonator and its anchors, reflecting wave energy back into the ring structure, minimizing energy losses, and maximizing the system  $Q$ .

The use of quarter-wavelength supports to maximize the  $Q$ 's of micromechanical resonators and filters is well documented in the literature [41], [80], [92], [93]. Indeed, the basic strategy of dimensioning a support to correspond to an odd multiple of a quarter wavelength at the frequency of resonance in order to transform the (ideally) infinite mechanical impedance at a fixed anchor to zero impedance at the support-to-resonator attachment location, has been instrumental here in attaining the highest  $Q$  micromechanical resonators, to date. In effect, if the supports can be made to present zero acoustic impedances at locations where they attach to a resonator structure, the resonator effectively “sees” no anchors at resonance, so is effectively isolated from its surroundings (i.e., from its substrate) and vibrates as if it were virtually levitated, with ideally no path for energy loss to its surroundings.

### A.3.2 Realizing Exact Quarter-Wavelength Dimensions

Alas, although quarter-wavelength design is seen to maximize  $Q$  [92], [94], its ultimate efficacy depends upon device design, and seems to be governed in large part by the degree to which quarter-wavelength dimensions can be exactly realized. The difficulty in specifying exact dimensions stems from not only the finite tolerances of the lithographic and etching processes used to define a resonator and its supports; but also from mode shape complexities that introduce loss when the support-to-resonator attachment cannot occur at a single point, but rather over a finite length, over which the attachment impedance might be complex and distributed.

For example, the support structure used for an extensional Wine-Glass mode ring resonator [80], depicted in Fig. A.3(b), would ideally attach to the ring resonator at a single point on the radial node line at the ring's outer edge. At this single point attachment, the motion of the ring is mainly rotational but not entirely, since there is a small tangential component. Although small, this tangential component still presents a path for anchor loss that should be removed if resonator  $Q$  is to be maximized. Additionally, even if the support attachment location were purely rotational, an exact quarter-wavelength support is not easy to achieve in this design due to the finite support beam width, over which the attachment boundary condition is comprised of both radial and rotational components (in addition to the tangential one already discussed). In this case, the simple boundary condition used to design the support beam is not quite appropriate, especially at high frequencies, where the finite attachment width becomes a larger fraction of the acoustic wavelength. As a result, the extensional Wine-Glass ring resonator of [80] was constrained to  $Q$ 's  $< 10,000$ .

On the other hand, the radial-contour mode shape of the spoke-supported ring resonator of this work presents a simpler support-to-resonator attachment interface, where all points at the interface experience only radial movements, as shown in Fig. 9.5. This means that a spoke support beam anchored at one end and designed to vibrate extensionally, as shown in Fig. 9.5, with dimensions corresponding to a quarter-wavelength at the frequency of the ring contour-mode resonance, will vibrate so that its free end provides an attachment that presents zero impedance to the ring inner sidewall at all attachment points, i.e., over the full width of the attachment. In other words, the simpler boundary condition of the contour-mode ring of Fig. 9.5 allows its balanced center-anchored spoke support to present a more ideal free attachment to the ring than tethered outer supports allow at the more complex attachment points of the extensional Wine-Glass ring of [80], allowing the former to achieve superior  $Q$ .

### A.3.3 Quarter-Wavelength Spoke Support Design

One simple way to specify quarter wavelength spoke support dimensions for the ring of Fig. 9.4 draws from an understanding of its lumped parameter mechanical equivalent circuit [39]. Figure A.4 presents two equivalent circuit choices: (a) the mobility analogy, in which nodes represent velocities; and (b) the impedance analogy in which nodes represent forces;

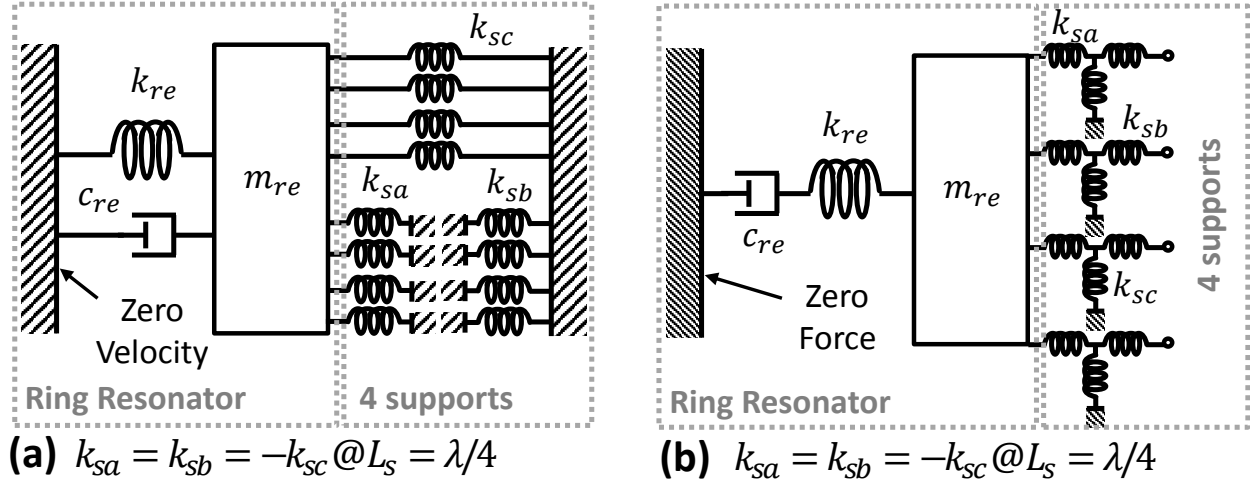


Figure A.4: Equivalent lumped mechanical model for a micromechanical spoke-supported ring resonator (a) using the mobility analogy, in which nodes represent velocities; and (b) using the impedance analogy, in which nodes represent forces.

each for a location at the inner edge of the spoke-supported ring of Fig. 9.4. These circuits are equivalent duals, and either can be used to model the spoke-supported ring. However, since the present device takes a voltage input to induce an electrode-to-resonator force, it is perhaps more intuitive to interpret nodes as forces as in the impedance analogy. For this reason, the impedance analogy of Fig. A.4(b) is used in the following analysis.

In Fig. A.4(b), the ring by itself is modeled well by a series mass-spring-damper circuit with element values specific to the chosen location at the inner edge of the ring. The model for the spoke-supported ring must include circuit branches that represent its four support beams, in this case  $T$ -networks of positive and negative springs that model their transmission line behavior at high frequencies. Via straightforward circuit analysis, the resonance frequency of this single degree of freedom mechanical system is easily determined to be

$$f_{om} = \frac{\omega_{om}}{2\pi} = \frac{1}{2\pi} \sqrt{\frac{k_{mre} + 4k_{sc} + 4k_{sa}}{m_{mre}}} \quad (\text{A.17})$$

where  $f_{om}$  is the mechanical resonance frequency without electrical effects,  $m_{mre}$  and  $k_{mre}$  are equivalent core mechanical mass and stiffness, respectively, of a ring resonator at the support attachment location(s), and where  $k_{sa}$  (or  $k_{sb}$ ) and  $k_{sc}$  model the equivalent stiffnesses of the support beams, where all support beams are assumed identical, as is the case in the current work. Eqn. (A.17) shows that the supports can significantly influence the resonance frequency of a ring if  $(k_{sc} + k_{sa})$  is not equal to zero. It follows that if the quantity  $(k_{sc} + k_{sa})$  can be set to zero by design, then this dependency disappears, and the ring frequency is as if there were no supports. Quarter-wavelength design is key to achieving this.

To see this, first recognize that the impedance analogy lumped mechanical circuit for each

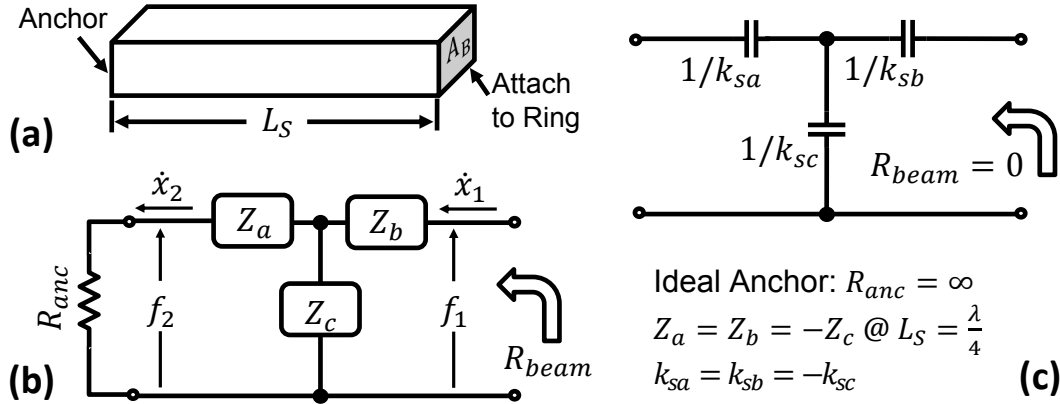


Figure A.5: Equivalent circuits for supporting beams. The beam (a) is modeled as a general transmission-line to give the effective  $T$ -network models (b). (c) shows the ideal  $T$ -network model when exact quarter wavelength design is used.

support of Fig. A.4(b) reduces to the equivalent circuit of Fig. A.5(b), where the springs in the mechanical  $T$ -network are simply replaced by impedances  $Z_a$ ,  $Z_b$ , and  $Z_c$ . The values of these elements can be determined from the matrix governing the mechanical impedance behavior of each support beam as seen by the attached resonator, given by [34]

$$\begin{aligned} \begin{bmatrix} \dot{x}_1 \\ f_1 \end{bmatrix} &= \begin{bmatrix} \cos(\alpha L_S) & jZ_0 \sin(\alpha L_S) \\ j \sin(\alpha L_S)/Z_0 & \cos(\alpha L_S) \end{bmatrix} \begin{bmatrix} \dot{x}_2 \\ f_2 \end{bmatrix} \\ &= \begin{bmatrix} A & B \\ C & D \end{bmatrix} \begin{bmatrix} \dot{x}_2 \\ f_2 \end{bmatrix} \end{aligned} \quad (\text{A.18})$$

where  $L_S$  is the beam length,  $Z_0$  is the characteristic mobility  $1/(A_B \sqrt{\rho E})$ ,  $\alpha$  is the propagation constant  $\omega_o/v_e$ ,  $v_e$  is the velocity  $\sqrt{E/\rho}$  of an extensional wave,  $A_B$  is the cross section area of the support beam, and  $\dot{x}_1$ ,  $\dot{x}_2$ ,  $f_1$ , and  $f_2$  are the velocities and forces at the ends of the support beam.

Equating the circuit of Fig. A.5(b) to the chain network described by Eqn. (A.18) [24], then solving for the series and shunt impedances in terms of chain matrix elements, yields

$$Z_a = Z_b = \frac{D-1}{B} = \frac{j}{Z_0} \tan\left(\frac{\alpha L_S}{2}\right) \quad (\text{A.19})$$

$$Z_c = \frac{1}{B} = \frac{-j}{Z_0 \sin(\alpha L_S)} \quad (\text{A.20})$$

Again, to eliminate support-induced resonance frequency offsets, support beam dimensions should be chosen so that the series and shunt arm impedances of Fig. A.5(a) take on equal

values and opposite signs at the ring resonance frequency, thereby canceling one another—a condition achieved when the dimensions of each support beam correspond to an effective quarter-wavelength. By inspection of Eqns. (A.19) and (A.20),  $Z_a$  and  $Z_c$  meet this condition when

$$D = \cos(\alpha L_S) = 0 \quad (\text{A.21})$$

The solution to Eqn. (A.21) yields the  $L_S$ 's that correspond to effective quarter-wavelengths at the operating frequency. (Note that there are multiple such lengths, allowing a designer to choose the value that works best with the geometry in mind.) With quarter wavelength support dimensions, the impedances of Fig. A.5(b) then become

$$Z_a = Z_b = \frac{j}{Z_0} = \frac{k_{sa}}{j\omega} \quad (\text{A.22})$$

$$Z_c = -\frac{j}{Z_0} = \frac{k_{sc}}{j\omega} \quad (\text{A.23})$$

In the electrical domain, Eqn. (A.22) corresponds to capacitors of value  $(1/k_{sa})$  and  $(1/k_{sc})$ , respectively, and the circuit reduces to the purely electrical form of Fig. A.5(c). Analysis of this circuit confirms that the impedance seen looking into the left side is zero, i.e., the support corresponds to a quarter-wavelength, when  $k_{sa} = k_{sb} = -k_{sc}$ , with stiffnesses governed by

$$k_{sa} = -k_{sc} = \omega_{om} A_B \sqrt{\rho E} \quad (\text{A.24})$$

where  $\omega_{om}$  is the radian mechanical resonance frequency of the device defined in Eqn. (A.17). Ultimately, when quarter-wavelength support dimensions are used, the lumped mechanical circuit model for the spoke-supported ring reduces to that shown in Fig. A.5(c), where all supports “cancel” out, leaving the ring itself in a “virtually levitated” state, where it operates as if it has no supports.

As an example, Fig. A.6 presents plots of the mechanical impedances at 433 MHz for a  $1\mu\text{m}$ -wide,  $2\mu\text{m}$ -thick support beam as a function of its length. Here, the impedances  $Z_a$  and  $Z_c$  are proportional to the mechanical stiffnesses  $k_{sa}$  and  $k_{sc}$ , respectively, as governed by Eqns. (A.22) and (A.23); while  $(Z_a + Z_c)$  is the total effective impedance affecting the resonator system in Fig. A.4(b). Once the length of the support beam  $L_S$  reaches the values corresponding to single or multiple quarter-wavelengths, this effective impedance  $(Z_a + Z_c)$  becomes zero as simulated in Fig. A.6 and has (ideally) no effect on the resonator system.

### A.3.4 The Center Anchor Advantage

It should be noted that “virtual levitation” can only be achieved under ideal conditions, when

1. each support is exactly dimensioned to quarter-wavelength specifications; and

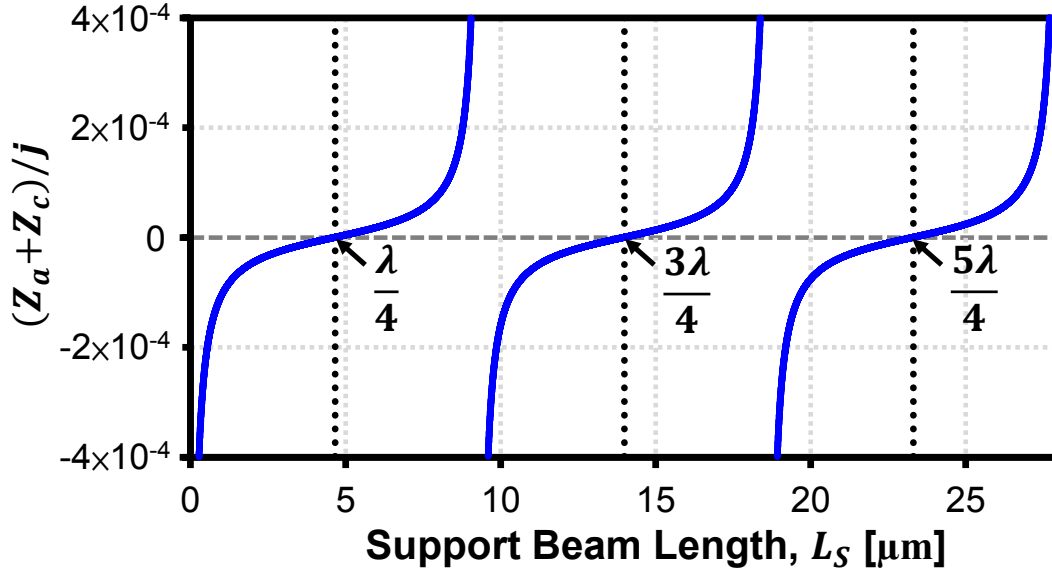


Figure A.6: Effective mechanical impedance,  $(Z_a + Z_c)/j$ , seen by a 433 MHz ring resonator for a  $1\mu\text{m}$ -wide,  $2\mu\text{m}$ -thick diamond support beam.

2. the anchors to which the supports attach are infinitely rigid, i.e., they present infinite acoustic impedances to the support beams.

Section A.3.1 already described how the spoke-supported ring can more effectively meet the first criterion than other designs, since the displacements along its support-to-ring attachment line are more uniform. Note that for the center supported design described here, a finite size stem causes a slight perturbation from the ideal beams. This, however, simply shifts slightly the beam length required for exact quarter-wavelength operation and does not change the overall behavior.

The second criterion follows from the fact that since a quarter-wavelength support operates by transforming an infinite anchor acoustic impedance to zero at the resonator attachment location, the degree to which it is effective is only as good as the degree to which the anchor impedance is truly infinite. In this respect, the spoke-support design of Fig. 9.5, with its centrally-located anchor and symmetrically-placed radial extensional-mode support beams, is far superior to alternatives. In particular, if every support beam is paired with an identical clone on the opposite side of the center anchor, like that shown in Fig. 9.4, then as long as perfect symmetry is achieved, any motion induced on the anchor by any one support is cancelled by the equal and opposite motion of the support on the other side of the anchor, and effectively, the very center of the anchor becomes an infinitely rigid end condition. This in turn allows a quarter-wavelength support to much more effectively present zero impedance to the ring at the attachment location, thereby much more effectively providing a state of virtual levitation.

As an additional advantage of the center support design, the balanced forces on the center peg anchor produce effective infinite stiffness, thereby reflecting incident acoustic energy and preventing dissipation to the substrate thus enhancing resonator  $Q$  even in the case of non-exact quarter-wavelength supports. While a non-quarter-wavelength design fails to provide a zero impedance load to the resonator, and so perturbing the mode shape and frequency, the center anchor design would still be expected to enable high- $Q$  operation, even in the face of real-world deviations from perfect support design.

The importance of attaining exact quarter-wavelength supports is perhaps best illustrated by visual comparison of the ring mode shapes achieved when the supports are perfectly quarter-wavelength versus a case where they are slightly off. To illustrate, Fig. 9.6 presents finite element (FEM) modal analyses on a spoke-supported ring resonator for the case of (a) quarter-wavelength ( $3\lambda/4$ ) support beams for a designed ring resonance frequency of 951.8 MHz, and (b) purposely non quarter-wavelength design ( $2.85\lambda/4$ ), where the resonance frequency now shifts to 954.4 MHz. Here, quarter-wavelength design leads to a symmetric and purely radial mode shape shown in Fig. 9.6(a). In contrast, slight deviation from quarter-wavelength in (b) distorts the ring's radial mode and induces consequent acoustic energy losses to the substrate that lowers the resonator's  $Q$ .

Additionally, if quarter-wavelength supports work by minimizing energy transfer from the ring attachment location on one-side of the support beam to the anchor on the other, then it makes sense to minimize as much as possible the movement at the ring attachment location. This can be done by attaching the support beam at a node in the resonance mode shape, where ideally there is zero motion. Figure 9.4(a) presents a ring design that employs this strategy, where the support beam is attached at the nodal circle in the  $n = 2$  mode shape using a simple notch [77].

### A.3.5 Practical Spoke-Supported Ring Design

Since quarter-wavelength design constrains the lengths of the support beams to a specific value for the desired ring resonance frequency, the use of centrally-anchored supports in this device forces a sequenced design procedure, where the support structure must be designed first. The design sequence is such that the length of the radial support beams  $L_S$  is first set to correspond to one or more (odd numbered) quarter-wavelengths at the desired resonance frequency  $f_o$ . Use of Eqn. (A.21) yields

$$L_S = \frac{n\sqrt{E/\rho}}{4f_{om}}, n = 1, 3, 5, \dots \quad (\text{A.25})$$

where  $E$  and  $\rho$  are the Young's modulus and density, respectively, of the structural material,  $f_{om}$  is defined in Eqn. (A.17), and  $n$  is the odd number of multiple quarter-wavelengths. The value of  $L_S$  then sets the inner radius of the ring  $r_i$ ; i.e.,  $r_i = L_S$ . The outer radius  $r_o$ , can now be determined by solving Eqn. (A.14).

It should be noted from Eqn. (A.14) that the frequency of this device is independent of thickness to first order. As such, filters at many different frequencies, such as required

by multi-band and RF channel-select applications, can be achieved in a single fabrication run, with one structural film deposition. This is a distinct advantage over most piezoelectric counterparts (e.g., FBARs, crystals) for which frequency is often determined primarily by thickness, making it difficult to manufacture several different multi-band frequencies on the same chip without the need for several structural film depositions, one for each frequency.

## A.4 Lumped Parameter Equivalent Circuits

Given that the spoke-supported ring targets RF frequency control applications, where the device will very likely populate some form of mechanical circuit [39], [40] that in turn must interface with transistor circuits [41], an electrical equivalent model for the device is paramount. Such a model is best derived by first specifying a lumped mechanical equivalent circuit for the spoke-supported ring, then using this to formulate an electrical circuit suitable for simulation using SPICE [42] or other circuit simulators.

### A.4.1 Lumped Parameter Mechanical Equivalent Circuit

Figure A.4 in Section A.3 already presented lumped mechanical equivalent circuits in two analogies for a location on the inner edge of the spoke-supported ring. Each circuit is comprised of a mass-spring-damper that models the core ring resonator structure and either  $\pi$ - or  $T$ -networks of springs that model its supports when using the mobility or impedance analogies, respectively. For reasons already mentioned, this work uses the impedance analogy of Fig. A.4(b).

Since this lumped circuit attempts to model a device that is actually distributed in nature, the elements of the circuit are location dependent, which means there is a unique equivalent circuit for every specific location on the ring. Regardless of location, the element values will depend fundamentally on the peak total kinetic energy in the vibrating spoke-supported ring, which can be determined for the ring operating in a radial-contour mode by integrating the kinetic energies of all infinitesimal mass elements  $dm$  making up the ring to yield

$$KE_{tot} = \frac{1}{2} \int_0^{2\pi} \int_{r_i}^{r_o} dm \times [v(r, \theta)]^2 \quad (\text{A.26})$$

where  $v(r, \theta)$  is the radial velocity magnitude at location  $(r, \theta)$  given by

$$v(r) = \omega \mathfrak{R}(r) = \omega [M J_1(pr) + N Y_1(pr)] \quad (\text{A.27})$$

Here,  $\omega$  is the radian frequency of motion, and the infinitesimal mass element takes the form  $dm = \rho \times h \times r d\theta \times dr$ .

The equivalent mass at position  $(r, \theta)$  is defined as peak kinetic energy divided by one-half the square of the velocity at that location [34]. Applying this to locations on the inner and outer perimeters of the spoke-supported ring, yields

$$m_{mr}(r_{i,o}, \theta) = \frac{KE_{tot}}{0.5[v(r_{i,o}, \theta)]^2} = \frac{\rho h \int_0^{2\pi} \int_{r_i}^{r_o} r [\Re(r)]^2 dr d\theta'}{[\Re(r_{i,o}, \theta)]^2} \quad (\text{A.28})$$

The equivalent stiffness at a location  $(r, \theta)$  is simply the multiplication of the equivalent mass at the location and the square of the resonance frequency. For locations on inner and outer perimeters, it takes form as:

$$k_{mr}(r_{i,o}, \theta) = \omega_{om}^2 m_{mr}(r_{i,o}, \theta) \quad (\text{A.29})$$

To specify an equivalent circuit like that of Fig. A.4, a reference point must be chosen that determines the values of the core mass-spring-damper circuit. The convention is typically to choose the highest velocity (or largest displacement) point on the resonator to which the transducer drive force is applied, i.e., over which the drive electrode overlaps. In the two-port ring resonator of Fig. 9.4(a), the drive electrodes overlap the ring at its inner perimeter, while the sense electrodes at its outer. Since the desired contour mode-shape here exhibits radial symmetry, any point along the inner edge of the ring can serve as the reference point. This means the core equivalent mass and stiffness for the ring merely takes on the value of Eqns. (A.28) and (A.29), or

$$m_{mre} = m_{mr}(r_i, 0) \quad \text{and} \quad k_{mre} = k_{mr}(r_i, 0) \quad (\text{A.30})$$

Expressions for the equivalent damping then readily follow from

$$c_{mre} = \frac{\omega_{om} m_{mre}}{Q} = \frac{k_{mre}}{\omega_{om} Q} = \frac{\sqrt{k_{mre} m_{mre}}}{Q} \quad (\text{A.31})$$

Since the support attachment locations of Fig. 9.4(b) are conveniently situated along the inner circumference of the ring, the springs representing the support beams can be directly attached to the mass of the circuit representing the ring. Otherwise, if a support were attached to a location moving at a different velocity from the ring's inner circumference, such as in Fig. 9.4(a), a velocity transformer would be needed between the ring mass-spring-damper and the coupling beam  $T$ -network to model the difference in velocity, as is commonly done in micromechanical filter design[39], [40].

As an example, for the measured 3-GHz 2<sup>nd</sup> mode spoke-supported diamond ring of this work with  $r_i = 13.8\mu\text{m}$ ,  $r_o = 16.6\mu\text{m}$ , and  $h = 2\mu\text{m}$ , the equivalent stiffness  $k_{mre}$  is 0.371 GN/m, which is substantially larger than the 4.5 MN/m posted by previous VHF micromechanical polysilicon disk resonators. Also, note that since the velocities of all points at the inner (and outer) circumference of the ring are independent of  $\theta$ , determination of the equivalent mass and stiffness of a radial contour mode ring does not require the complex integration needed to obtain accurate model parameters for Wine-Glass and extensional Wine-Glass mode resonator counterparts [13], [80].

### A.4.2 Lumped Parameter Electrical Equivalent Circuit

Having determined the lumped parameter mechanical equivalent circuit for the ring, an electrical equivalent circuit can now be generated to model the action of applied electrical signals that drive the ring into resonance and to predict the magnitudes and phases of the ensuing output currents. To be amenable to circuit simulation via well-established software, like SPICE, this circuit should utilize only electrical elements. Pursuant to this, dualities between the roles of mass, stiffness, and damping, and inductance, capacitance, and resistance, in the respective differential equations governing mechanical and electrical dynamics allow one to equate the different quantities as follows [39]:

$$l_x = m_{mre}; \quad c_x = 1/k_{mre}; \quad r_x = c_{mre} \quad (\text{A.32})$$

where mass, stiffness, and damping values corresponding to input electrode radial locations, i.e., along the inner edge of the ring, are chosen by convention.

There are six electrodes surrounding the ring of Fig. 9.4, and thus six distinct ports through which to access the device, each of which can be used as an input, an output, or for something else, e.g., electrical stiffness-based frequency pulling. A complete model should include the electrical stiffness contributions from each port and be general enough to be independent of whether a port is used for input or output. It should also model the stiffness contributions from the supports described in Section A.3, and be general enough to model the effect of attaching them at locations other than the inner ring circumference. In other words, the circuit model must account for the velocity transformation that ensues when attaching supports in this manner.

Figure A.7 presents a lumped parameter electrical equivalent circuit that satisfies all of the above criteria for the spoke-supported ring of Fig. 9.4. Here, both the electrical-to-mechanical transformations occurring at the electrode-to-resonator capacitive gaps, as well as the velocity transformations occurring between the inner and outer ring edges, are all modeled by transformers that specify the particular transformations via their turn ratios.

Transformers also model the velocity transformation between the rings inner edge and the attachment location of the support beams. For the case of Fig. 9.4, since the T-network-modeled support beams attach to the ring at its inner edge, so are at the same velocity as the lumped lcr reference point, the turns ratios of the transformers between the ring and each support beam are simply 1:1. This would not be the case if the supports attached to the outer ring edge, or at any location other than the inner ring edge.

The turns ratio  $\eta_{en}$  modeling the electromechanical conversion at the  $n$ th port is easily deciphered by first considering the functional behavior of an ideal transformer, then inspecting Eqn. (A.1) to find

$$\eta_{en} = V_{Pn} \frac{\partial C_{oen}}{\partial r} = \frac{V_{Pn} C_{oen}}{d_o} = V_{Pn} \frac{\epsilon_0 \theta_n h r_{en}}{d_o^2} \quad (\text{A.33})$$

where  $h$  is the ring thickness,  $C_{oen}$  and  $V_{Pn}$  are the overlap capacitance, and dc voltage, respectively, across the  $n$ th electrode-to-resonator gap, and  $\theta_n$  and  $r_{en}$  are the subtended

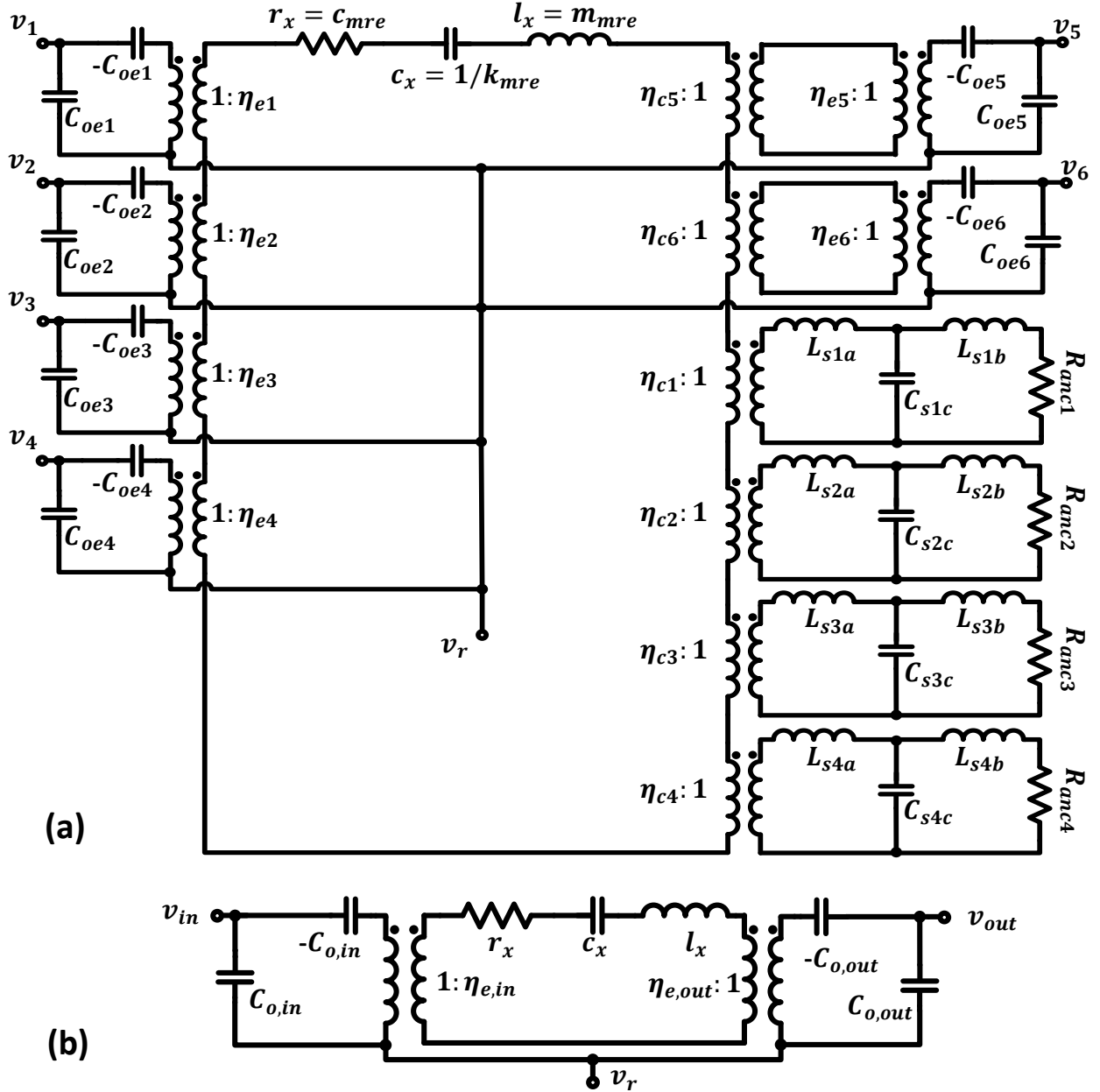


Figure A.7: (a) Complete equivalent circuit model for a spoke-supported ring resonator with four inner (electrode 1-4) and two outer (electrode 5-6) electrodes. (b) Physically consistent model using actual values of damping, stiffness and mass for elements in a two-port configuration when all input electrodes and output electrodes are connected respectively as shown in Fig. 9.4(a) and (b).

angle and radial coordinate location, respectively, of the  $n$ th electrode. Note that this coupling factor depends only on the electrode-to-resonator overlap geometry, the dielectric constant of the capacitor, and the voltage applied across it—just as it should.

The turn ratios modeling velocity transformations from the inner disk edge to the outer edge (that occurs between inner and outer electrodes) can be determined with similar reference to an ideal transformer and by inspecting transfer functions specifying the relationship between velocity magnitudes at different locations. For example, the relationship between velocity at a point on the inner ring edge and that at an outer ring edge can be expressed using Eqn. (A.27) as

$$\frac{v(r_o)}{v(r_i)} = \frac{\Re(r_o)}{\Re(r_i)} \quad (\text{A.34})$$

which can also be expressed in terms of equivalent mass or stiffness by

$$\frac{v(r_o)}{v(r_i)} = \pm \frac{\sqrt{KE_{tot}/m_{reo}}}{\sqrt{KE_{tot}/m_{rei}}} = \pm \sqrt{\frac{m_{rei}}{m_{reo}}} = \pm \sqrt{\frac{k_{rei}}{k_{reo}}} \quad (\text{A.35})$$

where  $k_{rei}$  and  $k_{reo}$  are the equivalent dynamic stiffnesses that include both mechanical and electrical components, at the inner and outer ring edges, respectively; and  $m_{rei}$  and  $m_{reo}$  are the corresponding dynamic masses that using Eqn. (A.28) simply take the forms  $m_{rei} = m_{mr}(r_i, 0)$  and  $m_{reo} = m_{mr}(r_o, 0)$ , respectively. In the circuit configuration of Fig. 9.4, the turns ratios for each of the velocity transformers between the ring (referenced at its inner edge) and its (identical) outer electrodes simply become this same ratio:

$$\eta_{c5} = \eta_{c6} = \frac{v(r_o)}{v(r_i)} = \frac{\Re(r_o)}{\Re(r_i)} = \pm \sqrt{\frac{m_{rei}}{m_{reo}}} \quad (\text{A.36})$$

The 1<sup>st</sup> contour mode, shown Fig. 9.5(a), produces positive  $\eta_{c5}$  and  $\eta_{c6}$ , as the inner and outer radii moving in concert imply current going into the inner electrodes in phase with current coming out of the outer electrodes (i.e. 0° phase shift). On the other hand,  $\eta_{c5}$  and  $\eta_{c6}$  for the 2<sup>nd</sup> contour mode (Fig. 9.5(b)) are negative since the inner and outer ring edges move in opposite radial directions, producing 180° phase shifted input and output currents.

Finally, static capacitors  $C_{on}$  model the physical electrode-to-resonator overlap capacitance at each port  $n$ . Note how the bottom terminals of these capacitors all go to a terminal that represents the physical conductive ring structure. In the normal case where the resonant structure is connected to the dc-bias voltage  $V_P$ , this terminal in the small-signal equivalent circuit should go to ground. Sometimes, however, an ac signal is applied to the structure terminal to effect mixing for certain applications [43], in which case the terminal in the small-signal circuit should receive the ac source. In either case, one must be careful to include any series resistance present between the ring edge overlapping the electrode and the ultimate point where the dc-bias or ac voltage is applied, as this resistance can heavily influence the performance of devices when used in applications such as filters and oscillators.

### A.4.3 Reduced Model

The circuit of Fig. A.7(a) provides a very general model for the device of Fig. 9.4, where the ports can be assigned to different purposes at will. In practice specification of port purpose greatly simplifies the equivalent circuit, as shown in Fig. A.7(c), which presents the equivalent circuit in Fig. A.7(a) corresponding to rings wired as in of Fig. 9.4(a) and (b). Here, the ring in Fig. 9.4(a) uses all inner electrodes as input and all outer electrodes as output while the ring in Fig. 9.4(b) splits both inner and outer electrodes in half for use as input and output. The constituent electrodes for each input and output can be combined into one equivalent input electrode and one output electrode, with electromechanical coupling factors modified as

$$\begin{aligned}\eta_{e,in} &= \eta_{e1} + \eta_{e2} + \eta_{e3} + \eta_{e4} \\ \eta_{e,out} &= |\eta_{c5}| \eta_{e5} + |\eta_{c6}| \eta_{e6}\end{aligned}\tag{A.37}$$

$$\begin{aligned}\eta_{e,in} &= \eta_{e1} + \eta_{e2} + |\eta_{c5}| \eta_{e5} \\ \eta_{e,out} &= \eta_{e3} + \eta_{e4} + |\eta_{c6}| \eta_{e6}\end{aligned}\tag{A.38}$$

where  $\eta_{e1}$  to  $\eta_{e6}$  are defined in Eqn. (A.33) while  $\eta_{c5}$  and  $\eta_{c6}$  are defined in Eqn. (A.36). Equations (A.37) and (A.38) correspond to input and output electromechanical coupling factors for rings with electrodes configured as in Fig. 9.4(a) and Fig. 9.4(b), respectively. The equivalent input and output electrode-to-resonator overlap capacitances becomes

$$\begin{aligned}C_{o,in} &= C_{oe1} + C_{oe2} + C_{oe3} + C_{oe4} \\ C_{o,out} &= C_{oe5} + C_{oe6}\end{aligned}\tag{A.39}$$

$$\begin{aligned}C_{o,in} &= C_{oe1} + C_{oe2} + C_{oe5} \\ C_{o,out} &= C_{oe3} + C_{oe4} + C_{oe6}\end{aligned}\tag{A.40}$$

where Eqns. (A.39) and (A.40) correspond to ring with electrodes configured as in Fig. 9.4(a) and Fig. 9.4(b), respectively.

The circuits of Fig. A.7(a) or (c) are the most useful for electromechanical design, since they support more general I/O port configurations, and they fully model all relevant design aspects of the spoke-supported ring resonator, from the amount of electrode-to-resonator overlap and gap spacing needed to attain a given coupling factor, to the impact that slight deviations from quarter-wavelength of the couplers have on resonance frequency and  $Q$ , to the degree to which external elements affect electrical stiffness and in turn impact the resonance frequency. However, for comparison with other tank circuits, e.g., quartz crystals, equivalent electrical  $LCR$  circuit elements are sometimes desirable. The expressions for the equivalent electrical elements result from merely reflecting the circuit of Fig. A.7(c) through the leftmost transformer. Doing so yields

$$R_x = \frac{\sqrt{k_{re} m_{mre}}}{Q \eta_{e,in} \eta_{e,out}}; \quad L_x = \frac{m_{mre}}{\eta_{e,in} \eta_{e,out}}; \quad C_x = \frac{\eta_{e,in} \eta_{e,out}}{k_{re}} \quad (\text{A.41})$$

Using Eqn. (A.41), the expression for the electromechanical coupling factor ( $C_x/C_o$ ) of the 1<sup>st</sup> electrode, which effectively equals the popular  $k_{eff}^2$  at low values, takes the form for the 2<sup>nd</sup> contour mode:

$$(C_x/C_o) \approx \frac{\varepsilon_0 \theta_1}{2\pi^3 \Lambda (1 + r_o/r_i)} \cdot \frac{V_{P1}^2}{d_o^3 f_o \sqrt{E \cdot \rho}} \quad (\text{A.42})$$

where  $\Lambda$  relates the static mass of the ring to its dynamic mass and depends on the mode shape function (A.11). From Eqn. (A.42), ( $C_x/C_o$ ) depends most heavily on bias voltage,  $V_{P1}$ , and electrode-resonator gap,  $d_o$ , where the latter shows a strong third power dependence. In fact, a  $10\times$  increase in dc-bias  $V_{P1}$  and a similar decrease in gap spacing  $d_o$  yields a 5 order of magnitude increase in ( $C_x/C_o$ ), giving an indication of just how adjustable this parameter is, given a capable technology. Note also the importance Young's modulus  $E$  and density  $\rho$ , where materials with smaller  $E \cdot \rho$  products yield better ( $C_x/C_o$ ). For example, polysilicon's  $E \cdot \rho$  of  $3.45 \times 10^{14}$  Pa $\cdot$ kg/m<sup>3</sup> is 12 times smaller than the  $4.19 \times 10^{15}$  Pa $\cdot$ kg/m<sup>3</sup> of diamond, which yields a 3.5 times better ( $C_x/C_o$ ) for designs using the same frequency, gap spacing, and bias voltage.

## Appendix B

# Planarized Process Traveler

The process traveler in the following pages is for a planarized process run using 3- $\mu\text{m}$  polysilicon as its interconnect layer.

*The rest of this page is intentionally left blank.*

1. Start with 2 blank Si wafers
2. Scribe wafers on the front, near right side of major flat
3. POCL<sub>3</sub> dope
  - Tool: tystar13
  - Recipe: 13POCL3A
  - Temp: 1050°C
  - Time: 02:00:00 + 01:00:00
  - Note: Remove PSG after this step on these two wafers with msink8 5:1 BHF dip
4. Pre-furnace cleaning
  - Tool: msink6, msink8
  - Step: piranha clean
  - Temp: 120°C
5. Isolation oxide deposition
  - Tool: tystar12
  - Recipe: 12SULTOA
  - Temp: 450°C
  - Time: 04:30:00
  - Goal: 30,000Å
6. Isolation oxide densification
  - Tool: tystar3
  - Recipe: 3N2ANNLA
  - Temp: 950°C
  - Time: 00:30:00
7. Metrology: isolation oxide thickness
  - Tool: Nanospec
  - Recipe: Program #1
  - Result: 27778(Å)
8. Standard UV resist coating – for PM marks
  - Tool: svgcoat6
  - Recipe: 1-2-1 (1.48 krpm spin speed)
  - Temp: 130°C
  - Note: Run three dummies first
9. Expose PM marks
  - Tool: ASML
  - Job: MAXFIELD\_DIE
  - Field: PM layer
  - Mask: COMBI reticle
  - Energy: 18mJ
10. Develop PM marks
  - Tool: svgdev6
  - Recipe: 1-1-9
  - Temp: 130°C
  - Note: Run three dummies first
11. Hard bake resist
  - Tool: uvbake
  - Recipe: Program U
12. Etch PM marks into isolation oxide
  - Tool: centura-mxp
  - Recipe: MXP-OXSP-ETCH
  - 500W, 200mT, Ar:120, CF<sub>4</sub>:10, CHF<sub>3</sub>:50
  - rate: 3,100A/min
  - Time: 180 s
  - Note: Inspect etched marks under microscope
13. Ash resist
  - Tool: matrix
  - Recipe: 400W
  - Time: 150 s
14. Pre-furnace cleaning
  - Tool: msink8, msink6
  - Step: piranha clean
  - Temp: 120°C
15. Isolation nitride deposition
  - Tool: tystar17
  - Recipe: LSNSTDA.017
  - 100DCS, 25NH<sub>3</sub>, 140mTorr
  - Temp: 835°C
  - Time: 02:30:00
  - Thick: 4344Å

16. Thick poly interconnect deposition  
 Tool: tystar16  
 Recipe: 16SUPLYA  
 Temp: 615°C  
 Time: 04:00:00  
 Goal: 30,000Å  
 Note: Add two 1,000Å oxide monitors
17. POCL<sub>3</sub> doping  
 Tool: tystar13  
 Recipe: 13POCL3A  
 Temp: 1050°C  
 Time: 02:00:00 + 01:00:00  
 Note: This serves as stress anneal as well
18. Clean PSG over poly  
 Tool: msink8  
 Recipe: 5:1 BHF tank  
 Time: 10 min
19. Metrology: Poly-1 thickness  
 Tool: Nanospec  
 Recipe: Program #4  
 Notes: Measure poly over 1,000Å oxide monitors  
 Result: 26822 (Å)
20. Metrology: Poly-1 sheet resistance  
 Tool: resmap  
 Notes: Measure poly over 1,000Å oxide monitors  
 Result: 2.1888(Ω/sq)
21. Standard UV resist coating – for Poly1  
 Tool: svgcoat6  
 Recipe: 1-2-1 (1.48 krpm spin speed)  
 Temp: 130°C  
 Note: Run three dummies first
22. Expose interconnect  
 Tool: ASML  
 Job: MAXFIELD\_DIE  
 Mask: ThickPly1  
 Energy: 25mJ
- Notes: Could try exposure matrix on dummy first.
23. Develop resist  
 Tool: svgdev6  
 Recipe: 1-1-9  
 Temp: 130°C  
 Note: Run three dummies first
24. Descum  
 Tool: technics-c  
 Recipe: 50W, O<sub>2</sub> plasma  
 Time: 1 min
25. Hard bake resist  
 Tool: uvbake  
 Recipe: Program U
26. Etch thick poly  
 Tool: sts2  
 Recipe: DEEP SILICON 1  
 (Passivation: 7sec, 18mT, C<sub>4</sub>F<sub>8</sub>:80,  
 Coil: 600W, Bias: 0W  
 Etch: 10sec, 35mT, SF<sub>6</sub>:130, O<sub>2</sub>:13  
 Coil:600W, Bias:20W)  
 Time: 42 cycles (17 sec per cycle)
27. Strip PR  
 Tool: matrix  
 Recipe: 400W  
 Time: 150 s
28. Pre-furnace cleaning  
 Tool: msink8, msink6  
 Step: piranha clean  
 Temp: 120°C
29. Planarization oxide deposition - HTO  
 Tool: tystar17  
 Recipe: HTOSTDA.017  
 Temp: 910°C  
 Time: 12:24:00  
 Goal: 3.14 μm

30. CMP interconnect layer  
 Tool: cmp  
 Recipe: Tristan\_remove  
 Notes: CMP until all poly traces are exposed. Verify trace conductivity in probe station. During this CMP step, the backside CMP should be done to reduce wafer bow. Normally it is not needed to do another backside etch to correct wafer bow
31. Cleaning after CMP  
 Step-1  
 Tool: sinkcmp  
 Notes: QDR water rinse, 4 cycles. Follow with manual cleaning with sponge. Then the ultrasonic bath with NH<sub>4</sub>OH in DI solution for 10 minutes.  
 Step-2  
 Tool: misnk8  
 Notes: Piranha clean for 15 mins. Follow with QDR DI rinse. 5:1 BHF dip for 45 seconds, followed by QDR DI rinse. Then spin dry wafers. This cleaning step is very important to remove contamination from CMP process.
32. SEM after CMP  
 Tool: LEO or FEI  
 Notes: Look for dishing, key holes, surface pitting, dried residue and other contamination.
33. Metrology: wafer bow  
 Tool: flexus  
 Note: High compressive stress expected from HTO thickness imbalance on the backside of the wafer after CMP  
 Result: ~15 and ~17.2 (μm)
34. Metrology: cmp'ed poly interconnect sheet res.  
 Tool: Wentworth probe station
35. Metrology: Feedthrough from just poly-1  
 Tool: Lakeshore probe station  
 Recipe: Use GSG probes, typical filter pads  
 Result: \_\_\_\_\_(dB)
36. Pre-furnace cleaning - for LSN wafers  
 Tool: msink8, msink6  
 Step: piranha clean  
 Temp: 120°C
37. Bottom sacrificial oxide deposition  
 Tool: tystar12  
 Recipe: 12SULTOA  
 Temp: 450°C  
 Time: 00:45:00  
 Goal: 5,000Å  
 Note: Add 2 blank Si monitor wafers
38. Bottom sacrificial oxide densification  
 Tool: tystar3  
 Recipe: 3N2ANNLA  
 Temp: 950°C  
 Time: 00:30:00
39. Metrology: Bottom sacrificial oxide thickness  
 Tool: Nanospec  
 Recipe: Program #1  
 Result: ~4700 (Å)
40. Standard UV resist coating – for Stem  
 Tool: svgcoat6  
 Recipe: 1-2-1 (1.48 krpm spin speed)  
 Temp: 130°C  
 Note: Run three dummies first
41. Expose stem  
 Tool: ASML  
 Job: MAXFIELD\_DIE  
 Mask: StemMask  
 Energy: 28mJ
- Recipe: Use 4-pt probe test structure  
 Result: 2.33 and 2.4 (Ω/sq)

- Notes: Could try exposure matrix on dummy first
- Note: Follow with standard QDR and spin dry, then go to poly furnace ASAP.
42. Develop resist  
Tool: svgdev6  
Recipe: 1-1-9  
Temp: 130°C  
Note: Run three dummies first
43. Hard bake resist  
Tool: uvbake  
Recipe: Program U
44. Descum  
Tool: technics-c  
Recipe: 50W, O<sub>2</sub> plasma  
Time: 1 min
45. Etch stem holes in to oxide  
Tool: sts-oxide  
Recipe: C4F8: 15sccm  
He: 174sccm; H<sub>2</sub>: 8sccm; 13.56MHz Coil: 1500W; 13.56MHz Platen: 350W; Main Press: 4mTorr;  
Etch Rate: 4034Å/min  
Number of cycle: 6  
each cycle: 30sec each cycle.  
Time: 180 s (includes 150% over etch)
46. Strip PR  
Tool: matrix  
Recipe: 400W  
Time: 150 s
47. Pre-furnace cleaning  
Tool: msink8, msink6  
Step: piranha clean  
Temp: 120°C
48. Wet HF dip before structural poly deposition  
Tool: msink6  
Step: 10:1 HF bath dip 45sec to 1 min, right after piranha.
49. Structural poly deposition  
Tool: tystar16  
Recipe: 16SUPLYA  
Temp: 615°C  
Time: 03:30:00 – for 2um devices  
Note: First run a dummy on 1000Å oxide test wafer with NO real wafers to determine the dep. rate and adjust the given times. Add two 1000Å test wafers with process wafers for etch tests.
50. POCL<sub>3</sub> doping  
Tool: tystar13  
Recipe: 13POCL3A  
Temp: 1050°C  
Time: 02:00:00 + 01:00:00  
Note: This serves as stress anneal as well
51. Clean PSG over poly  
Tool: msink8  
Recipe: 5:1 BHF tank  
Time: 5 min
52. Metrology: Poly-2 thickness  
Tool: Nanospec  
Recipe: Program #4  
Notes: Measure poly over 1,000Å oxide monitors  
Result: 20000(Å)
53. Metrology: Poly-2 sheet resistance  
Tool: resmap  
Notes: Measure poly over 1,000Å oxide monitors  
Result: 3.13 (Ω/sq)
54. Hard mask oxide deposition  
Tool: tystar12  
Recipe: 12SULTOA  
Temp: 450°C  
Time: 02:00:00

- Goal: 12,000Å  
Note: Add one blank Si monitor.
55. Hard mask oxide densification  
Tool: tystar3  
Recipe: 3N2ANNLA  
Temp: 950°C  
Time: 00:30:00
56. Metrology: hard mask oxide thickness  
Tool: Nanospec  
Recipe: Program #1  
Result: 12641(Å)
57. Standard UV resist coating – for Poly-2  
Tool: svgcoat6  
Recipe: 1-2-1 (1.48 krpm spin speed)  
Temp: 130°C  
Note: Run three dummies first
58. Expose Structural layer  
Tool: ASML  
Job: MAXFIELD\_DIE  
Mask: Structure  
Energy: 8.5mJ  
Note: Run exposure matrix on dummy poly2+hard mask, pick the best energy
59. Develop Structural layer  
Tool: svgdev6  
Recipe: 1-1-9  
Temp: 130°C  
Note: Run three dummies first
60. Descum  
Tool: technics-c  
Recipe: 50W, O<sub>2</sub> plasma  
Time: 1 min
61. Hard bake resist  
Tool: uvbake  
Recipe: Program U
62. Etch oxide hard mask  
Tool: sts-oxide  
Etch Recipes (Zyren-oxide-etch (APS)no1-2): C4F8: 15sccm; He: 174sccm; H<sub>2</sub>: 8sccm; 13.56MHz Coil: 1500W; 13.56MHz Platen: 350W; Main Press: 4mTorr; Etch Rate: 4034Å/min (According to Zeying); Did 30% overetch of 12641Å oxide.  
Number of cycle: 8  
each cycle: 30sec each cycle.
63. Strip PR  
Tool: matrix  
Recipe: 400W  
Time: 150 s
64. Etch Structure into Poly-2  
Tool: lam8  
Recipe: Custom recipe  
RF 250W, Bias 60W, 10mT, Cl<sub>2</sub>:10, HBr:150, O<sub>2</sub>:1  
rate: Obtain from test wafer  
Time: Obtain from test wafer  
Note: Monitor endpoint while etching. Etch test wafers and SEM them before etching process wafers.  
Did 60sec overetch with a slightly different recipes (15mT, 250W, 45W bias, 50HBr, 1O<sub>2</sub>, 3He). It is critical to take SEM of the etch dummy wafer to make sure we have a good sidewall and there is no serious polymer issue before moving forward with the real process wafers.
65. Polymer removal after Lam8 etch  
Step 1  
Tool: msink18  
Recipe: EKC270, temperature: 70C, 10 minutes

- Step 2 (effective for HBr etches in literature)  
 Tool: msink6  
 Recipe: 20:1 HF bath  
 Time: 45 sec
66. Clean wafers after backside etch  
 Tool: msink8, msink6  
 Step: piranha clean  
 Temp: 120°C
67. Sidewall Oxide Deposition – 50nm  
 Tool: tystar17  
 Recipe: HTOSTDA.017  
 Temp: 910°C  
 Time: Run monitor wafer, use past data for start. If the tool has been down for a while, make sure to do a pin hole test by dipping the dummy wafer in to KOH to see whether there is any undercuts. Time used here is 13 min 30 sec.  
 Goal: 5,00Å
68. Etch backside oxide to correct wafer bow  
 Tool: sts-oxide  
 Recipe: Oxide etch (APS) no 1-2  
 (4mT, C<sub>4</sub>F<sub>8</sub>: 15, H<sub>2</sub>: 8, He: 174, RF: 1500W; Bias: 350W, 0.3µm/min)  
 Time: 5min  
 Note: This step is only needed when the wafer bow is high
69. Etch backside poly to correct wafer bow  
 Tool: sts2  
 Recipe: DEEP SILICON 1  
 (Passivation: 7sec, 18mT, C<sub>4</sub>F<sub>8</sub>:80, Coil:600W, Bias: 0W  
 Etch: 10sec, 35mT, SF<sub>6</sub>:130, O<sub>2</sub>:13, Coil:600W,Bias: 20W)  
 Time: 32 cycles (17 sec per cycle)  
 Note: Check the wafer's bow before you do this step
70. Metrology: wafer bow  
 Tool: flexus  
 Note: Accept if less than 15µm bow
71. Thick UV resist coating – for Anchor  
 Tool: svgcoat6  
 Recipe: 1-3-1 (7 krpm spin speed)  
 Use Deep UV resist.  
 Temp: 140°C – IMPORTANT!  
 Note: Run three dummies first
72. Expose Anchor  
 Tool: ASML  
 Job: MAXFIELD\_DIE  
 Mask: Anchor  
 Energy: 26mJ  
 Notes: Need to do exposure matrix to make sure the small anchor area are exposed.
73. Develop resist  
 Tool: svgdev6  
 Recipe: 1-1-9  
 Temp: 110°C – IMPORTANT!  
 Note: Run three dummies first
74. Hard bake resist  
 Tool: uvbake  
 Recipe: Program D?
75. Descum  
 Tool: lam6  
 Recipe: 100sccm Ar, 50sccm O<sub>2</sub>, 100W, 70m torr.  
 Time: 1 min  
 Note: Need to do a better uniform descum here. Therefore, lam 6 was used instead of standard technics-c. Ar is needed for low reflected RF.

76. Etch anchor in to oxide  
Tool: lam 6  
Recipe: lam 6 main etch.  
Time: 30 s on and 40 s off to make sure there is no PR burn.
77. Strip PR  
Tool: matrix  
Recipe: 400W  
Time: 5 min
78. Pre-furnace cleaning  
Tool: msink8, msink6  
Step: piranha clean  
Temp: 120°C
79. Wet HF dip before electrode poly deposition  
Tool: msink6  
Step: 25:1 HF bath, right after piranha and QDR  
Time: 10-15 sec – be careful of the sidewall oxide!  
Note: Follow with standard QDR and spin dry, then go to poly furnace ASAP.
80. Electrode poly deposition 1  
Tool: tystar16  
Recipe: 16SUPLYA  
Temp: 615°C  
Time: 4:15:00 – for 2.5um  
Note: This is the first poly deposition so that the electrode poly is conductive.
81. POCL<sub>3</sub> doping  
Tool: tystar13  
Recipe: 13POCL3A  
Temp: 1050°C  
Time: 02:00:00 + 01:00:00  
Note: This serves as stress anneal as well
82. Clean PSG over poly  
Tool: msink8  
Recipe: 5:1 BHF tank  
Time: 10 min
83. Metrology: Poly-3 thickness  
Tool: Nanospec  
Recipe: Program #4  
Notes: Measure poly over 1,000Å oxide monitors  
Result: \_\_\_\_\_(Å)
84. Metrology: Poly-3 sheet resistance  
Tool: resmap  
Notes: Measure poly over 1,000Å oxide monitors  
Result: 1.2036 (Ω/sq)
85. Pre-furnace cleaning  
Tool: msink8, msink6  
Step: piranha clean  
Temp: 120°C  
Note: dip in 10:1 BHF for more than 5min to remove native oxide.
86. Electrode poly deposition 2  
Tool: tystar16  
Recipe: 16SUPLYA  
Temp: 615°C  
Time: 4:45:00 – for 2.8um  
Note: Most of this second poly layer will be cmp'ed off. Therefore, no doping is needed.

87. CMP Electrode layer  
 Tool: cmp  
 Recipe: First Backside 6PSI DF, 4 PSI BP, 8 min in 4 min cycles. Condition the pad between each cycle.
- CMP front side~ 12min 4PSI DF, 2PSI BP, 33 RPM. 2 min cycles. Condition the pad every 4 min. This breaks through most of the poly. Then a gentle CMP step should follow.
- CMP front side 1 min cycles 2.5 PSI DF, 0.5 PSI BP 1 min cycles fill done ~ 2 cycles each.
- Cleaning after CMP  
 Step-1  
 Tool: sinkcmp  
 Notes: QDR water rinse, 4 cycles. Follow with manual cleaning with sponge. Then the ultrasonic bath with NH<sub>4</sub>OH in DI solution for 10 minutes. QDR and then hand dry.
88. Metrology: wafer bow  
 Tool: flexus  
 Result: ~14 (μm)
89. PR coating for electrode litho: Standard UV resist coating  
 Tool: svgcoat6  
 Recipe: 1-2-1 (1.48 krpm spin speed)  
 Temp: 130°C  
 Note: Run three dummies first
90. Expose electrode  
 Tool: ASML  
 Job: MAXFIELD\_DIE  
 Mask: Poly3  
 Energy: 26mJ  
 Notes: Could try exposure matrix on dummy first
91. Develop resist  
 Tool: svgdev6  
 Recipe: 1-1-9  
 Temp: 110°C – IMPORTANT!  
 Note: Run three dummies first
92. Hard bake resist  
 Tool: uvbake  
 Recipe: program U
93. Die the wafer to quarters. At this point, it is not needed to etch the whole wafer.
94. Descum  
 Tool: technics-c  
 Recipe: 50W, O<sub>2</sub> plasma  
 Time: 1 min
95. Etch Poly3  
 Tool: sts2  
 Recipe: Standard smooth sidewall  
 Time: 22 cycle etch and 22 cycle dep.  
 Note: This will give about 30% overetch. Take SEM to make sure there is no stringers. This is not a big problem for electrode CMP'ed process.
96. Dies the quarter wafer and the device are ready for the release.
97. RUN COMPLETE

**The release procedure for very small gap device are very crucial in attaining high  $Q$  resonators especially dealing with small dies required by a few of the measurement presented in this work.**

After the dieing saw, you always have PR on your die.

NOTE: All the DI water steps here use fresh DI water. In all steps using dipper basket, rotate the basket gently with hand after every 1-2min. It is important to have a clean setup.

1. DI Water: 3-5min.
2. Acetone: 5 min (stirred with a stirrer). (only step to use stirrer)
3. DI Water (time is not important. )
4. Acetone: 5 min (a fresh one). Move around the die in the beaker 1-2 times.
5. DI water: 5 min
6. IPA: 5min. Move around the die in the beaker 1-2 times.
7. DI water: 2-3min
8. Clamp the die on the die holder (NOTE: Die holder should be wet). Then put the die holder in the dipper basket.
9. DI water: 5 min
10. RCA1: 5min
11. DI water: 5min (change the water 3-4 times)
12. RCA2: 5min
13. DI water: 5min (change the water 3-4 times)
14. Piranha: 10min
15. DI water: ~ 10 min (change water every 2 min)
16. HF 49%: 35min. Rotate the basket gently every 3-4min. Don't use Triton-X. It turns out to attack oxide under nitride severely on small dies. For large die, using Triton-X is a good idea.
17. DI Water: 20-30min. Change DI water every 5min. And rotate the basket every 2-3min.
18. Unclamp the die from the die holder.
19. Put it back in DI Water for 10 min to get rid of residue chemical.
20. Gentle N2 gun.
21. Hotplate 80C: 10min
22. Hotplate 90C: 10min
23. Hotplate 110C: 5 min.
24. Cold down: 2min.